Himanshu Kaul
St Anne's College

A Multi-Paradigm Modelling Framework for Simulating Biocomplexity

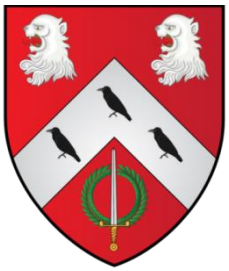

A thesis submitted for the degree of
Doctor of Philosophy
Michaelmas 2013

To my father, Dalip – the reason I dream; my grandfather, L. N. – the reason I think; my mother, Neelam – the reason I exist.

A thesis submitted for the degree of Doctor of Philosophy

A Multi-Paradigm Modelling Framework for Simulating Biocomplexity

By Himanshu Kaul, St Anne's College, Submitted Michaelmas 2013

Abstract

The following thesis presents a computational framework that can capture inherently non-linear and emergent biocomplex phenomena. The main motivation behind the investigations undertaken was the absence of a suitable platform that can simulate, both the continuous features as well as the discrete, interaction-based dynamics of a given biological system, or in short, dynamic reciprocity. In order to determine the most powerful approach to achieve this, the efficacy of two modelling paradigms, transport phenomena as well as agent-based, was evaluated and eventually combined. Computational Fluid Dynamics (CFD) was utilised to investigate optimal boundary conditions, in terms of meeting cellular glucose consumption requirements and exposure to physiologically relevant shear fields, that would support mesenchymal stem cell growth in a 3-dimensional culture maintained in a commercially available bioreactor. In addition to validating the default bioreactor configuration and operational parameter ranges as suitable towards sustaining stem cell growth, the investigation underscored the effectiveness of CFD as a design tool. However, due to the homogeneity assumption, an untenable assumption for most biological systems, CFD often encounters difficulties in simulating the interaction-reliant evolution of cellular systems. Therefore, the efficacy of the agent-based approach was evaluated by simulating a morphogenetic event: development of *in vitro* osteogenic nodule. The novel model replicated most aspects observed *in vitro*, which included: spatial arrangement of relevant players inside the nodule, interaction-based development of the osteogenic nodules, and the dependence of nodule growth on its size. The model was subsequently applied to interrogate the various competing hypotheses on this process and identify the one that best captures transformation of osteoblasts into osteocytes, a subject of great conjecture. The results from this investigation annulled one of the competing hypotheses, which purported the slow-down in the rate of matrix deposition by certain osteoblasts, and also suggested the acquisition of polarity to be a non-random event. The agent-based model, however, due to being inherently computationally expensive, cannot be recommended to model bulk phenomena. Therefore, the two approaches were integrated to create a modelling platform that was utilised to capture dynamic reciprocity in a bioreactor. As a part of this investigation, an amended definition of dynamic reciprocity and its computational analogue, dynamic assimilation, were proposed. The multi-paradigm platform was validated by conducting melanoma chemotaxis under foetal bovine serum gradient. Due to its CFD and agent-based modalities, the platform can be employed as both a design optimisation as well as hypothesis testing tool.

Statement of Originality

I hereby declare that this submission is my own work and to the best of my knowledge it contains no materials previously published or written by another person, or substantial proportions of material which have been accepted for the award of any other degree or diploma at the University of Oxford or any other educational institution, except where due acknowledgment is made in the thesis.

Any contribution made to the research by others, with whom I have worked at the University of Oxford or elsewhere, is explicitly acknowledged in the thesis.

I also declare that the intellectual content of this thesis is the product of my own work, except to the extent that assistant from others in the project's design and conception in style, presentation and linguistic expression is acknowledged.

Himanshu Kaul
8th November, 2013

Acknowledgments

I hope the reader, and those to whom this section is dedicated alike, will forgive me in my attempt to impose the gist of this thesis and the underlying philosophical thought on a section where the focus of my words should be anything but. However, the Fractalian links between the subject of my investigation and my attempt to produce this thesis, I am afraid, is too strong to ignore.

Like an actor on stage, a cricketer on the pitch, a cell in its environment, my system, technique, and 'expression' were influenced by multiple, heterogeneous, and non-linear interactions, that were guided by other actors (on stage and off it); initial and boundary conditions; and, ultimately, the seemingly unquantifiable, stochasticity. To each I am eternally grateful!

The universal random number generator worked in my favour on the occasions I needed it most. My admission and funding at Oxford were but two of a multitude of events beyond my control. When competing against the finest, a little something on your side can go a long way, and thank heavens for that! Oxford, with its rich traditions and unique structure, but more importantly its fearless, unfettered, and unreservedly ambitious students has been nothing short of inspiration to me. There are just too many people, places, and interactions that I am indebted to, to list here. However, they shall remain embedded in my consciousness, and in addition to being responsible for some lovely memories, they will continue to play a role in my on-going metamorphosis.

Still on the topic of environment, my most heartfelt thanks to the Engineering Science Department and St Anne's College for providing me the opportunity, as well as funding, to pursue the doctoral degree. I am especially indebted to Dr Anne Mullen and Principal Tim Gardam for their support, welfare and otherwise, during my stay at St Anne's College. Furthermore, the investigations conducted in this thesis would not have been possible without assistance from Prof Rod Smallwood and his research group at the University of Sheffield (Dr Salem Adra, Dr Mariam Kiran, and Dr Simon Coakley); and the ESI Group (Paris, France), especially Dr Mustafa Megahed who is responsible for making CFD-ACE+ platform available to the Fluidics and Biocomplexity Group (FBG), Oxford.

And, now to actors, with hope that our paths are forever intertwined!

First are the ones onstage. I will forever be grateful to Mrs Christine Foard, Mrs Donna Harper, and Ms Sarah Pinder, for without their efforts I would have never been able to make it to Oxford. They were always a source of hope and

encouragement at a time when I needed it most. I cannot thank them enough for their understanding, patience, and kindness.

Even though my project was a one-man-act, my life was enriched by the support I received from my colleagues. In particular, I am grateful to Drs Nick Hawker, Chao Wang, and Emilie Holland for their guidance that helped me morph into a computationalist. My discussions with Drs Cathy Ye, Julian George, and Jangho Lee were instrumental in facilitating an in-depth exploration of ideas, and reinforcing my understanding of the underlying Tissue Engineering concepts. Both Phillipus Putter and Nikolas Weissemuller deserve a special mention for being the people I could always bounce my ideas off of, and so does Katja Gera for single-handedly organising the FBG lab meetings. A special thanks to Malebogo Ngoepe for always encouraging me to "stay in school and don't do drugs". This is a piece of advice I shall take to my grave! Also, included in the honourable mention are Dr Paul Watton, Dr Brett Tully, Dr Alisa Selimovic, Haoyu Chen, Maria Pikoula, Jesse Boamah, and Katia Mandaltsi for their countless chit-chats and general merriment. It is an understatement to assume I would have survived the meanders of a doctoral degree, let alone retained my sanity, without any of the aforementioned names. However, my association with John Vardakis – a fierce critic, eccentric colleague, and a close personal friend – has been the most stimulating. Thank you, Johnny boy, for the rich, passionate, entertaining, though eventually pointless discussions we have had. Abusing my freedom of expression with you has been a pleasure!

I would also like to thank Dr Heiko Schiffter for agreeing to help me with the experimental side of my project, and being a selfless mentor. Acknowledgements are also due to Prof Brian Hall whom I only know through electronic correspondence on the subject of bone and cartilage condensations. Brian's piercing insight and depth of knowledge on the subject has given a special character to the osteogenic condensation model presented in this thesis. Very special thanks to Prof Zhanfeng Cui, who in picking up a phone call on one fateful night (3AM MST) in March 2008, became the reason for my arrival at Oxford. In his capacity as my co-supervisor, he has guided me ably, with precision and panache; but since that night has never picked up any of my phone calls!

Furthermore, I owe an enormous debt of gratitude to my supervisor Prof Yiannis Ventikos, who conducted himself more as a peer than a mentor. Any shred of confidence I have in my abilities as a researcher is a direct result of my interactions with him. Yiannis has been a kind, unassuming, and supportive supervisor – a man for all seasons – and I look forward to a more fruitful professional relationship with him in the future. I only hope that our agent-like interactions meant I was able to inspire him in some way, shape or form as well.

And, now time to travel backstage. It was my great fortune to meet Munish Sikka, Rani Subassandran, Soufia Siddiqi, and Julia (Camille) Hartley in Oxford. Their creative personalities, artistic flair, and enriching friendships have influenced my work in profound ways. My most enthusiastic acknowledgments are due to Prof Vincent Pizziconi and Ms Katayoun Seyedmadani for being my mentors and, more importantly, friends. Dr P, you are nothing short of brilliance and a true inspiration to me. The way I think has been shaped by the stimulating conversations I had with you. I owe a lot to you. Kathy, your friendship is a privilege and your company, a true pleasure. I find deep solace in the knowledge that you will be there to "kick my butt", if the need ever arose. Dr Guneet (Guga) Kalra and Abhinav (Gila) Saund, your friendship changed my life, and gave it the dimension I now find myself in. Every inch of my journey is a product of the time we shared, and I can never forget that. And, where will I be without my sister, Mansi Kaul, and cousins: Ranjana Jolly, Mayank Sharma, Kirty Jolly, and Ruchika Sharma? My childhood would have been monochromatic and stale had it not been for your company, allegiance, and love. I derive the meaning of my life from the moments we spent together. Acknowledgments are also due to my brother-in-law, Navdeep Minhas, for being a true gentleman.

And, finally, I would like to extend my sincerest gratitude to those who are the fundamental reason I could even think of embarking on this journey. Anil Sus: your company was soothing, and your approach to life a mellifluous melody. This world is poorer in your absence! Rajni Sharma: thank you for your unconditional support. You are an example I live my life by. Guru Dutt Mehta: dearest Nana daddy, thank you for being a father-figure in my life. I sorely miss your presence, your wisdom, and your loving and protective embrace. Pardeep Jolly: I can never fathom why you ever decided to walk the extra mile with me. My life would be incomplete without your guidance and affection. There is nothing I can do that will pay back the support I have received from you. Dalip Kaul: dear father, I miss you every day. Hopefully, you are smiling, wherever you are. Laxmi Narayan Kaul: thank you, papa daddy, for patiently bearing the brunt of my puerile inquiries and nurturing my philosophical sensibility. This thesis, and anything I have ever attempted to do, is a toast to your life! And, Neelam: thank you for being there, and supporting me through everything. Thank you for your rebukes, your love, your encouragement, and, above all, your sacrifice. I have not met God, but I am sure (s)he must have been created in Your image.

अहं अन्विषामी संकीर्णता संस्थानयोः तिमिरालोकयोः
ख्यापनशक्तियोः समावयमः

TABLE OF CONTENT

List of Figures

CHAPTER 4

CHAPTER 5

List of Tables

List of Boxes

Dissemination

Peer-Reviewed Articles

Published

Kaul H, Ventikos Y, Cui ZF. A Computational Analysis of the Impact of Mass Transport and Shear on three-dimensional Stem Cell cultures in perfused Micro-bioreactors. Chinese Journal of Chemical Engineering (In press), 2015.

Kaul H, Hall BK, Newby C, Ventikos Y. Synergistic activity of polarised osteoblasts inside condensations cause their differentiation. Scientific Reports, 2015, 5: 11838.

Kaul H and Ventikos Y. Dynamic Reciprocity Revisited. Journal of Theoretical Biology, 2015, 370: 205-208.

Kaul H and Ventikos Y. Investigating Biocomplexity through the *Agent-based Paradigm*. Briefings in Bioinformatics, 2015, 16(1): 137-152.

Kaul H and Ventikos Y. On the genealogy of Tissue Engineering and Regenerative Medicine. Tissue Engineering Part B Reviews, 2015, 21(2): 203-217.

Kaul H, Cui ZF, Ventikos Y. *A Multi-Paradigm Modeling Framework to simulate Dynamic Reciprocity in a Bioreactor*. PLoS One, 2013, 8(3): e59671.

Kaul H, Cui ZF, Ventikos Y. *A Coupled Agents-Transport Modelling Framework as a Design Tool for Bioreactors*. Histology and Histopathology, 2011, 26 (Supplement 1), 131-132.

Conferences

Talks

West Coast Developmental Biology Conference, Cambria, CA, Computational Techniques for Developmental Biology; 2013[i]

PGBioMed, Glasgow, UK, A Multi-Paradigm Modelling Framework to capture Dynamic Reciprocity; 2011

Tissue Engineering & Regenerative Medicine International Society (TERMIS) – EU, Granada, A Coupled Agents-Transport Modelling Framework as a design tool for Bioreactors; 2011

UK-Biomedical Engineering Society, University of Nottingham, Computational Modelling of Cell Growth in a Virtual Environment: A combined Agents-PDEs Approach; 2010

[i] I was unable to attend

Posters

12th Annual Meeting, International Society of Stem Cell Research, Vancouver, Canada, Osteocytes form due to concerted efforts of polarised osteoblasts in condensations; 2014.

Biomedical Engineering Society Annual Meeting, Atlanta, GA, USA, Capturing dynamic reciprocity using a multi-paradigm modeling framework; 2012[ii]

Biomedical Engineering Society Annual Meeting, Austin, TX, USA, A coupled Agents - Transport Modelling approach for bioreactor design; 2010

[ii] I was unable to attend

CHAPTER 1 Introduction

"When you measure what you are speaking about, and express it in numbers, you know something about it; but when you cannot measure it, when you cannot express it in numbers, your knowledge is of a meagre and unsatisfactory kind: it may be the beginning of knowledge, but you have scarcely, in your thoughts, advanced to the stage of science."

– Lord Kelvin

1.1 COMPUTATIONAL TISSUE ENGINEERING AND REGENERATIVE MEDICINE: WHY?

A scenario of novel therapy delivery that we should strive to achieve in the future would be described along these lines: A patient in need of a new organ visits a hospital. The clinicians, after noting patient-relevant details and conducting appropriate biopsies to extract cells from the patient's body, feed the customised data as well as the cells in an automated bioreactor, push the 'start' button, and in a matter of days retrieve the working organ. This synthetically devised organ being syngenic requires no immunosuppressants and is transplanted into the body of this patient without complications. An even more ambitious scenario would eliminate the need of surgery all together: the patient is given certain tissue-inducing substances and targeted cues that trigger regeneration of the failed organ (using nothing more than the molecules, proteins, cells, and genetic information already available) inside his/her body. The fact that we already possess the basic technological framework required to realise this concept (discussed in Chapter 2) should come as little surprise. However, upscaling laboratory conquests to allow mass production of products that can convert this platform technology into a viable therapeutic alternative will not occur until our understanding of the dynamics governing development and regeneration, as Lord Kelvin pointed out, is "*express(ed) it in numbers*", or, in other

words, quantified. This, in turn, will not be possible until relevant computational approaches based on accurate and fully descriptive ontologies of biological entities, such as the cell or the extra-cellular matrix, are advanced to the point where the three-dimensional development of a tissue, organ, or organism can be reproduced *in virtuo* and visualised. This thesis addresses some of the missing links by providing a modelling platform with suitable ontologies for both the cell as well as its microenvironment that has the capability to quantify the development of any cellular system and, thus, can help expedite the translation of experimental Tissue Engineering and Regenerative Medicine into a major clinical rehabilitator.

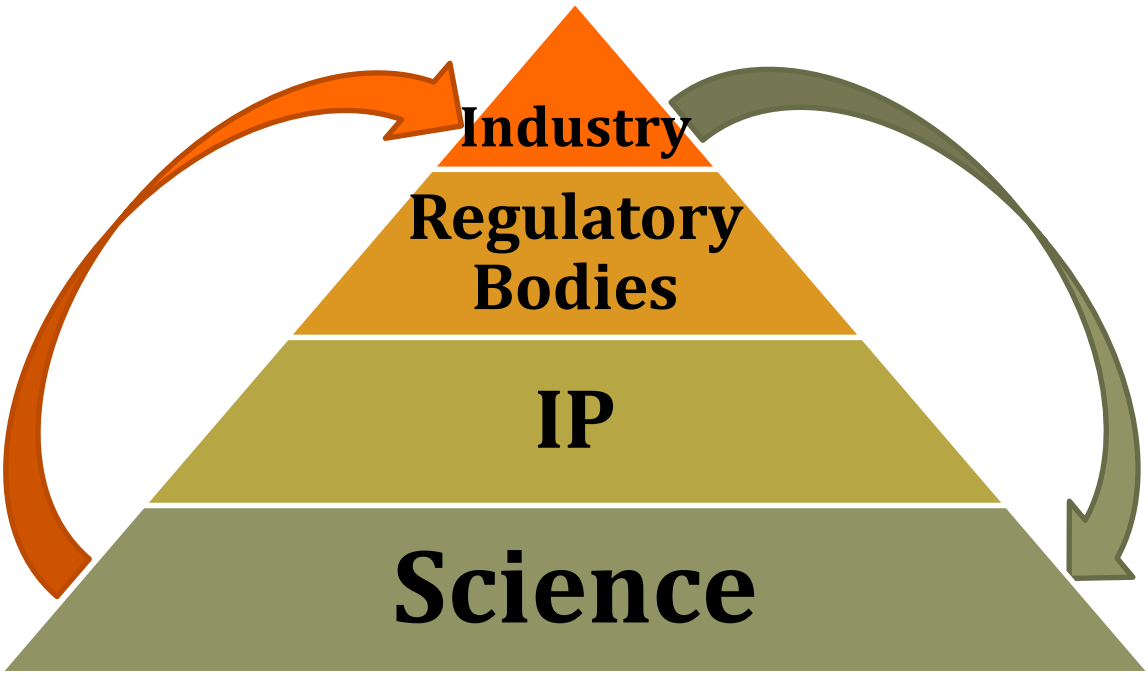

Figure 1. 1: The TERM Pyramid. The figure represents the four dynamically feeding sectors of the Science and Technology of Tissue Engineering and Regenerative Medicine. From base to top, each component plays a vital role in ensuring mass availability of TERM products, which in turn help accelearate our understanding of the basic Science. However, with the basic Science associated with TERM not quantitatively understood, upscaling the production of TERM related products as well as ensuring their viability and efficacy has been a significant issue, affecting the translation of this field from bench to bed-side.

Despite the experimental techniques of TERM, based on harnessing the regenerative potential of cells, showing tremendous promise as potential therapeutic and rehabilitation healthcare alternatives; upscaling that potential to meet clinical demands has presented the

community with hitherto impregnable challenges. Although this problem concerns the entire TERM ecosystem – science, industry, IP, and relevant regulatory mechanisms – the problem rests at the base of that pyramid (refer to Figure 1.1): the science being the stumbling block. Biological systems, including cells that form the functional unit of TERM, due to their inherent complex nature are treated primarily as *black-boxes*, at least in the context of regenerative medicine. Even instances where the role of certain key players is quantitatively known – for example, critical concentration of growth factors, elastic modulus of polymeric scaffolds, or spatial location of cells with respect to other structures inside a scaffold –, the overall experimental methodology remains of the trial and error flavour.

In the last 15 years, however, aided with the availability of increasingly powerful and sophisticated semi-conductor chips and customized way of packaging digital computing services,[1] the TERM community has made significant efforts in addressing this issue. Computational TERM entails encoding the biophysicochemical mechanisms of development or regeneration into mathematical algorithms or equations with tightly controlled, quantitative variables. When simulated, these computational models trace the spatiotemporal evolution of the relevant processes resulting in patterns or output that can be quantitatively verified. In doing so, computational TERM offers the means, via the manipulation of tightly controlled variables to not only understand normal system behaviour (during regeneration, for example) but also pathological departure from normality, quantitatively. Computational TERM, thus, offers a new paradigm to contextualise tissue engineering, regenerative medicine, and developmental biology, thereby providing further momentum to enable the translation of TERM-based therapies to clinic. More precisely, computational TERM in making available, for example, (i) 3D flowfields over and through scaffolds inside a bioreactor or the growing mass of cells inside a womb; (ii) shear stresses experienced and mechanotransduced by endothelial cells due to blood flow in vascular

constructs; (iii) interactions between cells; and (iv) 3D growth of tissue – can vastly aid our understanding of the governing principles that regulate development and regeneration. *New*, because it is only in the last 20 years[2] that interest has been generated in understanding the role of system hydrodynamics in influencing cellular behaviour. *New* also because most computational treatments generally abstract away cellular heterogeneity, system complexity, or the full array of cellular behaviours. It is worth reminding the reader that the interplay between local transport processes and the cell, as well as their impact on each other, still requires elucidation. Furthermore, as a research tool, computational TERM also provides a new perspective for looking at the evolution of biological systems that would not be possible by physical experimentation alone. Capturing flow-fields within a cell-seeded scaffold, which is under perfusion by a bioreactor with pulsating flow being a prime example of the novelty computational TERM has to offer. Moreover, aided by the highly detailed and insightful *visual depictions* that computer models offer, better designs (of devices such as the bioreactor or polymeric scaffold) can be proposed that provide optimal growing conditions for evolving biological structures (demonstrated in Chapter 3).

Furthermore, computational TERM offers an alternative mode of experimentation: *virtual numerical experimentation*, which is an exercise in condensing a lab into a computer, and the experiment into a program, with associated convenience, mobility, and relevant cost and ethical implications. Computational approaches can, therefore, be employed to inform the design and development of novel therapeutics and devices. A prime example of this application is in the design of bioreactors – devices that are employed to carry out controlled expansion and differentiation of cells. Depending upon the desired outcome, i.e. expansion or differentiation or both, computational analyses can be carried out to optimise bioreactor design so that the resulting bioreactor hydrodynamics influence cell fate in the intended manner. Similarly, if the cellular response to shear and transport is quantitatively

understood, the bioreactor design can be further optimised to ensure production of homogeneous cell populations. Such approaches can also be utilised to predict the outcome of a treatment course (as in the case of catheters for aneurysms[3]), and whether or not a particular intervention should be pursued. Moreover, in constructing models of biological systems or processes, such as the bronchi or osteogenesis, model parameters can be varied to understand variables contributing to pathologies (as demonstrated later in Chapter 4). The models can, thus, be utilised to test, *in silico*, clinical approaches that in turn can help devise protocols and methodologies to develop new drugs.

The challenge, however, is that biological systems being inherently complex and non-linear in nature and lacking a central organising structure evade the mechanistic undertones of most mathematical models, and, hence, are difficult to capture computationally. There are three aspects to this challenge. Firstly, the unavailability of a computational paradigm that can offer suitable representational formalisms, or ontologies, to map biological entities mathematically and handle the vast array of informational cues available to biological systems is the key reason quantifying them has been a challenge. Secondly, in order to simulate the complex behaviour of any biological system – whether it is a collection of proliferating cells in a Petri dish, polymeric scaffold, or uterus – the applied computational paradigm must be able to faithfully capture the dynamic interactions between cells and their microenvironment: encapsulated by the dynamic reciprocity principle. This requires a computational tool that can account for both the complexity of the microenvironment as well as the mutual dependence of cells on their microenvironment (and vice versa). While computational tools exist that can account for both environmental and cellular aspects of a biological system, these approaches tend to be limited, either due to the governing reductionist approach (continuum methods), significant computational costs (discrete methods), or lumped treatment of biological sub-components (statistical methods).

Thirdly, there are systems where reductionist principles struggle to provide the appropriate resolution required to quantify, explain, and predict global observable phenomena. These systems, called *complex systems*, are characterised by a multitude of parts that interact non-linearly with each other, with the interactions playing a pivotal role in shaping the macroscopic observables exhibited by them. Biological systems, which integrate the inherent structural, morphological, and genetic information with that available from their (micro)environment, are a special class of complex systems.

Computational tools utilised to model biological phenomena can be categorised, broadly, as continuum or discrete. Whereas the former describe the numerical changes of the variables that represent the system, the latter can indicate how and why the dynamics involving system components operate.[4] Continuum approaches, such as those used to address traditionally the governing laws of fluid or solid dynamics, employ differential equation-based models that may have numerical or approximate solutions. The underlying assumption, while employing the continuum approach, is that a system can be divided into infinitesimally small, identical, numerous, constituents, which obey the identified equations similarly. However, the isolated use of mathematical equations representing either a collection of cells or organisms or their (micro)environment do not lend themselves as the most precise form of ontologies for biological systems. While the continuum approach has been applied successfully to predict macroscopic observables such as regional cell numbers, traction forces, wound morphometry, to name a few, classic continua are not dynamic – unlike biological systems they do not change their material properties over time[1] (although of course numerous continuum computational methods that attempt to incorporate such variations have been proposed). Their shortcoming is even more pronounced when simulating emergent behaviour that *"arises through 'self-organisation' and that could not have otherwise been characterised a priori"*[5] – an event that is probably beyond the remit

of the continuum approach. Discrete approaches, on the other hand, represent and execute the models using operational descriptions in the form of computing programs.[6] The approach assumes that system behaviour can be captured by a set of rules that combine qualitative as well as quantitative information, thereby allowing each modelled entity to respond to its environment.[6] Discrete approaches, such as *cellular automata*[7,8] (CA) – that employ interacting *finite-state machines*[9] – or the cellular Potts modelling approach (CPM)[10] – which simulates systems by mapping *cells* to domains on a lattice, can capture (i) the non-homogeneous character of biological systems (which is also responsible for their complexity) and (ii) the emergence of global patterns from underlying rules, in a manner more faithful to cellular systems than their continuum counterparts.

Biological systems in addition to possessing a "physical" aspect display a "logical"[11] aspect as well. The physical aspect is associated with the mechanical attributes of the constituents: such as, chemotaxis, secretion, polarity, chemical reactions occurring within the environment or mechanical features of the extra-cellular matrix, etc. The logical aspect, on the other hand, relates to the functionality of the constituents in the overall system and the manner in which the function is carried out. The two methodologies, continuum and discrete, cannot, on their own, fully account for both aspects, at least practically.[iii] As such, they have been combined to produce hybrid models that can account for both the physical as well as logical aspects of biological constituents.[12-15]

The fundamental advantage offered by the hybrid paradigm is that it does not assume cellular homogeneity and, therefore, considers the contribution of each cell (or isolated cell

[iii] While the discrete approach allows for the incorporation of both, the equations that can account for physical aspect of system constituent as well as logical statements describing the constituent, the fact that it is a computationally expensive methodology makes its use impractical while modelling the biological microenvironment (especially cases that include diffusion of molecules, changes in permeability, reaction between chemical species, etc.)

populations) to the development of the overall system, as can be argued is the case physically. This feature enables the paradigm to not only capture environmental variables but also the emergent patterns observed at the macroscopic level due to the activity of each cell in relation to the cues offered by its microenvironment. While an array of hybrid computational platforms exist that can capture a host of cellular behaviours along with quantifying the environment, there is scope for novelty in what can be achieved (as explored in Chapter 5).

In this thesis, the author presents a novel multi-paradigm modelling framework with the capability of providing biological systems with an appropriate ontology to model the environment as well as the cellular behaviour (and interactions between the two). The framework employs the finite volume discretisation of the general transport equation (including the Navier-Stokes equation for momentum transport) to account for the environmental variables, and *stream communicating X-machines*[16] to account for cellular behaviour and simulating interactions between the cells and their environment. The framework is quite modular and can account for a variety of physicochemical stimuli, such as: (turbulent) flow, shear, transport (convection and diffusion) and reaction of chemical species within the environment, electrical and magnetic fields, etc. Similarly, the modularity applies equally to capturing an array of biological behaviour such as migration (directed or random), cell death (necrotic or apoptotic), differentiation, proliferation, colony formation, matrix synthesis and degradation, etc. This range enables the framework to capture a wide permutation of interactions between the cells and their environment, such as: shear-dependent differentiation, galvanotaxis, changes in permeability due to matrix formation or cell aggregation, amongst others.

The framework can, therefore, be employed to quantify a biological system by capturing a diverse array of data structures, which can then be employed to create models

with strong predictive power. The platform, as such, offers data that is more amenable to analysis (as opposed to qualitative results) and can, therefore, yield insights into the principles of development and regeneration. The approach is itself a *platform* concept that can be adopted to capture, simulate, and predict the evolution of many biological systems, especially in the TERM context. The framework can be used as a concept selection tool, capable of rationalising and optimising specifications of devices employed to control cell proliferation and differentiation. It can, therefore, ensure qualitatively homogeneous autologous substitutes and make the process of directed development of tissue substitutes automated, standardised, traceable, cost-effective and amenable to the various regulatory requirements, thereby bringing regenerative medicine closer to bedside application.

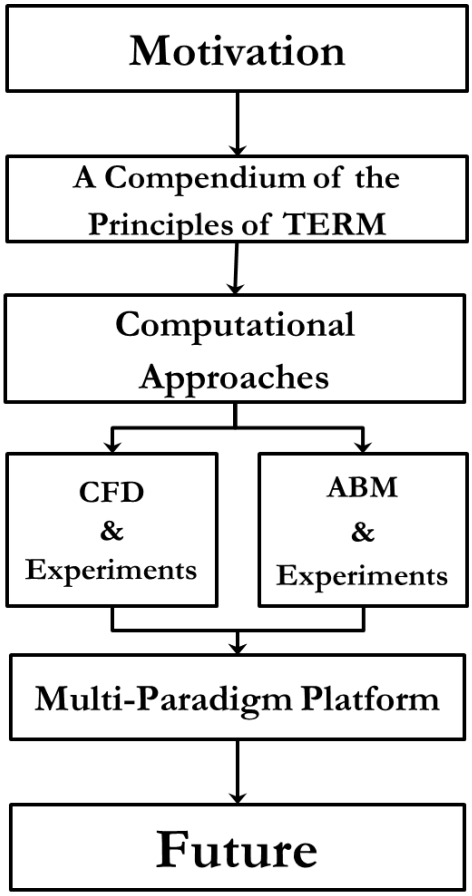

Figure 1. 2: Schematic highlighting the organisation of material in this thesis.

In Chapter 2, the author introduces and discusses the continuous and discrete techniques employed to simulate the environment and cellular behaviour (also within the

TERM context). This includes a discussion on the existing platforms currently employed to model biological systems within the TERM context, as well as dimensionless numbers utilised while analysing the continuum aspects of the system. In Chapter 3, a continuum model capturing flow and transport of glucose within a commercially available bioreactor is presented. The model illustrates the predictive and design capabilities of computational fluid dynamics (CFD), thereby suggesting it to be a suitable approach in simulating the physicochemical features of any (commercial/non-commercial) biological system. In Chapter 4, a novel 3D agent-based model of *in vitro* intramembranous ossification is presented. The model illustrates the ability of the agent-based paradigm to capture emergent phenomena, and is utilised to provide insights into an important question in orthopaedic biology: *How do osteoblasts transform into osteocytes*?[17] In Chapter 5, the coupling of methodologies presented in Chapters 3 and 4 is achieved towards the development of the multi-paradigm, hybrid framework. While the model presented in Chapter 5 is fairly basic, it highlights the capability of the framework to capture *dynamic reciprocity*[18] within the TERM context. The chapter also features proof of concept in the form of a virtual chemotaxis assay and its comparison against a physical chemotaxis assay is also provided. The thesis concludes with Chapter 6, with a brief discussion on the future work in store for further development of the framework as well as the future of hybrid frameworks.

2 CHAPTER

Computational Tissue Engineering & Regenerative Medicine

This chapter evaluates TERM's contribution to healthcare as well as global economy, and discusses a few reasons why the technology has failed to translate its latent potential. Lack of a robust computational platform that can enable quantification of the complex relation between cells and their microenvironment is identified as a chief impediment. In keeping with the overarching aim of this chapter, various computational approaches employed to quantify biological systems are introduced and reviewed. The state-of-the-art in computational software is presented and critiqued, identifying the gap towards which this thesis aims to address. This is followed by a discussion on Dynamic Assimilation and existing computational platforms that can display this capability, hinting that hybrid approaches are best suited to the task. The objective of this chapter is to provide context for the rest of the thesis, set the landscape of the existing computational methodologies, and in doing so identify the gap amongst existing hybrid platforms, which this thesis aims to address.[iv]

2.1 INTRODUCTION

The ability to reactivate developmental processes, *ex vivo*, to form products that can help alleviate healthcare problems related to the diseases of *cellular deficiency*[19] lie at the heart of the research fields of Tissue Engineering and Regenerative Medicine (TERM). This reactivation of developmental pathways, demonstrated so remarkably by lower invertebrates to restore homeostasis following injury[20,21], is known as regeneration[20]. Where the objective of tissue engineering (TE) is to produce functional, preferably autologous, substitutes that can improve or replace a failing tissue[22-25]; regenerative medicine, as per Daar & Greenwood (2007)[26] and Mason & Dunhill (2008)[27], aims to 'repair, replace or regenerate cells, tissues, or organs to restore impaired function'[20,26,27]. Non-clinical benefits of TERM products include usage as drug screening

[iv] *Certain sections presented in this chapter have been published as follows:*

- *Kaul H and Ventikos Y. On the genealogy of Tissue Engineering and Regenerative Medicine.* ***Tissue Engineering Part B Reviews****, 2015, 21(2): 203-217.*
- *Kaul H and Ventikos Y. Investigating biocomplexity through the agent-based paradigm.* ***Briefings in Bioinformatics****, 2015, 16(1): 137-152.*

platforms (for toxicity as well as efficacy) and as *in vitro* models to investigate governing dynamics that regulate developmental processes as well as diseases[28].

Figure 2. 1: The Auriculosaurus. The 'human-ear-bearing' mouse developed by the Vacanti lab that went on to epitomise Tissue Engineering. License to reproduce the image was obtained from the © (2002) BBC Photo Library.

TERM are interdisciplinary sectors of research and clinical application that encompass principles from disciplines such as stem cell biology; developmental biology; genetics; cell and molecular biology; cell, tissue and organ transplant; material science and drug delivery amongst others (refer to Figure 2.2). Already, despite the field being in its early stages of development, examples abound of successful clinical implementation[29] of corneal surfaces[30], replacement of a bronchus segment[31], and reconstitution of bone[32] and cartilage[33] defects and diseased bladder[34]; as well as external support devices such as extracorporeal liver[35] or engineered tissues that can serve as *in vitro* models to investigate pathogenesis, stem cell behaviour and developmental processes, and develop new molecular therapeutics[28,36,37].

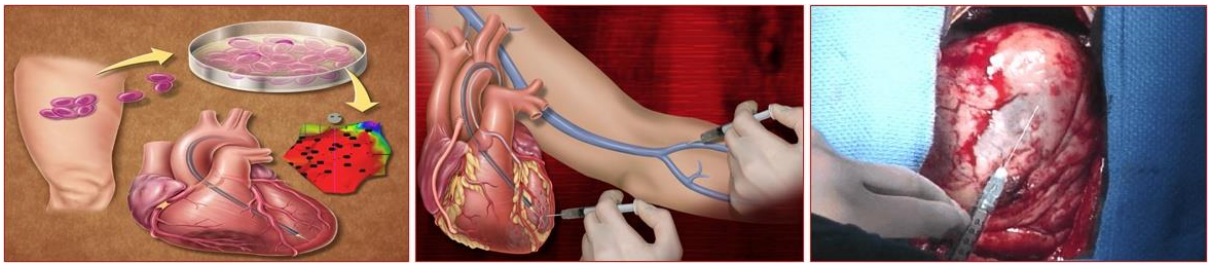

Figure 2. 2: Tissue Engineering and Regenerative Medicine in action. The figure captures the protocol followed during regenerative therapy. Multipotent stem cells from a patient are harvested, expanded, and manipulated to be delivered to the damaged tissue (in this case, an infarcted heart). Expanded/differentiated cells can be delivered systemically (as shown in the figure) or via the use of polymeric scaffolds. Picture courtesy: Dr Nabil Dib and his (erstwhile) team at Arizona Heart Hospital.

2.1.1 TERM AS A CLINICAL AND ECONOMIC PLAYER

Treatment options that have emerged from TERM and are currently in operation include *glybera* (treatment of lipoprotein lipase deficiency by gene therapy)[38] and *ChondroCelect* (the classical TERM approach, as highlighted in Figure 2.2, where cells obtained from a patient's cartilage following biopsy are cultured and expanded in the laboratory to treat cartilage defects in knees).[39] Both treatment options are approved by the European Union Marketing Authorisation.[v] Bone marrow transplantation, another example of the latter approach, involves transplanting healthy bone marrow stem cells of a person to another (allogenic substitute, as opposed to a patient's own). 14,366 bone marrow transplants were performed in the UK in the five year period 2004-09.[25] Furthermore, transplantation of islet cells, derived from pancreas of a deceased donor, into the liver of patients suffering from Type I diabetes resulted in a >95% reduction in severe hypoglycaemia in these patients. Not only was the overall insulin dependence halved, the treatment precluded the need for insulin in a significant number of patients, with associated reduction in costs.[40] The treatment was developed by the Scottish National Blood

[v] More information can be found in:
http://www.ema.europa.eu/ema/index.jsp?curl=pages/medicines/human/medicines/002145/human_med_001480.jsp&mid=WC0b01ac058001d124
http://www.ema.europa.eu/ema/index.jsp?curl=pages/medicines/human/medicines/000878/human_med_000698.jsp

Transfusion Service.[25] Most eagerly anticipated TERM treatments in the UK include embryonic stem cell transplants for *retinitis pigmentosa* (inherited eye disorder), injection of neural stem cells for the elderly disabled due to an ischaemic stroke (blockage of blood flow to the brain), and mesenchymal stem cell transplants to treat Multiple Sclerosis (disease affecting the nerves in the brain and the spinal cord resulting in problems with balance, movement, and vision).[25]

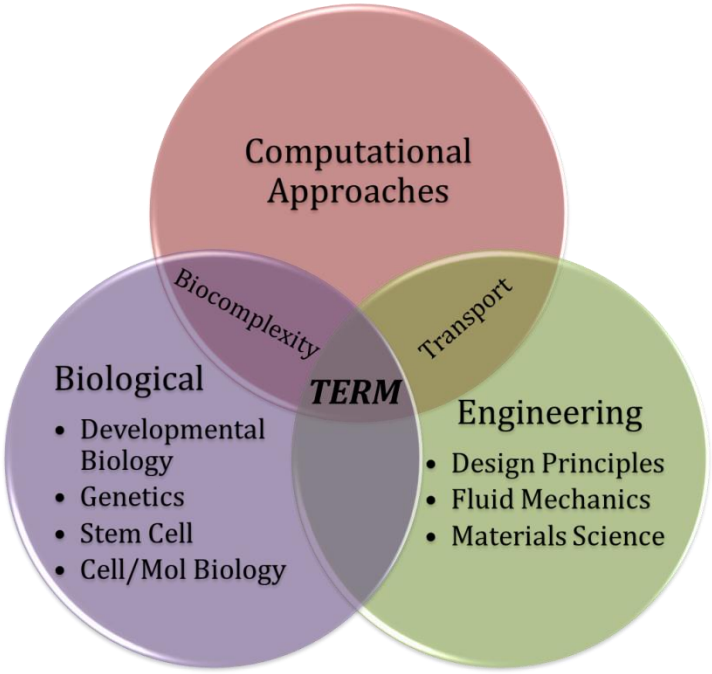

Figure 2. 3: TERM Venn Diagram. The figure shows a Venn diagram representing the contribution of various experimental and computational disciplines to the sector of Tissue Engineering and Regenerative Medicine.

In addition to the unparalleled therapeutic and rehabilitation potential, the TERM industry has established itself as a significant player on the global economic landscape despite the unique commercial, regulatory, and IP challenges[29,41-43] (owing to the unconventional nature of the innovation paradigm associated with the field) that have impeded the translation of the technology from gaining clinical ubiquity. Still, a global sector activity of $3.6 billion, with companies employing about 14,000 full-time employees and generating $3.5 billion in sales, bodes well for the future of the industry that is, for the first time in its recorded history, operating at breakeven.[44] In the last four years, the TERM

industry created over 7,710 jobs[44] with an estimated increase in the sale of commercial products by a factor of 2.5.[45] The UK Regenerative Medicine Community estimates the contribution of the TERM industry to around £150 million of production and £80 million gross value added to the UK economy.[25] The Scottish TERM sector, comprising of 4 companies in 2004, has mushroomed by more than 500% in the following nine years.[25] This astonishing success and rise of the TERM industry is better put into perspective when one considers that these heights were scaled against the backdrop of a global financial meltdown.

2.2 THE "*TRANSLATION*" SITUATION

Two decades have passed since *Tissue Engineering* was published in *Science*,[23] and in these twenty years, TERM, aided by development in microfluidics, 3D printing, controlled release matrices, and other fabrication techniques, has established itself as a modern scientific discipline. Successful implementation of TERM principles has not only added, to an extent, to our understanding of developmental principles,[46] but also contributed to the advancement of healthcare (refer to Figure 2.4).[34,47] As technologies often do, TERM, in the wake of its advancements, has already established itself as a significant player on the economic landscape (refer to §2.1.1). Although, as per a report published by the House of Lords (London), TERM has the "*potential to deliver new innovative therapies, or even cures, where conventional approaches do not provide adequate solutions*",[25] regenerative medicine has thus far underperformed,[48] with the industry in aggregate yet to make a profit. A multitude of non-quantifiable reasons have contributed to this modest performance of the TERM industry. These include extraneous factors such as misconceptions regarding the genuine achievements of the sector,[49] lack of strong political leadership,[49] the historical lack of an industry voice,[50,51] amongst others.[45,52] Regulatory challenges,[29,43] such as lack of quality control biomarkers and potency markers, process and product variability, risk factors

associated with operator handling, have further stymied the marketability of TERM products. Similarly, a complex IP situation, parallel to the biotech industry,[41] owing to uncertain outcomes with poorly defined and overlapping patents constitutes another reason behind TERM's impeded industrial and clinical translation.

Figure 2. 4: Ear growth on the arm. TERM principles were employed by a team of surgeons to grow an external ear for this patient on her own arm. The set of images show the compromised organ, perfusion to meet the transport demands of the synthetically growing new organ, the fully developed organ, and, finally, its attachment to the patient. Cartilage for the new ear was derived from the patient's ribs, matched with her right ear, and implanted under the arm for growth. The work was carried on by surgeons led by Dr. Patric Byrne at Johns Hopkins University in 2012. *The photographs issued along a media release belong in the public domain.*[vi]

The greatest hindrance to TERM's growth, however, remains a lack of quantitative understanding of the underlying developmental principles that influence the *ex vivo* synthesis of biologically functional autologous substitutes – a need widely appreciated within the community.[53-60] As a result, systems that are used to synthesise these substitutes are treated as functional *black-boxes*, where trial and error eventually leads to the desirable outcome. While this approach might nourish scientific curiosity, an industry based on

[vi] The set of images was retrieved from an online article published by *CBS Baltimore*. The slideshow can be accessed here: http://baltimore.cbslocal.com/2012/09/26/hopkins-doctors-give-woman-a-new-ear/

probability does not attract many investors. Furthermore, with the four basic aspects of the regenerative medicine industry (scientific, regulatory, commercial, IP) closely intertwined (refer to Figure 1.1), the ecological impact of this apparent lack of understanding on the entire TERM ecosystem explains the unfulfilled promise. This lack of clarity which ails the basic science behind product development has a negative impact on the regulatory, IP and commercial aspects of the regenerative medicine industry ecosystem.

The solution calls for a more accurate understanding of the *biology* behind regenerative medicine. Tackling this challenge requires synergistic efforts between experimentalists and their theoretical counterparts, as extrapolating cellular behaviour within an organism to *ex vivo* environments will require precise models with quantifiable predictions. Such models can only be developed via a robust computational framework that can offer (i) ontologies relevant to biological systems and (ii) an accurate and computationally economical way of capturing the physicochemical attributes of the environment to enable appropriate and relevant comparisons against physical data.

It is worth reminding the reader that TERM based therapies involve either delivering isolated cells, or substances that induce tissue growth (such as morphogens or growth factors), or cells placed on or encapsulated within a biocompatible scaffold.[23] The toolkit of a TERM investigator, therefore, includes, but is not limited to: (stem) cells, polymeric scaffolds or controlled release devices, tissue-inducing substances, and bioreactors. Advances in computational modelling, as well as computer power, have ensured that each component of the TERM toolkit can be captured by a computational equivalent: partial differential equations (like the *Navier-Stokes* equations, for example) for flow and transport, *poroelastic* formulations to investigate the role of scaffold porosity and mechanics, and *cellular automaton* grids as representations of cells. These tools have, by providing novel

insights into previously untested hypotheses and questions, provided a fertile base upon which more sophisticated, complete, and mature models can be built.

The following section is meant to set the computational TERM landscape in terms of the various mathematical/computational approaches, formulations, and (proprietary or open-access) platforms that are in current use. As such, a selective and relevant, yet broad, review of computational tools covering the entire range of the aforementioned analogues is presented. The selectivity was motivated by the staggering breadth of literature that exists on the subject of computational TERM. However, efforts were made to ensure that the broad spectrum of computational tools was covered, even if their specific applications (e.g. dental, cardiovascular, pleural, etc.) were excluded from being reviewed here.

2.3 THE COMPUTATIONAL TOOLKIT

A computational paradigm, from a TERM standpoint, must be able to realistically quantify the various modalities of the native tissue; which includes the mechanical substrate, soluble bioactive factors, local mass transport, and homo- and heterogeneous cell-cell interactions; as well as dynamically assimilate each of the aforementioned cues to simulate the growth of the evolving structure. The computational approaches that are currently utilised to capture these governing phenomena can be broadly classified as statistical, continuum, and discrete. Each of these approaches utilise a wide array of formulations. For example, the continuum approach includes discretising the governing equations through the *finite-element*, *finite-volume*, *finite-difference*, *level-set* method etc. Similarly, the discrete approach can utilise the lattice-based *cellular automata* (CA) and *cellular potts modelling* (CPM) or the off-lattice based stream communicating X-machines. Furthermore, there exist a variety of platforms for each mathematical approach and formulation: (the following are mentioned as a very limited set of examples) *CFD-ACE+* (ESI, Paris, France) – continuum

and finite-volume discretisation of the governing equations), *CompuCell3D* (CC3D) – grid based discrete approach, and *Flexible Large-scale Agent-based Modelling Environment* (FLAME) – off-lattice discrete approach.

Continuum models are used to investigate time-varying quantities, such as concentration gradients, populations etc.[1,61] Continuum approaches, such as fluid dynamics, employ classical differential equation based models that in most cases have only numerical, or approximate, solutions. A continuum approach entails identifying the set of partial differential equations and boundary conditions that best fit the system. This is followed by discretising the continuous model into discrete counterparts that represent the geometric domains on which the problem is solved. Finally, a solution method is applied and convergence criteria set.[62] The methodology of Computational Fluid Dynamics (CFD), a continuum approach, is presented in detail in the following pages of this section. Continuum approaches are usually employed when large amounts of quantities (or *continua*, where population behaviour supersedes individual behaviour) are involved (to describe them with rate equations and average changes)[61] and have also been used, with limited success, to predict system behaviour based on lower level activities.[1] This limited success is a result of the underlying assumption, while employing the continuum approach, that a system can be divided into infinitesimally small, identical, numerous, constituents, which obey the identified equations similarly.

The two assumptions (continua and infinitesimally small and identical constituents), however, fail when considering biological systems, especially the ones undergoing morpho-, histo-, or organo-genesis, as heterogeneity in information is key to the spatiotemporal evolution of these systems. For such cases, discrete approaches are normally recommended. Discrete approaches (not synonymous with 'discretisation' as indicated above) on the other hand represent and execute the models using operational descriptions in the form of

computing programs.[6] The approach assumes that system behaviour can be captured by a set of rules that combine qualitative as well quantitative information, thereby allowing each modelled entity to respond to its environment.[6] More importantly, though, non-continuous, heterogeneous systems can be easily modelled via the discrete approach.[6,8,53,63] The methodology, therefore, is a suitable approach to investigate cellular systems that show non-linear, adaptive behaviour. The discrete approach is traditionally employed if the number of entities to be modelled are relatively small (less than a million[64]), spatial considerations important, and emergent phenomena the primary interest.[64] As considering system heterogeneity is an essential feature of this approach, the size restriction is necessitated due to the computationally expensive nature of discrete models, whether cellular automata or agent-based modelling. Therefore, the fundamental unit of the system being modelled, where the governing equations/rules are implemented, need to be carefully chosen. For example, if investigating intercellular activity, choosing an intracellular protein molecule as the agent will make the model unnecessarily bulky. For the same reason, the discrete approach is not recommended for simulating continuous phenomena, where the number of entities to be modelled far-exceeds the limit specified for the discrete approach above.[vii]

Molecular dynamics (MD) is another computer simulation technique, which models systems at the molecular level. A system is comprised by molecules, which interact with each other based either on the laws of classical mechanics (Classical MD) or quantum/first principles (Quantum MD).[65] Molecules in the former approach are treated as classical objects, with atoms represented by 'soft' balls and bonds between the atoms by elastic sticks. Quantum MD, however, takes into account the quantum nature of the chemical bond, which is computed using quantum equations. Ions, in quantum MD, are treated classically.[65] MD

[vii] For example, 1μL of water contains 10^{19} water molecules approximately. A discrete model of diffusion of a solute into volume of water as little as 1 mL will be too cumbersome, not to mention impractical, to yield any meaningful insights.

is considered practical for systems containing "*many thousands of atoms over time scales of nanoseconds*".[65] As computations occur at molecular level (or below), at time scales which are exceptionally minute,[65] MD is computationally very expensive and is only employed to investigate mechanics of nucleic acids or proteins. The technique, although quite powerful and useful, was, therefore, not utilised in this thesis as it is not practical to simulate interactions at inter-cellular and cellular-environmental level.

As Chavali *et al*. (2008)[5] state, any modelling approach required to simulate cellular behaviour must be able to simulate non-linear and dynamic behaviour, synthesise cell-cell and cell-environment interactions, track various cells that are heterogeneous in nature, develop memory of various prior cellular interactions, adapt to the – or as directed by the – external environment, and permit visualisation of emergent phenomena that will result from the combined interactions of the stem cell system under the scanner. As this task is too complicated for either approach, *hybrid* models that contain discrete as well as continuous modalities are usually applied.

2.3.1 CONTINUUM MODELS

Whether it is the case of a zygote undergoing embryogenesis, stem cells trying to assemble and expand in a scaffold before the construct is implanted in the human body, or, quite simply, cell expansion in an *in vitro* culture, the computational aspect of TERM has traditionally dealt with the problems of transport phenomena and biomechanics, as well as the integration of the two together to explain morphogenesis. After all, providing optimal quantities of nutrients, signalling molecules, and physical cues is central to both regeneration as well as development. Cells are quite sensitive about their metabolic and mechanical needs, which, if unmet, will most certainly result in tissues that are not robust enough to perform their normal function. In the technology context, this means that a bioreactor with

sub-optimal mass transport and/or mechanical stimulation may produce a synthetic substitute that does not possess the properties to supplement or replace the host tissue. The continuum approach, entails representing biological behaviour with a set of partial or ordinary differential equations, derived from the basic *physical laws*,[viii] which can be solved via a variety of numerical approaches to account for transport and biomechanics.

2.3.1.1 DIMENSIONAL ANALYSIS

Dimensional analysis, which involves the fundamental unit of dimensions, is a useful tool to analyse and predict physical parameters that influence transient continuous processes (flow and transport, for example). Calculating the dimensionless *Knudsen* (*Kn*) number is usually a first step before employing the continuum approach, to ensure that the continuum hypothesis is indeed a suitable assumption for the system under consideration. Kn is the ratio of the mean free path length (λ) of the molecules of a fluid to a certain representative physical length scale (L), and is defined as:

$$Kn = {}^{\lambda}/_{L} \tag{2.1}$$

The length scale could be the radius of a body in the fluid, such as a cell. While this varies for various cells, one can safely assume a radius of 10 μm. Assuming water as the fluid in which a cell is immersed, the mean free path of water molecules – i.e. the average distance they can travel between collisions – at physiological temperatures is approximately 2.5 Å. The continuum approach is general applied for systems with Kn < 1, certainly the case for every system containing cells and water in the fluid phase. Similarly, when looking into the transport of glucose and growth factors into cells, the continuity assumption can be verified using Kn. For example, the mean free path of the molecules of glucose and a typical protein

[viii] The physical laws, amongst others, include: conservation of mass, momentum and energy

(albumin) can be approximated to 200 Å and 8 Å,[ix] respectively, which yield Kn < 1 when compared with the size of a cell. The continuum assumption and the conservation laws (and boundary conditions), which correspond to that assumption are, therefore, safely confirmed for most (in fact all) bioreactor models published in literature (and utilised towards the investigations conducted in this thesis).

Fluid patterns (i.e. whether the flow is laminar or turbulent), can be determined by calculating the *Reynolds* number (*Re*). Re is the ratio of convective to viscous forces, and is defined in (2.2).

$$Re = {}^{\rho V d}/_{\mu} \tag{2.2}$$

In (2.2), ρ is the fluid density, V the fluid velocity, d the characteristic length for the flow, and μ the fluid viscosity. Depending upon bioreactor characteristics, such as manner of achieving mixing and perfusion, the Re can vary significantly across the various bioreactor types. For example, spinner flask and wavy wall bioreactors, which employ a stirrer to achieve mixing of the culture medium, can result in Re > 1000,[66,67] suggesting the presence of turbulent hydrodynamic regime per the critical impeller Re of 1000 determined by Nagata (1975).[68] Hollow fibre membrane bioreactors, which consist of a network of hollow fibre membranes (through which the medium is fed into the bioreactor) running through scaffold material encapsulating cells,[69] results in very low Re (<10),[70] reflecting laminar or occasionally even creeping flow regime. Similarly, a rotating-wall bioreactors, designed to culture shear-sensitive cells in a microgravity environment also yields low Re (~100), though under microgravity conditions Re can drop to markedly low values (<1).[71,72] Laminar flow, as discussed in Chapter 3, is considered optimal for cellular expansion.

[ix] $\lambda = {}^{kT}/_{\sqrt{2}\pi d^2 P}$, where k = Boltzmann constant (1.38×10^{-23} J/k), T = temperature (310 K), P = pressure (1.013×10^{5} Pa), and d = length scale of particles (7 Å for glucose and 35 Å for albumin).

In order, similarly, to capture the overall effectiveness of the combination of diffusive and convective transport of a chemical species other dimensionless numbers – such as the *Schmidt* number (*Sc*), *Sherwood* number (*Sh*), *Peclet* number (*Pe*) – can be calculated, measured, or estimated.[73] The transport of a chemical species to the cells within a bioreactor occurs via two ways: external transport, which involves the transport of the scalar from the medium to the outer layer of the clustered cells due to convection; and internal transport, which involves transfer from the exterior of the cellular cluster to the cells located within the cluster. The external transport mainly depends on the ratio, *k*, of the diffusion constant (D_m) to the boundary layer thickness (δ).

$$k = {}^{D_m}/_{\delta} \tag{2.3}$$

Obviously, the higher the ratio, the more effective the external transport. A boundary layer is established when a flowing fluid encounters a solid surface. A fundamental feature of fluids is that they obey the *no-slip* condition if in contact with a solid surface: i.e. their velocity relative to that of the solid surface is zero. There is, as such, a region close to the surface where the velocity of the fluid increases very sharply – this region is known as the boundary layer.[74] One of the several ways of defining the thickness of a boundary layer is the distance from the solid surface at which the fluid reaches 99% of its initial value. The thickness of this boundary layer is dependent on flux characteristics that in turn regulate the external mass transfer of a given scalar from bulk to the inside of the scaffold.[73] The latter is a fluid-zone in which scalar concentration ranges from that observed in bulk flow to that observed on the cell cluster surface (i.e. the exposed area of the cell cluster facing the bioreactor medium), and usually varies based on flux characteristics. The thickness is relevant, for it indicates the effectiveness of transfer of the scalar from the bulk to cell cluster surface.

Sc, the ratio of momentum diffusivity (kinematic viscosity) to mass diffusivity, is commonly employed to determine the effectiveness of the external transport.

$$Sc = {}^{v}/_{D_m} \tag{2.4}$$

In (2.4), *v* represents the kinematic viscosity (i.e fluid viscosity/fluid density) and D_m the diffusion coefficient of the molecular species under consideration. *Sc* provides the importance of convection to the transport of the scalar within the bioreactor. *Sh*, the ratio of external diffusion to mass diffusivity, can be also employed towards this end by calculating *k*. Using the Frössling correlation for spherical particles,[73] *Sh* can be calculated from *Re* and *Sc*: refer to (2.5).

$$Sh = {}^{kd}/_{D_m} = {}^{d}/_{\delta} = 2 + 0.6Re^{1/2}Sc^{1/3} \tag{2.5}$$

The effectiveness of mass transport can also be evaluated by quantifying the difference between external transport of the relevant molecular species and its internal diffusion.[75] This can be determined by calculating the *Peclet* number (*Pe*) – the ratio of the rate of advection of a physical quantity by the flow to the rate of diffusion of the same quantity, and is defined by:

$$Pe = {}^{dV}/_{D_m} \tag{2.6}$$

In (2.6), *d* is the characteristic length and D_m the mass diffusion coefficient of the molecular species under consideration. *Pe* between 0 and 1 indicates presence of effects that hinder convection.[73]

Limitations of the internal mass transport can be similarly determined by calculating the *Biot* Number (N_{Bi}) – the ratio of mass transfer of the molecular species of interest across the inside of the scaffolds to mass transport of the species across the boundary layer outside the scaffolds. The Biot number can be calculated as represented in (2.7):

$$N_{Bi} = \frac{L}{D_e} \Big/ \frac{\delta}{D_{fluid}} \tag{2.7}$$

where L = diffusion length, D_e = effective glucose diffusivity inside the cellular medium, δ = thickness of the mass transfer *boundary layer* around the construct, and D_{fluid} = glucose diffusivity in the culture medium. The Biot number, when considered for cases involving mass transfer, is the ratio of resistance encountered by the internal transfer of scalar to the boundary layer scalar transfer resistance.

For cases where the concentration profile of a secreted cytokine(s), which is transporting via diffusion, over the entire cellular domain within a perfusion bioreactor (i.e advection present) is of interest, the dimensionless *Graetz* number (*Gz*) can be employed. *Gz* is defined as ratio of diffusional time to transit time, as shown in (2.8). It measures the relative time of diffusion to convective transit time through the bioreactor.[76] A lower *Gz*, which means lower diffusive time relative to transit time, implies that the releasing cytokine will have enough time to build up within the cellular structure and have an overall impact (example: differentiation, proliferation, etc.). Conversely, a higher *Gz* implies that the secreted cytokine will be swept out due to fluid flow, and local cytokine concentrations will be low. This may be essential, if the cytokine triggers apoptosis (or differentiation, etc.) within the growing cell population.

$$Gz = \frac{H^2/D_m}{v/Q} \tag{2.8}$$

In (2.8), H represents the depth over which the scalar is diffusing, v the volume of the bioreactor, and Q the media flow rate.

2.3.1.2 COMPUTATIONAL FLUID DYNAMICS & TRANSPORT PHENOMENA

In terms of capturing transport, the following laws govern fluid flow: (1) conservation of mass; (2) conservation of momentum; and (3) conservation of energy. As transport within the TERM context occurs at constant temperature, the mathematical treatment of the law of conservation of energy is not considered in the thesis. The laws of conservation of mass and momentum, however, can be mathematically represented by the following equations:

$$\frac{\partial \rho}{\partial t} + \nabla.(\rho U) = 0 \tag{2.9}$$

$$\frac{\partial}{\partial t}(\rho U) + \nabla.(\rho UU) = -\nabla P + \mu \nabla^2 U + f \tag{2.10}$$

Equation (2.9) forms the *continuity* equation. In (2.9), ρ represents the density of the fluid and U the flow velocity vector (u_1, u_2, u_3). The equation represents the balance of masses entering and exiting the control volume (CV) per unit time with the rate of change of ρ, assuming no change of volume. Similarly, the principle of conservation of momentum, Newton's second law of motion, is represented by the *momentum equation*, as shown in (2.10). Equation (2.10) equates the sum of body forces, such as weight and electromagnetic forces, to the sum of surface forces, such as shear and normal stress, and pressure, acting on the CV. In (2.10), μ represents the dynamic viscosity of the fluid, P is the pressure acting on the fluid, and f represents other body forces. These two governing equations – a system of coupled partial differential equations (PDEs) – are known as the Navier-Stokes equations, as they were first derived, independently, by the French Engineer Louis Navier, and Sir George Stokes.[74]

Tissues, colony of cells secreting extra-cellular matrix (ECM), or scaffolds encapsulating cells, all are usually modelled as porous structures. One way of treating such

cases is to consider them a fluid filled porous matrix with certain porosity (ε) and permeability (κ), which generally tend to vary anisotropically. While ε is the ratio of the volume occupied by the pores to the total volume occupied by the solid, κ is measure of the flow conductance of the matrix.[77,78] The following modified continuity and momentum equations are used when handling such porous media:

$$\frac{\partial \varepsilon \rho}{\partial t} + \nabla.(\varepsilon \rho U) = 0 \tag{2.11}$$

$$\frac{\partial}{\partial t}(\varepsilon \rho U) + \nabla.(\varepsilon \rho U U) = -\varepsilon \nabla P + \frac{\varepsilon^2 \mu}{\kappa} \nabla^2 U + f \tag{2.12}$$

The Darcian porous resistance is also incorporated in (2.12).[79] Mass transfer of nutrients, metabolites, wastes, gases constitutes a significant part of a biological system. The molecules of interest are henceforth referred to as *scalars* (given that mass is a scalar, specified completely by its magnitude). Scalar mass transfer can be described as the movement of scalar molecules relative to fixed references due to convective and diffusive flow[75] with the addition of either generation or consumption of the scalar. The convection-diffusion equation in two or more directions is derived from the continuity equation and can be mathematically represented as:

$$\frac{\partial C}{\partial t} + \nabla.J = S \tag{2.13}$$

In (2.13), *C* represents scalar concentration, *S* the sink or source term for the scalar, and *J* the flux of scalar quantity through the CV. The sink/source term accounts for changes in scalar concentration due to biological processes such as enzymatic reactions, secretion, consumption, injury etc. The molar flux can be further represented as:

$$J = d_C + b_C \tag{2.14}$$

where d_C represents diffusive flux that arises due to random motion of the scalar molecules, and b_C represents convective flux or the flux that results from the bulk movement of the fluid. Equation (2.14) can be further expanded as follows:

$$J = -D.\nabla C + UC \tag{2.15}$$

The expression *UC* on the right hand side of (2.15) indicates that the concentration of solute is a factor of flow velocity magnitude *U*. In (2.15), *D* represents the scalar diffusion coefficient in the fluid. Assuming constant diffusivity, substitution of (2.15) into (2.13) yields the following equation:

$$\frac{\partial C}{\partial t} - D\nabla^2 C + U.\nabla C = S \tag{2.16}$$

The mass conservation equations for the fluid-phase species within a porous structure can be written as:

$$\frac{\partial(\varepsilon\rho\phi)}{\partial t} + \nabla\cdot(\varepsilon\rho U\phi) = \nabla\cdot J + S \tag{2.17}$$

where Φ represents the mass fraction of the diffusing species, *J* the diffusion flux, and *S* the production rate of this species. As biological systems operate under isothermal conditions, the diffusion flux in porous media can be specified as:

$$J = \rho D_e \nabla\phi \tag{2.18}$$

Here, D_e represents effective mass diffusion coefficient within the porous medium and depends upon the porosity of the medium. The effective diffusion coefficient can be represented as:

$$D_e = \varepsilon^{\zeta} D \tag{2.19}$$

In (2.19), ζ represents tortuosity of the porous media, which is typically described as the difference between the actual distance travelled by fluid particles and the macroscopic travel distance, though the definition of the concept is not unique (as discussed elsewhere).[80] Usually, a (measurement based) value of *1.5* is recommended.[77]

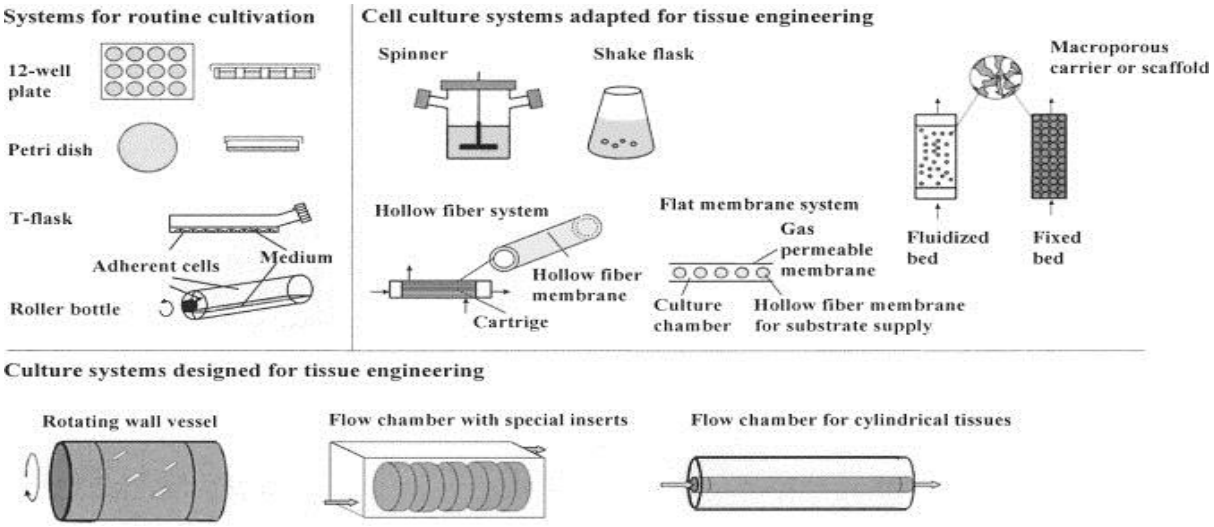

Figure 2. 5: Bioreactors. The figure shows schematic representations of the various cell culture systems employed in Tissue Engineering. The culture systems presented here include both static as well as perfusion-based devices. *Reproduced with kind permission from Ref.* 42 *© (2006) Elsevier.*

These equations cannot be solved analytically but for the simplest cases. Thus, we have to employ, almost invariably, computational techniques to derive numerical solutions of practical use. Computational Fluid Dynamics (CFD) has been applied to characterise flow-fields in bioreactors of all configurations. Examples abound of the following types (refer to Figure 2.5): spinner flasks,[66] roller-bottle, wavy-walled,[67] RWV, perfusion, and pulsatile bioreactors. CFD involves transforming the equations described above into discretised algebraic forms to quantify flow-field values at discrete points in space and time.[81]

CFD involves transforming the equations described above into discretised algebraic forms to quantify flow-field values at discrete points in space and time.[81] Briefly, identification of the relevant mathematical equations (concomitantly with a suitable

coordinate system for expressing velocity vector and stress tensors) is followed by selecting a suitable discretising method. Discretisation involves approximating the differential equations by a system of algebraic equations for the variables at some set of discrete locations in space and time.

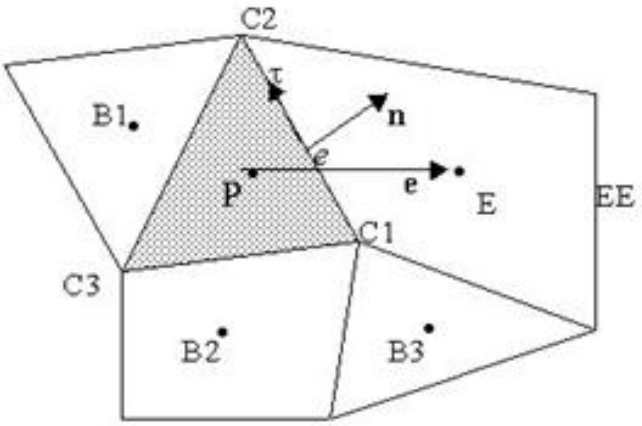

Figure 2. 6: Computational Cell. The figure depicts a two-dimensional Computational Cell (Control Volume)[77] utilised to discretise the governing Navier-Stokes equations via the Finite Volume Approach. In this case, a mix of polyhedral elements is used (triangles and quadrilaterals). The image was derived from CFD-ACE+ user manual.[77]

A "mesh" or a "grid" defines these discrete locations at which the variables are calculated. A numerical grid is a discrete representation of the geometric domain on which the problem is to be solved. Grids divide the solution domain into a finite number of sub-domains such as elements or CVs etc. (refer to Figure 2.6). Grids can be structured (or regular), block-structured, unstructured or any combination of the above. They can also be conforming (where a node has meaning for all adjoining elements or volumes, or non-conforming, where nodes on a side/face may be relevant to one cell that shares that side/face but not the other(s).[82] The choice of grid type is followed by selecting the approximation to be used in the discretisation process. The choice of approximation varies based on the nature of discretisation approach selected for the problem. Discretisation is followed by applying the appropriate solution method (usually iterative) and, finally, setting the convergence criteria for the solution method.

The conservation of any quantity, ϕ, such as mass, momentum, concentration of an arbitrary nutrient, etc., can be more conveniently expressed via the more general transport equation[83]:

$$\frac{\partial}{\partial t}(\rho\Phi) + \nabla.(\rho U\Phi) - \nabla.(\Gamma_\Phi \nabla\Phi) = S_\Phi \qquad (2.20)$$

Transient	Convection	Diffusion	Source

In (2.20), Γ_Φ represents the diffusivity coefficient of Φ, and S_Φ represents the source or the sink term. Here, the continuity equation can be recovered by simply setting $\Phi = 1$, $\Gamma_\Phi = 0$, and $S_\Phi = 0$; the convection-diffusion equation by setting $\Phi = C$, $\Gamma_\Phi = D$, and $S_\Phi = S$; and the (x-)momentum equation by setting $\Phi = u$, $\Gamma_\Phi = \mu$, and treating forces due to pressure via the source term.

In the Finite-Volume Method (FVM), the physical domain is divided into a finite number of sub-domains known as control volumes (CVs) where the integral form of the equations is solved. Integrating equation (2.20) over the CV yields:

$$\int_{CV}\left[\frac{\partial}{\partial t}(\rho\Phi) + \nabla.(\rho U\Phi) - \nabla.(\Gamma_\Phi \nabla\Phi)\right] dV = \int_{CV} S_\Phi dV \qquad (2.21)$$

Applying the divergence theorem, (2.21) is converted into a surface integral, as shown in (2.22), which helps evaluate the net-flux through the entire CV. The surface integral form of the equation is thus employed to determine the convective and diffusive terms of the equation.

$$\int_{CV}\frac{\partial}{\partial t}(\rho\Phi)dV + \sum_{faces}^{surface}\int_S [\nabla.\rho U\Phi - \Gamma_\Phi\nabla\Phi].\vec{n}_S dS = \int_{CV} S_\Phi dV \qquad (2.22)$$

In (2.22), S represents any of the faces on the CV, whereas $\mathbf{n}_S$ is the unit vector normal to that surface. The source term, which usually depends on the existing scalar concentration, is represented as follows:

$$\int_{CV} S_\Phi dV = S_C + S_P \Phi_P \tag{2.23}$$

S_C represents a constant source/sink term and $S_P\Phi_P$ shows the linear dependence of the source term on scalar concentration, if such exists. The source term needs to be linearised in cases where the relationship is non-linear.[84]

ϕ_S (S representing any of the faces on the CV) can be calculated by employing a variety of interpolation schemes, such as *upwind schemes*, *central differencing scheme*, etc. The first-order upwind scheme, one of the most stable convection schemes, has first-order accuracy and involves assigning Φ_s the value of Φ at the upstream grid point. As such, depending upon the direction of flow at the cell face s, Φ can be either Φ_E (if $U < 0$) or Φ_P (if $U > 0$). The central difference scheme, on the other hand, assumes linear variation of Φ between the two cell centres P and E and calculates Φ_s by weight-averaging the values at the cell centres. After the equation set for a variable has been assembled it is solved by using, preferably because they are economical in terms of memory, iterative equation solvers, such as the *conjugate gradient squared* (*CGS*) or *algebraic multigrid* (*AMG*) *solvers*.[62] The AMG solver, for example, uses a hierarchy of grids, from fine to coarse, and back to fine, to solve the resulting set of pseudo-linear equations. After obtaining the residual field on the fine grid, iterations are performed on the coarse grid to obtain corrections (imposing fine-grid residuals as the source term). The AMG solver works by interpolating the corrections to the fine-grid and updating the fine grid solution, and repeating the entire procedure until the residual is reduced to the desired level.[77] This results in reducing error of multiple wavelengths at once, with the significant advantage of faster convergence.[77]

Sucosky *et al*. (2004)[66] used the CFD approach discretised via the finite-volume method to model the dynamic environment inside a spinner flask, which uses a magnetic stirrer to achieve mixing, operating under conditions employed to produce cartilage. Particle-image Velocimetry (PIV) was employed as the experimental strategy to validate the model. This was achieved by determining velocity and shear-rate fields in the vicinity of the cell-scaffold construct closer to the magnetic stir-bar. The investigators utilised the commercially available package FLUENT (Fluent Incorporated, New York, USA) to perform the computations. The software employs the *finite-volume approach* to solve the governing equations (2.9) and (2.10). The relevant variables were determined at each cell node subsequent to which the flux through each cell face is obtained by interpolation. In this investigation, the *k*-*ε* model was used to model turbulence and solve the Reynolds-averaged Navier-Stokes equations. In the *k*-*ε* model, *k* is the turbulent kinetic energy and *ε* the dissipation. They are defined as:

$$k(x,t) = \frac{1}{2}\overline{u_\iota(x,t)u_\iota(x,t)} \tag{2.24}$$

$$\epsilon(x,t) = 2\nu\overline{\frac{\partial u_\iota}{\partial x_J}(x,t)\frac{\partial u_\iota}{\partial x_J}(x,t)} \tag{2.25}$$

Scaffolds were modelled as both solid and porous structures. Flow generated by the stir bar was turbulent as well as unsteady in the mean. This posed challenges to both its measurement and numerical simulation. Reasonable agreement, however, was observed between the experimental and computational data (especially with respect to stress level within the bioreactor). Furthermore, the computations provided the first estimates of flow through porous constructs within the spinner flasks.

Bilgen *et al*. (2006)[67] characterised the hydrodynamic environment within a wavy-walled bioreactor (WWB), a variant of the spinner flask, employing the finite-volume

formulation. WWBs also rely on magnetic stirrers to achieve mixing, which can expose the tissue constructs encapsulated within the bioreactor (depending upon their positioning) to varying hydrodynamic environments. The investigators wished to characterise this variety to better understand the tissue growth process. Bioreactor conditions optimal to develop tissue-engineered cartilage were simulated. The investigators used the PIV technique, implemented by Suckosky *et al.* (2004)[66] above, to validate their model. Flow in WWB was found to be turbulent and time-periodic much like the spinner flask, as flow is generated in both bioreactors by a magnetic stir bar. However, flow within WWB was different from spinner flask in having reduced tangential-velocity and increased axial-velocity components. The investigators also reported recirculating regions within the bioreactor, which they conjectured provide additional stimuli more conducive to cartilage growth. Placing cartilage constructs within the bioreactor led to a dramatic change in the flow patterns and turbulence characteristics compared with the absence of these constructs. The mean shear stress increased from 0.01 – 0.02 Pa for WWB without constructs to 0.04 – 0.06 Pa for WWB with constructs. The flow was also found to be dependent on the position of the constructs within the bioreactor, as the position changes from centre towards the bioreactor walls. The investigators found that the mean-shear stress encountered by constructs within a WWB is less compared with the spinner flask, and concluded this to be the reason behind optimal performance of WWB in terms of achieving enhanced ECM deposition and cell proliferation compared with the spinner flask.

Begley & Kleis[71] employed a similar methodology to characterise a Rotating-Wall Perfused-Vessel (RWPV) bioreactor in terms of flow and shear stress environment and validated it via Laser Doppler Velocimeter (LDV) measurements. The RWPV bioreactor is based on a concentric cylinder arrangement. The inner cylinder is porous with a disc attached to one of its ends (referred to as the viscous pump), which enables the rotation of the inner

cylinder. The inner and outer cylinders can be, and are, independently rotated. The investigators, via the numerical model, intended to investigate the impact of changes in operating parameters (such as cylinder rotation rates and perfusion rates). The investigators assumed an axisymmetric flow field due to the symmetry of the bioreactor geometry and boundary conditions. They solved for the basic momentum and continuity equations: i.e (2.9) and (2.10), albeit in cylindrical coordinates. The geometry was gridded using a staggered mesh where the equations were solved under steady state conditions. The three shear components within the bioreactor were defined as follows:

$$S_{r\theta} = \mu \left[r \frac{\partial}{\partial r} \left(\frac{v}{r} \right) \right] \tag{2.26}$$

$$S_{\theta z} = \mu \left[\frac{\partial v}{\partial z} \right] \tag{2.27}$$

$$S_{rz} = \mu \left[\frac{\partial w}{\partial r} + \frac{\partial u}{\partial z} \right] \tag{2.28}$$

where *u*, *v*, and *w* represent the radial, azimuthal, and axial velocity; *r* the radial coordinate; θ the azimuthal coordinate; *z* the axial coordinate; and μ the fluid viscosity. The mean shear force per unit area was calculated using:

$$S_m = \frac{1}{3} \left(S_{r\theta}^2 + S_{\theta z}^2 + S_{rz}^2 \right)^{1/2} \tag{2.29}$$

The investigators employed this model to compute flow-field under microgravity (i.e. rotation of the inner cylinder and disc higher than the outer cylinder) and ground-based (i.e. equal rotation rates for the inner and outer cylinders and the disc) operating conditions. Obviously, the flow profile differed for the microgravity and ground-based conditions. The model showed good agreement with the LDV measurements, and suggested that an increase in differential rotation rates enhances the radial-axial distribution of the inlet media, while maintaining low mean shear stress levels. The investigators found that for typical cell cultures changes in perfusion rates have little effect on mean shear environments in both

microgravity as well as ground-based conditions for mammalian cells. Finally, the *Pe* for oxygen mass transport within the bioreactor was calculated to be 34,400 for ground-based conditions and 76 for microgravity. The *Sh* number for oxygen transport within the bioreactor under ground-based conditions was calculated to be 22× the diffusion limit, but only 2x the diffusion limit under microgravity; implying that microgravity conditions could easily become mass transport limited.

In a bid to evaluate bioreactor scale-up, Williams *et al*. (2002)[85] used CFD to calculate flow-fields, shear stresses, and oxygen profiles around cartilage constructs in a concentric cylinder bioreactor (which typically accommodate 16 constructs). They tested transport within the bioreactor for two cases: i) increased number of constructs (24 and 32), and ii) increased bioreactor volume. Their approach involved solving the Navier-Stokes equations and the transport equation for Oxygen (2.20). The investigators utilised two models to account for oxygen consumption: (i) *fluid-phase O_2 control model* – cells immediately consume all oxygen reaching the construct surface; and (ii) *zero-order oxygen consumption* – oxygen consumption fixed at a maximal value. Constructs were modelled as non-porous solids with a no-slip boundary condition, which mimicked the physical condition where constructs have reached maximal cell density. The investigators concluded that approximately 80% of the construct surface experiences a shear stress between 0.15 – 0.4 Pa, thereby validating the assumption that concentric cylinder bioreactors offer homogeneous hydrodynamic environment. However, their conclusion that changes in oxygen concentrations in the bioreactor "*do not*" affect chondrocyte growth was rather interesting and counter intuitive. This was based on the fact that the minimum pO_2 values they observed were still higher than oxygen concentrations observed in a cartilage *in vivo*. Most importantly, the 'scale-up' computations revealed that incorporating additional rows of constructs reduced shear stress distribution across themselves, though it also led to an

overall decrease oxygen transport. Furthermore, increasing bioreactor volume increased both, albeit not substantially. This piece of data, which points to the application of CFD as an effective design optimisation and concept selection tool, was perhaps the most far-reaching piece of conclusion reported within the article; one that motivated the investigation reported in Chapter 3.

2.3.1.2.2 LATTICE-BOLTZMANN APPROACH

Instead of directly discretising the Navier-Stokes equations, the Lattice-Boltzmann (LB) method derived from the linearised Boltzmann equation[86] has also been employed to model flow within complex geometries.[86,87] In the LB method, the physical space is discretised into a large number of sites or nodes, which bear a set of mass probability distributions. The distributions translate, at each time step, from node to node along (any of 18) fixed velocity vectors, and subsequently undergo collisions that conserve physical properties, such as momentum. In the LB method, the collision operator is designed so that particle velocity distributions obey the Navier-Stokes and advection-dispersion equations at each node.[87,88]

The underlying algorithm of the LB approach involves *streaming* and *collision* steps, which are usually combined with no-slip boundary conditions. In the streaming step, all distribution functions are advected with their respective velocities. As the movement of an incompressible fluid is also governed by inter-particle collisions, in the collide step the distribution functions of a cell are weighted with the equilibrium distribution functions (f_i^{eq}), which represent the state of the fluid where the amount of particles pushed out of each discrete direction due to collision equals the amount pushed into each direction.[89] The particle distribution function f_i evolves as follows:

$$f_i(x + e_i, t + 1) = f_i(x, t) - (f_i(x, t) - f_i^{eq}(x, t))/\tau \qquad (2.30)$$

where x is the node position in the lattice; t the time step, e_i one of i allowed velocities and τ the BGK relaxation parameter, which determines the viscosity and diffusion coefficients. In the LB approach, particle movement is restricted to a limited number of directions. For example, *D3Q19* is a commonly utilised 3D model with 19 velocities (though 3D models with 15 and 27 velocities also exist). The model and its velocity vectors $e_{1\ldots19}$ are illustrated in Figure 2.7. The streaming function performs the left side and collision function the right side of (2.30).

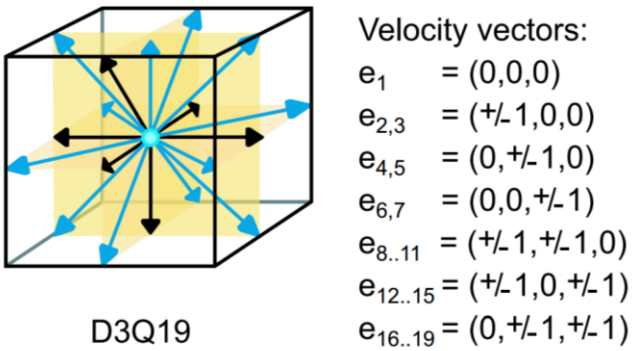

Figure 2. 7: The D3Q19 model. The figure depicts the D3Q19 model with a description of the 19 velocity vectors. A "rest" particle can be observed in the middle (cyan coloured sphere from where arrows can be seen to diverge). The vectors with weight $1/18^{th}$ are along the Cartesian axes (coloured in black), and the vectors with weight $1/36^{th}$ are in the *x-y*, *y-z*, and *x-z* planes (coloured in blue). *Reproduced with kind permission of the authors of Ref. 89.*

Porter *et al.* (2005)[88] applied the Lattice-Boltzmann (LB) method to simulate flow within a cell-seeded 3D cylindrical scaffold perfused inside a parallel-plate (perfusion) bioreactor. The objective of the study was to understand the effect of perfusion on cell culture. Microcomputed Tomography Imaging was employed to create a 3D image of human trabecular bone, which was used to define the boundary conditions for the simulation of flow through the scaffold. Shear stress was calculated by multiplying the symmetric part of the gradient of the velocity field by the dynamic viscosity (v) of the culture medium using the following equation:

$$s = \nu\left(\frac{1}{2}\right)(\nabla U + \nabla U^T) \tag{2.31}$$

where *s* is the shear stress tensor and *U* the 3D velocity vector. The investigators calculated the derivative of the velocity field by employing a finite-differences formula. Shear stress was validated against a model simulating flow between infinite parallel plates and comparing the calculate shear stress to the analytical solution. A mean surface shear stress of 5×10^{-5} Pa, concluded the investigators, correlates to increased proliferation, while higher stresses corresponded with upregulated bone marker genes.

2.3.1.2.3 LEVEL-SET METHOD

Ex vivo synthesised biological substitutes also present a 'moving boundary' problem, which poses significant challenges in its own right. Lappa[90,91] tackled this problem by simplifying the growth of the developing substitute into two simultaneously occurring phenomena: (i) *transport*: by determining the concentration fields and surface shear stress due to bioreactor hydrodynamics, and (ii) *organic tissue growth*: by determining the interface of the developing tissue and the perfused medium. Lappa employed the level-set method (LSM) to characterise (ii).[91]

The LSM is a numerical technique that can be used, amongst others, to solve moving boundary problems.[92] It entails[93] defining a smooth function $\varphi(x, t)$ that represents an interface Γ – where $\varphi(x, t) = 0$ – and employing the function to compute the motion of the interface under a velocity field. φ has the following properties:

$$\begin{gathered}\varphi(x,t) > 0, for\ x \in \Omega \\ \varphi(x,t) < 0, for\ x \notin \Omega \\ \varphi(x,t) = 0, for\ x \in \partial\Omega = \Gamma(t)\end{gathered} \tag{2.32}$$

where Ω represents the region bounded by the interface. Therefore, the interface can be captured temporally by locating the set $\Gamma(t)$ for which $\varphi = 0$. Interface motion is computed by convecting the φ values (or levels) with the velocity field as follows:

$$\frac{\partial \varphi}{\partial t} + \vec{v}.\nabla\varphi = 0 \tag{2.33}$$

In (2.33), $\vec{v}$ represents the desired velocity on the interface, and as only the normal component of v is required, the equation becomes

$$\frac{\partial \varphi}{\partial t} + v_n|\nabla\varphi| = 0 \tag{2.34}$$

because

$$v_n = \vec{v}.\frac{\nabla\varphi}{|\nabla\varphi|} \tag{2.35}$$

The underlying equation, which Lappa[90,91] employed to capture nutrient concentration at the tissue surface is given below.

$$\left.\frac{\partial C}{\partial n}\right|_i = \lambda(a\tau)^{1/2}C_i \tag{2.36}$$

In (2.36), C_i the concentration of the nutrient (for example, glucose) at the construct/liquid interface, D the diffusion coefficient of the nutrient within the medium, λ a 'kinetic coefficient' with the units of velocity (mm/s, for example), τ the fluid-dynamic shear stress on the surface of the interface, a is a constant having the reciprocal units of the shear stress, and n the direction perpendicular to the advancing front. The exponent for the shear stress, in this case, was based on a parametric investigation conducted by Obradovic *et al*. (2000).[94] In non-dimensional form, the equation can be represented as

$$D\frac{\partial C}{\partial n}\Big|_i = \tilde{\lambda}(\tilde{a}\tilde{\tau})^{1/2}(C_i) \tag{2.37}$$

where $\tilde{\lambda} = \lambda L/D$ (L being a reference distance = 1 cm) and $\tau = \left(\frac{\partial u}{\partial y} + \frac{\partial v}{\partial x}\right)$ with u and v being the velocity components along x and y, respectively.

In order to determine the velocity of the advancing front (v_n) and C, Lappa discretised the Navier-Stokes (refer to equations 2.9 and 2.10) and species equations (2.16). These equations accounted for transport within the perfusing bioreactor. Again, at the construct surface ($\varphi = 0$) equation (2.36) must be satisfied. Now, as

$$\frac{\partial C}{\partial n}\Big|_i = \nabla C_i . \hat{n} \tag{2.38}$$

where

$$\hat{n} = \frac{\nabla\varphi}{|\nabla\varphi|} = (\alpha, \beta) \tag{2.39}$$

is the unit vector perpendicular to the surface of the developing tissue. Therefore,

$$\alpha = \frac{\partial\varphi}{\partial x}\Big/\sqrt{\left(\frac{\partial\varphi}{\partial x}\right)^2 + \left(\frac{\partial\varphi}{\partial y}\right)^2}$$
$$\beta = \frac{\partial\varphi}{\partial y}\Big/\sqrt{\left(\frac{\partial\varphi}{\partial x}\right)^2 + \left(\frac{\partial\varphi}{\partial y}\right)^2} \tag{2.40}$$

Equation (2.36) can, thus be written as:

$$\alpha\frac{\partial\varphi}{\partial x} + \beta\frac{\partial\varphi}{\partial y} = \tilde{\lambda}(\tilde{a}\tilde{\tau})^{1/2}(C_i) \tag{2.41}$$

Here, $\tilde{\lambda}(\tilde{a}\tilde{\tau})^{1/2}(C_i)$ represent the mass exchange flux between the tissue and perfusion medium, driven by the demands of the developing tissue. The interface advance velocity can, therefore, be computed as follows:

$$v_n = \frac{\tilde{\lambda}(\tilde{a}\tilde{\tau})^{1/2}(C_i)}{\rho_S} \tag{2.42}$$

where ρ_s is the total density of the perfused media, with C_i satisfying (2.41).

The domain was discretised with a uniform mesh with flow-field variables defined over a staggered grid. The solution algorithm entailed the following steps: (i) advancing rhe interface (2.34) and reinitialising the level-set function; (ii) solving for the concentration and velocity fields in the liquid; (iii) adjourning local values of *C* at the tissue-medium interface (2.41); and (iv) computing the surface growth rate distribution (2.37). Lappa concluded that LSM should be considered a robust approach to simulate problems concerning the growth of biological tissues and related slow surface kinetics.

2.3.1.3 MECHANOBIOLOGY

While the foregoing set of equations deal with transport phenomena, continuum equations are also employed to account for the problems of mechanobiology. Mechanobiology integrates the principles of traditional mechanics with molecular biology and genetics.[95] At its core, though, lies the process of mechanotransduction, i.e. the sensing and response by cells to mechanical (or, in general, biophysical) stimuli. Mechanobiology can be employed to determine the solution of problems that concern deformation at cellular and sub-cellular level due to forces acting at organ or tissue level and adaptation of the tissue/organ construct to the mechanical stimuli. Computational TERM deals mostly with the latter.

The finite element method (FEM) is a numerical technique that discretises the domain (such as a tissue or scaffold encapsulating cells) into sub-domains, known as elements. Each element contains a certain number of vertices referred to as nodes, where the field variable (i.e. the value of interest) is computed. Nodes and elements together constitute the finite element mesh. The solution is determined at the nodes and interpolation functions are employed to compute the solution everywhere else on the domain. Loads and constraints form the boundary conditions for the models. Whereas loads acting on a body are modelled as forces applied to the aforementioned nodes, constraints are simulated by preventing nodal displacements along the direction of each constraint. Forces and displacements at each node can, therefore, be calculated by

$$F = K\delta \tag{2.43}$$

where K is the global stiffness matrix, F is the vector of applied force on the nodes or the load vector, and δ nodal displacements. Unless force has been applied to a node, it is zero for all nodes. Knowing stiffness and force for each node, (2.43) can be employed to determine the complete set of nodal displacements. This is followed by computing the partial derivatives of each displacement component and combining them to obtain deformations. Eventually, constitutive equations that relate stress and deformations are employed to compute stresses.

The impact of mechanical loading on cells can then be characterised by employing *mechano-regulation algorithms*, which have been defined as a *finite set of rules that govern the effects of mechanical loading*[95] on cells and tissues. Essentially, these algorithms account for cellular processes such as cellular dispersal, proliferation, apoptosis, etc. Cellular dispersal, for example, can be accounted for by utilising the *diffusion* equation – the

underlying assumption being that cellular movement can be thought of as an assemblage of particles.

$$\frac{dc}{dt} = D\nabla^2 c \tag{2.44}$$

In (2.44), *c* represents the concentration of stem cells in a given domain and *D* the diffusion coefficient. However, as cells do not necessarily attempt to achieve a homogeneous distribution within the domain under consideration, the equation calls for more realistic variables. Inclusion of proliferation and apoptosis into (2.44) provides a more accurate way to account for cell dispersal. The rate of change in cell concentration can, therefore, be represented as:

$$\frac{dc}{dt} = D\nabla^2 c + p(S)c - k(S)c \tag{2.45}$$

where, *p* describes rate of mitosis per cell and *k* accounts for cell death (or removal) as a function of a biophysical stimulus *S*.

Kelly and Prendergast,[96] in order to determine mechanical properties of a scaffold optimal for promoting the differentiation of mesenchymal cells towards the chondrogenic phenotype to assist osteochondral defect repair, applied a mechanoregulation algorithm for tissue differentiation on a finite element model of an osteochondral defect. The model considered an array of cellular behaviours, dispersion, proliferation, and apoptosis, refer to (2.45), including differentiation into cells of different phenotypes (from the mesenchymal phenotype to fibrogenic, osteogenic, or chondrogenic phenotypes) represented by *i*, which subsequently produced different connective tissue (fibrous tissue, bone, cartilage; respectively) represented by *j*. The net change in number of cells was represented by:

$$\frac{dc^i}{dt} = D^i \nabla^2 c^i + p^i(S)c^i - k^i(S)c^i \tag{2.46}$$

The investigators assumed a quadratic relationship between cell proliferation and cell death and the magnitude of the biophysical stimulus (*S*). This is shown in (2.47).

$$p^i(S)c^i - k^i(S)c^i = a_i + b_i S_O + c_i {S_O}^2 \tag{2.47}$$

where S_O represents the octahedral shear strain. Depending upon the strength of the stimulus experienced by dispersing cells, they underwent differentiation into a particular phenotype, as demonstrated in Fig. 2.8. *S* itself was considered a function of the octahedral shear strain and interstitial fluid flow in the extracellular environment of cells. This relationship is shown in (2.48):

$$S = \frac{\gamma}{a} + \frac{v}{b} \tag{2.48}$$

where γ is the shear strain, v the fluid flow, and a (3.75%) and b (3 μm/s) are empirical constants.

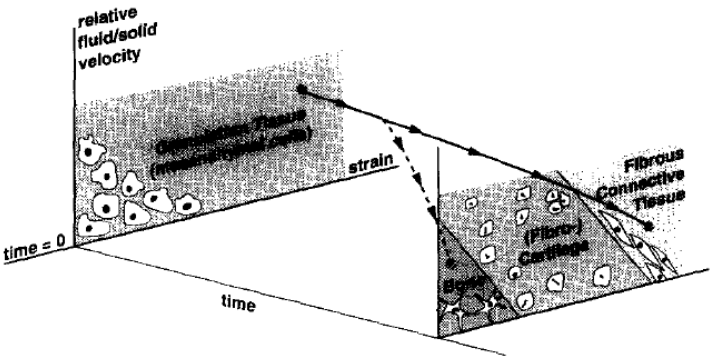

Figure 2. 8: Mechanoregulation of tissue differentiation. The figure depicts the mechanoregulation algorithm proposed by Prendergast *et al.* (1997)[97] and employed in the study to account for tissue differentiation. *Reproduced with permission from Ref. © 97 (1997) Elsevier.*

S was determined via a linear, poroelastic, axisymmetric finite element model of an osteochondral defect. The investigators, via the model, studied the healing process of cell invasion within the defect (from the marrow), their differentiation, and synthesis of the extracellular matrix, which eventually altered the mechanical properties of the tissue.

Equation (2.46) was used to account for distribution of cells. Material properties of every element were computed based on the number and phenotype of cells within each domain element. Subsequently, *S*, is computed based on the material properties, cell numbers, and phenotypes.

The model relied on various idealisations that included describing cell movement via diffusion equation, not accounting for the inhomogeneous nature of soft tissues, and ignoring scaffold degradation with passage of time. The investigators included two different types of scaffolds in their study: homogeneous (modelled as a linear poroelastic model) and heterogeneous (modelled with two distinct phases: chondral and bone). They predicted that increasing scaffold stiffness (to a certain threshold) increases cartilage and reduces fibrous tissue formation and that reduction in scaffold permeability to a certain threshold value (1e-15 m^4/NS) leads to less fibrous tissue within the defect. The investigators then computed optimal (approximately 1% fibrous tissue in repair tissue) scaffold design that would yield cartilage tissue in the chondral phase and bone tissue in the bony region of an osteochondral defect. By parametrically varying scaffold mechanical properties through its depth, the investigators concluded that the Young's modulus for such a scaffold to reduce (non-linearly), from 60MPa in the superficial layer, to 10MPa in the base, with a non-linear increase in permeability from 1e-16 m^4/NS (superficial layer) to 2e-15 m^4/NS (base). They confirmed the need for a scaffold to mimic the mechanical properties of the native tissue it aims to replace. Despite capturing features observed during spontaneous osteochondral defect repair, conclusions from the model towards scaffold development are for *in vivo* chondrogenesis alone[98].

The algorithms employed in this study were further utilised, and expanded, by Byrne *et al.* (2007)[99] to elucidate possible interactions between various design parameters; such as scaffold porosity, Young's modulus, and dissolution; in controlling bone regeneration. The

investigators implemented a random walk algorithm to account for proliferation and migration. This was achieved by dividing each finite element of the granulated tissue into a 'lattice', with each lattice point representing a region of space for both the cell and the ECM. Proliferation was modelled by assuming that cells moved stochastically into one of its surrounding lattice site, and one of the remaining neighbouring positions chosen for the daughter cell. This continues until the end of the simulation or confluence. Migration was also modelled by randomly selecting a neighbouring site. However, as migration occurs at a faster time scale than proliferation, new location for the migrating cells was chosen *i* times per iteration of the proliferation process. The investigators employed (2.48) to determine the biophysical stimulus for each lattice site, which in turn regulated differentiation for cells within those lattice sites. High stimulus level promoted the fibroblastic phenotype, intermediate the chondrogenic phenotype, low levels the osteoblastic phenotype, and very low levels resorption.

The investigators considered a 3D finite-element model of a regular structured bone, which yielded geometry similar to printed scaffolds. The initiation of modelling was considered as the point where granulation tissue infiltrates the scaffold. Vertical displacement was applied on the surface model nodes. Additionally, the investigators considered scaffold dissolution, which led to an increase in the amount of granulation tissue, thereby allowing more lattice points in the finite-elements. A combination of rate law (2.49) and rule of mixtures (2.50) was used to account for material properties of each element.

$$E_i = K_i e^{\beta_i t} \tag{2.49}$$

$$E(iter+1) = \frac{n_i}{n_{max}} \bar{E} + \frac{(n_{max} - n_i)}{n_{max}} E_{granulation} \tag{2.50}$$

In (2.49), E_i serves as the Young's modulus for tissue phenotype *i*, *t* as the time, and K_i and β_i regulate the shape of the exponential curve (refer to the original article). In (2.50), *iter*

represents iteration, $\bar{E}$ the average Young's modulus for a particular element over the last ten iterations, n_{max} the maximum concentration of mesenchymal stem cells, n the number of cells for phenotype i, and $E_{granulation}$ the Young's modulus of the granulation tissue. As there is no evidence to suggest that the bulk modulus, permeability, and Poisson's ratio of the granulation elements increase exponentially with time, the rate law was not used to determine these mechanical properties for the granulation elements (only the rule of mixtures was employed).

The model was an advance on the previous model by Prendergast, which employed diffusion to account for migration, thereby offering more realistic simulations in bone tissue engineering. The model considered three vital design characteristics of a scaffold: porosity, Young's modulus, and dissolution rate. The simulations predicted that the three design features can influence the amount of bone regeneration quite critically. Qualitatively speaking, in a low-load environment, the investigators suggest, that a higher porosity and higher stiffness along with a medium dissolution rate gives the greatest amount of bone. However, in a high-load environment a lower dissolution rate is preferred to prevent the scaffold from collapsing, once the scaffold has dissolved beyond its critical limit. The model made certain idealisations: such as it assumed that cells can permeate through the entire volume until all the available space is colonised, cell death was not considered, and degradation was linear. Still, the model, more realistic than many of its predecessors, illustrated the growing demand for computational methods in aiding design of TERM products and the crucial role continuum methods have played towards this end.

Although various techniques have been employed to quantify biophysical cues as they develop inside a scaffold, maintained in either perfused or static states, the finite-element method of approximating PDEs to achieve this has met with reasonable success. The fact that FEM can handle arbitrary geometries with non-homogeneous pores is an

additional advantage. In order to achieve this, the geometry of the scaffold is first reconstructed virtually. This can be achieve by using any CAD software or, if recreating the specific architectural aspects of scaffolds is of interest, employing computed-tomography (CT) or micro CT to characterise the scaffold and approximating the structure in 3D.[100-102] The configuration is then ready to be discretised for further analysis.

Towards this end, McMahon *et al*. (2008)[103] employed the poroelastic FEM analysis of 3D collagen type I-glycosaminoglycan (GAG) to quantify the biophysical stimuli developed within the scaffold during loading. They validated their numerical model by perfusing the MSC-seeded scaffold by a custom designed 5-station uniaxial stretching bioreactor with the aim of applying cyclic tensile loading. The investigators concluded that biophysical stimuli, such as strain and fluid-flow, generated within the scaffold were the main contributors to the observed mechanoregulation of MSC differentiation. Similarly, Sandino *et al*. (2008)[101], who employed FEM to investigate stress-strain distribution at microscopic levels inside a scaffold ended up confirming the impact of non-uniform scaffold architecture, which is responsible for creating areas of high fluid flow, strain and stress distribution, on cellular behaviour.

Poroelastic formulations are employed when dealing with a porous matrix interconnected with a network of fluid-filled pores, where the solid matrix is undergoing deformation.[104] In effect, the term poroelasticity captures interactions between solid deformation and fluid-flows within a (usually fully saturated) porous structure. Application of external load on the porous medium alters the volume fraction. As such, a change in pressure is observed by fluid filled pores under this mechanical stress, which leads to fluid motion (referred to as solid-to-fluid coupling). This flow and concomitant variations in pressure subsequently causes the solid material to deform elastically, producing a change in the volume of the porous material (referred to as fluid-to-solid coupling). Such formulations

can, therefore, be employed to study mechanics and transport within biomaterials (for example, the collagen scaffold investigated by McMahon and co-workers) and native tissue.[98] While computationally elegant and essential in capturing the impact of the deformation of the porous medium on fluid flow (and vice versa) the topic is not considered within this thesis. This is because the thesis is a first step to enable a working, basic prototype of the framework, which would be subsequently advanced and expanded to incorporate the relevant constitutive equations.

The finite element method, beyond capturing biomechanics, has also been employed to study bioreactor hydrodynamics and cell growth. Peng and Palsson[105] assessed the impact of bioreactor geometry on cell growth and differentiation by solving the Navier-Stokes and convection-diffusion equations (describing the physicochemical environment) using the finite-element approach. The investigators used a unilineage model to simulate cellular behaviour. They concluded that the behaviour of the solution was governed by two dimensionless numbers: the *Graetz number* (that describes the relative rates of convection and diffusion) and, a ratio they introduced in this paper, *P* (that describes the interplay of growth factor production, diffusion and stimulation). The investigators observed that *P* determined the spatiotemporal development of tissues and the *Graetz number* the cell density inside the bioreactor. The optimal values for the two dimensionless numbers were reported as follows: $0.01 < P < 0.1$ and $0.1 < Graetz < 1$. Furthermore, out of the four geometries of parallel-plate bioreactors that were simulated (slab, gondola, diamond, and radial) they predicted the radial geometry to offer the most uniform environment for the growth and differentiation of parenchymal cells as a result of flow paths creating slow flowing regions.

Despite the utilisation of the computationally efficient and convenient continuum equations to account for cell dispersal, cells do not migrate by employing the diffusive mechanism. In fact, while continuum equations can be utilised to model cellular behaviour, including proliferation and apoptosis, the approach assumes component homogeneity to relate system observables using mathematical equations. Moreover, classic continua are not dynamic – unlike biological systems they do not change their material properties over time[1] (although of course numerous continuum computational methods that attempt to incorporate such variations have been proposed). Furthermore, the homogeneity condition struggles to offer detailed solutions when applied to systems with dynamically interacting heterogeneous components. As the functionality and architecture of most biological systems is a product of multi-faceted individual interactions at sub-system level, continuum models rarely offer much beyond qualitative similarity. In order to model cellular behaviour and interactions between cells and between cells and their microenvironment recourse to the discrete approach is recommended.

2.3.2 DISCRETE APPROACH

Discrete approaches, such as the *cellular automata*[7,8] (CA) – that employ interacting *finite-state machines*[9] – or the cellular Potts modelling approach (CPM)[10] – which simulates systems by mapping *cells* to domains on a lattice, can capture (i) the non-homogeneous character of biological systems (which is also responsible for their complexity) and (ii) the emergence of global patterns from underlying rules, in a manner more faithful to cellular systems than their continuum counterparts.

2.3.2.1 CELLULAR AUTOMATA

Cellular automata (CA) belong to the class of lattice-based discrete approaches that utilise rules-based local interactions between system components (i.e. finite-state machines)

to map the spatiotemporal evolution of a system. Traditionally, CA consists of the cellular space and transition rules governing cell states.[106,107] The cellular space is a lattice of N identical finite-state machines (FSM), each with identical pattern of local connections with other FSMs for input and output, along with relevant boundary conditions.[106,107] The FSMs, or the CA grids, are formally defined as *finite-state machines* (FSM),[108] which are represented as:

$$FSM = (S, \sigma, T, s_0, F) \tag{2.51}$$

In (2.51), S is the finite set of states, σ is a finite alphabet of input symbols, T is the transition function ($S \times \Sigma \rightarrow S$), $s_0 \in S$ represents the initial state, and $F \subset S$ represents the set of final states. The FSMs derive their input from neighbouring FSMs, and based on the transition rule update their state. Traditionally, in CA, FSMs interact directly with their neighbours and, generally, do not display global interactions[11] (although cases exist where such behaviour has been incorporated in the system). This makes CA quite appealing in terms of computational efficiency. CA possess linear computational complexity,[11] commonly denoted as $O(n)$, where n represents the number of elements in the system. This means that computational time is directly proportional to the number of elements in the system. Doubling the number of elements will *only* double (not quadruple) the computational time. A feature, however, that makes CA more attractive is that it is an intuitive way to represent the algorithmic decision-making displayed by cells, and that they require lesser time investment than its continuum counterparts.

Galvao *et al*. (2008)[109] used a rule-based model to investigate the role of stem cell therapy in tissue regeneration. They chose to model the chronic chagasic cardiomyopathy after bone marrow stem cell transplantation and, therefore, better understand the kinetics of cardiac tissue regeneration. The model employed a set of *local* rules governing the set of

states on a 2D rectangular lattice, and based on the observations that chronic chagasic cardiomyopathy is characterised by inflammation, presence of pro-inflammatory cytokines, and severe fibrosis. The agents occupying the lattice sites included: the inflammatory agent, fibrosis area/site(s), cardiomyocyte agent, tumour necrosis factor-α (TNF-α, a pro-inflammatory cytokine), bone marrow stem cell, and *Trypanosoma cruzi* agent (a parasite implicated in the disease). The lattice possessed 250,000 sites and periodic boundary conditions. The total number of agents and initial fraction of fibrosis area, inflammatory cells, bone marrow stem cells, TNF-α, and *T. cruzi* formed the initial conditions of the simulations. The following transition rules were employed by the investigators:

- If in the neighbourhood of an inflammatory cell the number of bone marrow stem cells > 0 (based on the *Moore* neighbourhood, i.e. each site had 8 neighbours: north, south, east, west, northeast, southeast, northwest, and southwest), the inflammatory agent undergoes apoptosis (site changes to an empty state),
- If in the neighbourhood of a fibrosis site the number of bone marrow stem cells > 0, reduction in fibrosis site (or area) ensues (site changes to an empty state),
- If in the neighbourhood of an empty site there is a cardiomyocyte and the number of bone marrow stem cells is greater than a set value, the empty site changes into a cardiomyocyte (i.e. the bone marrow stem cells undergo differentiation),
- If in the neighbourhood of an empty site the number of the inflammatory cells and *T. cruzi* > 0, the empty site changes into an inflammatory cell, and, finally,
- If in the neighbourhood of an empty site the number of TNF-α and fibrosis site/area > 0, the empty site changes into a fibrosis site.

The model was able to capture, refer to Figure 2.9, apoptosis and differentiation, and implicated concentration patterns of fibrotic regions and inflammatory cells as the most important factors in the kinetics of chronic chagasic cardiomyopathy regeneration after

bone marrow stem cell transplantation. The results also attributed the reduction in fibrotic area to the initial fraction of bone marrow stem cells and TNF-α.

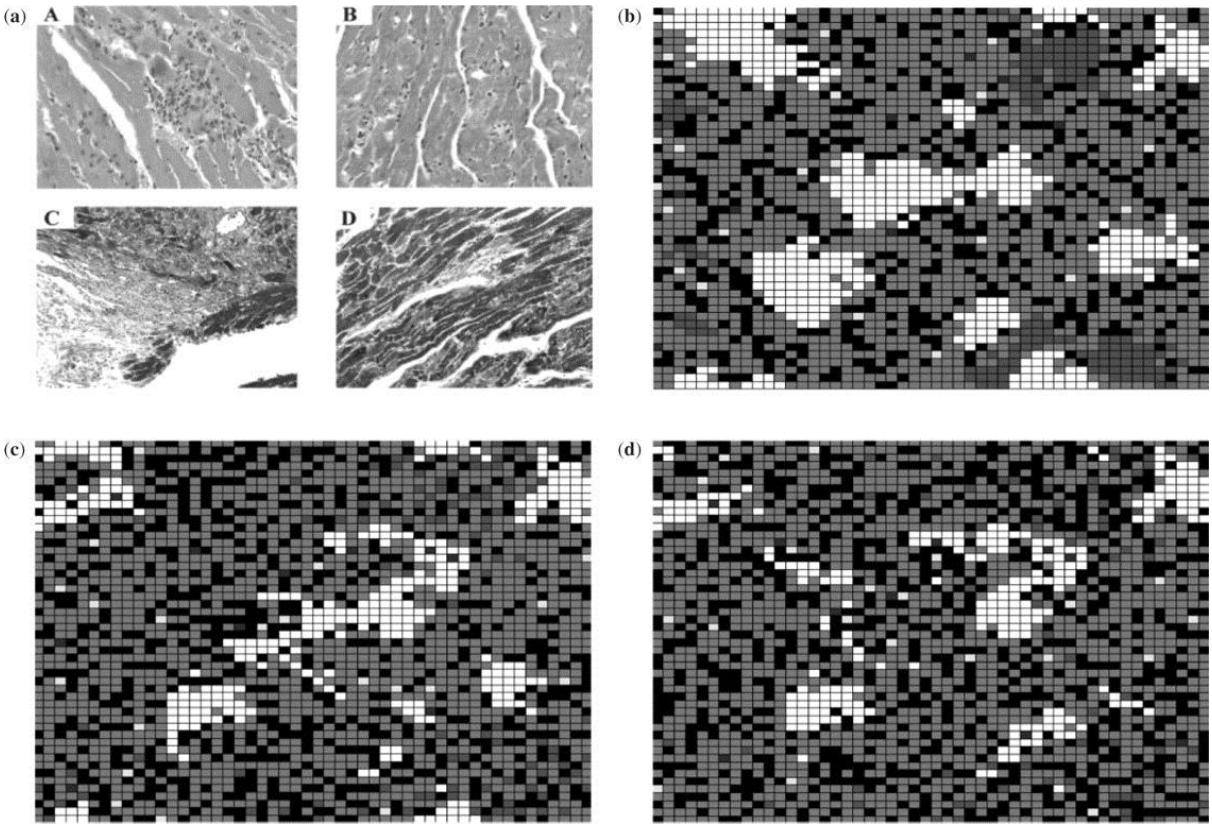

Figure 2. 9: Chagasic cardiac tissue: *in vivo* vs *in virtuo*. The figure shows comparison of the computational results (b, c, and d) against samples collected from chronic chagasic mice (a) treated with control (A and C) and bone marrow stem cells (B and D). Fibrotic region in the specimen obtained from mice and the computational lattice appears in white. Sub-images (b) – (d) represent the computational model at different time points: t = 0 – (b), t = 3 days – (c), and t = 6 days (d). *Figure (a) was reproduced with kind permission from Ref. 110 © (2004) Elsevier. Figures (b) – (d) were reproduced* with kind permission from Ref. 109 © (2008) *Oxford University Press*.

2.3.2.2 CELLULAR POTTS MODELLING

Cellular Potts Modelling (CPM), like CA, is a discrete lattice-based framework. In CPM, cells are represented as a set of lattice sites, refer to Figure 2.10, which are assigned variables referred to as the *spin* (σ) and *type* ($\tau > 0$).[11] Each lattice site (i,j), therefore, forms part of a cell $\sigma(i,j)$, which has a type $\tau(\sigma(i,j))$. In addition to the cell types, the medium in which the cells exist is represented by another type (M).[11] Like CA, CPM relies on rules that govern the transition of the state of a site depending upon the state of its neighbours. The framework operates by iteratively attempting to copy the spin of a randomly selected lattice

site into a randomly chosen adjacent neighbour site. The spin is accepted if it decreases the *total energy* of the lattice or with Boltzmann probability if it increases the total energy of the lattice.[111,112] The total energy of the lattice is represented by the *Hamiltonian* (*H*) of the system. CPM employs the *Metropolis algorithm*, which belongs to the family of *Monte Carlo* stochastic algorithms. In CPM, random configuration of the lattice sites is generated based on Boltzmann distribution. As higher energy states are less favoured in Boltzmann distribution, applying the Metropolis algorithm successively moves the system towards states with less energy.

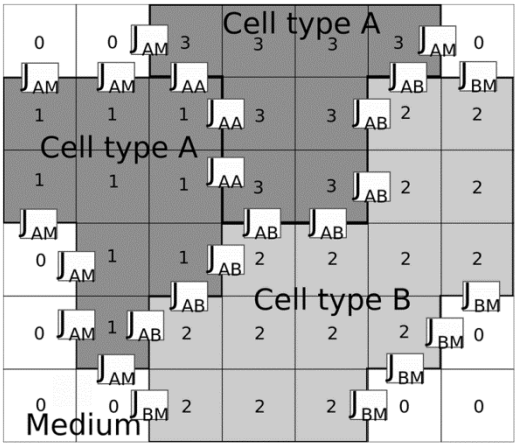

Figure 2. 10: Lattice and cell representation in Cellular Potts Modelling. The figure depicts a two-dimensional CPM lattice with three cells with indices 1, 2, and 3, and types *A* and *B*. As evident, once cell can cover multiple lattice sites and interact with others at the cell surfaces. The strength of interaction, i.e. *J*, is proportional to the cell types. Furthermore, medium on this lattice is represented by grids with index 0. The image was derived from Voss-Böhme (2012)[112] and was reprinted under *Creative Commons Attribution License*.

The Hamiltonian, as represented in (2.52), has two components: *volume energy* and *bond energy*.

$$H = H_{vol} + H_{bond} \tag{2.52}$$

H_{vol} assumes that cells are elastic and resist deformation. In 2D models, elastic areas are used instead. The volume component is shown in (2.53).

$$H_{vol} = \lambda \sum_{\sigma \neq M} \left(a(\sigma) - A_{\tau(\sigma)}\right)^2 \tag{2.53}$$

In (2.53), λ represents the stiffness of the cell area, $a(\sigma)$ the equilibrium area of the cell, and $A_{\tau(\sigma)}$ the current area of the cell. A cell makes no contribution to H if it is at its equilibrium size. However, if compressed or stretched, its energy increases quadratically. Bond energy emerges from the contact between two cells or between a cell and the medium. This component is proportional to the size of the interface between the two relevant constituents, and is represented by:

$$H_{bond} = \sum_{\substack{(i,j),(i',j') \\ neighbours}} J\{\tau(\sigma(i,j)), \tau(\sigma(i',j'))\}\{1 - \delta_{\sigma(i,j),\sigma(i',j')}\} \tag{2.54}$$

In (2.54), $J(\tau_1,\tau_2)$ captures the bond energy resulting from two neighbouring sites of cell types τ_1 and τ_2. The second component clears any contribution from neighbouring sites within the same cell. Incorporating (2.53) and (2.54) into (2.52) gives us (2.55):

$$H_{bond} = \sum_{\substack{(i,j),(i',j') \\ neighbours}} J\{\tau(\sigma(i,j)), \tau(\sigma(i',j'))\}\{1 - \delta_{\sigma(i,j),\sigma(i',j')}\} \tag{2.55}$$

$$+\lambda \sum_{\sigma \neq M} \left(a(\sigma) - A_{\tau(\sigma)}\right)^2$$

The simulation step consists of iteratively applying the following algorithm subsequent to the definition of the Hamiltonian:

- Choose a lattice site (i, j) randomly;
- Choose a neighbouring site (i', j') randomly, which is located within the next nearest neighbourhood of the initial site (i, j);

- Calculate ΔH caused by setting $\sigma(i, j) \rightarrow \sigma(i', j')$;
- If $\Delta H \leq 0$, then set $\sigma(i, j) \rightarrow \sigma(i', j')$;
- If $\Delta H > 0$, then $\sigma(i, j) \rightarrow \sigma(i', j')$ with probability $P = exp(-\Delta H/kT)$, where k is the Boltzmann constant and T > 0 is a simulation parameter known as the temperature.

Key advantages of the CPM include the fact that they do not make the simplifying assumption that cells are shapeless points and that it provides a straightforward 'module', in the form of the Hamiltonian, to incorporate any new phenomena (as we shall see in the following examples and over the course of examples reviewed in this thesis). By adding a term to the energy function anything that can be quantified with a scalar can be accounted for. Processes that reduce the total energy cost of the system are preferred with the implication that the user does not need to specify exactly how the constraints need to be met. Furthermore, as discussed in some of the literature above, the paradigm can be easily integrated with modelling frameworks of different flavour to develop hybrid models, which allow for the development of more sophisticated and elegant models of biological phenomena.

Using this approach, Merks *et al*. (2006)[113] developed a model capturing the assembly of human umbilical vein endothelial cells (HUVEC) into a network of connected cells in a Matrigel environment. The investigators aimed to understand aspects of vascular development that result from self-organisation of endothelial cells and those that require additional cell types and guidance. The model was based on simple behaviours displayed by endothelial cells: secretion of morphogens that inactivate the ECM, preferential extension of filopodia up the morphogen gradient, and rapid elongation following contact with the ECM. The investigators further worked with the observation that shape change of cells in this context is driven by remodelling of the actin cytoskeleton.

The following assumptions were employed to build the model: endothelial cells (i) assumed an elongated shape driven by cytoskeleton remodelling, (ii) secrete a chemoattractant, and (iii) move up the chemoattractant; and the chemoattractant (iv) diffuses in the ECM, and (v) slowly decays producing a gradient around endothelial cell clusters. The virtual cells were seeded on a rectangular numerical grid. Active, random extension of filopodia and protrusions of the first cell displacing the surface of the second cell was modelled by repeatedly replacing the spin at the cell interface by a neighbouring grid point's spin. Adhesion, target area deviations, and chemotaxis were expressed in terms of the effective energy *H* (refer to 2.55). By introducing an extra reduction of energy, refer to (2.56), in (2.55) whenever the cell protrudes into an area with higher chemoattractant concentration, the investigators implemented preferential extension of the filopodia.

$$\Delta H_{chemotaxis} = \chi[c(x) - c(x')] \tag{2.56}$$

In (2.56), *c(x)* refers to the local chemoattractant concentration, x' the neighbour into which site *x* copies its value, and χ is the strength of the chemotactic response, which was set to 1000. The chemoattractant concentration was determined by discretising (2.57) via the finite-difference approach.

$$\frac{\partial c}{\partial t} = \alpha\left(1 - \delta_{\sigma x,0}\right) - \delta_{\sigma x,0}.\varepsilon.c + D\nabla^2 c \tag{2.57}$$

In (2.57), α is the rate of chemoattractant release, ε is the chemoattractant clearance rate, and *D* the diffusion coefficient, and $\delta_{\sigma x,0}$ = 1 inside the cells. The ECM was modelled as a generalised CPM cell without volume constraint and with σ=0. The investigators added a cell length constraint to the free energy to model cell elongation due to cytoskeletal remodelling:

$$H' = H + \lambda_L \sum_{\sigma} (l_\sigma - L_\sigma)^2 \tag{2.58}$$

where σ_l was cell length (of the cell σ) along its longest axis, L_σ the target length, and λ_L the strength of the length constraint.

The model generated patterns, both qualitatively and quantitatively, in close agreement with those observed *in vitro*, suggesting primarily that the underlying behaviours considered in the model are indeed central for vasculogenesis *in vitro*. Secondly, the model suggests that the elongated cell shape is important in morphogenesis. Furthermore, the model was able to provide insights into the physicochemical properties of the diffusing chemoattractant. In order to observe *in vitro* vasculogenesis patterns, the model suggested, that the diffusing chemoattractant should be roughly two orders of magnitude slower than $VEGF_{165}$, an isoform of VEGF identified as the main inter-endothelial signalling molecule.

This model was further extended by Guidolin e*t al.* (2009)[114] to model *in vitro* angiogenesis under conditions that involve pro-angiogenic stimulation of cells. In particular, they used the model developed by Merks *et al.* (2006)[113] to simulate the growth of human saphenous vein endothelial cell (HSVEC) cultured on Matrigel and stimulated with the peptide adrenomedullin. The investigators, however, extended the model to incorporate cell proliferation to test whether the presence of mitotic events can enable a more accurate representation of the morphology of the patterns formed by endothelial cells. The following algorithm was employed whenever during the simulation mitosis was to occur:

- Pick a cell randomly,
- Divide it into two children cells through its centre of mass along the axis of minimum length,

- The children cells inherit the same physical properties as the parent cell.

Just as Merks *et al.* (2006), Guidolin *et al*. (2009) were able to accurately reproduce the self-assembly of cultured, unstimulated HSVEC. When stimulated with the peptide adrenomedullin, the investigators observed a capillary-tube like formation that subsequently led to a meshwork of increased extension and complexity. Most importantly, however, the extended model of Guidolin and coworkers predicted quantitatively the amount of mitoses that needs to occur to observe the best match against *in vitro* data. They predicted that while for unstimulated cells a very low (~0%) proliferation level allowed the formation of realistic capillary-like patterns, stimulated cells need at least 13% increase in cell numbers to achieve the same.

What the two examples serve to demonstrate is the modularity of the CPM approach. With relative ease and simplicity any cellular behaviour can be incorporated into the CPM framework. Furthermore, like the CA approach, the CPM also has the capability to capture emergent patterns (also demonstrated by the two examples) and can be used as a hypothesis testing tool, as successfully employed by Merks *et al*. (2006)[113] and several others.[111,115-119] Most importantly, the technique can be employed to shed novel insights into the biophysicochemical mechanisms underlying the behaviour of biological systems, as demonstrated by insights obtained from Merks and co-workers above (on the physicochemical nature of the diffusing chemoattractant) and Guidolin and coworkers (quantifying the proliferation levels needed to generate more accurate *in vitro* patterns).

2.3.2.3 COMMUNICATING STREAM X-MACHINES

Introduced by Laycock[16], an *agent* (or a *stream X-machine*[16]) is a finite-state machine[64] which contains a finite set of internal states, a set of transition functions operating between states, an internal memory set, and a language for interacting with other agents

(XMML in the implementation described herein).[120] According to Jennings,[121] agents are the new theoretical model of computation.

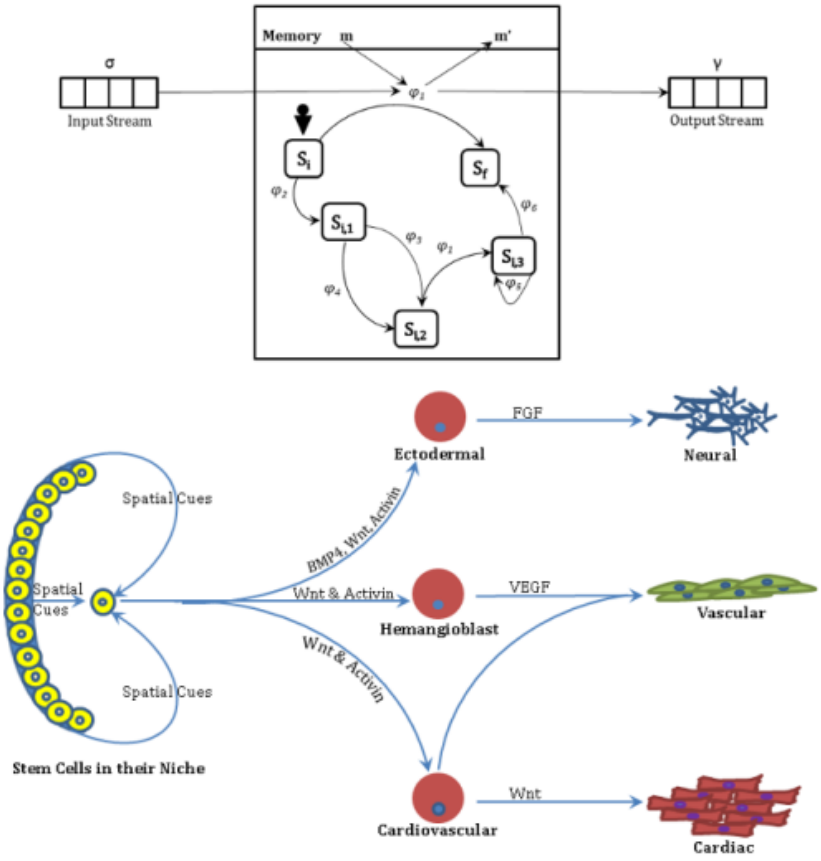

Figure 2. 11: Agents. This figure highlights the parallels between an agent and a cell. **Top**: A *communicating agent* (stream X-machine); adapted from Ref. 64. **Bottom**: Cell decision-making; signalling cues derived from Ref. 19. Depending upon the multitude of input signals that a cell responds to, it transitions into a phenotype based on hitherto unknown biological rules. The input signals (represented on the arrows) can be spatial, chemical, or electrical and induce a response from the cell. The cell in its new transition state seems to be quite aware of its latest phenotype, a feature that in the ABM is represented by the update of agent-memory.

From a qualitative perspective, as defined by Wooldridge,[122] "*an agent is an encapsulated computer system that is situated in some environment and that is capable of flexible, autonomous action in that environment in order to meet its design objectives*." Therefore, by definition, an agent possesses well defined boundaries and interfaces, has the ability to sense its environment (and act on its environment), can control its internal state as well as behaviour, has particular goals to achieve, can act in the anticipation of future goals, and respond in timely fashion to changes that affect its environment.[121]

An agent X can be represented quantitatively[8] as:

$$X = (\sigma, \gamma, S, M, \phi, F, s_0, m_0) \tag{2.59}$$

where σ are the set of input, γ are the set of output, S denotes the set of states, m denotes the variables in the memory, Φ denotes the set of partial functions φ that map an input and memory variable to an output and a change on the memory variable (φ: $\sigma \times M \rightarrow \gamma \times M$), F is the next state transition function: F: $S \times \varphi$, s_0 is the initial state and m_0 is the initial memory. A common message board to (and from) which messages are posted (and read) assists the agents in communicating with each other. Figure 2.11 shows an X-Machine agent and Figure 2.12 represents communication between two X-machines.

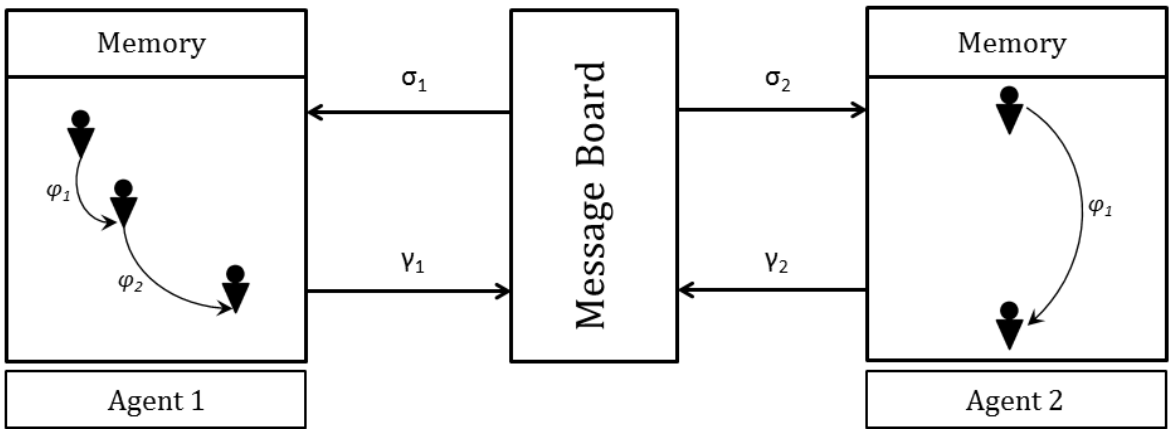

Figure 2. 12: The dynamics of X-machine communication. The message board maintains a database of all the messages sent by the agents. The agents read, and send, messages from (and to) the message board. Adapted from the **FLAME** user manual available at http://www.flame.ac.uk/docs/

The state transition functions (φ) respond to events considering both the environmental input σ as well as the current internal state. For example, a communicating X-machine with an initial state i and an initial memory m upon receiving input σ, depending upon σ and m, will/may(/will not) change its state producing an output γ and updating the memory to m'. This modelling mechanism provides a sensible way of dealing with problems associated with state explosion, which afflict many efforts at modelling complex biological systems.[5,64] Also, being inherently hierarchical, an X-machine is able to link different modelling paradigms.[64]

Walker *et al*. (2006, 2004)[123,124] developed multiple models of epithelial tissue employing the agent-based approach. Their models were based on social behaviour of cells and employed *global* rules, in contrast to the *local* rules in the previous example. Walker *et al.*[123,124] employed a continuous domain which gave the investigators the opportunity to model cells in a morphology other than a square or cube and simulate continuous cellular migration, which is more realistic than grid based 'jumps'. In their initial proof-of-concept model,[123] the investigators modelled cells that could interact with each other and the environment, which comprised a 2D square substrate and modifiable exogenous calcium ion concentrations. Intercellular communication was achieved by employing a global "communication matrix", which, essentially, was a data structure *N* cells long by *N* cells wide. For example, if cell *i* formed a bond with cell *j*, a 'stick' message would be posted in row *i*, column *j* of the communication matrix; and cell *j* would receive the message so it can update its internal parameters as well.

The investigators used rules explaining cellular behaviour such as cell cycle, bonding, spreading, migration, and apoptosis to simulate growth characteristics of epithelial cells in monolayer culture under low and physiologic Calcium ion concentration [Ca^{2+}]. Cell cycle formed the central hinge of the model, which governed the transition of cells through the various cell phases:

- *G1:* Growth phase – cells double their volume,
- *G0:* Quiescence – halfway through G1 a checkpoint was added, which identifies contact-inhibited cells (with 4 or more bonded neighbours),
- *G2:* Preparation for mitosis,
- *M:* Post-mitosis, the cell returns to its original, rounded shape, and a new cell agent is added in the environment.

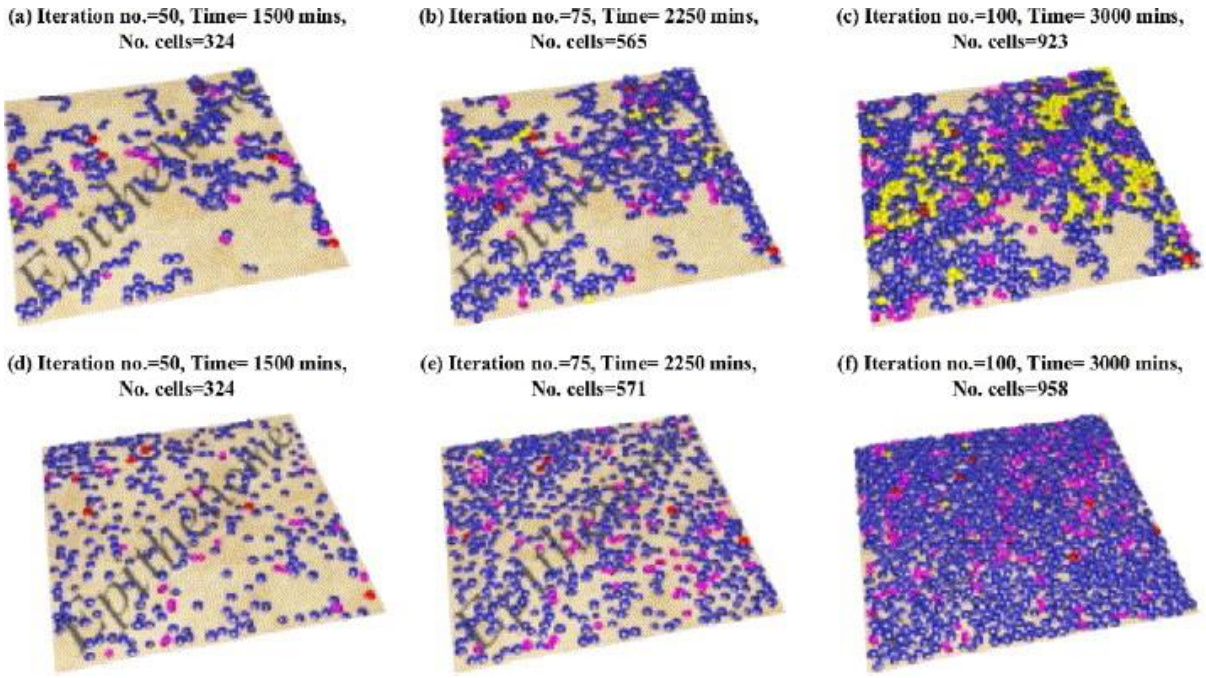

Figure 2. 13: Culture growth simulated under physiological (a-c) and low (d-f) calcium concentrations. Stem cells in the figure are represented in red, transit amplifying cells in blue, mitotic cells in pink, and quiescent cells in yellow. R*eproduced with kind permission from Ref. 123 © (2004) Elsevier*.

As the model did not account for intracellular phenomena, phases beyond G0 were accounted for by simply incrementing the 'cycle clocks' – inherent to each agent – by a tick/iteration. The computations were conducted in a substrate of dimensions 1.2 mm × 1.2 mm and exogenous [Ca^{2+}] of 0.09 and 2.0 mM. An initial cell density of 7×10^3 cells/cm^2 was employed. Results were found to qualitatively replicate the trends observed *in vitro*. Cells in both computational and experimental models were observed to be fairly distributed over the substrate for exogenous [Ca^{2+}] of 0.09 mM, and showed increased tendency to colonise when the [Ca^{2+}] was increased to 2.0mM, refer to Figure 2.13. Furthermore, in agreement with the experimental data, it was observed that lower exogenous [Ca^{2+}] led to greater cell density.

An advanced version[124] of this model was used to describe the impact of extra-cellular calcium on the growth and differentiation of human keratinocytes, and test the hypothesis that increased proliferation of the transformed HaCat (epithelial) cell line (compared with keratinocytes) is due to their differentiation pathway being "turned off. The

computational study was supported and validated by an experimental study where the two cell types were grown in monolayer cultures with low and physiologic [Ca^{2+}]. Similar to the last model, execution of rules was controlled by the internal state of the agents (reflected by position in the cell cycle, attachment to substrate, etc) and environmental conditions (reflected by nearest neighbours, [Ca^{2+}], etc). However, two new rules governing differentiation and stratification were added:

- *Inclusion of calcium-dependent differentiation*. This was regulated through increase in involucrin – a hypothetical substance analogous to the cytoplasmic protein involucrin known to be associated with differentiation. The amount of involucrin was linearly dependent on [Ca^{2+}]. This allowed the cells to leave the cell cycle, i.e. differentiate, when an arbitrary involucrin threshold was reached. The algorithm, for the *ith* agent, worked as follows:

  Cell(i)_involucrin = Cell(i)_involucrin + ([Ca^{2+}]/500)

  If (Cell(i) is proliferating ***and*** *Cell(i)_involucrin > 0.5), then* ***differentiate***

- *Inclusion of calcium-dependent stratification*. This rule allowed cells that experienced a compressive force by three of its neighbours to move upwards. The probability of a cell's movement was, again, dependent upon [Ca^{2+}]. As with the previous rule, the amount of involucrin played a central role. This was done because high involucrin was associated with differentiation, and differentiated cells were hypothesised to lose affinity to substrate. The movement was also dependent upon cell radius, as the cell under compression will first get 'squashed' and then stratify. The algorithm, for the *ith* agent, worked as follows:

  If (force_on_cell(i) > 0.1 ***and*** *cell(i) is in contact with 3 others cells)*

  Radius_probability_index = minimum radius/cell(i)_radius

  Differentiation_probability_index = cell(i)_involucrin

  Calcium_probability_index = tanh(π × ([Ca^{2+}] – 1.5)) + 1

If (product of probability indices > random number)

Then cell(i)_layer = cell(i)_layer + 1

In order to model keratinocyte behaviour, 9 [Ca^{2+}] between 0.05 mM and 2.5 mM were used on a rectangular substrate 1 mm × 1mm. HaCat cells were modelled differently from keratinocytes in that their differentiation pathway was disabled, which means HaCat cells either permanently left the cell cycle or did not express involucrin. HaCat cell behaviour was simulated similarly though under two slightly different scenarios: 0.5 mm × 0.5 mm substrate with 100 seeded cells or 1 mm × 1mm substrate with 400 cells. Due to the inclusion of the two rules, higher [Ca^{2+}] related to higher cells differentiating (or permanently leaving the cell cycle), which in turn decreased the growth rate; where stratification tends to increase growth rate as it increases the net space available for growth. The overarching observation was that growth in [Ca^{2+}] rich environment was slower as differentiation effect dominated, which agreed rather well with the *in vitro* data. This, furthermore, raised the question whether impairing the differentiation pathway can cause increased proliferation in [Ca^{2+}] rich environments. Comparing the proliferative behaviour of computational HaCat against their *in vitro* counterpart via the amount of involucrin produced and HaCat growth suggested that differentiation alone cannot explain the differences in population growth characteristics between normal keratinocytes and HaCat cell line. This was a perfect demonstration of the manner in which agent-based models can be employed as hypothesis testing tools in biological investigations.

Comparatively, Artel *et al*. (2011)[125] modelled sprouting angiogenesis in a porous scaffold using the agent-based approach. The objective of this investigation was to examine the impact of scaffold pore size on the rate of angiogenesis. Agents in this study represented capillary segments that were attributed behaviours such as elongation, branching, and anastomosis. These behaviours were either stochastic or influenced by microenvironmental

conditions. Based on, for example, the presence of soluble factors each blood vessel segment could be transformed into a tip cell, which would subsequently elongate/proliferate or branch. The extent to which a tip cell can elongate was limited to 16 μm in the study, following which a new tip cell is generated to continue elongation based on a growth factor concentration gradient. The investigators employed a search algorithm to enable tip cell pathfinding, which worked by avoiding collisions with the scaffold and selecting a location with the lowest cost among neighbouring locations – the cost is inversely proportion to the growth factor gradient.

The probability of branching was also contingent upon the growth factor concentration – an experimentally observed phenomenon known as the 'brush-border' effect (Ref#20 from the paper). The scaffold geometry was constructed to have circular pores, which ranged in diameter from 40 μm to 270 μm, and was assumed to be non-deformable, which works well for polyanhydrides and polyesters. Vessel invasion was driven by growth factors, which were made available in all scaffold conditions. The growth factor concentration profile was determined by:

$$C_{GF}(y) = -\left(\frac{\gamma_{max}}{2} - y^2\right) + {\gamma_{max}^2}/{4} + \epsilon \tag{2.60}$$

In (2.60), C_{GF} represents growth factor concentration; γ_{max} is the maximum concentration location, which for the purposes of the investigation was chosen to be the centre of the scaffold; and ε is a positive number which ensures that initial locations have concentration > 0 so that sprouting can be initiated. Rules employed by the investigators were along two strands:

1. *Action I*
    a. *Agent senses for the highest concentration gradient*
    b. *If the blood vessel section is not fixed*
        i. *Then elongate stochastically in the direction of two highest gradients*

ii. *Change direction if this leads intersection with a pore*
iii. *Initiate proliferation, if maximum stretch limit reached*

c. *Search for other vessel sections in the 'stretch' distance to connect*

2. *Action II*
   a. *Agent senses for the highest concentration gradient*
   b. *Change the tip direction to highest growth factor gradient, if not connected to a blood vessel section.*

The investigators relied on *in vivo* results to define the speed of vessel sprouting. Results showed positive correlation between pore size and the rate of scaffold vascularisation. Specifically, pore size between 160-270 μm was observed to support "*rapid and extensive angiogenesis throughout the scaffold*", as the network of larger pores behaved much like the control, which had no steric hindrance for the evolving vessel. In comparison, shorter pores offered higher steric hindrance to the evolving vessel and, therefore, led to delayed and slower angiogenesis as a result of slowed vessel invasion. The model, the investigators concluded, can be employed to understand how alterations in scaffold morphology as well as increased delivery of soluble growth factors can aid vascularisation.

2.3.3 COMPUTATIONAL PLATFORMS

For most of the continuum and discrete formulations discussed above (and more), a multitude of open source and proprietary computational software exists. Depending upon the underlying assumptions they can be broadly classified as continuum, discrete, and hybrid. The continuum tools include the classic partial-differential equation solvers such as *COMSOL* (COMSOL Ltd., Cambridge, UK), *FLUENT* (ANSYS, Canonsburg, USA), *CFD-ACE+* (ESI, Paris, France), *ABAQUS* (SIMULIA, Vélizy-Villacoublay, France), etc. While additional platforms, such as *MATLAB*, which can be employed to solve partial differential equations, do exist the aforementioned frameworks reflect the most mature, state-of-the-art in multiphysics software. Similarly, the state-of-the-art in discrete computational tools includes *NetLogo* (https://ccl.northwestern.edu/netlogo/), *Flexible Large-scale Agent-based Modelling Environment* (FLAME: www.flame.ac.uk), *CellSys*

(http://msysbio.com/software/cellsys), and the commercial *Complex Systems Modeling* (CoSMo: CoSMo, Lyon, France). Finally, CompuCell3D (CC3D: www.compucell3d.org/) and *Cancer Heart And Soft Tissue Environment* (CHASTE: www.cs.ox.ac.uk/chaste) constitute the most sophisticated hybrid platforms currently existing in the literature.

The three continuum platforms mentioned above (FLUENT, COMSOL, and CFD-ACE+) are proprietary multiphysics software, which offer the user the ability to generate CAD renditions of the physical domain, meshing software to discretise the physical domain, and a numerical solver to perform the computations. Whereas ABAQUS and COMSOL employ finite-element approximation, FLUENT and CFD-ACE+ utilise the finite-volume approach to solve the governing partial-differential equations. The platforms are generally utilised to quantify mechanical forces, flow, transport, and gradients within a physical domain. They are essentially of great utility, as the simulations can provide information that in many cases cannot be obtained empirically. For example, it is near impossible to determine flow profiles experimentally within a microscopic scaffold, let alone in that very same scaffold containing cells. However, the aforementioned software can be utilised to determine this computationally. Despite this significant advantage, their underlying assumption of system homogeneity (as discussed in the previous section) makes their use redundant in mapping the spatiotemporal evolution of a biological system based on inter-cellular and cell-environmental interactions. This is where the discrete platforms are utilised.

NetLogo is a programmable modelling environment utilised to simulate the behaviour of complex systems[126]. NetLogo is a free, open source software, which models a system as composed of mobile agents (referred to as *turtles*) that can move over a grid of stationary agents (referred to as *patches*). The software relies on certain pre-defined functions. The sequence of NetLogo commands is known as a procedure. The software allows the user the option to visualise and display a variety of simulation-relevant data,

though the visualisation library is rather limited. NetLogo, a lattice-based, cellular automaton environment, models the spatiotemporal evolution of system based on the specified interaction protocols (equivalent to the partial-differential equations in the continuum frameworks) between turtles, patches, and turtles and patches.[126]

CellSys is a cell-level platform introduced by Hoehme & Drasdo (2010).[127] It is written in ANSI C++ and uses the OpenGL API for visualisation. CellSys is an object-oriented toolkit that implements modelling, simulation, and visualisation functionality for individual-cell based models. CellSys is an off-lattice simulation platform that allows for simulation of multicellular systems in both 2D and 3D (an outright advantage over NetLogo). The platform models cells as isotropic, elastic, and adhesive objects. It consists of basic classes formulating a major abstraction (such as model cells or finite grid elements), collection of algorithms to model cellular behaviour & the environment, and modules for visualisation.[127] From a discrete-approach perspective, the model does not allow for simulation of 'taxes-based movement and considers cellular interaction only from a 'stress' perspective (disadvantage compared with NetLogo), i.e. interacting cells exert force on each other, proliferating cells exert pressure on their neighbours, etc.

FLAME is based on the logical communicating extended finite state machine (X-machine) theory. It uses C (in order to specify the functions of the agents) and *extensible mark-up language* (XML), to describe the model: the agents, their structure, and the environment they exist in. The resulting XML syntax is known as the X-machine mark-up language, or XMML[8]. FLAME allows the user to simulate a system in both 2D and 3D. While the developers of FLAME also offer a visualisation toolkit, which is relatively mature and practically as informative as NetLogo, it does not offer the option to visualise agents in complex shapes. An advantage that FLAME has over NetLogo is the fact that FLAME allows modelling in continuous space, unlike the lattice-restricted behaviour in NetLogo.

Features that make FLAME of great utility include (i) the manner it is implemented (offering a realistic representational formalism to biological entities), (ii) the flexibility of introducing user defined data, and (iii) the option to analyse the phenomena in continuous three dimensions, which collectively enable the platform to capture complexity at a level higher than other platforms of similar flavour. Few additional agent-based platforms, such as Framsticks, SeSam, ECHO, LDS, and CoSMo exist, but are not as functional and mature as FLAME, NetLogo, and CellSys. A major drawback common to these platforms is their inability to simulate complex and 3D interactions, lack of options to incorporate user-defined data, and simplistic visualisation toolkits.

CC3D[128] is based on the *Glazier-Graner-Hogeweg* (*GGH*) approach, which facilitates multi-scale simulations by defining spatially-extended generalised cells, thereby allowing tuning of the level of detail from intracellular to continuum without switching simulation framework. GGH utilises regular cell lattices and regular field lattices, with the simulations requiring a list of objects, description of their interactions and dynamics, and appropriate initial conditions. Objects can either be cells or continuous variable concentrations (each of which reside on its own lattice) in 2D or 3D. In terms of implementation, behaviours and interactions are embodied in the effective energy (refer to §2.3.2.2). While the biochemical behaviour can be represented through a variety of differential equations, the cell lattice evolves probabilistically.

CHASTE, on the other hand, is perhaps the most mature hybrid platform currently available.[x] The features that CHASTE is composed of confer to it a wide range, in terms of the options for the users. CHASTE is an open-source C++ library for computational simulations of physiology with initial applications in cardiac electrophysiology and

[x] The current avatar of CHASTE and the multi-paradigm framework reported in this thesis were published in the same month by the PLoS group of journals.

cancer.[129] The code includes (i) global component for basic mathematics; (ii) input-output code for reading, writing, and converting various files; (iii) the capability to generate meshes; (iv) code to conduct vector and matrix operations, (v) codes for defining and solving ODEs and PDEs, as well as (vi) the capacity to solve compressible and incompressible general non-elasticity problems.[129] Like CellSys, CHASTE models cellular interactions via force laws, and allow the user to define various force laws (e.g. Johnson-Kendall-Roberts model, extended Hertz-model, etc.).

2.4 DISCUSSION

Here, the author aimed to present various continuous and discrete computational techniques that have been employed to capture biological phenomena, especially in the TERM context. The two overarching methodologies encompass a vast number of models and formulations, and although only a small selection of these approaches and models were presented in this chapter, they provide a high-level overview of the landscape, especially with respect to the tool-kit of the TERM investigator (refer to §2.2).

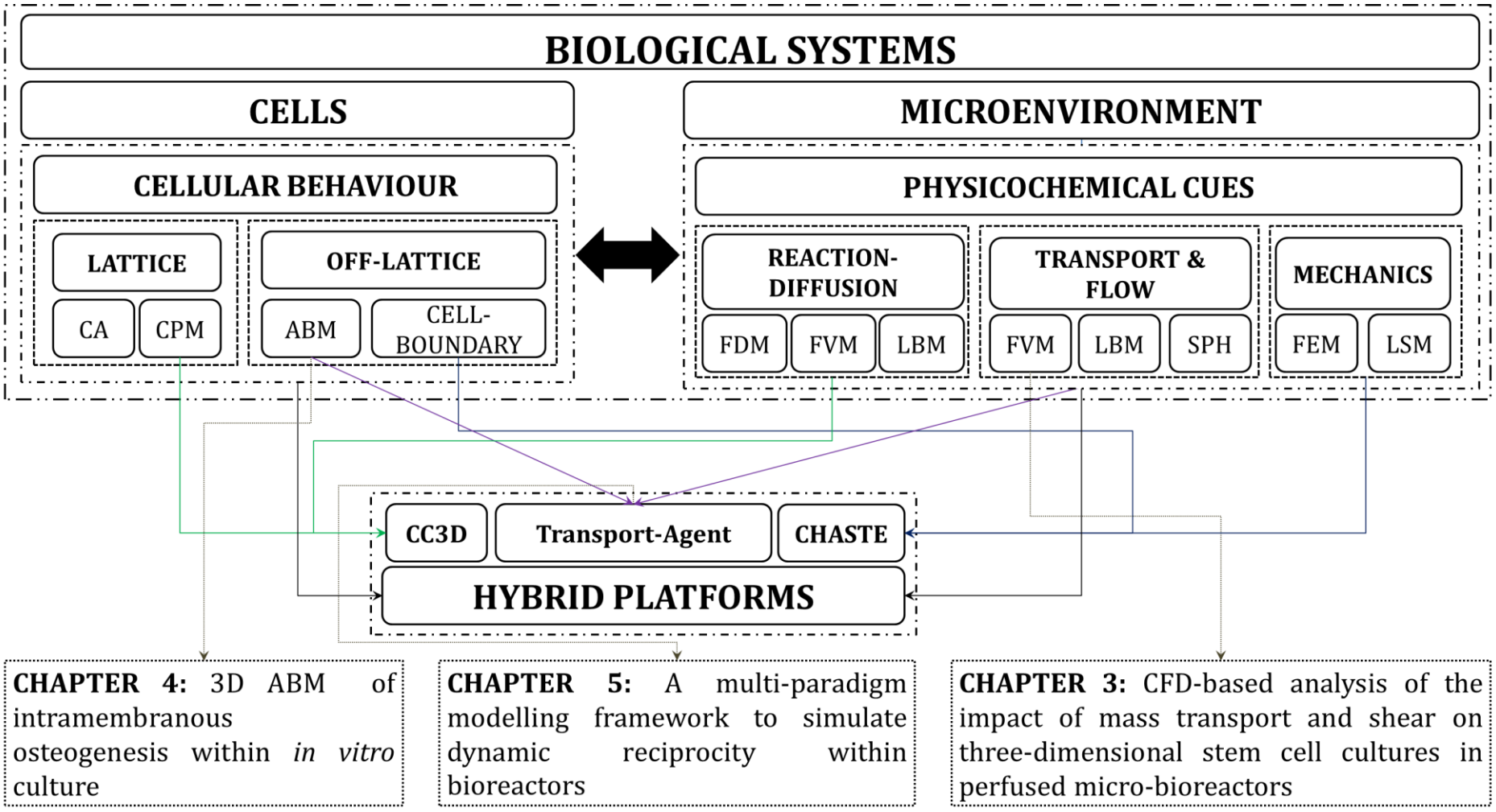
BIOLOGICAL SYSTEMS
CELLS
MICROENVIRONMENT
CELLULAR BEHAVIOUR
PHYSICOCHEMICAL CUES
LATTICE
CA
CPM
OFF-LATTICE
ABM
CELL-BOUNDARY
REACTION-DIFFUSION
FDM
FVM
LBM
TRANSPORT & FLOW
FVM
LBM
SPH
MECHANICS
FEM
LSM
CC3D
Transport-Agent
CHASTE
HYBRID PLATFORMS
CHAPTER 4: 3D ABM of intramembranous osteogenesis within *in vitro* culture
CHAPTER 5: A multi-paradigm modelling framework to simulate dynamic reciprocity within bioreactors
CHAPTER 3: CFD-based analysis of the impact of mass transport and shear on three-dimensional stem cell cultures in perfused micro-bioreactors

Figure 2. 14: Computational TERM – The Landscape. The figure displays the various computational techniques and formulations that are currently employed to capture biocomplexity. Amongst the standalone continuum and discrete methodologies exists the hybrid paradigm, which is ontologically better suited to handle the wide array of data structures necessary to assimilate information dynamically. The figure also shows hybrid platform that are currently exist and display dynamic assimilation and, in doing so, contextualises the contribution of this thesis in developing a coupled transport-agents based multi-paradigmatic modelling framework.

It is clear from the review conducted above that the continuum approach (FVM, FEM, LSM, etc.) has enjoyed immense success in capturing a wide range of key biological processes associated with fluid flow, transport, and mechanotransduction. This success of the continuum approach rests on the *continuum*[74] assumption,[xi] which allows the various formulations to achieve a balance between capturing physical complexity and computational efficiency. CFD, and in particular the finite-volume formulation, has been pervasively employed in simulating transport and flow within complex 3D geometries. There are several reasons why the finite-volume approach has been (almost) universally adopted towards this task. In the finite-volume approach, the governing equations are integrated over all the finite control volumes of the domain, which means that the resulting statements express conservation of the relevant properties for each control volume. This makes the approach ideal to handle discontinuities, as the integral conservation laws hold at discontinuities, and make the approach easily extended to unstructured meshes, which are crucial while handling 3D geometries of arbitrary complexity. Furthermore, application of the divergence theorem, which converts volume integrals to surface integrals, yields fluxes. This is quite convenient as velocity and flux (rate of flow of a property per unit area; e.g. momentum, diffusion, volumetric, etc.)[130] of a fluid are of interest while investigating mass transport of a given species. This clear, and more intuitively accessible, relationship between the numerical

[xi] Continuum is defined as a continuous distribution of matter with no empty space. Although that is of course not entirely true, for fluids possess a molecular structure where the molecules are far apart from each other, the continuum assumption, however, has served us well and helped immensely with analysis, as treating each individual molecule would be too cumbersome.

algorithm and the underlying physical principles forms one of the main attraction[131] of the FVM, as the concepts are easier to follow.

The LB approach, on the other hand, solves the kinetic equation (the LB equation), and offers a very simple algorithm due to the linear form of the differential term of the kinetic equation. This makes the approach quite efficient and attractive for simulating complex fluid flows.[132] Furthermore, the LB approach requires no special treatment of the pressure equation, as is the case in the finite-volume method. The LB approach, moreover, offers advantages over the finite-volume method for cases where the continuity approximation in the Navier-Stokes equations does not hold, which include multi-phase/component flows and non-Newtonian fluid (within complex and/or porous geometries).[132,133] Finally, the approach is more amenable to parallel computation compared with conventional Navier-Stokes solvers. This is an important feature, for even the simpler cases, especially in the TERM context, usually call for high-performance computing.

Besides transport and flow, growth of cells/tissue structures is another feature of biological systems. The growing specimen gives rise to a moving boundary problem, which can be addressed, amongst other techniques,[90,91] by the LSM. LSM enables the user to compute geometric quantities easily, converts codes developed to address 2D geometries to 3D rather quickly, and handle topological changes simply and efficiently.[134] Furthermore, LSM can be easily implemented within a finite-volume code, thereby enabling the user to study the dynamic relation between tissue growth, transport, and fluid flow. The finite-element approach, on the other, hand is usually employed to investigate the impact of biophysical cues on cell behaviour and vice versa. In this regard, FEM remains the flagship continuum approach to simulate mechanical features of 3D structures of arbitrary geometry. The approach can also be integrated with a finite-volume code to better appreciate the relation between biophysical & biochemical cues and cellular behaviour. Moreover, the

LSM and FEM can be employed to investigate scaffold degradation and simulate the mechanical impact of this loss on cell behaviour (proliferation, differentiation, etc.). However, scaffold degradation is intimately linked with the release profile of the eroding monomers, the ensuing autocatalysis, and the resulting gradients. These phenomena, in an integrated manner, play a crucial role in influencing cell behaviour, which are either encapsulated within the scaffolds or seeded around controlled-release matrices. While the finite-element or level set formulations can be utilised to quantify stresses and recession of scaffold, the finite-volume approach can be utilised to model the process of polymeric degradation by including constitutive equations that account for autocatalysis, transport of the released entities including degradation by-products and signalling and nutrient molecules, etc. Finite-volume is especially recommended here as achieving the aforementioned (*sans* mechanical impact) requires determining the mass flux associated with the processes of polymeric degradation and controlled release, as it deals with fluxes.

A cell responds to the spatiotemporal gradients of a variety of cues that it receives from its environment, which basically consists of other cells embedded in the extra-cellular matrix (ECM) and capillaries. The ECM provides cells with mechanical, physical (in terms of regulating cell shape),[135] and architectural information that it may need to express certain genes. Capillaries, on the other hand, ensure that the metabolic requirements of the developing tissues are met, and that regulatory molecules (such as hormones etc.) are delivered as required. Based on the foregoing discussion, it is evident that CFD, especially with the finite-volume approximation, can handle the environmental features of a biological system (flow, bioreactor hydrodynamics, mass transport, scaffold degradation, shear, morphogen synthesis and interactions, etc.) robustly and efficiently. The approach can handle discontinuities due to the integral form of the conservation laws and can handle 3D geometries of arbitrary complexity. However, cells, as we shall see, operate quite differently

than the rather passive bioreactors and degradable polymeric matrices; and therefore tend to escape the reductionist and averaged contours of the continuum approach.

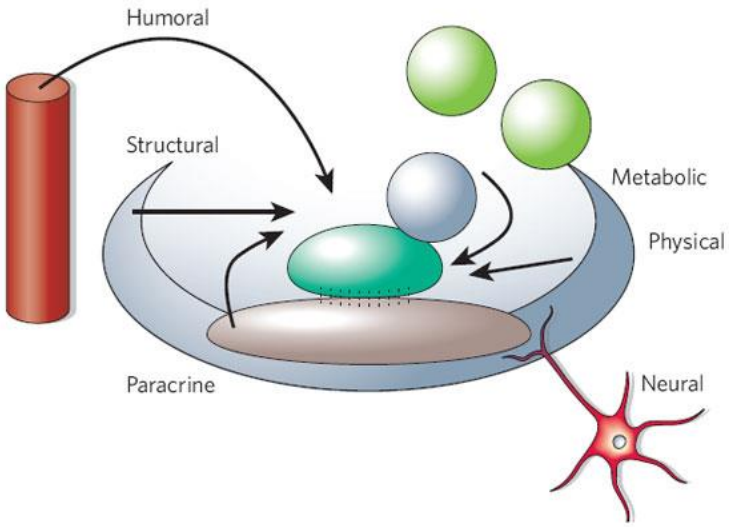

Figure 2. 15: The stem cell niche. The figure is a schematic representation of the stem cell niche and shows the various elements in a cell's microenvironment that can influence the expression of its genotype. The figure also shows the variety of regulatory signals a cell has to consider in the course of its lifetime. In order to capture the dynamism exhibited by the cellular system, a computational framework must be able to offer suitable ontologies to not only the dynamic structure that is the niche but also capture the broad array of regulatory cues (such as electrical, chemical, mechanical, architectural) that a cell relies on for growth as well as instructions. *Reproduced with kind permission from Ref.* 136 © *(2006) Nature Publishing Group*

In developmental biology experiments conducted in the mid-twentieth century[137,138], the corneal cells of a chick were placed over murine dermal cells. The ectodermal chick cells present on the mesodermal mouse cells resulted in feathers. This occurred due to the fact that ectodermal cells present on mammalian skin are instructed to form hair. However, the chick cells, although ectodermal, did not have the information to form hair. They could nevertheless form something analogous: feathers. Similarly, reptilian ectodermal cells would have led to the formation of scales[139]. This elegant experiment not only demonstrated the importance of cellular interactions to gene expression as well as histogenesis, but also gave us, what seems like, a biological *rule*: mesodermal cells *instruct* the expression of ectodermal cells. This *rule* was not violated when tested across species[140] (refer to the recombinant experiments between Reptiles, Birds, and Mammals[139]).

The discrete paradigm is best suited to capture this algorithmic nature of biological entities as they assume the spatiotemporal evolution of a system based on a set of rules, like the mesenchymal-epithelial rule mentioned in the last paragraph. There are three basic formulations to capture the emergent behaviour displayed by cells: the lattice-based *cellular automata* (CA) and *cellular-potts modelling* (CPM), and the non-lattice based *agent-based modelling* (ABM). The techniques simulate a system by dividing it into discrete decision making entities (*grids* in case of cellular automata, and off-lattice *agents* in case of agent-based modelling) and capturing their behaviour by specifying a set of rules that each of the discrete entities obey at each discrete time point.

CA is perhaps the simplest to implement. They are (typically) not computationally intensive and do not require sophisticated algorithms or data-structures, which makes them user-friendly. Secondly, the presence of lattice sites precludes the need, on part of the user, to incorporate sub-models for collisions, motility, etc. Furthermore, the fact that the rule-sets employed have, in most implementations, a local character makes them ideal for parallelisation on computer clusters composed of multiple networked computing nodes. This reduces computational complexity as well as "*communication overhead of distributed implementations of the model program*".[11] This reduction emanates from the fact that no particular piece of data is shared by all nodes and that no node needs to inspect arbitrary positions within the domain. Furthermore, models with local rules typically display linear computational complexity, which means that computing time needed to run a simulation is directly proportional to the number of grids. Compare that to an approach like ABM, which utilises global rules (in addition to local rules), the complexity of the model quadruples, represented as $O(n^2)$.[xii] The CA paradigm, however, has its own set of challenges: which

[xii] This is not strictly true for every case. Well-framed global rules can increase computational efficiency.

include immobile agents, lack of three-dimensionality (in classic CA), and local rules – the latter limiting the ability of the approach to capturing the impact of global processes, variables, and interactions.

CPM, a form of lattice-based discrete approach, is an advance over the CA paradigm. The obvious advantage is that it offers a 3D environment to model cellular behaviour. However, its greatest strengths include the fact that it provides a reasonably straightforward way to incorporate new phenomena via the *Hamiltonian* and it is rather easy to implement. Furthermore, the paradigm can handle most types of cells (motile, non-motile, loose cells, aggregates) and cell behaviours. Moreover, as the paradigm operates by avoiding behaviour that comes with a high energy cost, the user does not need to necessarily specify how the constraints are to be met. As such, any phenomenon that can be captured by the energetic formalism can be incorporated within the framework. Additionally, its flexibility in handling a diverse array of biological phenomena is the chief reason why the approach has been utilised so extensively, as reviewed by Merks & Glazier (2005).[119] Furthermore, CPM simulation length is measured in terms of Monte Carlo steps, which do not necessarily translate to a fixed unit of time. Finally, the dynamics observed are only realistic if long stretches of time steps are considered as, Tamulonis[11] points out that, *cells can briefly split and spontaneously appear within other cells*; though this behaviour is penalised by the Hamiltonian and, therefore, corrected.

Both the CA and CPM paradigms are lattice-based, which typically do not allow as much resolution as lattice-free models when simulating processes that involve migration, range of cell shapes, and geometries that change globally as the system evolves. The lattice-free ABM can be utilised in such instances. Like the CA approach, ABM also relies on rule-sets that are often derived from physical observations. Being lattice-free also affords the user the freedom to choose desired shape both for the individual agent as well as the global

structure. As such, in comparison to CPM, fewer sites/agents are required, generally speaking, to represent a single biological cell of arbitrary shape. Furthermore, an agent: (i) possesses well defined boundaries, (ii) has the ability to sense its environment and act on its environment, (iii) can control its internal state as well as behaviour, (iv) has particular goals to achieve, (v) can act in the anticipation of future goals, and (vi) respond in timely fashion to changes that affect its environment. Cells can be easily visualised as "agents" in the light of an agent's aforementioned properties. After all, cells are in fact embedded in an environment; possess boundaries; maintain a dynamic bidirectional cross-talk with their environment,[28,53,136,141-146] thus being acted by and acting on their environment; have the ability to control their behaviour through secretion of relevant autocrines; and act in anticipation of future goals as a result of metabolic sensing (when cells try to gauge the 'needs' of a tissue, as suggested by Scadden[136]) or signalling (as occurs in a functional immune system[147,148]). This analogy can be easily extended to tissues, organs, organisms, and colonies, in equal measure.

ABM, however, is not without its disadvantages. In most current implementations, it is shown to require advanced programming skills, so has a relatively steeper learning curve. Furthermore, although the paradigm can be employed to capture a wide range of biological phenomena, the implementation, unlike the CPM, is non-trivial. For example, while tackling the simplest case of cell proliferation (or migration), one needs to incorporate algorithms (such as collision detection and correction) to ensure two cells do not breach each other's boundaries. Secondly, as the approach relies on local as well as global rules, the model complexity is quadrupled (compared with CA models) with addition of each new agent. As such, often the computing time required is higher. Another limitation generally associated with ABM is the flexible and dynamic nature of agent interactions, which makes the patterns and outcomes of these interactions inherently unpredictable. This is a *necessary*

evil associated with the agent-oriented approach, for it is precisely these flexible and dynamic interactions that enable agent-based models to capture emergent phenomena. Problems associated with the unpredictability, however, can be mitigated by conducting sensitivity[149] and parametric[150] analyses, and optimisation procedures.[5,151,152] Finally, a key disadvantage of employing ABM is that the models need to be constructed at the right level: after all, "*you can't model bulldozers with quarks*".[153] ABM, however, yield more realistic representations of biological systems as they are not inhibited by restrictions imposed by the presence of an underlying lattice on the location and migration patterns of cells compared with its lattice-based counterparts where cells can only move through pre-defined points on the lattice.[154] It is worth stressing that the complexity and sophistication of a model depends upon the question being explored, and that more complexity does not necessarily amount to a better model.

2.5 DYNAMIC ASSIMILATION

The main theme that reverberates through the experimental and computational annals of TERM is that of dynamic assimilation. By *dynamic assimilation*, is meant the non-linear reliance of a system on information, both physical (spatial, mechanical, biological, or chemical) and noetic, generated by its constituent elements and its environment (including fellow individuals). Dynamic assimilation is the act of receiving diverse structures of data – which could be continuous, discrete, binary *etcetera* in nature – integrating them with an equally diverse sets of information from either sub-components or individuals existing in the same microcosm; processing the information to carry out a set of (design) objectives; and, finally, the iteration of this process as many times as desired.

Dynamic assimilation is as much a property of the individuals as much it is of the environment. For example, cells possess information, encoded as genes, to create an entire

organism, but the expression of these genes is dictated by the environment the cells grow in. In the absence of right environmental instructions, the same genes will either fail to express themselves, or may result in an unexpected phenotype.[140] Similarly, the environment, in terms of its architecture or functionality, relies on the evolution of the cellular system,[143,155,156] which in turn relies on the environment. Information, therefore, dynamically flows between cells and their environment.[xiii]

It is quite difficult to fully grasp this phenomenon via currently existing physical experimentation means alone:[xiv] for important pieces of observation, such as flow-profiles and concentration gradients, remain inaccessible to direct observation even in devices that do not contain cells. Therefore, recourse to computational tools is helpful. However, there remains on the landscape, refer to Figure 2.14, a need for hybrid computational paradigms as well as frameworks that can capture, incorporate, and process (in other words, dynamically assimilate) the diversity of information (such as the pH of the microenvironment, the phenotype of the neighbouring cell(s), the 3D configuration of an enzyme and endless other factors) available to it. This is because the two flagship methodologies, i.e. continuum and discrete, cannot on their own capture the full array of data-structures observed in biological phenomena. Between the two, however, they can capture both, the microenvironmental details and the entire array of cellular response to the microenvironment and other cells, as well as the diverse array of information structures that are available to biological systems. Furthermore, a combination of both can cover the working principles from every discipline regenerative medicine feeds on (refer to Figure

[xiii] The interactions between cells and the environment are globally directed by the need to pass on the genetic information (refer to *The Selfish Gene* by Prof Richard Dawkins)

[xiv] This is only to say that our ability to observe a given phenomenon is limited to the availability and resolution of a given apparatus and, therefore, in certain cases, such as the ones mentioned in the sentence, computational strategies may provide a better understanding of the phenomenon being investigated. This is what has been termed as the *third approach*. However, this approach is only meant to serve the experimental as an aide and not a substitute.

2.3). Fully coupled hybrid models, by integrating the two via a feedback loop, take this a step further and capture the true bi-directional relationship observed in biology: referred to as *dynamic reciprocity*,[18] and display dynamic assimilation. But what form of hybrid formulation offer the most realistic representational formalism to simulate biological systems?

Ideally, this requires, from cell-level up, an integrated approach to account for mechano-biophysicochemical features of a biological system. This entails a coupling of approaches and algorithms that can capture flow, transport, mechanical stimuli, and cellular behaviour. However, while this level of integration has been witnessed in hybrid models (of mechanobioregulatory nature[157]), a framework with in-built capability to account for all is still missing. For a variety of technological, logistical, and computational reasons this grand computational vision will take a while to be realised. This thesis is meant to be a stepping stone in this direction. CC3D and CHASTE, however, are the most mature hybrid paradigms that can display dynamic assimilation, but only to an extent: CC3D does not have an in built mechanical and flow solver and is lattice-based, whereas CHASTE can only simulate mechanical interactions between cells. This, for example, will provide technical challenges (1) CC3D in developing *ex vivo* environments (as in bioreactors and lab-on-a-chip-devices) where the complexity of the geometry plays a key role in influencing hydrodynamics[xv] and, therefore, cell behaviour, and (2) CHASTE in capturing emergent patterns from basic cellular behaviour (though it is arguably the best technique to capture cellular mechanics especially for the cardiac system). However, being modular both possess the feature to incorporate the missing elements (e.g. through the *Hamiltonian* in CC3D and the off-lattice solver in CHASTE). Still, there remains, a gap between the two hybrid platforms, which this

[xv] CC3D primarily utilises the finite-difference approach for discretising reaction-diffusion equations, which do not handle discontinuities as well as the finite-volume approach

thesis addresses: a dynamically assimilating framework that allows the user to simulate biological behaviour based on the biophysicochemical features of natural and (commercial) artificial environments.

In order to achieve this, CFD, and in particular, the finite-volume formulation, was coupled with the off-lattice agent-based approach. The finite volume method seems to capture most physicochemical processes of functional relevance (especially to a TERM investigator – refer to §2.4). In particular, the methodology handles discontinuities robustly, which makes it amenable to handling unstructured meshes: an advantage while simulating 3D geometries of arbitrary geometry. Similarly, the off-lattice, rule-based agent-based modelling was deemed most suitable to be coupled with the continuum methodology. Despite its drawbacks, ABM offers the most realistic representation of biological behaviour (refer to §2.4) and, being hierarchical, is most amenable to coupling with continuum methodologies that utilise unstructured mesh. Of the computational platforms discussed in this chapter, CFD-ACE+ employs the finite-volume approach and FLAME the off-lattice agent-based approach. FLAME, additionally, allows the user to incorporate user-defined data-sets and simulate phenomena in 3D constituted the primary reason the agent-based formulation, as implemented in FLAME, was utilised towards framework development.

In the following three chapters, the capability of CFD-ACE+ as a design tool and computational platform to simulate environmental dynamics, FLAME as a discrete framework to capture cellular behaviour and observe emergent growth patterns, and a novel transport-agents multi-paradigm computational framework developed by integrating the two for the purposes of simulating biological systems in capturing *dynamic reciprocity* within an artificial TERM-oriented environment (i.e. a bioreactor) is evaluated hinting that the novel platform may be general enough for application in a wide range of artificial and natural systems.

2.6 SUMMARY

The principles underlying computational TERM, along with relevant examples, though quite broad in scope, have been explored in sufficient detail here, for it is impossible, given the staggering breadth of literature that exists on the subject of TERM, to cite all topics. Via this chapter, the author meant to introduce and identify suitable approaches that can be employed to quantify biocomplexity, and due to their strong predictive value used them to serve as design optimisation tools. The computational approaches were broadly classified as continuum and discrete. Although, a host of continuum (FEM, FVM, LBM) and discrete (CA, ABM, CPM) formulations are available for computational purposes, CFD – which employs the finite-volume method to approximate the Navier-Stokes equations – and ABM – a class of discrete mathematical approach that models systems as a collection of agents – were identified as the two approaches fit to design a hybrid platform for the purposes of simulating biocomplexity.

CHAPTER 3

A CFD analysis of the impact of transport and shear on stem cell culture in a bioreactor

In Chapter 2, several mathematical approaches currently utilised to model biocomplex phenomena, especially within the TERM context, were introduced and discussed. A review of the application of these approaches was also carried out, which itself pointed to the advantages of using certain formulations to simulate the biophysicochemical features of a given system. The continuum approach, especially the finite-volume formulation, was identified to be the most appropriate to model the environmental (physicochemical) aspects of a system. This chapter aims to test the predictive and design capabilities of the continuous Computational Fluid Dynamics (CFD) by simulating flow and transport within a 3D geometry of arbitrary complexity. Given the TERM oriented nature of this thesis, a commercially available bioreactor was employed as the exemplar. In this chapter, therefore, a novel computational model evaluating the efficacy of the commercial TissueFlex® bioreactor in supporting the expansion of mesenchymal stem cells and the suitability of CFD as a robust design tool is presented.[xvi]

3.1 INTRODUCTION

Computational Fluid Dynamics (CFD) have proven to be a valuable computational tool for the characterisation of transport and flow fields, yielding detailed results that, after validation, form the cornerstone of design processes.

Within the context of tissue engineering, CFD can be utilised as both a tool to investigate the fundamental developmental principles governing cellular behaviour in biological systems (*in vitro* as well as, given relevant boundary and initial conditions, *in vivo*) and as a design & optimisation tool. The application of CFD to characterise local fluid dynamics in a variety of bioreactor systems (concentric cylinder, direct-perfusion, rotating hollow-fibre, rotating-wall perfused, wavy-walled) can already be found in the literature.[85,158-162] Some of these investigations, especially the ones with implications in TERM generally, were discussed in §2.3.1.2.1.

[xvi] The investigation reported herein has been accepted for publication, and is currently in press, as: *Kaul H, Ventikos Y, Cui ZF. A Computational Analysis of the Impact of Mass Transport and Shear on three-dimensional Stem Cell cultures in perfused Micro-bioreactors.* ***Chinese Journal of Chemical Engineering*** *(In press), 2015.*

Song *et al.* (2010)[163] used CFD to predict 3D flow fields at the length scale of stem cells. They employed the *Microscale Particle Image Velocimetry* technique to experimentally measure flow values, and thereby validate the CFD model. Their investigation concluded that CFD predicts flow regimes within 12% of experimentally measured values in the absence of cells (i.e. 12% difference between computationally predicted and experimentally measured shear rate values). CFD was also used to model perfusion and the influence of perfusion generated shear stress on 3D cultures.[164] Boschetti *et al*. (2006)[165] investigated shear stress generation as a function of parameters, such as scaffold porosity and pore size, medium flow rate, and diameter of the perfused scaffold section. A 3D CFD model[161] was created to investigate mass transfer interactions between the culture medium and micro-carrier attached aggregated hepatocytes seeded within a hollow-fibre bioreactor. In particular, distribution of oxygen within the cellular compartment and cellular consumption of oxygen as an index of cell metabolic activity were analysed. The overall performance of the numerical model in predicting optimal conditions for culturing viable microcarrier-attached aggregated hepatocytes, despite certain limitations that were a by-product of unavoidable simplifications, was reported to be satisfactory.

Yu *et al.* (2007)[166] created a numerical model to simulate fluid-flow and oxygen transport in a rotating magnetic bar mixer micro-bioreactor, aiming to determine the operating parameters for animal cell culture. A comparative analysis between a bi-axial bioreactor vessel and its uni-axial counterpart using CFD simulations revealed significant increase in velocity when the bi-axial configuration was used, thereby recommending bi-axial rotation of the vessel as a solution to the problem of inadequate fluid and metabolite transport to and from the cells.[167] CFD simulations were also used to test the hypothesis that geometrical design of micro-pillars in a microfluidic channel will affect fluid flow profiles and therefore cell immobilisation efficiency of the micro-pillar array.[168] According to the

CFD analysis, parallelogram shaped micropillars were found to be superior compared with their semi-circular counterparts as the former delivered more optimal flow profiles that minimised the risk of clogging. The results were verified experimentally. Similarly, the trajectory of microcarrier beads within a rotating bioreactor vessel was investigated using CFD and verified using experiments.[169] Based on this analysis, Pollack *et al*. theorised a basic relationship between fluid density, density of microcarrier beads, and the resulting trajectories of the beads. Ye *et al*. (2006)[69] utilised the FEM formulation to determine mass transfer and nutrient distribution profile within a hollow-fibre membrane bioreactor. The investigation was sought to determine the impact of certain bioreactor operating parameters such as cell density, medium flow rate, and cellular matrix thickness on the distribution of nutrients within the bioreactor. The modelling framework utilised in the study was based on the Krogh cylinder assumption and considered zero-order overall cell consumption rate of the substrate. Another simplification of the study included considering lack of radial convection within the cellular region, due to the resistive impact of the scaffolding material across the fibre wall. Results from the model indicated that it was possible to maintain sufficiently high substrate concentrations to enable the growth of dense bone tissue.

The bulk of models cited in this section employed as governing equations the Navier-Stokes equations for flow and transport of relevant nutrients (though Laplace's equation of *potential flow* can also be utilised), which have been reviewed in §2.3.1.2. While the discretisation methods and iterative solvers applied by the investigators varied, the investigations, and many others of similar nature, have validated certain assumptions on the hydrodynamic environment of various bioreactors types (rotating-bar, hollow-fibre, concentric-cylinder, rotating wall vessel, etc.) and demonstrated the utility of CFD to design bioreactors for the growth of bioengineered tissues. These investigations also point to the pervasive application of CFD as a robust methodology to understand bioreactor

hydrodynamics, especially in the absence of experimental techniques and apparatuses that can allow measurement of shear and flow distributions within microstructures supporting cell growth inside bioreactors.[165] Given, however, that an immense array of bioreactors (varying in type, geometry, and size), scaffolds (varying in porosity, permeability, degradation), and cell types (varying in genotype and phenotype) are currently in application, previously published results on a particular bioreactor type suffused with a particular variety of cells may not always find direct relevance for a novel scenario – an aspect of computational modelling that necessitated this investigation. This methodology too is not without its limitations, which have been addressed later in *Discussion*.

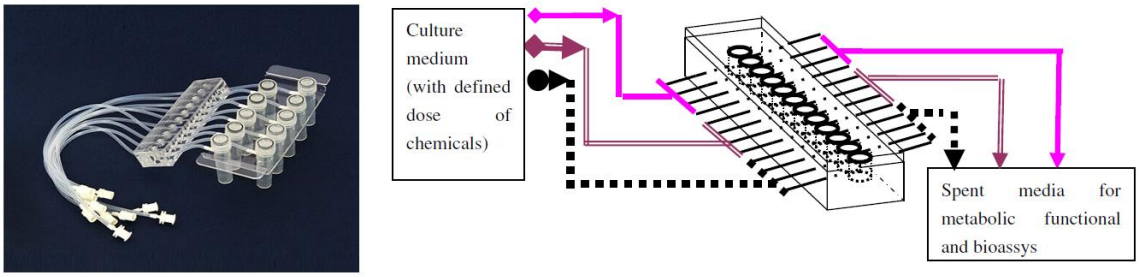

Figure 3. 1: TissueFlex® Microbioreactos. The photograph and schematic diagram of TissueFlex® microbioreactors is shown. The schematic represents the microbioreactors being operated in a parallel set-up. In the figure, twelve bioreactors are being supplied with culture medium (employing a multi-channel peristaltic pump), and the effluent being collected individually. *Permission to reprint to be sought from Ref.* 170 *(c) (2007) Elsevier. Photograph courtesy: Zyoxel Ltd.*

The aim of this chapter was to test the predictive and design capabilities of CFD by simulating flow and transport within a 3D geometry of arbitrary complexity. As such, CFD was used to investigate and compare the impact of bioreactor variables (such as its geometry, medium flow-rate, scaffold configuration, number of cells encapsulated in the scaffold) on the local transport phenomena and, hence, their impact on human mesenchymal stem cell (hMSC) growth and expansion. The geometric characteristics of the TissueFlex® (Zyoxel

Limited[xvii], Oxford, UK) microbioreactor (refer to Figure 3.1) were considered, to set up a virtual bioreactor containing alginate (in both slab and bead configuration) scaffolds. The bioreactor was developed to conduct cell and tissue culture under almost uniform (in terms of distribution of metabolite/non-metabolite concentrations and shear, as demonstrated in the results) and precisely controlled environment in a mid-throughput and parallel manner.[170] The bioreactor and scaffolds were seeded with cells that were modelled as glucose consuming entities, i.e. localised glucose sinks. The widely used glucose medium, DMEM, supplied at two inlet rates of 25 and 100 μL/hr, was modelled as the fluid phase inside the bioreactors. Model variables included, refer to Table 3.1, bioreactor configuration, scaffold morphology, media inlet velocity, glucose concentration in culture media, mesenchymal stem cell metabolism (in terms of glucose consumption), cell density, and apoptotic threshold. The two bioreactor configurations tested are shown in Figure 3.2.

3.2 MATERIALS AND METHODS

3.2.1 BIOREACTOR DIMENSIONS AND CONFIGURATION

In order to design the geometry of the model bioreactor, dimensions of TissueFlex® (Zyoxel Limited, Oxford, UK) microbioreactor were considered. The microbioreactor, constructed with polydimethylsiloxane (PDMS), has the format of a standard 96-well cell culture plate and is perfused using silicone tubing via a multi-channel peristaltic pump or multiple syringe pumps.[170] The bioreactor geometry can be modified so that the silicone tubing serving as the inlet and outlet ports can be arranged in different styles – two of which are explored in this study. Figure 3.1 shows a schematic diagram, as well as a photograph, of TissueFlex® with 12 microbioreactors. Each microbioreactor has a dimension of 6.6 mm

[xvii] Disclosure: Prof Zhanfeng Cui, the co-supervisor on this thesis, is the academic founder and a non-executive director of Zyoxel Ltd, a spin-off company of the University of Oxford. Zyoxel commercialises TissueFlex® microbioreactors as part of its business.

× 11 mm. For the purposes of this study, fluid flow and mass transport in only one microbioreactor was considered.

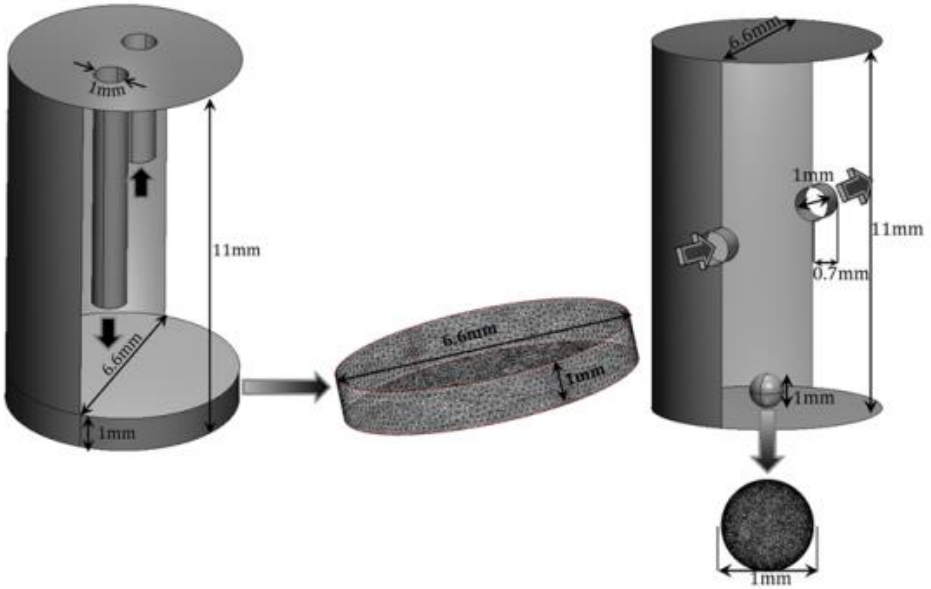

Figure 3. 2: Bioreactor and scaffold configurations employed in this investigation. The figure shows the two bioreactor as well as scaffold configurations used in this study. The geometry on the left is referred as *top-inout* whereas the one on the right as *symmetrical*. Bioreactor dimensions are also listed in the figure. Solid arrows (near the ports) indicate the direction of medium flow. The two scaffold morphologies, along with their dimensions, are also shown: slab (left) and bead (right). Each scaffold was assigned porosity of 85%.

3.2.2 SCAFFOLD AND CELLS

In this investigation, mass transport within two 3D cell culture constructs was simulated. The constructs were modelled as a 1 mm thick porous slab structure and as a porous bead of diameter 1 mm, both synthesised using alginate. Scaffold porosity and permeability are regulated by a multitude of factors, which include concentration of alginate and cross-linking solutions, method of synthesis, and, eventually, the pore size. As such, there is a whole array of case specific porosity and permeability values that can be introduced in the model. Given that scaffold porosity in excess of 90% can be easily achieved and glucose diffusivity in alginate, proportional to its porosity, can be as high as 90%,[171] both slab and spherical scaffolds were assigned isotropic porosity of 85%. As permeability is rather difficult to characterise there was lack of reasonably consistent values. As such, the two scaffolds were assigned a suitable permeability of 10^{-10} m^2.

Variable	Value
Bioreactor Geometry	Symmetrical Side Inlets, Inlet/Outlet at the Top
Construct Geometry	Slab and spherical bead (3D)
Media Inlet Velocity	25 µl/hr and 100 µl/hr
Glucose Concentration	2.5×10^{-5} kM (4.5 g/L) and 5.56×10-6 kM (1 g/L)
hMSC Glucose Consumption Rate	270 fM/hr/cell
Cell Density	1 Million: corresponding to 400 cells in the bead and 35,000 in the slab; 10 Million: corresponding to 4,000 cells in the bead and 350,000 in the slab
Apoptotic Threshold	5% of 1g/L glucose and 20% of 4.5g/L glucose
Deff,g in Water at 37°C	9.3e-6 cm^2/s [172]
Deff,g in Alginate at 37°C (10g/L)	6.59e-6 cm^2/s [173]

Table 3. 1: Investigation related variables. The table lists variables utilised in the model.

Alginate, in particular, was considered in this analysis due to its wide application[174] in synthesis of micro-carriers employed to immobilise cells due to its inertness, biocompatibility, high porosity, and amenability to various preparation methodologies[171,174-177]. Furthermore, alginate 'capsules' have been used as micro-carriers in various companies developing therapeutics; prime examples include: *CellMed AG* (Alzenau, Germany), *Encapsulife* (Washington D.C., USA), *FMC Biopolymer* (Sandvika, Norway), and *Zyoxel Ltd.* (Oxford, UK).

Slab and sphere morphologies were modelled due to their ease of preparation and, as such, pervasive application. Spherical scaffolds can be prepared by extruding alginate solution as droplets into a cross-linking solution[176]. While the simplicity of preparation and reproducibility make the two morphologies ideal for laboratory-based investigations, the shapes are especially amenable to mathematical analysis due to ease of implementation in almost all computational platforms and reduction in computational overhead due to their

elementary nature. Scaffold dimensions were also based on ease of synthesis. Transferring alginate solution through a syringe results in beads roughly equal to or greater than 1 mm, though greater control and reduced size can be achieved via mechanical means.[177] As such, the diameter of the spherical scaffold was set to 1 mm. The height of the slab was limited to 1 mm as the resulting volume provides optimum growing space enabling cell expansion without presenting, in itself, diffusional limitations.

The metabolic behaviour of human mesenchymal stem cells (hMSCs) was simulated in this study, with glucose modelled as the metabolite being transported to the cells. Optimal partial pressure of oxygen was assumed to be present within the scaffolds. Oxygen transport was not considered in this model for a variety of reasons. Firstly, hMSCs are exposed to very low partial pressures of oxygen within their native environment[178] and there is evidence for their survival under extremely hypoxic conditions (i.e. 0.2% O_2).[179] Secondly, the diffusivity of oxygen in alginate being an order of magnitude higher than glucose (2.5×10^{-9} m^2/s [180] vs 6.59×10^{-10} m^2/s, respectively) and both solutes being relatively small (32 Da and 180 Da, respectively) with almost no interactions between them, the simulated results, in terms of trends, can safely assumed to be similar. Add to that the fact that the consumption rate of oxygen by human mesenchymal stem cells is an order of magnitude lower than glucose ($1.22 - 3.20 \times 10^{-8}$ vs $0.23 - 1.22 \times 10^{-7}$ mg/h/cell, respectively). It was, therefore, concluded that glucose (and not oxygen) mass transport will form the limiting factor in our analysis, since oxygen diffuses faster, is consumed slower and these cells are very resilient to its absence. As such, oxygen distribution, even if lower than expected, would have informed us little about the impact of oxygen partial pressure on the differentiation, expansion, and survival of hMSCs encapsulated within the bioreactor. Secondly, co-transport of glucose and oxygen was not considered as a 3D bioreactor system was modelled in its entirety, and not just scalar diffusion in 2D plane within the system, which necessitated

a very fine mesh structure. Adding oxygen, beyond the mere solution of an additional transport equation, would have introduced additional Courant-Friedrichs-Levy (CFL)-related restrictions due to the enhanced diffusivity of Oxygen, which would have necessitated a decrease in the required time-step; an effect that cannot be remedied with parallelisation. As such, including oxygen would have vastly added to the computational costs without a substantial contribution to the question that was being explored.

As the main aim of the study was to investigate the maximal load under which the bioreactor can deliver optimally, two static cell densities were considered in the model: 1 million/mL and 10 million/mL of the cell suspension. The two cell densities represented the typical and extreme cell densities for cell therapy and tissue engineering applications. As such, cell growth was not considered in the model. Therefore, cells were assumed to have been encapsulated homogeneously throughout the two scaffolds. This is equivalent to the initial culture conditions and the nutrient transport would decide the survivability of the encapsulated cells. Each cell was assumed to consume glucose at a fixed rate of 270 fM/hr/cell.[178] Glucose diffusivity in alginate and water at 37°C were considered to be 6.59×10^{-10} m^2/s and 9.3×10^{-10} m^2/s,[172,173] respectively. hMSCs were modelled as sinks within the slab and the bead, consuming glucose at a set rate, based on the values of glucose consumption and volumetric cell count mentioned above. The variables investigated are listed in Table 3.1. The two bioreactor geometries and scaffold morphologies, along with boundary conditions, have been shown in Figure 3.2.

3.2.3 NUTRIENT MEDIUM

Glucose concentrations of 4.5 g/L and 1 g/L were considered for analysis. This was done for practical purposes as a nutrient medium most commonly used for cell culture, Dulbecco's modified Eagle medium (DMEM), contains 4.5 g/L glucose (high

concentration). For practical reasons, as recommended by the manufacturer of TissueFlex®, Zyoxel Ltd, media inlet rate of 25 μL/hr was utilised. To compare its efficacy and efficiency, an inlet rate of 100 μL/hr was also investigated. A common practice while culturing cells is the use of Foetal Bovine Serum (FBS) as a supplement to aid cell survival, growth, and proliferation. While the addition of FBS in DMEM may result in the fluid behaving in a non-Newtonian manner, the overall concentration of serum generally added is not concentrated enough to alter the flow characteristics of DMEM. Therefore, the fluid phase was assumed to be Newtonian.

3.2.4 MODELLING FRAMEWORK AND GOVERNING EQUATIONS

In silico bioreactor geometries were constructed using a CAD/meshing software platform, CFD-GEOM (ESI Group, Paris, France). The bioreactor geometry was then meshed to create *finite volumes* (or *control volumes*), where fluxes are calculated, along with discrete locations where the variables are defined. In this flavour of the finite volume method, all variables (velocities, pressure and concentrations) were defined on the same location on the grid (cell centre), resulting thus in a *collocated* mesh formulation. Unstructured tetrahedral meshes were used for this study, since they allow for great flexibility and automation in mesh generation, especially in complex geometries. Unstructured meshes introduce ease in mesh generation but imply a requirement for a larger number of elements, when compared to structured hexahedral meshes for example, to achieve the same level of accuracy. This requirement was indeed met by the resolutions examined and employed, as discussed in §3.2.5.

CFD-ACE+ (ESI Group, Paris, France) was used to formulate the model representing the bioreactor system and to solve the discretised governing equations. CFD-ACE+ primarily solves the general transport equation, (2.20), which captures the basic

conservation laws of interest. This equation can, furthermore, represent the transport of any substance when Φ equals the concentration of that substance. In that case, the source term can represent consumption of this quantity by cells in the domain, as is the case in our model. Additional parameters needed (diffusivities, viscosity, density) are all set to constants, as is the case with the common DMEM medium used in cell cultures (Newtonian incompressible fluid).

$$\frac{\partial}{\partial t}(\rho\Phi) + \nabla.(\rho U\Phi) - \nabla.(\Gamma_\Phi \nabla\Phi) = S_\Phi \tag{2.20}$$

This equation is integrated over the control volumes described above; subsequently the divergence theorem is applied, converting volume quantities to surface fluxes and ensuring a conservative formulation of the discretised equations, as shown in (3.1):

$$\int_{CV} \frac{\partial}{\partial t}(\rho\Phi)dV + \sum_{faces}^{surface} \int_S [\nabla.\rho U\Phi - \Gamma_\Phi \nabla\Phi].\vec{n}_S dS = \int_{CV} S_\Phi dV \tag{3.1}$$

In (3.1), S represents any of the faces of the control volume, whereas $\boldsymbol{n}_S$ is the unit vector normal to that surface.

As the evaluation of bioreactor performance while operating at full capacity, a zero-order overall cell consumption rate was assumed, which can be expressed as $s \times d$, where s is the consumption rate for a single cell and d is the cell density. As a result the cell growth rate, practically zero, did not depend upon glucose concentration. Furthermore, the model did not rely on any chemical reactions involving glucose or any other chemical substrate. The model, therefore, did not consider any additional kinetic model; the metabolic activity of the cells was accounted for by assigning appropriate spatially distributed sink terms in the transport equations, thus accounting for consumption, as quantified in the sequel.

The values of relevant quantities (e.g. Φ) inside the CV were determined by employing a central, second order, differencing scheme. The transport equations were solved in their full transient form. A variant of the Crank-Nicolson scheme, again second order, was employed to march the discretised equations in time and ensure temporal accuracy (refer to *Appendix* for relevant details). The segregated solver employed (i.e. solving for the different variables one after the other and iterating to convergence) necessitates special handling of the continuity and pressure (the author reminds the reader that pressure does not appear in the conservation of mass equation). To achieve the simultaneous evaluation of the pressure field, we employed the inherently iterative *Semi-Implicit for Pressure-Linked Equations Consistent* (SIMPLEC) scheme,[181] an adaptation of the *Semi-Implicit for Pressure-Linked Equations* (SIMPLE) method,[182] to couple the pressure and velocity fields by introducing a new variable, the *pressure correction*, and solving for that variable to improve upon an initial pressure field, till convergence (refer to *Appendix*).

The aforementioned sets of equations result in pseudo-linear sparse systems of equations that have to be solved, at least to partial convergence, within each iteration. The *Algebraic MultiGrid* (AMG) scheme was employed for this, a method that offers rapid convergence by creating a succession of coarser and finer grids and *injecting* or *interpolating* solutions from one grid refinement level to the other, thus achieving the reduction of multiple wavelengths of error (proportional to average cell size) simultaneously.[183]

Domains with different properties (like, for example, the porous cell-seeded regions) were accounted for by creating a multi-block mesh structure; each block with its own topology and connectivity. In the case of this study, two blocks were always used. A higher order interpolation *arbitrary interface* method was used on the common surface of the two blocks, ensuring continuity of the solution variables across this interface. Dirichlet (inflow

and walls) and Neumann boundary conditions were applied as required. The time step used in the simulations was 450s, but other, finer, time step values of 50s, 150s, 300s were used to confirm time step independence. Each time step required between 200 – 500 iterations to reach satisfactory convergence. In this set of simulations a drop of eight to ten orders of magnitude of residuals was shown to be adequate. Finally, the code was executed in parallel on 8 cores (Intel Xeon, clocked at 2.66GHz), using the MPI protocol and domain decomposition.

3.2.5 GRID INDEPENDENCE ANALYSIS

Grid independence analysis was conducted on one of the test cases to ensure convergence and insensitivity of the results obtained on numerical parameters. The test cases examined involved structured (50,000; 100,000; 200,000 and 400,000 elements) as well as unstructured (100,000 and 400,000 elements) meshes. The mesh independence study showed excellent convergence, with the finest grids (200,000 and 400,000 elements structured and 400,000 elements unstructured) yielding practically indistinguishable results. The author opted to use unstructured tetrahedral meshes with 400,000 elements. The geometry employed in this investigation consisted of multiple sub-components (the bioreactor, the port, and the scaffold), the interface of which required greater resolution and, thus, very fine grid structure. Unstructured meshes, whether 2D (triangles or quadrilaterals) or 3D (tetrahedral or hexahedral), treats individual cell as a block, which has the advantage that no implicit structure of co-ordinate lines is imposed by the grid. As such, the mesh can be easily concentrated where necessary without wasting computer storage. This constituted a key reason as to why unstructured mesh was preferred as it ensured smooth transition from one domain (e.g. alginate bead) to the other (e.g. bioreactor and its ports). Tetrahedral grid generation being more straightforward and the mesh structure computationally less expensive than its hexahedral counterpart constituted the main reasons tetrahedral grids were

employed. Therefore, unless otherwise noted, unstructured tetrahedral meshes with 400,000 elements were used. The various test cases and relevant boundary conditions utilised in this investigation are listed in Table 3.2.

Test Case	Boundary Conditions				
	Media Inlet-Outlet	**Media Flow Rate**	**Cell Density/mL cell suspension**	**Glucose Concentration**	**Culture**
Case I	Symmetrical	25 µL/hr	1 million	2.5×10^{-5} kM	Slab
Case II	Symmetrical	100 µL/hr	1 million	2.5×10^{-5} kM	Slab
Case III	Symmetrical	25 µL/hr	10 million	2.5×10^{-5} kM	Slab
Case IV	Top-Inout	25 µL/hr	1 million	2.5×10^{-5} kM	Slab
Case V	Symmetrical	25 µL/hr	1 million	5.56×10^{-6} kM	Slab
Case VI	Symmetrical	25 µL/hr	1 million	2.5×10^{-5} kM	Sphere
Case VII	Symmetrical	100 µL/hr	1 million	2.5×10^{-5} kM	Sphere
Case VIII	Symmetrical	25 µL/hr	10 million	2.5×10^{-5} kM	Sphere
Case IX	Top-Inout	25 µL/hr	1 million	2.5×10^{-5} kM	Sphere
Case X	Symmetrical	25 µL/hr	1 million	5.56×10^{-6} kM	Sphere

Table 3. 2: Computational Boundary Conditions. The table lists various test cases and relevant boundary conditions utilised in this investigation.

3.2.6 DIMENSIONAL ANALYSIS

The effectiveness of mass transport was evaluated by calculating the Peclet number (*Pe*). Limitations of the internal mass transport were determined by calculating the Biot Number (N_{Bi}): the ratio of glucose mass transfer across the inside of the scaffolds to glucose mass transport across the boundary layer outside the scaffolds. The nature of flow was determined by calculating the Reynolds Number (*Re*).

3.3 RESULTS

3.3.1 DIMENSIONAL ANALYSIS

The culture media flow rate resulted in laminar flow inside the bioreactor with the *Re* (based on bulk flow velocity and the inlet port diameter) being 0.01 and 0.04 for the flow rates 25 µL/hr and 100 µL/hr, respectively. The default bioreactor specifications yielded *Pe* ~13 for the recommended flow-rate (for both slab and sphere), indicating that in both cases

convection plays a dominant role in the external transfer of glucose. Furthermore, the N_{Bi} for each test case was >> 1 indicating that there were no major limitations to the transport of glucose across the fluid-cell or fluid-scaffold interface within the bioreactor.

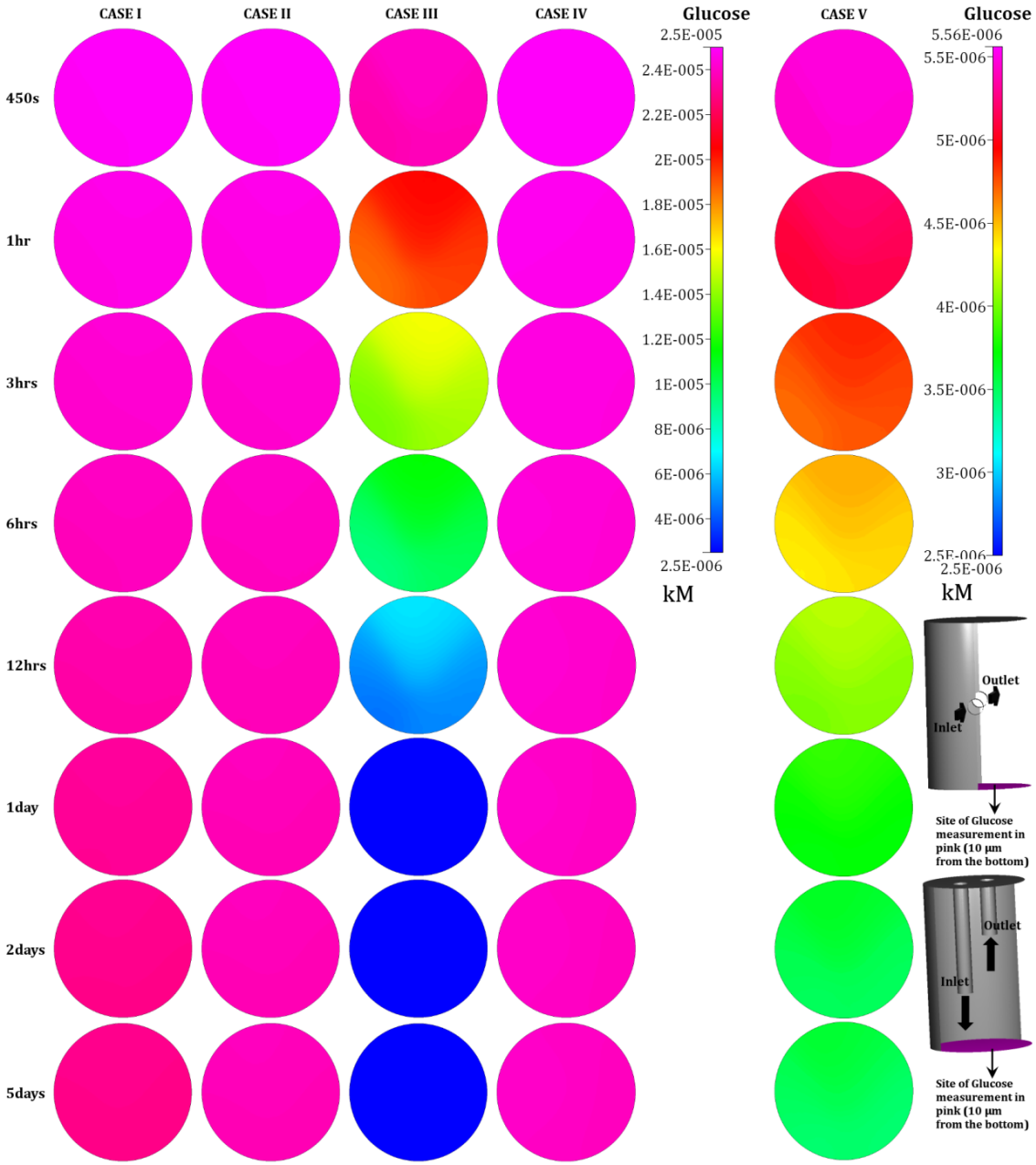

Figure 3. 3: Time evolution of glucose concentration at the bottom of the alginate slab. A comparison of glucose concentrations computed at a distance of 10 µm from the bottom in the slab configuration perfused under the different boundary conditions. The figure shows glucose concentration as measured on a transverse section of the scaffold made 10 µm from the bottom of the slab. The two bioreactor configurations shown on the right end of the figure display the boundary conditions as well as the site of glucose measurement. Arrows indicate the direction of medium flow. All other cases, apart from *III* and (partially) *V* (for reasons discussed), meet the criteria required to ensure cell viability for any duration of time. Glucose concentration, as shown in the legend, was measured in *kM*.

3.3.2 IMPACT OF ALGINATE MORPHOLOGIES

Given that the slab configuration of thickness 1 mm contained (about two orders of magnitude) more cells compared with the spherical scaffold of diameter 1 mm, nutrient demand was higher in the former. This is evident from Figures 3.3 and 3.4 that show the glucose distribution at a distance of 10 μm from the bottom in the slab and in the middle of the alginate sphere, respectively. This is made particularly apparent if glucose concentration is compared after the system has achieved steady state. In Figure 3.5, notice the steady state glucose concentrations in the alginate slab and bead; while both are sufficiently high to ensure adequate nutrition, the drop in the alginate slab is higher. The default boundary conditions recommended for the microbioreactor, listed in Table 3.2 as *case I*, seem to be sufficient to carry out glucose transport to the innermost layer of cells seeded in both the slab, as well as the spherical scaffold. The data indicate that the system remains capable of supporting cell expansion and maintaining cell viability at steady state. This is achieved by ensuring that at least 10% of the initial glucose concentration (2.5×10^{-6} kM) is still available to the innermost regions of a cell culture.

3.3.3 IMPACT OF FLOW-RATE

As reported above, the default flow-rate of 25 μL/hr was found suitable to sustain hMSC cultures operating at full capacity by ensuring supply of adequate amount of glucose to the innermost scaffold regions in both morphologies. *Cases II* and *VII* represent computations where the nutrient media inlet velocity was increased by a factor of four, to 100 μL/hr. Unsurprisingly, the increased flow-rate, as can be observed in Figures 3.3, 3.4, and 3.5, led to a far improved distribution and supply of glucose within the slab and bead morphologies.

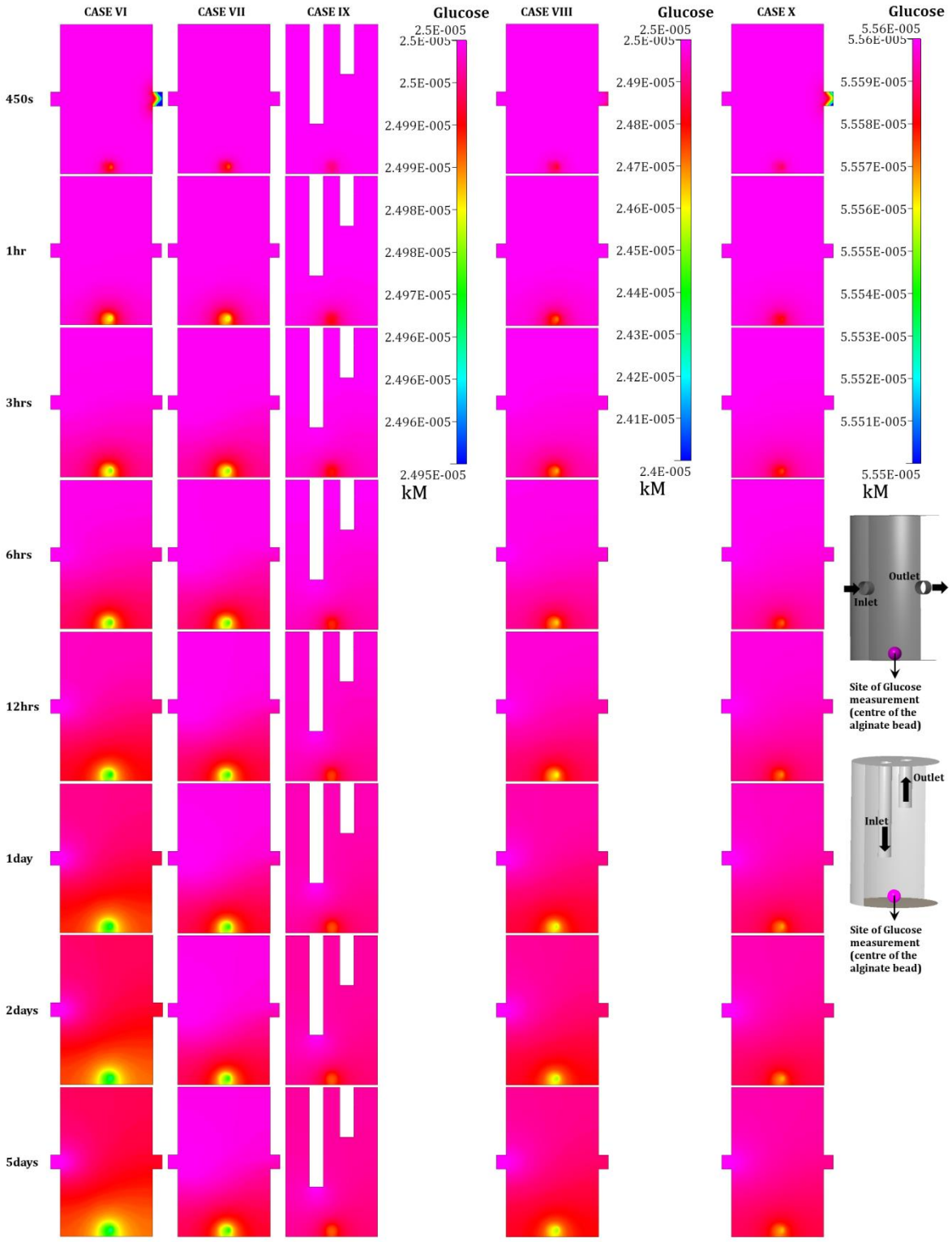

Figure 3. 4: Time evolution of glucose concentration in bioreactors containing the spherical scaffold. A comparison of glucose concentrations computed at the centre of the alginate bead perfused under the various boundary conditions. The figure shows glucose concentration as measured on a frontal section made at the centre of the bioreactor. The two bioreactor configurations shown on the right end of the figure display the boundary conditions as well as the site of glucose measurement. Arrows indicate the direction of medium flow. All test cases seem to meet the criteria to ensure cell viability for any duration of time, as the glucose consumption requirements, compared to the slab, are quite low. Glucose concentration, as shown in the legend, was measured in *kM*.

3.3.4 IMPACT OF CELL DENSITY

While the standard recommended flow-rate was found optimal for cell growth for the recommended 1 million/mL cell suspension density, it, however, fails if cell density of 10 million cells/ml suspension (*case III*) is used, as evident by a rapid decline in glucose concentration within the slab. Here, glucose concentration plummeted well below the critical concentration (10% of the initial value) within the first 24 hours, indicating that necrosis will set in soon after, in case the flow rate is not altered. The drop in glucose concentration within the spherical scaffold encapsulating the higher cell density was observed to be the largest across cases involving the alginate bead. However, with the total cell count within the bead still quite low, transport across the bead was found adequate to sustain the expansion and viability of the encapsulated cells.

3.3.5 IMPACT OF BIOREACTOR CONFIGURATION

Similarly, data obtained for the alternative bioreactor configuration (*top-inout, cases IV and IX*) indicated that the boundary conditions are sufficient to ensure that even the innermost cells continue to receive at least the critical concentration of glucose at all times; refer to Figures 3.3 and 3.4. However, rather surprisingly, the performance of the *top-inout* configuration with media inlet velocity of 25 µL/hr, outperformed the default boundary conditions (*cases I* and *VI*) as well as *cases III and VII* where the symmetrically organised ports were perfused with media inlet velocity of 100 µL/hr. This is best evident in Figure 3.5, especially for alginate bead, where the drop in glucose concentration within the *top-inout* configuration was recorded to be the smallest. This observation underpins the importance of analysing transport phenomena and flow in such reactors rigorously and using detailed first-principles methodologies to quantify the bioreactor's fluid mechanics.

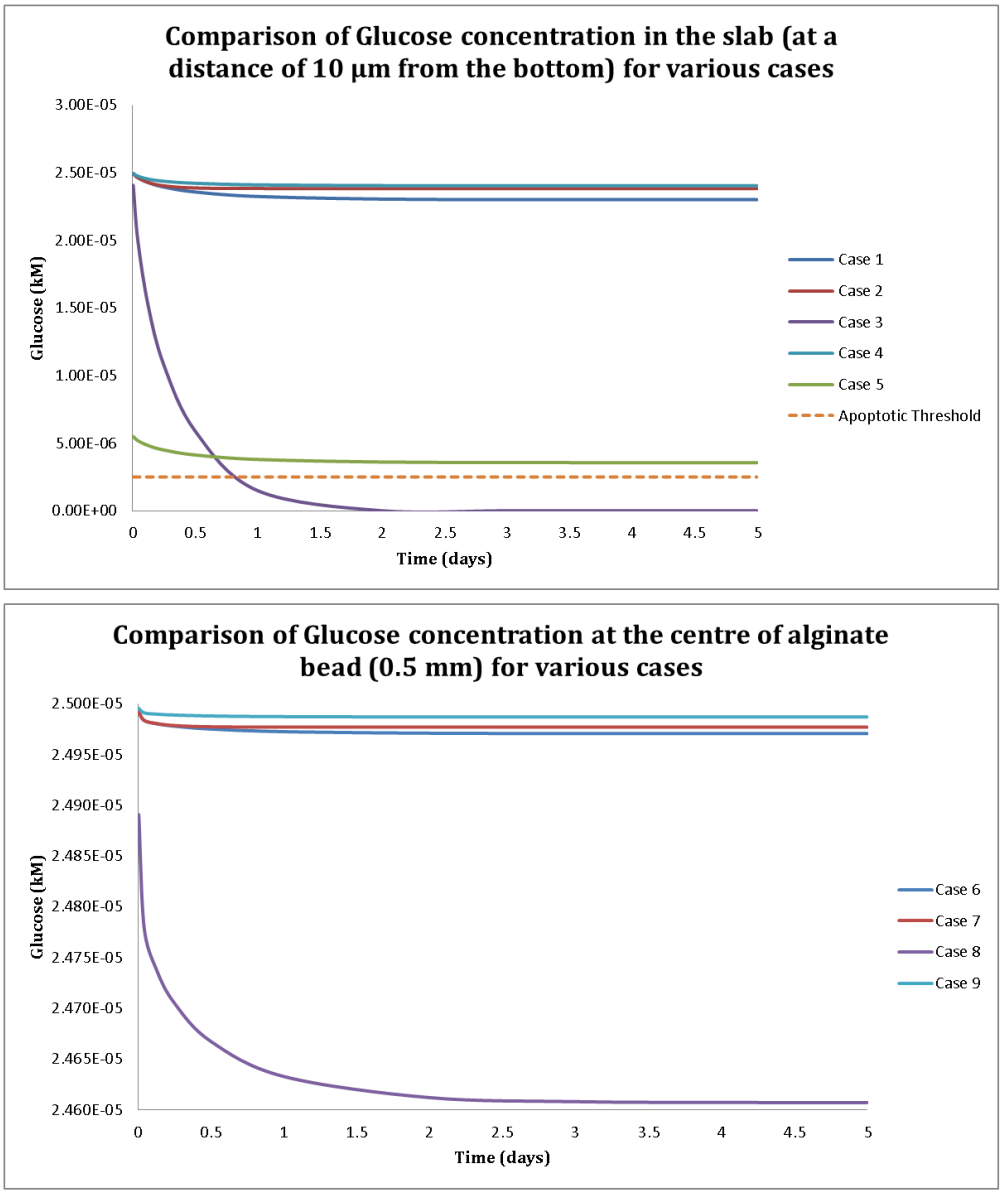

Figure 3. 5: Comparison of glucose concentration in the slab vs spherical scaffold. (Top) The figure compares glucose concentration at a distance of 10 µm (from the bottom) in the slab as the system achieves steady state. (Bottom) The figure compares glucose concentration at the centre of the alginate bead as the system achieves steady state. The figure at the bottom does not indicate the apoptotic threshold as all configurations with alginate bead performed substantially above that threshold.

3.3.6 IMPACT OF NUTRIENT MEDIA

When low concentration glucose media (1 g/L, *case V*) was utilised, although the overall glucose concentration in the bioreactor stayed above the critical concentration (as can be seen in Figure 3.5), the analysis suggests that the standard recommended flow rate may lead to sub-optimal distribution of glucose (at least in the physical scenario where proliferation of cells and the act of matrix deposition by them will alter the permeability of

their immediate microenvironment). Use of low concentration glucose medium had no negative impact on the spherical scaffold.

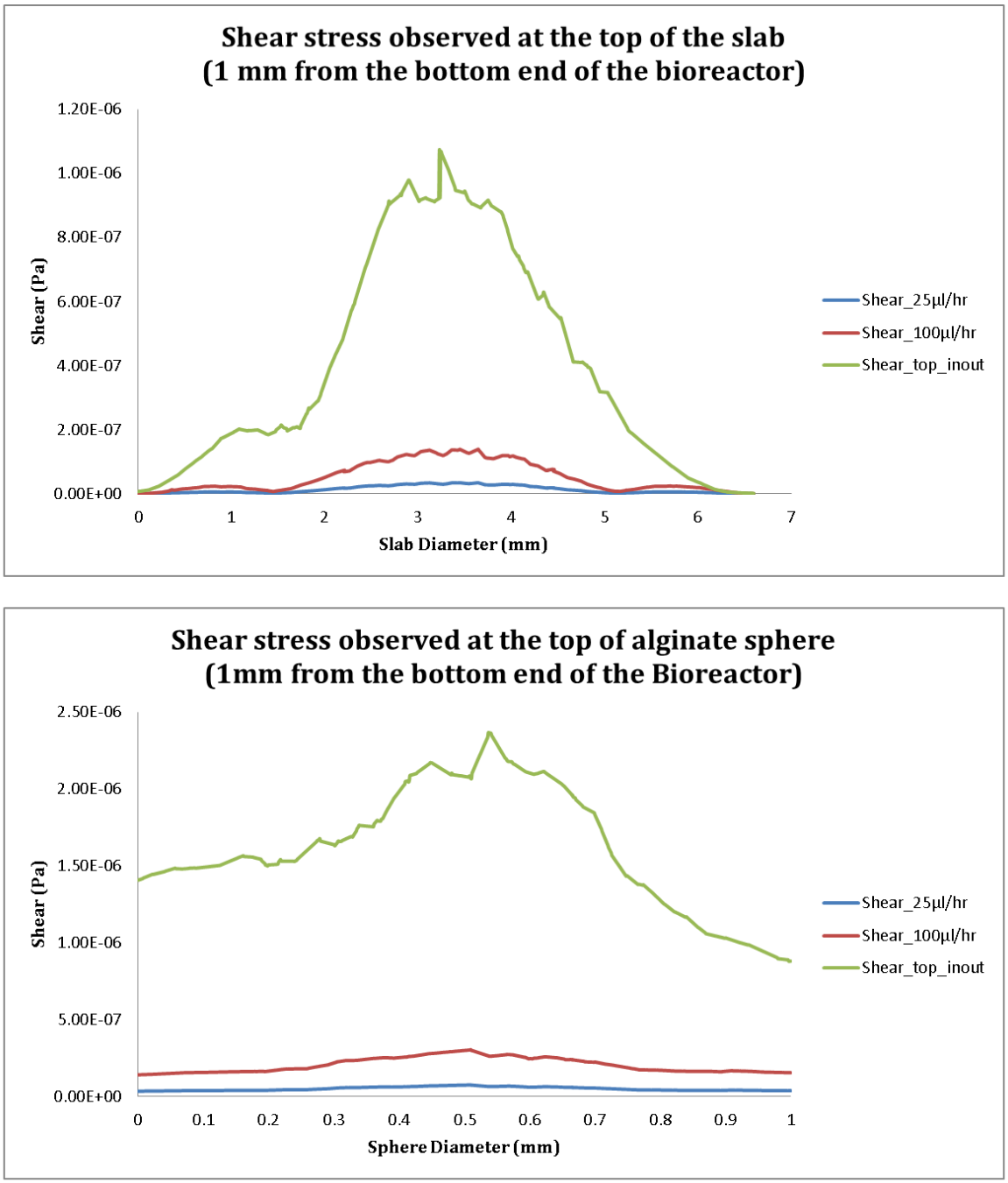

Figure 3. 6: Comparison of shear stress observed in bioreactors with different configurations and flow regimes. A comparison of shear stress observed at a distance of 1 mm from the bottom (the top of the cellular slab and the alginate bead), in the symmetrical bioreactor for three different boundary conditions: inlet rate of 25 µl/hr, inlet rate of 100 µl/hr, and the *top-inout* configuration. Figure at the top captures the shear stress observed at the top of the slab configuration. The horizontal axis represents the length/diameter of the slab/bead. Although shear stress for all three boundary conditions observed was physiologically ineffective, shear stress observed for the "*top-inout*" configuration, achieved at a flow rate of 25 µl/hr, was the highest.

As shown in Figures 3.6 and 3.7, the resulting shear stresses in all the test cases were on the lower end of the scale and physiologically neutral, with the maximum stress being 10^{-6} Pa (*cases IV and IX*) followed by 10^{-7} Pa (*cases III and VIII*). Shear stress was calculated at the top surface of both scaffolds, which is 1 mm from the bottom end of the bioreactor (refer to Figures 3.6 and 3.7), along an imaginary line/plane running across the two scaffolds.

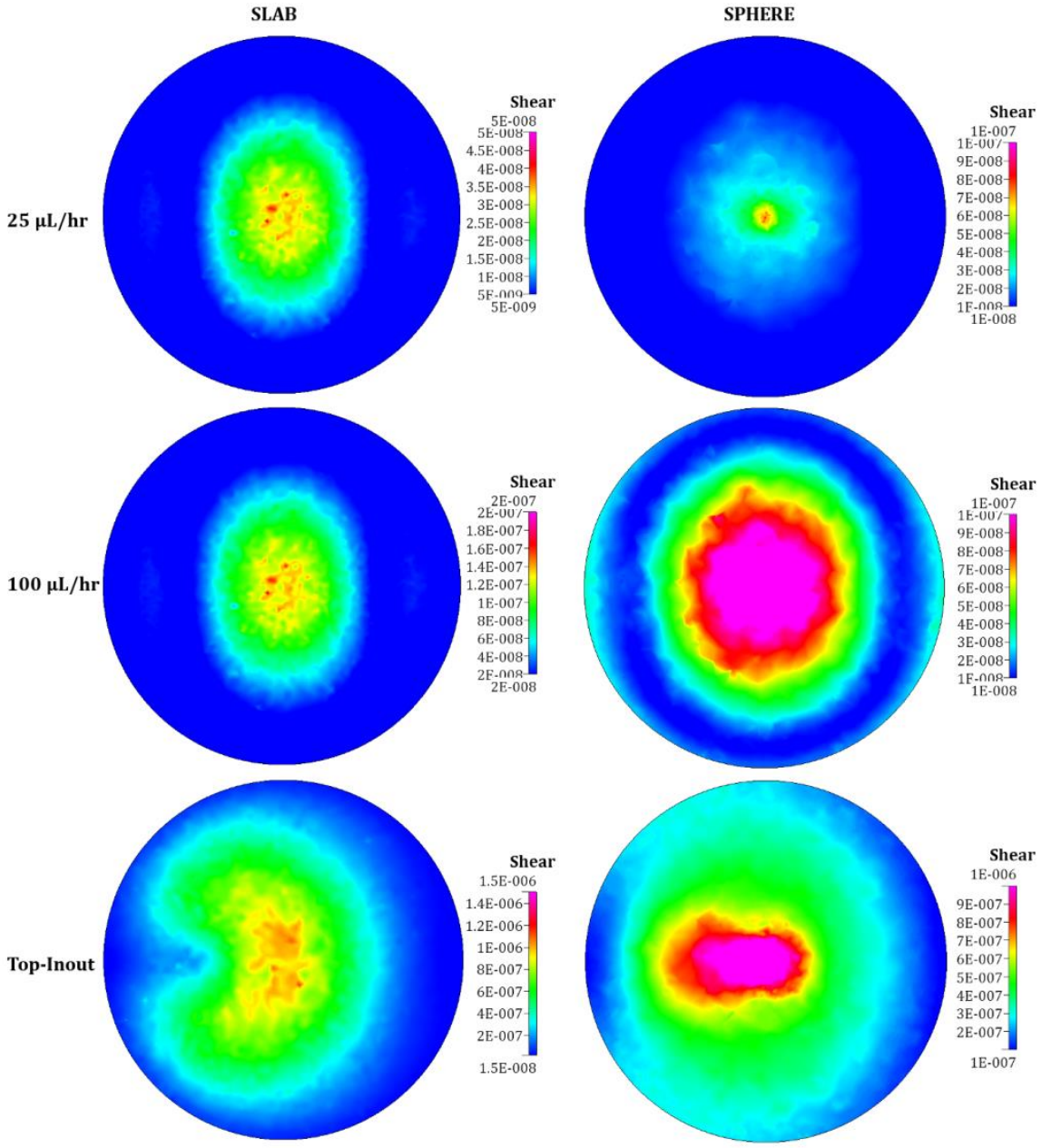

Figure 3. 7: Visualisation of shear stress in the three cases discussed in Figure 3.6. Shear Stress observed on the top (approximately 1 mm from the bottom) of slab and alginate sphere for three cases. Shear, as displayed in the legend, was measured in *Pa*.

Shear stress for all the cases evaluated was found to be highest at the top where the alginate scaffold was fully exposed to the perfusion medium, with shear being almost the same in the middle and close to the bottom for the slab. This, however, was not true for cases with the spherical scaffold where the lowest stress was observed in the middle. For cases involving the slab construct, shear stress dropped by three orders of magnitude between the middle and top. Furthermore, as can be observed in Figure 3.7, shear stress in the *top-inout* configurations was observed to be higher than their *symmetrical* counterparts for the same media inlet velocity (25 µL/hr).

3.4 DISCUSSION

Carrier *et al.* (2002)[184] observed that in a culture of cardiac cells the region beyond a layer of 100 µm thick cells could not be supported via diffusion under static conditions. *In vivo*, cells are generally located no more than approximately 100 µm from capillaries[75] that supply them with oxygen and nutrients, such as glucose. A feature central to the functionality of bioreactors is their ability to carry out mass transport so as to maintain cell viability within 3D cultures.[75] Similarly, shear stress has been implicated in influencing mammalian cell differentiation, as well as pattern and quality of growth. For example, endothelial cells tend to orient themselves in the flow direction;[185] shears of approximately 0.01 Pa have been found to be ideal for cell growth;[186] and application of shear stress can influence MSC fate.[187-189] Unlike unicellular organisms, animal cells tend to have low tolerance to fluid forces which rule out high nutrient flow rates that, despite achieving sufficient mass transport, may create fluid flow patterns leading to high shear stresses.[57] With the exception of cells present in tissues that are exposed to significant haemodynamic loading, such as endothelial (direct loading) or smooth muscle cells (indirect loading), the majority of cells in the human body do not experience high shears.[57,75] As a result, they react differently to shear stresses *in vitro*. Down-regulation of endothelial cell proliferation under laminar flow

(steady shear stress conditions) and up-regulation of survival factors, such as *Kruppel-like factor-2*, while the cells experience both pulsatile and reciprocating oscillating flow;[190] development of a fibrous capsule in chondrogenic cell-matrix constructs when exposed to turbulent flow conditions;[191] and increased mineralised deposition in osteoblasts due to enforced differentiation as a result of long-term exposure to shear stress[192-195] are but a few examples. Therefore, if designed properly, fluid dynamics inside a bioreactor can be exploited to either initiate desired cellular differentiation processes or enhance cell proliferation, expansion, and attachment.[57,75,196,197] A bioreactor that utilises pulsatile flow to fabricate cardiovascular patch tissues is a perfect example where this concept was successfully utilised.[198]

As indicated in §3.3.1, the media flow rates utilised in simulations yielded laminar flow inside the bioreactor. Furthermore, in bioreactors, mass transport to cells is achieved by maintaining a balance between the external transport of the relevant molecular species, i.e. transport of the species to the external surface of cells/scaffold, and internal diffusion, i.e. penetration of the species to the inner cells[75]. The former can be evaluated by calculating the *Pe* associated with the bioreactor, which for TissueFlex® was calculated to be roughly 13, indicating that within TissueFlex® convection plays a dominant role in the external transfer of glucose. This seems to suggest that test cases where glucose concentration in the innermost regions of the slab dropped below the critical concentration could be salvaged by increasing the flow rate of the culture media as that would increase the molar flux of glucose reaching cells. Limitations of the internal mass transport can be similarly determined by calculating the N_{Bi}, which for each test case was found to be >> 1. This indicated lack of major limitations to the transport of glucose across the fluid-cell or fluid-scaffold interface within TissueFlex®. This most conclusively explains why even at a very low flow rate the standard boundary conditions recommended for the microbioreactor are adequate to sustain

cell growth and viability by providing metabolites to even the innermost regions of cell populations inside the bioreactor. Figure 3.5 contains plots detailing the change in glucose concentration for slab and spherical 3D culture as the bioreactor achieves steady state.

In addition to efficient glucose transport, laminar flow within the bioreactor resulted in low, physiologically neutral, shear environment (10^{-7} Pa) for encapsulated cells. This constitutes a very useful piece of information, for low shear environments (typically less than 10^{-4} Pa as reported elsewhere[199]) can play an augmentative role in tissue formation by inducing and facilitating cell-cell contact and cell aggregation, as well as cell-matrix associations.[200] High shear stresses, though, can disrupt the process of cell expansion creating micro-pockets that may result in gradients or gaps within the growing cell colonies compromising the homogeneity of resulting cell population. High shear also results in differentiation of the mesenchymal cells into the osteoblastic phenotype, which may be useful if osteoblasts are the desired output but not in case hMSC expansion while preserving their differentiation potential is of interest. This was not the case with the bioreactor geometry and recommended operational parameters tested here. The results obtained are, therefore, consistent with the expected behaviour of TissueFlex®, along with alginate, high-glucose DMEM, as well as the media flow-rate in terms of supporting perfused expansion of hMSCs while maintaining their differentiation potential.

The most interesting result to emerge from this investigation was the performance of the *top-inout* configuration in terms of both glucose transport as well as shear. Perfused with media inlet rate of 25 µL/hr, the *top-inout* configuration resulted in a more efficient transport of glucose, in comparison with the symmetrical configuration perfused with media inlet rate of 100 µL/hr. Additionally, an increase in shear stress by two orders of magnitude for the bioreactors containing the slab, and by an order of magnitude for the bioreactors containing the bead (for the same media inlet rate) was also observed. This piece of data has significant

design implications, for it suggests that shear dependent differentiation can be induced by modifying bioreactor design to generate physiologically relevant shear stress at a laminar media inlet rate. As such, a variety of designs can be tested using CFD prior to the construction. This reinforces the significance of CFD as an investigative tool in general, and is a testament to CFD's strength as a concept selection and design optimisation tool.

Factor	Parameters	Day	Glucose Consumption	Standardised (fmol/hr/cell)
Time[201]	Days<7	<7	12 - 14 pmol/day/cell	583.3
	Days>7	>7	13 - 15.8 pmol/day/cell	658.3
	Days<7	<7	14 - 17 pmol/day/cell	708.3
	Days>7	>7	14 - 15 pmol/day/cell	625.0
Cell Number[178]	2×10^5	Averaged	357.3 ± 45.2 fmol/hr/cell	357.3
	1.5×10^5	Averaged	327.6 ± 47.8 fmol/hr/cell	327.6
	1×10^5	Averaged	272.8 ± 43.3 fmol/hr/cell	272.8
	0.5×10^5	Averaged	378.2 ± 127.7 fmol/hr/cell	378.2
Cell Density[202]	100 cells/cm^2	Averaged	0.609 ± 0.029 pmol/hr/cell	609
	1000 cells/cm^2	Averaged	0.155 ± 0.023 pmol/hr/cell	155
Differentiation[203]	Osteogenic	7	150 fmol/hr/cell	150
		21	250 fmol/hr/cell	250
	Chondrogenic	7	380 fmol/hr/cell	380
		21	360 fmol/hr/cell	360
Oxygen Concentration[201]	Normoxia	<7	12 - 14 pmol/day/cell	583.3
	Normoxia	>7	13 - 15.8 pmol/day/cell	658.3
	Hypoxia	<7	14 - 17 pmol/day/cell	708.3
	Hypoxia	>7	14 - 15 pmol/day/cell	625.0

Table 3. 3: Variations in glucose consumption by mesenchymal stem cells. The table lists glucose consumption rates by the mesenchymal cells under factors such as culture time, cell density and population size, the amount of available oxygen, and the phenotype towards which the cells are progressing. While the range of consumption can vary by a factor of 4, it varies within the same order of magnitude.

The boundary conditions utilised herein, however, cannot be used when employing the slab morphology to either seed the higher cell density (10 million cells/mL of cell suspension) or deliver low-glucose DMEM (1 g/L). In both cases, especially the former, a rapid decline in glucose concentration was observed that could potentially result in cell death

or differentiation due to glucose depletion. Glucose distribution in the spherical morphology, however, due to low transport requirements, was not affected by any of the tested parameters.

While the computational model was able to demonstrate that the default recommended operational parameters for TissueFlex® can support growth of hMSCs and that the bioreactor design can be slightly altered to obtain better transport and higher shear (which formed the basis of a new bioreactor morphology that is currently being developed), the model was not without limitations. The model did not consider proliferation or cell apoptosis, and assumed the presence of a constant cell population. This may have worked for this particular investigation, which aimed to investigate the capacity of TissueFlex® in supporting cell expansion at maximum capacity, however the model will need to be modified if it is to be utilised for other purposes, for example, determining ideal media perfusion rate.

Secondly, the model considers expansion of hMSCs consuming glucose at a zero-order rate of 270 fM/hr/cell. This does not fully reflect hMSC expansion in vitro, where alterations in glucose consumption are observed based on factors such as seeding density, quantity of oxygen (normoxia vs hypoxia), extent of expansion, and cell fate (i.e. chondrogenic vs osteogenic), as displayed in Table 3.3. For example, glucose consumption is inhibited during osteogenesis,[178,203] is higher for a lower cell-density,[178,202] varies between normoxic and hypoxic cultures (initial 7 days),[201] and slightly variable (higher initially) between the early (first 7 days) and late phases of cell culture.[201] Furthermore, this range is further widened by the fact that the consumption rate reported in Table 3.3 is determined for a heterogeneous population of mesenchymal cells, which makes it particularly challenging to report individual cell-to-cell variability. The averaged glucose consumption rate utilised in the model, thus, accounts only for hMSC growth period, which limits the model to hMSC expansion under culture conditions (precisely what is being simulated via the model).[178]

However, given that various rates, listed in Table 3.3, are within the same order of magnitude, the model prediction of sub-optimal performance, when low glucose concentration medium and a cell density of 10 million cells/mL cell suspension are employed as operation parameters with TissueFlex®, still stands.

Moreover, the model considers glucose consumption at zero-order, independent of glucose concentration and cell growth rate. This, again, is an idealisation, which served this study as the model was developed to investigate bioreactor performance at full capacity. These simplifications, although they further restrict the model to the particular conditions listed in *Methods*, do not impact the aforementioned conclusions reported in this chapter. Still, the model must be advanced with components such as a concentration dependent consumption, growth dependent consumption, variable consumption rates at the different expansion and differentiation stages, etc. to be able to make more generally applicable predictions. Furthermore, the investigation relied on media which are generally categorised as containing low glucose concentration (1g/L) and high glucose concentration (4.5 g/L). High glucose concentration is generally associated with induction of apoptosis within growing cells or impairment of function,[204] especially the pancreatic β-cells.[205] For example, in rats, high glucose induces cellular senescence, whereas reduction in glucose amounts to increased proliferation and increased number of colony forming units.[206] However, high glucose concentrations, both short- (4 days) and long-term (4 weeks), tend to have no (short-term) or little (long-term) impact on the proliferation of hMSCs.[207] Even a putatively toxic glucose concentration – 7.2 g/L – has, overall, no impact on cell viability or proliferation (both in the short- and long-term). In fact, shot-term exposure was associated with inhibitory effect on apoptosis.[207] In the absence of relevant experiments (where concentration >7.2 g/L were tried) it is difficult to put a cap on glucose concentration deleterious to viability and

proliferation of hMSCs. As such, the concentrations of glucose utilised in this investigation can be safely assumed to promote hMSC viability and proliferation.[207]

Finally, through this investigation the performance of the bioreactor system operating at maximum capacity in providing optimal mass transport to sustain cell growth was being evaluated. This meant the model considered constant permeability, in a worst-case-scenario approach (regarding resistance, supply to the cells and consumption). The assumption of fixed permeability and porosity, however, is another limitation of the model. This will not be the case physically as both will vary due to scaffold degradation and deposition of matrix by the growing cell population. This is a non-trivial set of processes to incorporate within any model, scaffold degradation and matrix deposition will have opposing impact on permeability, which needs to be experimentally evaluated. This, however, does not influence the results presented here with respect to transport of glucose, for the boundary conditions assumed the maximal loading state, and, thereby, minimal permeability, that the same system would eventually evolve to *in vitro*.

The parameters considered in this analysis were based on their practical utility. For example: the shape and dimensions of the bioreactor were based on the wells of a 96-well cell culture plate, concentration of glucose based on a commonly available nutrient medium, the choice of scaffold material, morphology, and dimensions were based on ease of preparation, and cell phenotype on the more widely employed cell types because of their robustness, plasticity, and ease of availability. As such, the results can be applied as a guide while setting up culturing experiments for cells where cell expansion may be desired over shear-dependent differentiation. Furthermore, the evidence that low media inlet rates can lead to higher shear by varying bioreactor configuration proves how CFD can be employed to design bioreactors to expose cells to physiologically relevant shear at laminar flow rates.

3.5 SUMMARY

Investigations presented in this chapter aimed to evaluate the efficacy of CFD as a robust analytic and design tool. CFD was, therefore, utilised to simulate flow and transport within the TissueFlex® microbioreactor to determine their impact on hMSC expansion. The default recommended configuration and operational parameter ranges of the TissueFlex® microbioreactor were found to be suitable for cell survival and expansion. Furthermore, the data revealed that if mechanical conditioning is of interest the *top-inout* configuration (after optimising the culture media delivery rate) can potentially be utilised to induce physiologically neutral shear stress at construct surfaces while at the same time maintaining laminar flow. This finding, accessible only via computational modelling further demonstrates the capability of CFD as a design optimisation tool. Despite the fact that the methodology captures the continuous phase of a given biological system with high fidelity, it, however, cannot be used to capture the interactions based evolution of a cellular system, due to reasons discussed previously, for which recourse to the discrete paradigm is suggested. This is due to the underlying assumption of component homogeneity. The model, and the approach, however, can still be employed to develop a framework that can simulate the dynamic relationship between cells, their environment, as well as mass transport (discussed in Chapter 5) – but only as the modality that accounts for the physicochemical aspects of a biological system. In the next chapter, the author presents and explores a computational paradigm that offers realistic representation formalism for modelling the entire array of biological behaviours.

4 CHAPTER

An Agent-based model of in vitro Intramembranous Osteogenesis

In Chapter 3, a CFD methodology – solving Navier-Stokes equations via the Finite-Volume formulation – was utilised to model the impact of bioreactor hydrodynamics on the expansion of a mesenchymal stem cell population. The investigation, of commercial interest, also displayed the significance of CFD as a design optimisation tool. However, as discussed in Chapter 2, the formulation cannot be applied without assuming system homogeneity. As such, the methodology cannot be used to quantify cellular behaviour, its impact on microenvironment, and vice versa. The overarching aim of this chapter is to present the technique of agent-based modelling (ABM) as suited to the task of quantifying cellular behaviour. Here, the Flexible Large-scale Agent-based Modelling Environment, an agent based platform, is used to create a novel validated 3D model of in vitro osteogenesis to determine the mechanism of osteoblast differentiation within intramembranous condensations. Images and certain sections have been reused under the ***Open-Access License.***[xviii]

4.1 INTRODUCTION

Capturing the dynamism that pervades biological systems requires a computational approach that can accommodate both the continuous features of the system environment as well as the flexible and heterogeneous nature of component interactions. This presents a serious challenge for the more traditional mathematical approaches that assume component homogeneity to relate system observables using mathematical equations. While the homogeneity condition does not lead to loss of accuracy while simulating various continua, it fails to offer detailed solutions when applied to systems with dynamically interacting heterogeneous components. As the functionality and architecture of most biological systems is a product of multi-faceted individual interactions at sub-system level, continuum models are challenged to offer much beyond qualitative similarity. Agent-based modelling is a class of algorithmic computational

[xviii] The work presented in this chapter appeared as: *Kaul H, Hall BK, Newby C, Ventikos Y. Synergistic activity of polarised osteoblasts inside condensations cause their differentiation.* ***Scientific Reports****, 2015, 5: 11838.*

approaches that relies on interactions between agents to simulate, from the bottom-up, macroscopic properties of a system. In recognising the heterogeneity condition, they offer suitable ontologies to the system components being modelled, thereby succeeding where their continuum counterparts tend to struggle. Furthermore, being inherently hierarchical, they are quite amenable to coupling with other computational paradigms. In this chapter an investigation into the dynamics of osteoblast differentiation within intramembranous condensations is presented, which is aimed to fulfil the objective of this chapter: to simulate a 3D morphogenetic phenomenon with implications in the TERM context. The 3D agent-based model provides novel insights into a long standing question in bone morphogenesis: how do osteoblasts differentiate into osteocytes? The results presented herein open an alternative path for the development of novel approaches aimed to treat skeletal defects of development, repair, and remodelling. The model itself promises to play a key role towards the design, optimisation, and testing of ways to stimulate and/or enhance osteogenesis.

As discussed in Chapter 2 and in the following section (§4.2.1), the discrete paradigm has been utilised to model pattern formation,[116,208] osteogenesis,[209] chondrogenesis,[210,211] angiogenesis,[113] epithelial renewal in skin,[212] ureteric bud branching in kidney,[117] and limb formation.[115] Osteogenesis was chosen as the subject of this investigation as it scored heavily on the following criteria: (i) ease of model development due to availability of biological and computational literature; (ii) rapid translation of model conclusions to bench, and (iii) experimental/commercial exploitability of the exemplar. On each account, especially considering the time constraints associated with the thesis, osteogenesis performed better. For example, although the feasibility of growing microvascular networks *ex vivo*, including models that generate features of the *in vivo* vascular microenvironment with fine resolution, has been demonstrated in a number of recent investigations,[213-216] these models ideal are distant from the ideal scenario of employing the developing vasculature to construct a fully

functional multicellular tissue structure. Considerable advancement, however, has been made in developing osteogenic (as well as chondrogenic and epidermal) structures *in vitro*, relatively speaking. Furthermore, the amount of developmental and evolutionary literature published on osteogenesis, especially on the subject of osteoblast differentiation made it an obvious contender for this investigation. Chondrogenesis, as such, was not considered. However, given that the two processes share quite a few steps, the model presented can be easily altered and optimised to simulate chondrogenesis. Developing an epidermal model, as it did not score very heavily on criterion (iii) and the lack of expertise within the group on this topic, was, therefore, also disregarded.

4.2 THE CONTEXT

The last few years have witnessed a global surge in the number of patients receiving bone defect repairs with associated costs expected to exceed $5 billion by the year 2020.[217] The rapidly burgeoning field of bone tissue engineering is expected to reduce the bulk of this burden by developing constructs that will enhance bone repair and regeneration.[218] Bone tissue engineering relies on exploiting the principles of bone development, which regulate the *decision-making* and *executive* events observed, initially, during embryogenesis and, later, in the form of regeneration. An essential feature of the template followed, observed as the decision-making event during osteogenesis as well as development of other mesenchymal structures, is the formation of *condensations*, which are considered as the fundamental unit of morphological change in organogenesis during vertebrate evolution.[219] Condensation is defined as cellular aggregates that result in the formation of more specialised tissues either during embryogenesis and/or regeneration, and is a product of epithelial-mesenchymal interactions. Hall and Miyake[220] identify condensation as a multi-step process involving initiation, establishment of boundary conditions, cell adhesion,

proliferation, growth, and cessation of growth. The foregoing series of events in turn *facilitate regulation of genes*[220] for either chondrogenesis, which can be replaced by bone (as occurs during *endochondral* ossification where the initially formed cartilage is replaced by bone), or osteogenesis (as occurs during *intramembranous* ossification)[221]. Condensation maturation is, eventually, followed by the differentiation of precursor cells into an osteoblastic lineage, deposition and mineralisation of osteoid, and the terminal differentiation of osteoblasts into osteocytes – collectively, the *executive* event.

In endochondral ossification the mesenchymal cells differentiate into cartilage, which is gradually replaced by bone. This process of osteogenesis initiates prenatally and forms compact bones. Endochondral ossification is divided into five stages: (i) mesenchymal cells, instructed by paracrine factors released by nearby cells, commit to differentiating into cartilage cells; (ii) committed cells condense into compact nodules and differentiate into chondrocytes; (iii) chondrocytes proliferate rapidly, while also secreting cartilage-specific extracellular matrix, to form the model for the bone; (iv) chondrocytes terminate proliferation and increase their volume to turn into hypertrophic chondrocytes, which alter their matrix production to make it mineralised; and, finally, (v) the invasion of the cartilage by blood vessels, apoptosis of the hypertrophic chondrocytes (providing the space for bone marrow), differentiation of cells surrounding the cartilage model into osteoblasts that deposit bone matrix on the partially degraded cartilage, and the eventual replacement of cartilage by bone.[222] In intramembranous ossification, mesenchymal tissue is directly converted into bone forming flat bones of the skull, which are immature at birth with ossification continuing postnatally. During intramembranous ossification mesenchymal cells proliferate and condense into nodules. Some of these cells develop into capillaries and others transform into osteoblasts. Osteoblasts secrete a collagen-proteoglycan matrix, referred to as osteoid, which can bind with calcium salts resulting in

mineralised matrix. The osteoblasts that get trapped within the calcified matrix differentiate into osteocytes, i.e. bone cells.[222]

Whether endochondral or intramembranous, the mechanics of bone development – especially condensation, its impact on bone deposition, and the subsequent formation of osteocytes – are poorly understood.[17] Thirty five years ago, Knese[223] hypothesised osteoblast entrapment within osteoid (secreted either by the cell itself causing self-entrapment or by neighbouring cells) as responsible for triggering their differentiation into osteocytes. In the years that followed, Ham and Cormack[224] suggested that (i) pre-osteoblasts located within condensations deposit osteoid in all directions; Bloom and Fawcett[225] and Ferretti *et al*.[226] opined (ii) non-selective deposition of osteoid due to random orientation of polarised osteoblasts; Romer[227] and Windle & Nonidez[228] implicated (iii) synchronised activity of polarised osteoblasts; and Palumbo *et al*.[229] and Nefussi *et al*.[230] proposed (iv) termination of osteoid deposition as the potential mechanisms responsible for the differentiation of osteoblasts into osteocytes. The aforementioned viewpoints, building further on the entrapment hypothesis – (i), (ii) implicating self-entrapment whereas (iii), (iv) entrapment due to activity of neighbouring cells – are predicated on osteoblast polarity, which in influencing the direction of osteoid deposition regulates osteoblast entrapment. Franz-Odendaal *et al*.[17], in the most complete and detailed review on the subject, further elucidated the entrapment hypotheses and outlined, based on the work of the aforementioned investigators, four mechanisms (Figure 4.4), by which osteoblast entrapment can occur. They are as follows:

1. Osteoblasts are apolar and deposit osteoid in all directions. They, therefore, become 'buried' in their own osteoid;

2. Osteoblasts can be polarised, and polarity is a property of individual cells. As such, each polarised osteoblast secretes osteoid in one direction only, causing self-entrapment;

3. Multiple osteoblasts can be polarised in the same direction, and polarity is a property of a cellular layer. Therefore, new osteoblast generations (or layers) bury their preceding counterparts; and, finally,

4. Multiple osteoblasts can be polarised in the same direction, but certain osteoblasts in each layer slow down their rate of, or stop, osteoid deposition, thereby undergoing entrapment due to activity of neighbouring osteoblasts.

The manner in which the cells' organisation,[227,228], or lack thereof,[225,226] contributes to their (self-) entrapment, and subsequent differentiation, remains unclear. Clarity on the mechanics of osteogenesis, especially from a quantitative perspective, is crucial to enable the design and development of more robust and optimal bone tissue engineering strategies. As an example, understanding the dynamics governing osteogenesis can help develop more precise culture methods and cellular therapeutics targeted to particular stages of bone development, fracture healing, and correction of segmental defects. Quantified understanding will also assist in determining the optimal number of relevant cells required in a tissue engineered graft to be employed to treat growth deficiencies and/or augment bone density around a foreign implant. Moreover, in quantitating the initiation of mineralisation and osteoblast recruitment, interventions to augment osteogenesis in osteoporosis can be further developed and/or optimised. Furthermore, clarity on the mechanics of osteogenesis is crucial also, as many skeletal abnormalities and syndromes have their origin in cellular condensations[231] and deviation from the normal mechanism of osteoid deposition. Finally, a quantitative understanding of mesenchymal condensation, in addition to providing insights

into the foremost stage of bone development, will inevitably provide foray into the process of mesenchymal condensation and, thus, mesenchymal organogenesis.

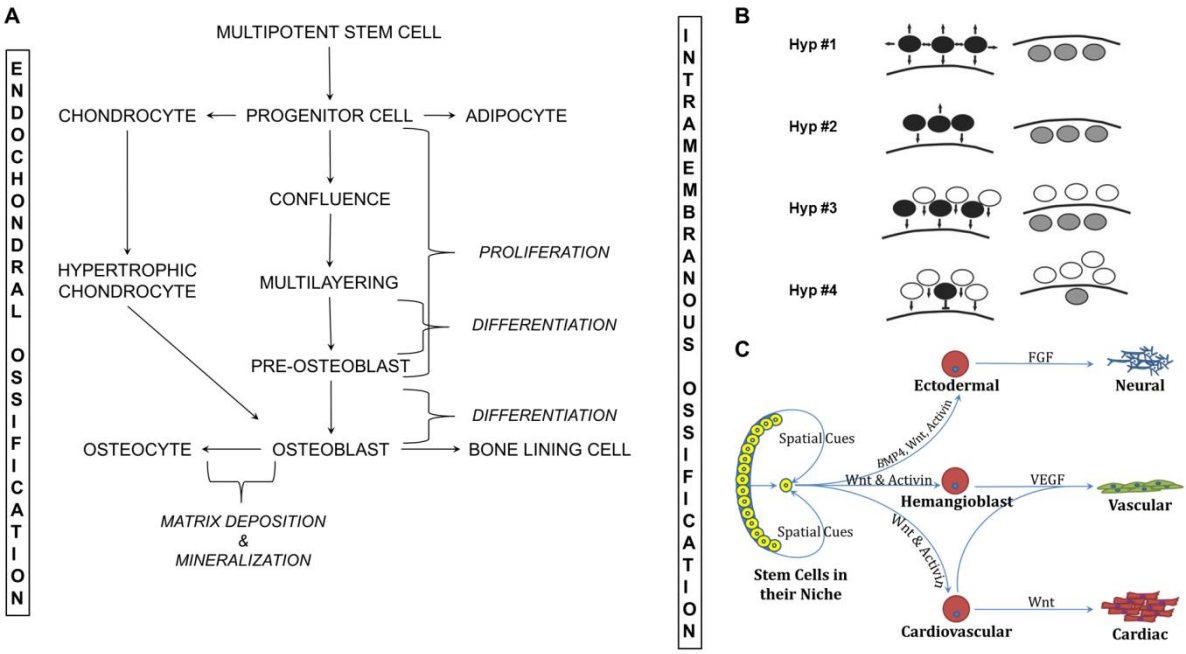

Figure 4. 1: Osteoblast differentiation pathway, the underlying mechanisms, and the ontological relevance of 'agents' to cells. (A) represents the list of events and differentiation pathways that progenitor cells undergo before transitioning into osteoblasts and, eventually, osteocytes. Of relevance to this investigation are events displayed in the centre, in which bone forms through intramembranous ossification. In endochondral ossification, the alternative pathway, hypertrophic chondrocytes have been indicated to differentiate into osteoblast-like cells. The figure was adapted from *Ref. 232*. In **(B)**, the possible ways (hypotheses #**1-4**) of matrix deposition by osteoblasts, as presented in *Ref. 17*, are shown. The left column represent the situation before osteoblasts are trapped within the matrix. The arrows represent the direction of matrix deposition by osteoblasts. Black shaded cells represent the cells that will be entrapped within the matrix and the solid line represents the bone surface. The grey shaded cells in the right column indicate former osteoblasts that turn into osteocytes. **(C)** Agents are computer programs that are capable of detecting local information and initiate decision making based on a set of rule-set attributed to them at discrete time steps. In that sense, they act very much like a biological cell. In this frame, a parallel between an agent and a cell is shown. Based on the incoming cue (signalling molecule, architectural constraint, mechanical conditioning, etc.) both the agent and the cell end up changing their 'state' (to chemotaxis or differentiation, etc.), producing an output signal (autocrine or paracrine), and updating their memory (i.e. the new differentiated state, etc.). ***(B)*** *was reproduced with kind permission from Ref.* 17 © *(2005) John Wiley and Sons.*

In this chapter, using intramembranous osteogenesis as an exemplar, the author aims to shed light on the mechanics of bone formation. However, observing (one or all of) the hypothesised mechanisms in operation experimentally is almost impossible due to inherent logistical and technical issues. These include the dynamic nature of osteogenesis and the

developmental complexity of condensations, which provide the cellular resource from which individual skeletal elements arise. Furthermore, as these hypotheses represent a collage of periodic static snap-shots of osteogenesis, they provide little insight into the initial and boundary conditions required to initiate, observe, and assess the validity of each mechanism. A computational strategy is a useful investigative approach for cases such as this, where either suitable experimental techniques/apparatuses do not yet exist; or the level of complexity associated with the system under observation makes it difficult to design as well as conduct experimentation; or the enormity of experimental data necessitates algorithms to link data existing across a variety of hierarchical levels to assess the complexity of the system. The approach allows for comparison of alternative hypotheses continuously over long periods inexpensively, making them ideal for studying dynamics of biological organisation.[212] As the process of condensation initiation and growth, matrix deposition, and osteoblast differentiation in general, especially as presented in the hypotheses, all have spatial and interactional context to them, agent-based modelling[233] was employed to (i) simulate the process of condensation formation and osteoid mineralisation, (ii) evaluate the hypotheses in terms of their ability to capture the differentiation of osteoblasts into osteocytes, and (iii) investigate parameters related to osteoblast recruitment and osteoid synthesis that have been implicated in pathological eventualities, such as osteoporosis.

4.2.1 THE COMPUTATIONAL LANDSCAPE

Garfinkel *et al*. (2004)[208] modelled the self-organisation of vascular mesenchymal cells (VMCs) by a 2D model of morphogen interaction in a reaction-diffusion process, first proposed by Turing.[234] The reaction-diffusion partial differential equations capture pattern formation, such as condensation, by modelling the interactions of activators and their inhibitors. Garfinkel and co-workers hypothesised bone morphogenetic protein-2 (BMP-2) as the activator and matrixcarboxyglutamic acid protein (MGP) as the inhibitor for their *in*

vitro VMC culture. A system of partial differential equations were developed by the investigators to represent interactions between BMP-2, represented as *U(x, y)*, and MGP, represented as *V(x, y)*, which were informed by reaction kinetics as observed *in vitro*.

$$\frac{\partial U}{\partial t} = D(\nabla^2 U) + \gamma\left[\frac{U^2}{(1+kU^2)V} - cU\right] \quad (4.1)$$

$$\frac{\partial V}{\partial t} = (\nabla^2 V) + \gamma(U^2 - eV + S) \quad (4.2)$$

In equations (4.1) and (4.2), the effective concentrations of the activator and inhibitor evolve based on dimensionless variables $D = D_U/D_V$ – the ratio of the diffusion coefficients of the activator and inhibitor and γ – the factor that relates the chemical kinetics, spatial domain size, and the diffusion rates. The autocatalytic impact of the activator on its concentration can be observed in (4.1), which uses the sigmoidal form $U^2/(1+kU^2)$ to account for autocatalysis saturation. The presence of inhibitor in the denominator accounts for the inhibition. In (4.1), the (first-order) degradation of the activator is modelled with the decay rate of *c*. In (4.2), the presence of U^2 accounts for the "*greater than linear*" impact of BMP-2 on MGP expression, *eV* accounts for first-order degradation of the inhibitor at rate *e*, and *S* accounts for an exogenous source of inhibitor. The model was able to robustly predict how changes in activator/inhibitor concentration and chemical intervention (the investigators treated their cell culture with *Warfarin*, which partially blocks the inhibitory action of MGP on BMP-2) will lead to changes in patterns.

Kiskowski *et al*. (2004)[210] utilised the lattice based approach to investigate chondrogenic condensations by integrating the rule-based approach with a reaction-diffusion model. Their model allowed for cell movement, cell-matrix adhesion, and a very basic activator-inhibitor coupled reaction-diffusion. In the model, transforming growth factor-β (TGF-β) acted as the activator (represented as *A*) and a *lateral inhibitor* of

condensation acted as the inhibitor (represented as *B*). Just like the model proposed by Garfinkel and co-workers,[208] *A* autocatalysed its own synthesis, stimulated production of *B* at low-levels, and diffused at a slower rate than *B*. *B*, on the other hand, inhibited *A* and underwent a decay following its inhibitory activity. These interactions are captured by the following equations:

$$\frac{\delta C_A}{\delta t} = \varphi_A(n_c) - \beta_A C_B \tag{4.3}$$

$$\frac{\delta C_B}{\delta t} = \varphi_B(n_c) - {}^{\Delta C_A}/_{C_B} \tag{4.4}$$

where, n_c represents the number of cells, *C* the concentration of *A* and *B*, and ΔC_A the change in concentration of *A* due to inhibition. In (4.3) and (4.4), φ is a step-function that accounted for the concentration-dependent production of *A* and *B* (both on the concentration of *A*), which is shown below:

$$\varphi_A = \begin{Bmatrix} (\alpha_A C_A), if\ (\alpha_A C_A) < A_{max} \\ A_{max},\ \ if\ (\alpha_A C_A) \geq A_{max} \end{Bmatrix} \tag{4.5}$$

$$\varphi_B = \begin{Bmatrix} (\alpha_B C_A), if\ (\alpha_B C_A) < B_{max} \\ B_{max},\ \ if\ (\alpha_B C_A) \geq B_{max} \end{Bmatrix} \tag{4.6}$$

where, α_A is an arbitrary parameter > 0 that influences the autocatalytic synthesis of *A*; A_{max} and B_{max} the maximum concentrations of *A* and *B* that a cell can produce. Inhibition of *A* by *B* occurs in proportion to another arbitrary parameter $\beta_A > 0$, which indicates the strength of inhibition. Following the update of morphogen concentrations, each cell created a substrate adhesion molecule (SAM), if the concentration of *A* exceeded a certain threshold A_t. Diffusion of SAM was also incorporated within the model though to neighbouring nodes. Increase on the amount of SAM had an inhibitory impact on cell movement, which could be trapped within a certain area. This was modelled as a probabilistic event. These set of equations was integrated with the CA model via the following developmental model:

- *Cells migrate randomly with a constant diffusion rate unless their environment, with respect to SAM, alters*
- *All cells produced A, which stimulated cells to produce more of it*
- *Cells in incipient condensation produced B*
- *A induces cells to produce SAM*
- *Cell motility was impeded in domains with elevated SAM concentration*

In the model, uniformly distributed cells on the lattice produced activators, which stimulated cells to up-regulate activator and inhibitor production. Once a critical amount of activator was deposited, cells produced substrate adhesion molecule that impeded cell movement. Despite the simplifications the model was successful in reproducing the patterns and spacing of pre-cartilage condensations. The model also proved useful in studying the impact of relevant parameters on these patterns; for example, decreasing the initial cell density resulted in increased spaces within the condensations (also an empirical observation).

The model, however, had certain limitations, which included lack of correspondence between experimental and temporal scales, omission of the combined impact of other cell adhesion molecules, and a single scale for both the cells as well as morphogen "units".[211] The model was refined by Christley *et al*. (2007)[235] who combined substrate adhesion with reaction-diffusion. Their advancement included modelling cells and the cells' molecular products (i.e. the morphogens and the extracellular matrix molecules) at different scales (a more appropriate choice), attributing condensations to 'rounding up' (in shape) of cells rather than their movement, and adding the observation that cellular movement rate increases (despite their accumulation) in regions of cell-ECM adhesive interactions. The investigators achieved this by modelling a single cell as an extended object occupying multiple grids (7 for normal, and 5 for 'rounded' cells ready to condense) and increasing cell 'diffusion' rate in response to fibronectin (the cell SAM). The basic structure of the reaction-

diffusion equations was the same as described for Kiskowski and co-workers.[210] Cell behaviour, molecular dynamics, and fibronectin production were integrated into a simulation code through the algorithm shown in Box 1.

For each iteration
Generate a randomised list of agents
For each agent
Undergo migration (probabilistic)
Undergo shape change
End
Calculate the concentration of the activator and inhibitor
Determine if any cells have reached threshold for differentiation
Calculate fibronectin production
End

Box 4. 1: Algorithm utilised by Christley and co-workers to integrate cell behaviour, molecular dynamics, and fibronectin production.

In addition to being biologically more relevant, the model identified two distinct parameter regimes of behaviour depending upon the rate of chemical reactions. Slow reaction rates led to stable morphogen peaks, whereas fast reaction rates led to oscillatory peaks. The latter proved more stable with respect to changes in parameters. Experimental data indicating oscillatory response to TGF-β was pointed as evidence for the existence of oscillatory regimes observed in the simulations.

Employing a different methodology – that of cellular potts modelling (CPM) – Zeng *et al*. (2004)[116] investigated whether substrate adhesion independently can account for chondrogenic patterning. They modelled cells, like Christley and co-workers, as extendable, multi-pixel objects and focused on the role of TGF-β as an up-regulator of fibronectin. The investigators, based on observations that implicated cell attachment to the ECM as well as enhanced cell-cell adhesion as sufficient to promote condensation, devised the model to test if a simpler mechanism could account for biological, and in particular chondrogenic, patterning. The CPM *Hamiltonian* – modified from equation (2.55) – employed in the model is described in equation (4.7).

$$H = \sum_{(i,j),(i',j')} J_{\tau,\tau'}(\sigma(i,j),\sigma(i',j'))\{1-\delta_{\sigma(i,j),\sigma(i',j')}\} + \sum_{\sigma} \lambda_A(\tau)(A(\sigma)-A_t(\tau))^2 + \sum_{(i,j)} \mu(\tau)C_f(i,j) \quad (4.7)$$

In equation (4.7), as in equation (2.55), the first two terms account for (i) surface adhesion energy between cells and between cells and their environment – the investigators employed 20 fourth nearest neighbours, and (ii) a cell's resistance to compression. The third term, added by the investigators in this case, which reflects the flexibility and ease of implementation of CPM, captured the preferential attachment of cells to fibronectin. In (4.7), $C_f(i, j)$ represents fibronectin concentration at the site (i, j), and $\mu(\tau)$ the strength of fibronectin binding. Additionally, an assumption was made that all cells possess the same value of μ, and that the energy of a cell decreases by $\mu C_f(i, j)$ if it occupies a pixel previously occupied by medium (and increases by the same factor if the reverse is true).

The model showed that pattern formation can indeed be obtained with a density-related mechanism independent of the Turing approach. In their model, the instability arose from positive feedback in fibronectin production: cells stayed longer in regions with fibronectin, became more adhesive, and produced more fibronectin until cells stick closer and cluster could not coalesce any more. The model robustly reproduced certain experimental observations, such as the dependence of patterns on the initial cell density.

Osteogenesis has been also investigated by a range of continuum methods, albeit in the context of fracture healing, which progresses due to activation of regenerative pathways that recapitulate aspects of pre- and post-natal bone growth.[236] There exist a plethora of mechanoregulatory models that simulate osteogenesis in the form of regeneration, modelling, or remodelling.[237] Lacroix and Prendergast[238] discuss tissue differentiation patterns during fracture healing of long bones. The authors were working with the hypothesis

that fluid flows in combination with the shearing strain regulate tissue differentiation within the fracture callus. They developed a finite-element model where tissues were represented as biphasic materials with solid and fluid components, which worked with a regulation algorithm proposed previously by Prendergast *et al*. (1997).[97] According to the algorithm, high levels of biophysical stimuli prompted differentiation into the fibroblastic phenotype, intermediate levels into chondrocytic phenotype, and low levels into osteoblastic phenotype. The model considered resorption to be dependent upon the decrease in strain *and* fluid flow, and also considered cellular proliferation and differentiation. Various gap sizes and loading magnitudes were simulated confirming the working hypothesis of the investigation. A shortcoming of these mechanoregulatory models is that they do not consider biological mechanisms or the impact of mechanical cues on biological mechanisms (and vice versa). A more complete picture emerges with *bioregulatory*[157] models, which simulate bone regeneration as directed by biochemical cues (i.e. growth factors and precursor cells), and hybrid mechano-/bio-regulatory models.

The model proposed by Bailon-Plaza & van der Meulen (2001)[236] is a case in the point. It captures the impact of growth factor on intramembranous and endochondral ossification observed during bone healing. Their model relied on seven biochemical factors: (i-iii) density of cells (mesenchymal, chondrocytes, and osteoblasts); (iv-v) growth factors (chondrogenic and osteogenic); and (vi-vii) extracellular matrix (cartilaginous and bone). This diversity of variables allowed the investigators to capture a wide range of cellular behaviours: proliferation, migration, differentiation, growth factor production, as well as ECM synthesis and degradation. The densities of cells change due to migration (mesenchymal only), proliferation, differentiation, endochondral replacement (mesenchymal cells only), and apoptosis (osteoblasts only); whereas changes in matrix density occurs as a result of synthesis and degradation. Changes in growth factor

concentration occur due to a combination of diffusion, production, and decay. The model was mathematically captured by (the partial-differential) equations (4.8) – (4.13),[xix] which were solved using the finite-difference scheme. Intramembranous ossification was modelled as the direct differentiation of mesenchymal cells into osteoblasts due to presence of critical growth factor concentration, and endochondral ossification as localised degradation of cartilage and simultaneous formation of bone, occurring due to the replacement of chondrocytes by osteoblasts under the influence of TGF-β.

$$\frac{\partial c_m}{\partial t} = \nabla.[D\nabla c_m - C c_m \nabla m] + A_m c_m[1 - \alpha_m c_m] - F_1 c_m - F_2 c_m \tag{4.8}$$

$$\frac{\partial c_c}{\partial t} = A_c c_c[1 - \alpha_c c_c] - F_2 c_m - F_3 c_c \tag{4.9}$$

$$\frac{\partial c_b}{\partial t} = A_b c_b[1 - \alpha_b c_b] - F_1 c_m + F_3 c_c - d_b c_b \tag{4.10}$$

$$\frac{\partial m_c}{\partial t} = P_{cs}(1 - \kappa_c m_c) \times (c_m + c_c) - Q_{cd2} m_c c_b \tag{4.11}$$

$$\frac{\partial m_b}{\partial t} = P_{bs}(1 - \kappa_b m_b) c_b \tag{4.12}$$

$$\frac{\partial g}{\partial t} = \nabla.[D\nabla \mathrm{g}] + E_g c - dg \tag{4.13}$$

This framework was later expanded by the same investigators[239] by incorporating the stimulatory and inhibitory impact of mechanical stimulus on ossification. The rate of mesenchyme cell differentiation into osteoblasts, bone synthesis, and chondrocyte

[xix] In equations (4.8) – (4.13), variables labelled c_x, m_x, and g_x represent the cell and matrix densities, and growth factor concentration respectively. The sub-scripts to these, i.e. *m*, *c*, and *b*, refer to mesenchymal cells, chondrocytes, and osteoblasts respectively. Equation (4.1) represents change in the density of mesenchymal cells due to migration, proliferation, and differentiation. D and C represent haptotactic and haptokinetic migration speeds, *m* matrix density, F_1 and F_2 relate cell differentiation to growth factor concentrations. A_m, A_c, and A_b represent proliferation rates; and α_m, α_c, α_b are non-dimensional parameters derived from limiting cell densities. F3 in (4.9), which captures change in density of chondrocytes due to proliferation, differentiation, and endochondral replacement, also relates differentiation to growth factor concentration. In (4.10), which captures change in concentration of osteobalsts due to proliferation, differentiation, and apoptosis, *db* captures rate of apoptosis. Equation (4.11) and (4.12) capture rate of change of cartilage and bone matrix density (respectively) due to synthesis and degradation. Here, P_{cs} and P_{bs} represent synthesis constants; Q_{cd1}, Q_{cd2}, Q_{bd} represent degradation constants, and κ_b and κ_c are non-dimensional numbers capturing the ratio of synthesis and degradation constants. Finally, equation (4.13) represents change in growth factor concentration due to synthesis, diffusion, and decay. Here, D represents the diffusion coefficient of the growth factors, E_g relates growth factor synthesis to growth factor concentration, and d is the decay constant.

replacement and cartilage degradation during endochondral ossification was made dependent upon the local mechanical environment. The finite-element approach was used to determine the strains in the callus. The element's Young's modulus ($E_{element}$) and Poisson's ratio ($\upsilon_{element}$) were calculated based on the element's bone and cartilage density fractions if the element's bone or cartilage density exceeded a certain threshold, as represented by equations (4.14) and (4.15), (mixture's law).

$$E_{element} = \frac{(E_c \times m_{c'}) + (E_b \times m_b)}{(m_{c'} + m_b)} \tag{4.14}$$

$$\nu_{element} = \frac{(\nu_c \times m_{c'}) + (\nu_b \times m_b)}{(m_{c'} + m_b)} \tag{4.15}$$

Here, E_c, υ_c, E_b, υ_b represent the elastic constants for cartilage and bone, and $m_{c'}$ the fraction of connective/cartilage density (m_c) produced by chondrocytes (refer to (4.16)). The model was calibrated by employing well-defined *in vivo* experiments and demonstrated the dependence of successful healing on moderate mechanical loading and adverse effects of insufficient, delayed, or excessive mechanical loading.

$$m_{c'} = \left(\frac{c_c}{c_c + c_m}\right) m_c \tag{4.16}$$

This mechanobioregulatory model, though extensive in terms of the number of agents considered towards ossification, had certain limitations, which included absence of angiogenesis, lack of distinction between cartilagenous and fibrous tissue components of the callus, and a very simplistic treatment of endochondral ossification. These limitations were specifically addressed by Geris *et al*. (2008),[240] who advanced the bioregulatory model developed by Bailon-Plaza & van der Meulen (2001),[236] i.e. equations (4.8) – (4.13), and proposed a more inclusive and complete model of osteogenesis. Geris and co-workers included a description of angiogenesis, separated the description of cartilage and fibrous

tissue, and incorporated chemotaxis as a migratory mechanism (in addition to haptotaxis). Angiogenic effects on ossification were incorporated by adding endothelial cells, vascular matrix, and a generic angiogenic growth factor (c_v, m_v, g_v respectively). The fibroblastic component was incorporated by adding fibroblasts and fibrous tissue density (c_f and m_f resectively). In doing so, the investigators generated a PDE model of "*taxis-reaction-diffusion*". Migration of mesenchymal cells in the model was handled by haptokinetics and a chemotactic response to osteogenic and angiogenic growth factors, and stem cell proliferation was dependent upon the surrounding matrix density. Presence of fibroblasts was accounted for as a result of mesenchymal cell differentiation and migration (modelled by means of a constant diffusion rate). Endothelial cell invasion into the callus was accounted for by random and chemotactic (up the angiogenic growth factor concentration) migration. Matrix production, in the model, was assumed to decrease with increase in the surrounding matrix density. Growth factors were able to diffuse (with constant diffusivity) within the callus. Angiogenic growth factors were produced by osteoblasts and hypertrophic chondrocytes; the production rate being proportional to existing growth factor concentrations.

Intramembranous ossification, in this model, was accounted for by differentiation of mesenchymal cells into osteoblasts in the presence of angiogenic and osteogenic growth factors, as shown in (4.17). Here, F_i is the function relating differentiation to growth factor concentration and which is fed into the modified forms of equations (4.8) and (4.10) in the model proposed by Geris *et al*. (2008)[240]; and Y_1, Y_2, H_1, H_2 are relevant constants.

$$F_i = \frac{Y_1 g_b}{(H_1 + g_b)} . \frac{Y_2 g_v}{(H_2 + g_v)} \tag{4.17}$$

Endochondral ossification was modelled through an initial removal of fibroblasts from the callus and growth factor induced drop in proliferation and a concomitant maturation

of chondrocytes towards a hypertrophic phenotype (the latter modelled by attainment of a certain cartilage density and represented as the first factor in (4.18). Hypertrophic chondrocytes ceased production of chondrogenic growth factors (which drop to zero) but upregulate growth factors that recruit endothelial cells (second factor in (4.18) as well as osteoblasts (second factor in (4.18). The migration of osteoblasts, however, is chemotactic, dependent upon the concentration gradient of the osteogenic growth factor. Following invasion of the callus by osteoblasts, they start producing matrix and are deposited within the matrix and either apoptosed or differentiate into osteocytes (this "removal" was modelled using a constant decay term). In equation (4.18), Y_3, B_{ec}, B_v, and H_3 act as relevant constants. For brevity, only the two most relevant equations were discussed, as the rest are, fundamentally, similar to the original model proposed by Bailon-Plaza & van der Meulen (2001).[236]

$$F_e = \frac{m_c^6}{(B_{ec}^6 + m_c^6)} \cdot \frac{m_v^6}{(B_v^6 + m_v^6)} \cdot \frac{Y_3 g_b}{(H_3 + g_b)} \tag{4.18}$$

Due to the length scale involved, few approaches have been individual-/agent-level based. A simple, yet comprehensive, lattice-based discrete model was proposed by Checa and Prendergast (2009),[209] which, much like the model proposed by Geris *et al*. (2008),[240] integrates mechanical, biochemical, and angiogenic cues to account for ossification. Their approach included coupling the mechanoregulation algorithm proposed by Prendergast *et al*. (1997)[97] with a stochastic lattice-based model capturing cell activity (migration and proliferation based on random walk theory) to simulate tissue regeneration and capillary network formation. The algorithms capturing cell behaviour is shown in Box 2.

Cell differentiation was based on shear strain and fluid/solid velocity, which were determined through a finite-element analysis[97] of the physical domain on which the lattice with (potential) positions for the cells is imposed. The material properties of the elements,

within the finite-element model, are altered as cells undergo differentiation. A rule of mixtures was utilised if an element was occupied by cells of multiple phenotypes. Capillaries were modelled as a sequence of endothelial cells, which could move (depending on their location) randomly with directional persistence and bias. Chemotaxis, here, was modelled by assigning biased probabilities to relocate towards hypertrophic chondrocytes, which were basically mature chondrocytes under mechanical stimulus. Similarly, sprout formation was modelled as a stochastic process, with the probability for sprouting being proportional to segment length. Combination of high shear strain and fluid flow were considered detrimental to capillary formation. The model successfully captured the overall dentritic structures and pattern of capillary network as observe *in vivo*.

Cell Proliferation
Following mitosis, select two positions on the lattice randomly
If the site is occupied, select another site; until both cells have a new site
Continue until both cells are placed or no more sites are available (simulating contact inhibition)
Cell Migration
Randomly select a neighbouring site
If the site is occupied, select again
Continue until no more sites are available
Cell Differentiation
Determine the mechanoregulatory stimulus as per (2.48)
If the stimulus is osteogenic *AND* oxygen concentration is low, then form cartilage
If the stimulus is osteogenic *AND* oxygen concentration is high, then form bone
Oxygen concentration is high, if the cell is within a certain distance (L) from the vessel

Box 4. 2: Algorithm capturing cell behaviour employed by Checa & Prendergast.[209]

Following condensation and ossification, other models and frameworks have been proposed that investigate limb formation, which is, in a way, a summation of the two processes with other morphogenetic phenomena. These include a framework[115] created by integrating the discrete stochastic CPM for capturing cellular behaviour, the continuum reaction-diffusion equations to account for morphogen production and diffusion, and a type-change map for genetic regulation. The framework was employed to model cartilage development as occurs during the embryonic growth of the early stage avian limb bud. Integration across the various modules was achieved by matching the spatial grid for the

reaction-diffusion equations and CPM and defining the relative number of iterations for the reaction-diffusion and CPM evolvers. Like the afore-discussed CPM and reaction-diffusion models, the framework determined activator concentrations, which informed the cells' ability to secrete fibronectin, undergo fibronectin-based haptotaxis, and aggregate with each other. As such, the fibronectin concentration and cell condensation followed activator pre-pattern. The framework was able to simulate both normal and abnormal limb bud development, providing insights into parameters that affect the location and periodicity of skeletal condensations. This integrated framework, and the model, served as the platform towards the development of CompuCell3D,[241] which was discussed in §2.3.3. Boehm *et al*. (2010),[242] on the other hand, utilised a 3D finite-element approach to model limb bud growth. They wished to investigate whether cellular activity crucial for outgrowth is directional or isotropic (the latter meaning lack of orientation). They utilised a modified version of the Navier-Stokes equations to capture movement of the mesenchyme and employed the artificial compressibility method to account for pressure coupling. The investigators altered the continuity equation to allow a distributed material source, which can vary spatiotemporally. The model, complemented with an experimental analogue, suggested that the spatial control of proliferation rate has little influence on morphogenesis and cannot account for distally directed limb bud outgrowth. The model predicted that shape generation must be driven by directional cellular activities (such as migration or intercalation) and that isotropic activity, such as cell proliferation and apoptosis, make little contribution to the major observed shape changes.

The foregoing array of computational methodologies captured processes at the cellular, tissue, and organ levels. The current investigation adds to the list of discrete, agent-based models that have been devoted to capturing the process of osteogenesis at the multi-cellular level, and investigates a major question in bone formation: *How do osteoblasts turn*

into osteocytes?[17] Bone formation, in the computational TERM context, has been modelled using the structural mechanics paradigm, employing the finite-element methodology, quite extensively. The following investigation, however, does not rely on the continuum paradigm, neither fluid mechanics nor solid mechanics, to simulate osteogenesis due to the underlying homogeneity assumption, which does not lend itself to capturing emergent growth patterns that emanate from the heterogeneity observed at the cellular level. Instead the agent-oriented approach is utilised as the process of condensation initiation and growth, matrix deposition, and osteoblast differentiation in general, especially as presented in the hypotheses, all have spatial and interactional context to them. Furthermore, the fact that in ABM a biological system is represented by introducing multiple loci of control[121,243] makes it an intuitive way of capturing biological phenomena, as decision-making is limited to the agent's local situation rather than some external entity's perception of the situation[121] enabling the user to observe a variety of growth and developmental patterns that could not have been predicted *a priori*. ABM achieves this by decomposing the problem in terms of entities that engage in flexible, high-level interactions.[5,121,243,244] A significant benefit of the flexible nature of agent interaction is that the agent decision-making regarding the nature and scope of its interactions can occur at run-time. This allows the user to bypass the need to specify every possible inter-agent link[121] (an impossibility given the levels of the complexity involved).

In this investigation, the model probes the mechanisms underlying matrix deposition by osteoblasts, their burial within this matrix, and their ensuing transformation into osteocytes. While it does not provide an alternative to the ossification models discussed above, which address the process existing at a higher level and scale, the model addresses the gap between the pattern-formation and ossification models, thereby complementing the

progress that has already been achieved by the aforementioned investigators on bone formation.

4.3 MATERIALS AND METHODS

4.3.1 COMPUTATIONAL PLATFORM

The Flexible Large-scale Agent-based Modelling Environment (FLAME), as the name indicates, is an agent-based modelling framework, which allows simulation of large numbers of agents to be run on parallel computers.[245,246] The FLAME framework, which enables creation of agent-based models that can be run on high-performance computers, is based on the logical communicating extended finite state machine (X-machine) theory. This grants more power to the agents and thereby enables the casting of complex models for large complex systems.[246] Agents are modelled as communicating stream X-machines, an attribute that allows them to interact with each other at both the local and global level.

FLAME uses C (in order to specify the functions of the agents) and *extensible mark-up language* (XML), to describe the model: the agents involved, their structure, and the environment they exist in. The resulting XML syntax is known as the X-machine mark-up language, or XMML.[8] A simplified mitosis model specified using a XMML model is represented in Figure 4.2. FLAME uses a simulation program known as Xparser, which parses a model XML definition into simulation program source code. For running any simulation, a simulation package is produced by compiling Xparser (which is a series of compilation files) with the modeller's files. Model descriptions in XML allow easy human and computer readability. FLAME provides the programmer with the freedom to visualise the XML output, after a format conversion, through any visualisation engine. A block diagram of the FLAME files has been presented in Figure 4.3. Describing a system in FLAME involves identifying the agents and their functions, identifying the input and output

messages of each function, and identifying the set of variables (memory) that are accessed by functions.

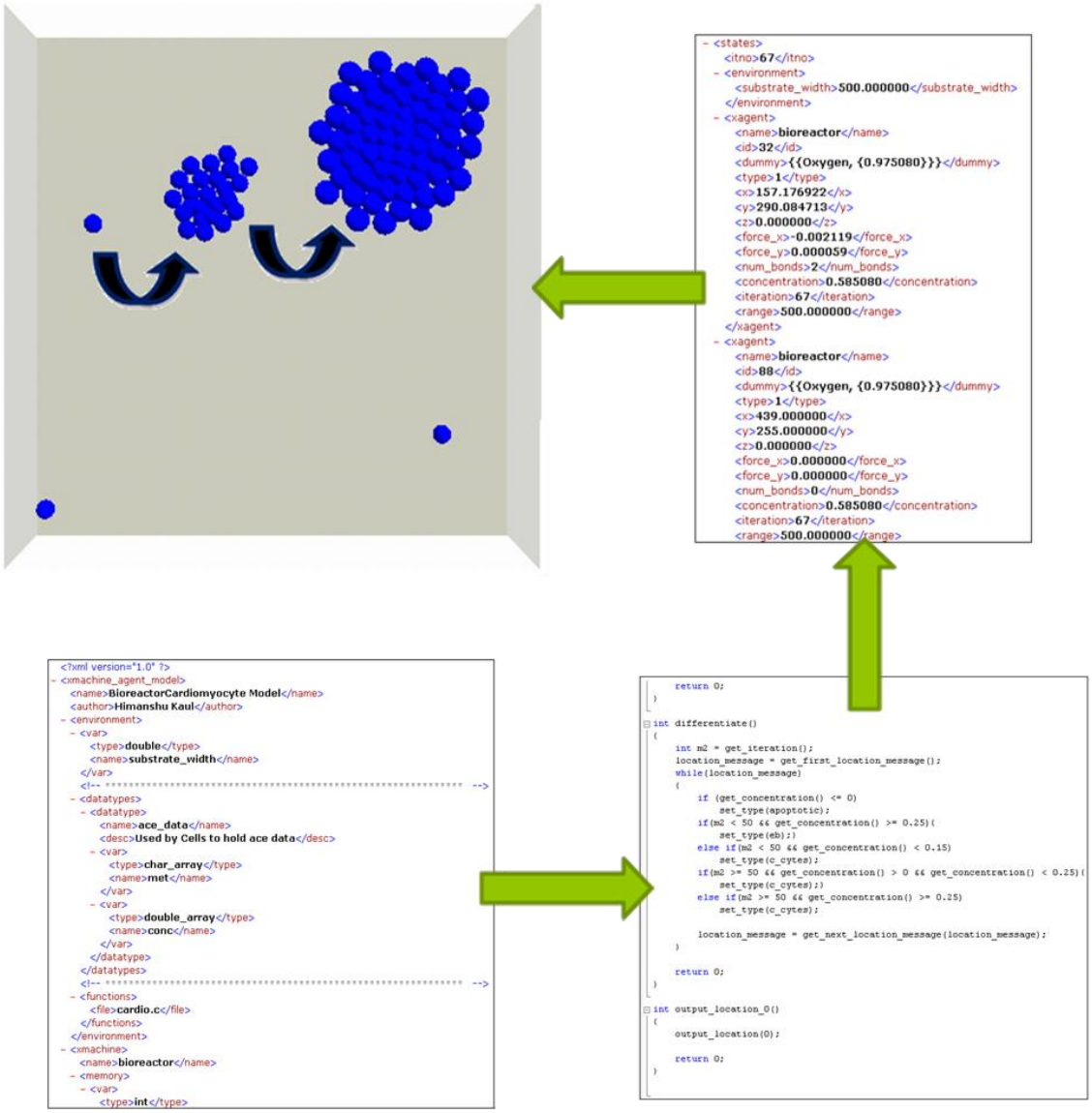

Figure 4. 2: THE FLAME PROTOCOL. Bottom Right: The figure shows an XML mode file. The file contains the whole structure of the model which includes agent descriptions, memory variables, functions, and messages. Top Right: The figure shows a C file that contains the implementations of the functions specified in the xml file. Top Middle: **FLAME** output in the form of a XML file, which could be parsed to obtain the tagged information in any format for additional analysis. The output contains information such as agent coordinates, type, id, concentration, number of bonds formed etc. Left: Visual representation of a set of FLAME simulations (in this case mitosis).

Finally, but perhaps most importantly, FLAME being an open platform, allows communication with a variety of pre-and post- processing tools, as well as with add-on modules that empower it with additional capabilities; these features, together with its

inherent three-dimensional manipulation capabilities make it an obvious choice for accurate biological representations of the types we are interested in.[64,120,245,246]

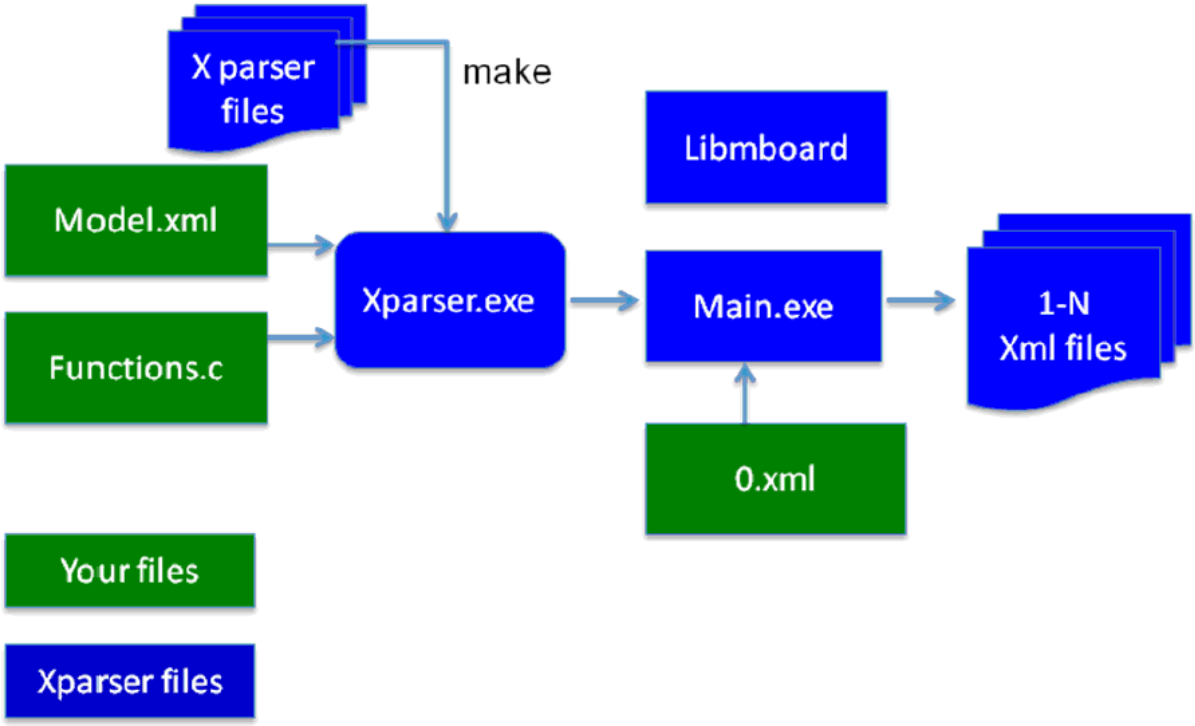

Figure 4. 3: Xparser in action. The figure shows a block diagram of the Xparser. Xparser is the simulation program employed by **FLAME**. Blocks (files) represented in blue are automatically generated, whereas blocks (files) represented in green are provided by the modeller.[246] The figure was reprinted with kind permission from Prof Rod Smallwood.

A model in FLAME consists of three parts: environment, agents, and messages. The environment contains information that may be required by the system but is not part of an agent or a system. This includes global constant variables, the path to the implementation of agent functions in C files, and data type definitions. FLAME allows the user to incorporate user defined data types as well (one of the attributes that made FLAME an obvious choice for this project). An agent type contains information regarding agents such as their names, description, memory, and functions. An agent's memory is its identity. As such, it will contain information likes its coordinates, age etc. Agent functions are defined in a C file and contain information such as the name of the function, the (initial/current) state an agent has to be in for the function to be executed, the state after the function, conditions for function transition, and possible input and output messages. Figure 4.2 shows a XML file describing

a model outlining the three (aforementioned) parts of a FLAME model.[120,246] Figure 4.4 depicts an agent undergoing state transition.

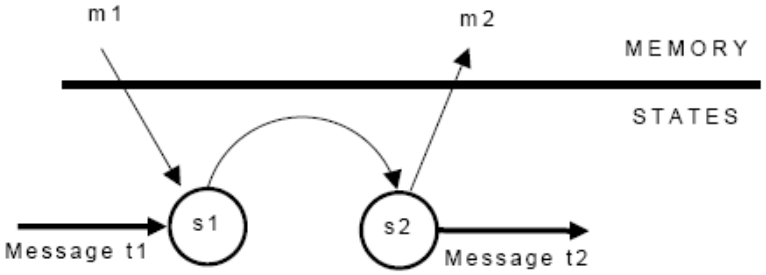

Figure 4. 4: The transition function. Transition functions allow agents to change their current state and modify their behaviour accordingly. Depending on the current state (s1) and memory (m1), and arrival of a message (m1) (all serving as the inputs), an agent changes its state (s2), updates its memory (m2) and optionally sends out a message (t2).[120] The figure was reprinted with kind permission from Prof Rod Smallwood.

4.3.2 AGENTS

The model used the major actors observed in the process of *in vitro* ossification, which include: fibroblast-like, colony-forming, precursor mesenchymal cells; pre-osteoblasts; osteoblasts; osteoid; mineralised osteoid; and osteocytes. To save computation time, other actors such as pre-osteoblastic osteoblasts or osteoid osteocytes were not considered without any effect on simulation outcome. All agents were modelled as non-deformable spheres, 20 μm in diameter. Although the platforms allows for the application of more complex and arbitrary 3D morphologies, the relatively simpler shapes were utilised to keep computational costs of running the model on a single desktop low.

While representing cells as agents was relatively straightforward – each cellular agent corresponded to one cell – computational representation of osteoid was slightly more challenging due to its heterogeneous nature. Osteoid is the unmineralised bone matrix synthesised by osteoblasts that consists of fibrous components (such as type I collagen) as well as ground substances (such as osteocalcin, bone sialoprotein, osteopontin, and chondroitin sulphate)[247]. However, as the set of behaviours explored in this investigation did not depend upon the heterogeneity of osteoid components, fibrous- and protein-based

variations within osteoid were not considered, and an osteoid agent represented an arbitrary amount of homogeneous bone matrix, until it mineralised and turned into a separate agent (mineralised osteoid), as is the case physically.

4.3.3 ENVIRONMENT

Osteoid maturation and mineralisation *in vitro* is usually achieved by growing the cells to confluence in a culture dish followed by the addition of osteogenic factors.[248] As such, the environment used as the backdrop to the aforementioned agents constitutes a culture dish capable of supporting proliferation. The culture dish is assumed to be a 300×300×300 μm^3. The size of the culture dish was limited to reduce computational costs. The nutrient media employed to support cell viability, proliferation, and growth, in order to induce osteogenic fate and mineralisation, are supplemented with adequate levels of either ascorbate, or phosphate esters (e.g. β-glycerol-phosphate), or glucocorticoids (such as dexamethasone), or all of them. The interested reader is directed to a review by Beresford *et al.* (1993)[249] on this topic. The studies quoted in this manuscript relied on static *in vitro* cultures, where the media was exchanged periodically; instead of applying dynamic perfusion. However, as supplement concentrations proved optimal in these investigations, resulting in normal mineralised condensations[250-252] the virtual culture dish was assumed to contain optimal concentration of signalling molecules, growth factors, and hormones promoting ossification.

In the simulations presented here, the centre of this virtual culture dish served as the site of condensation in this model. It must be emphasised that any part of the culture dish can potentially serve as the site of condensation, but the author opted for the centre of the culture dish for visualisation purposes, to fully display the growth, maturation, and mineralisation of the condensation.

4.3.4 RULES

In this novel attempt to use rules, and the agent-based paradigm to capture (intramembranous) osteogenesis through cellular interactions, a very basic set of rules was derived by mining the literature on *in vitro* and *in vivo* osteogenesis manually. Rules assigned to the agents covered the entire spectrum of behaviours displayed by cells and, more specifically, pertained to proliferation, migration, differentiation, and apoptosis. Additionally, the four hypotheses of osteoblast transformation, explored in *Introduction*, were also converted into rules that governed bone deposition. The rules have been summarised in Table 4.1.

4.3.4.1 MECHANICAL PROPERTIES

Forces between the aforementioned agents were resolved by implementing the *explicit* overlap detection and correction scheme. The term explicit implies that cellular displacement was determined based on the previous time step, instead of considering more than one previous time steps. The scheme detected and corrected any cellular overlap that occurred during mitosis and osteoid deposition. Any inter-agent overlap was corrected by applying a repulsive force proportional to the extent of the overlap. The underlying idea was to inhibit cell-cell overlap and, therefore, be able to model confluence dynamically, irrespective of the dimensions of the culture plate (a pervasive observation *in vitro*). The scheme, adapted from the model employed by Adra *et al*. (2010),[245] accounted for the contribution of mitosis and matrix apposition towards condensation growth, and has been mathematically described below. For each iteration, the code checked whether any two neighbouring agents, *i* and *j*, are overlapping, and, in case of overlap, applying a repulsive force $F_{c,ij}$, proportional to the overlap O_{ij}, on the cell *i* by its neighbour *j*.

Activity	*Agent(s)*	*Rule*		*Agent Fate*	*Visualisation*
Proliferation	Precursor	Initiates at the very beginning		Agent divides to produce more daughter agents	Blue Sphere
		The agent divides every 12 hours producing a daughter agent in a randomly chosen direction.			
		The agent cannot divide in the third dimension			
		Stops once confluence has been achieved			
	Pre-osteoblasts	Initiates after confluence		Agent division promote condensation development	
		The agent divides every 12 hours producing a daughter agent in a randomly chosen direction. Time was varied while testing for sensitivity to 12±3, 12±1, and 8 hours.			
		The agent can divide in the third dimension			
		Proliferation continues until the condensation height reaches 90 μm			
Matrix Deposition	Osteoblasts	Initiates once the condensation height reaches 70 μm		Agent deposits matrix that further leads to condensation development. The agent is then entrapped in the calcified form of the matrix to undergo differentiation into an osteocyte	Green Sphere produces Red Cubes
		H#1	Agent deposits matrix randomly in any of the three-dimensions throughout the simulation		
		H#2	Agent, once formed, acquires polarity randomly and continues to deposit matrix in that direction for the entirety of the simulation		
		H#3	Polarity is treated as a property of an agent layer		
			Agents within 20 μm of each other were treated as belonging to the same layer		
			Agents acquired polarity once formed (with condensation height exceeding 50 μm)		
		H#4	Same as H#3		
			Within a certain duration, some randomly chosen agents, less than 2% of the entire population, turn off their genes to secrete matrix		
		Matrix secretion ceases once the condensation height exceeds 110 μm			

Table 4. 1: Agents, rules, and fates. The table lists the agents utilised in this investigation as well as the rules that governed their behaviour. The table also features the agent fate eventuating from the agents following the rules as well as the manner in which this was visualised in the figures presented in this chapter.

Activity	*Agent(s)*	*Rule*	*Agent Fate*	*Visualisation*
Differentiation	Precursor	Initiates after confluence	Agents differentiate into pre-osteoblasts that migrate to the skeletogenic site and initiate condensation development	Blue Sphere remains Blue (except in Figure 4.8B where they were changed to orange to better visualise migration)
		Randomly chosen agents differentiate into pre-osteoblasts		
		Stops once a certain randomly chosen number of agents have differentiated		
	Pre-osteoblasts	Initiates once the condensation height reaches 50 μm	Agent differentiates into an osteoblast that deposit osteoid to further develop the condensation	Blue Sphere turns Green
		The agent must be within the condensation (as such this feature constantly evolves with the condensation), OR		
		The agent is in contact with more than four Osteoblasts		
		Pre-osteoblasts turn into Osteoblasts		
		Osteoblasts can turn back into pre-osteoblasts if they are at the periphery of the condensation		
	Osteoblasts	Initiates once the condensation height reaches 100 μm	Agent differentiates into an osteocyte	Green Sphere turns Black
		The agent, if embedded within or surrounded by calcified matrix (6 matrix agents), differentiates into Osteocyte. In sensitivity analysis, the number of neighbours was decreased to 4.		
		Continues until all osteoblasts have either differentiated or apoptosed		
	Matrix Calcification	Initiates once the condensation height reaches 100 μm	Calcified matrix buries osteoblasts that assist their differentiation into osteocytes	Red Cube turns Grey
		All matrix agents calcify slowly		
Apoptosis	Osteoblasts	Initiates once the condensation height reaches 110 μm	Agent dies and plays no further role in the simulation. The space becomes available to other agents	Green Sphere disappears
		The agent will enter apoptotic cycle if it has not differentiated into an osteocyte at the aforementioned stage		

Table 4. 1 contd.: Agents, rules, and fates. The table lists the agents utilised in this investigation as well as the rules that governed their behaviour. The table also features the agent fate eventuating from the agents following the rules as well as the manner in which this was visualised in the figures presented in this chapter.

The sub-script 'c' stands for the relevant coordinate under consideration (x, y, or z). The repulsive force was calculated as follows:

$$F_{c,ij} = s_{ij} O_{ij} c_{c,i} \tag{4.19}$$

Considering the two agents have radii r_i and r_j (10 µm), and are centred at coordinates (x_i, y_i, z_i) and (x_j, y_j, z_j) respectively, the amount of overlap is shown in equation (4.20).

$$O_{ij} = \sqrt{\left(x_i - x_j\right)^2 + \left(y_i - y_j\right)^2 + \left(z_i - z_j\right)^2} - \left(r_i + r_j\right) \tag{4.20}$$

In equation (4.19), s_{ij} serves as an arbitrary 'stiffness' constant equal to the inverse of the separation between the two agents, refer to equation (4.21), and $c_{c,i}$ represents the damping constant for each co-ordinate of agent i, refer to equation (4.22).

$$s_{ij} = 1 \Big/ \sqrt{\left(x_i - x_j\right)^2 + \left(y_i - y_j\right)^2 + \left(z_i - z_j\right)^2} \tag{4.21}$$

$$c_{x,i} = \left(x_j - x_i\right)\alpha \tag{4.22.1}$$

$$c_{y,i} = \left(y_j - y_i\right)\alpha \tag{4.22.2}$$

$$c_{z,i} = \left(z_j - z_i\right)\alpha \tag{4.22.3}$$

In equations (4.22.1) – (4.22.3), α represents the proportionality constant assigned based on the amount of agent overlap. In case there is no overlap (i.e. $O_{ij} > 0$), $\alpha = 0.06$; but in case of overlap (i.e. $O_{ij} > 0$), $\alpha = 0.4$. The new agent coordinates ($x_{i,t}$, $y_{i,t}$, $z_{i,t}$) are determined by displacing the agent coordinates at the previous time step ($x_{i,0}$, $y_{i,0}$, $z_{i,0}$) by ($F_{x,ij}$, $F_{y,ij}$, $F_{z,ij}$) as shown in equations (4.23.1) – (4.23.3).

$$x_{i,t} = x_{i,0} + F_{x,ij} \tag{4.23.1}$$

$$y_{i,t} = y_{i,0} + F_{y,ij} \tag{4.23.2}$$

$$z_{i,t} = z_{i,0} + F_{z,ij} \tag{4.23.3}$$

The set of equations is based on the collision detection and correction scheme, which calculates the extent of (potential) overlap between spherical non-deformable spheres, and

exerts a repulsive force, proportional to the overlap, on the relevant agents to ensure separation between two agents. The scheme works by deriving location and size of each agent and determining, through (4.20), the amount of overlap between an agent and any of its neighbours. The force exerted on the linked pair of cells is based on this overlap and computed through (4.19). Following the calculation of this force as well as the new agent coordinates, calculated through equations (4.23.1) – (4.23.3), for each linked pair of cells. The solution is fed back into the individual agents. For more information please refer to the original articles from where the scheme was derived.[123,245]

4.3.4.2 PROLIFERATION

In vitro, and indeed *in vivo*, only the precursor colony-forming mesenchymal and pre-osteoblastic cells possess the capacity to proliferate. The remaining cells, i.e. osteoblasts and osteocytes, do not. As such, in the model, only the precursor mesenchymal and pre-osteoblast agents were allowed to undergo mitosis. These agents divided roughly every 12 hours,[253] producing a daughter agent in a randomly chosen direction. The division of mesenchymal agents was limited to forming cells in the same two-dimensional plane; their pre-osteoblastic counterparts were allowed proliferation in the third dimension as well. The division of precursor mesenchymal cells, therefore, resulted in the formation of a monolayer of the initial colony-forming cells, whereas the proliferation of pre-osteoblastic agents led to condensation growth in the third dimension (in addition to growth in the same plane).

Proliferation of these two agents was ‘decentralised’, which means that it was contingent on the environment as a whole. For example, the precursor agents could proliferate until confluence, but once the culture dish became confluent, proliferation discontinued. However, in the event the precursor monolayer lost confluence, due to apoptosis or necrosis, the remaining cells could proliferate to reclaim the available space.

This was achieved by adding the rule that each precursor agent could continue dividing until it achieves a maximum number of precursor neighbours. In computational terms, a non-overlapping agent in the vicinity, i.e. $Oij > 0$ but ≤ 10 μm, constituted as a neighbour. Refer to equation (4.20) for the formula to determine *Oij*. The critical neighbour number was set to *four* for 2D proliferation (north, south, east, west) and six for 3D proliferation (top, bottom, north, south, east, west). The agents could establish neighbourhood with more than four neighbours, due to their vicinity, but they could not divide once the critical number of neighbours was achieved. Furthermore, pre-osteoblast proliferation in the third dimension, in addition to being limited by their neighbours, depended on spatial constraints as well.

4.3.4.3 MIGRATION

Migration is central to condensation formation and is only displayed by pre-osteoblasts *in vivo* (or, to be precise, cells that are no longer the colony-forming precursors but that have not differentiated into osteoblasts). The pre-osteoblasts migrate towards certain focal points to initiate condensation that are pre-determined, due to architectural constraints imposed by the environment. Pre-osteoblast migration was, therefore, considered in the model. For visualisation purposes, the centre of the virtual culture dish served as the focal point towards which pre-osteoblasts migrated. In order to enable migration, each pre-osteoblast agent was assigned speed and directionality relative to the focal point. This was achieved by dividing the culture dish into four quadrants, which determined whether the cellular movement relative to the *x*- or *y*-axis was positive or negative. Assuming the coordinates of the focal point was represented by ctr_x and ctr_y, and those of the migrating (*ith*) agent by *xi* and *yi* (bear in mind that migration only occurred in the same plane), the velocity, with respect to the two axes, was calculated as shown in Table 4.2. Irrespective of their distance from the centre all mobile agents were assigned a constant speed of 0.2 μm/s.

$ctr_x - x_i$	$ctr_y - y_i$	*Velocity_x (µm/s)*	*Velocity_y (µm/s)*
+ve	*+ve*	*0.2*	*0.2*
+ve	*−ve*	*0.2*	*-0.2*
−ve	*+ve*	*-0.2*	*0.2*
−ve	*−ve*	*-0.2*	*-0.2*

Table 4. 2: Pre-osteoblast migration speed and direction. The table shows the manner in which pre-osteoblasts were assigned speed and direction. Only a selected number of precursor cells differentiated into pre-osteoblasts, which depending on their coordinates moved towards the focal point of the culture dish chosen for condensation. Based on their direction from the condensation site, they were assigned a particular velocity. For example, if an agent was on top left of the centre of the culture dish, it was assigned a velocity of 0.2 µm/s to move right and -0.2 µm/s to move down.

Considering ($x_{i,o}$, $y_{i,o}$) represents agent coordinates for the *ith* agent at the previous time step and ($x_{i,t}$, $y_{i,t}$) at the next time step "*t*", the new position of the migrating agent was calculated by:

$$x_{i,t} = x_{i,o} + v_x \Delta t \quad (4.24.1)$$

$$y_{i,t} = y_{i,o} + v_y \Delta t \quad (4.24.2)$$

In equations (4.24.1) and (4.24.2), v_x and v_y represent the velocities in the *x* and *y* directions respectively (refer to Table 4.2), and Δt the advance in iteration ($\Delta t = \Delta iteration = 1$ for all computations). At each iteration, the calculations, shown in Table 4.2, equation (4.24.1), and equation (4.24.2), were repeated to determine agent velocity and displacement. Displacement was, thus, determined explicitly, which means that agent coordinates from only the previous time-step were considered in determining the coordinates for the new time step.

4.3.4.4 DIFFERENTIATION

A multitude of agents undergo differentiation within condensations. These include: precursor agents differentiating into pre-osteoblasts, pre-osteoblasts into osteoblasts, and osteoblasts, finally, terminally differentiating into osteocytes (refer to Table 4.1). The agents representing each of these cells possessed the capacity to differentiate. The precursor agents' differentiation into pre-osteoblasts was stochastic. Only a limited number of precursor

agents differentiated into pre-osteoblasts following confluence. Following condensation growth in the third dimension, only those pre-osteoblasts positioned well inside the condensation (height less than 80 μm and 20 μm away from the periphery) differentiated into osteoblasts. This constraint was imposed to account for the fact that cells exposed at the top of the condensation tend to be pre-osteoblastic in nature and only the ones ensconced within adopt the osteoblastic phenotype.[250] Furthermore, it is these pre-osteoblasts that are recruited following resorption to differentiate into osteoblasts and deposit bone. Finally, osteoblasts surrounded by mineralised osteoid (at least 6 mineralised neighbours covering the osteoblasts) terminally differentiate into osteocytes. Condensation height, which regulated the differentiation of pre-osteoblasts, was quantified by comparing the *z*-coordinates of the pre-osteoblast agents.

4.3.4.5 APOPTOSIS

The osteoblasts within the condensation that that were unable to differentiate into osteocytes underwent programmed cell death, as has been reported elsewhere.[17] This, however, occurred stochastically and only after the nodule had acquired its maximum reported height (110 μm).

Case	Osteoblast Polarity	Osteoid Switch-off	Runs (n)	Computer #
hypothesis #1	Apolar	NA	11	1, 2, 3
hypothesis #2	Stochastic	NA	11	1, 2, 3
hypothesis #3	Layered	NA	11	1, 2, 3
hypothesis #4	Layered	Yes	11	1, 2, 3

Table 4. 3: Hypothesis testing approach. The table lists the mechanisms investigated in this study and the manner in which each treated osteoblast polarity. Each hypothesis was simulated 11 times on three different workstations to ensure the code was insensitive to stochastic variables within the code as well as dissimilar random number generation between different workstations.

4.3.4.6 OSTEOID DEPOSITION: THE FOUR HYPOTHESES

There are four hypotheses, as reported in §4.2, predicated on osteoblast polarity, which seek to explain the process of osteoid deposition and, thus, entrapment mechanism of osteoblasts. Osteoid could be deposited either in a random or a pre-determined direction. This feature is straightforward to incorporate into the model. The following rules for osteoid deposition were employed.

Hypothesis #1: Osteoblasts deposited osteoid in all directions. The direction at any given iteration was determined randomly. The osteoblast agent could alter its direction at any time during its lifetime.

Hypothesis #2: Each osteoblast, after its formation, randomly acquired a direction for osteoid deposition. However, unlike the mechanism represented in hypothesis #1, the osteoblast continued to deposit osteoid in that direction until its differentiation or apoptosis.

Hypothesis #3: Osteoblasts with similar z-coordinate, ±10 μm apart, were considered part of the same layer, and deposited matrix in the same direction. These osteoblasts continued depositing matrix in the same direction until their differentiation or termination. In order to assign 'layer' based directionality, the space along condensation height was discretised into regions (10-30 μm, 30-50 μm, 50-70 μm, and 70-90 μm) each acquiring stochastically determined polarity. Therefore, the polarity eventually displayed by osteoblasts was acquired dynamically at run-time. This reflects the situation *in vivo*, where the osteogenic regions, by virtue of architectural constraints imposed by the environment, transmit to cells, localised within them, pre-determined polarities informed by the presence of nearby structures. This assumption is justified by the fact that cells show awareness of others belonging in the same plane/layer. In addition to cell adhesion molecules (or adhesins), gap junctions, which have been implicated in facilitating intercellular communication,[254] are

responsible for this sensitivity. Cells tend to share more junctions with others on the same plane than with those on a different plane. Details, beyond the scope of this investigation, can be found here.[254]

Hypothesis #4: In this case, osteoblast agents acquired polarity as in Hypothesis #3. Certain number (or population fraction) of osteoblasts, however, switched off their ability to produce matrix for a specific amount of time. A variety of switch-off periods from *indefinite* to *twenty four* hours was tested in this investigation.

Case	Parameter	Classification	Variation	Original	Runs (n)
h3	Original	h3	Original	Original	3
S1	Pre-osteoblast proliferation	Osteoblast Recruitment	12±3 hours	12 hours	3
S2	Pre-osteoblast proliferation		12±1 hours	12 hours	3
S3	Pre-osteoblast proliferation		8 hours	12 hours	3
S4	Matrix surrounding Osteoblasts	Differentiation	4 neighbours	6 neighbours	3
S5	Matrix deposition rate	Osteoid Synthesis	6 hours	18 hours	3
S6	Matrix deposition rate		18±3 hours	18 hours	3
S7	Matrix deposition rate		1 hour	18 hours	3
S8	Matrix deposition rate/Pre-osteoblast proliferation	Osteoblast Recruitment & Osteoid Synthesis	1 hour/18 hours	18 hours/12 hours	3

Table 4. 4: Sensitivity testing on hypothesis #3. The table lists the various parameters altered as part of the sensitivity analysis to determine the features the model was sensitive to. Parameters varied could be divided into four categories listed in the table. Each new model (s1 – s8) was simulated three times.

Osteoid was only deposited by osteoblasts in the model. Computationally, this was achieved by adding a new osteoid agent close to the osteoblast agent based on the coordinates determined by the mechanisms encoded in the aforementioned hypotheses. The manner of osteoid deposition is justified as osteoblasts *secrete* the osteoid across their membranes. The mechanisms involved in secretion are beyond the purview of both the investigation as well as the discussion reported here. Furthermore, the model treated mineralisation stochastically – the 'osteoid' agent had to undergo two *if* loops before

mineralising. Each osteoid agent represented a collection of deposited bone matrix (fibres and proteins). Osteoid heterogeneity was not considered to minimise computational costs.

Case	Population Fraction	Switch-off Period	Switch-off Time (days p.c.)	Computer #	Runs (n)
h4	2%	indefinite	5.75	1	3
t1	2%	2 days	5.75	1	3
t2	10%	1 day	5.75	1	3
t3	2%	1 day	5.75	1	3
t4	30%	1 day	5.75	1	3
t5	10%	indefinite	5.75	1	3
t6	2%	indefinite	5.75	1	3
t7	2%	1 day	4.375	1	3
t8	2%	1 day	6.875	1	3
t9	2%	1 day	7.5	1	3
t10	10%	2 days	5.75	2	3
t11	2%	2 days	5.75	2	3
t12	10%	1 day	5.75	2	3
t13	2%	1 day	5.75	2	3

Table 4. 5: Sensitivity testing on hypothesis #4. The table lists the changes made to the model simulating osteoid deposition based on hypothesis #4. This sensitivity analysis was conducted to determine the parameters hypothesis #4 was most sensitive to. Three basic parameters were tested: 'population fraction' turning of osteoid deposition; the duration of time during which osteoid deposition was 'switched-off'; and the time when this switch-off came into effect. In order to ensure code's insensitivity to inter-computer and intra-code stochasticity, some of the models were simulated on another computer. Each model was simulated three times.

4.3.5 COMPUTATIONAL ITERATIONS AND SENSITIVITY ANALYSES

A total of four models, incorporating the four hypotheses, were simulated in series. Each model was run for 5000 iterations, with one iteration equivalent roughly to 20 physical minutes. Each model was simulated eleven times in total across three different workstations (to account for potentially different arithmetic of random number generations, significant digits, etc.). The workstations had the following operating systems and processors 32-bit Windows XP Professional: Xeon™ Processor, 2.8 GHz; 64-bit Windows 7: Intel® Core™ i7 CPU, 3.33 GHz; and 64-bit Windows 7: Intel® Core™ i5 CPU, 1.6 GHz.

Hypothesis #3, identified as the fittest model, was used to test for sensitivity. Several parameters, related to osteoblast recruitment, osteoblast differentiation, and osteoblast vigour, were varied, which resulted in eight new simulations. Each of these new simulations was conducted three times. Hypothesis #4 was also tested for sensitivity. Parameters that were varied included the population fraction terminating osteoid synthesis, termination period, and condensation age at which the termination period was applied. Overall, thirteen parameters were varied, and each new simulation was conducted three times. Finally, the ability of the virtual condensations to recover from a compromised state was tested. This was achieved by reducing the condensation to a height of 40 μm and observing remodelling governed by each of the four hypotheses (n=3). In order to further test the pathological nature of hypothesis #4, condensation remodelling by employing hypothesis #3 with abnormal osteoblast recruitment and osteoid deposition rate was observed (n=3). The various runs have been summarised in Tables 4.3 – 4.6.

Case	Title	Pre-osteoblast Proliferation	Osteoid Deposition	Runs (n)
h1	Hypothesis #1	12 hours	18 hours	3
h2	Hypothesis #2	12 hours	18 hours	3
h3	Hypothesis #3	12 hours	18 hours	3
h4	Hypothesis #4	12 hours	18 hours	3
r1	Matrix Overproduction	12 hours	1 hour	3
r2	Low Osteoblast Vigour	18 hours	27 hours	3

Table 4. 6: Remodelling following the 'resorption' challenge. The table lists the variables utilised to observe osteogenic remodelling following 'resorption' and necrosis of the mineralised osteoid and osteocytic/pre-osteoblastic cell populations, respectively. Remodelling was investigated using the original four hypotheses (h1 – h4), as well as using (abnormal) hypothesis #3, which was modified to represent the pathological states of (r1) matrix overproduction and (r2) low osteoblast vigour (i.e. low osteoblast recruitment and delayed matrix deposition). Each model was simulated three times.

4.3.6 STATISTICAL ANALYSIS

Statistical analysis was carried out in SPSS (IBM, New York, USA). Osteocyte population count was tested using Kruskal-Wallis Test for non-normally distributed data and ANOVA for normally distributed data. The number of osteoblasts/osteocytes over each

day and for each category was statistical tested using a two-way ANOVA with *time* and *case* as discrete outcomes. For post hoc correction of multiple comparisons of groups, two methods were used: Dunns and Bonferroni. Dunns was used when comparing the control only with the other groups, and Bonferroni was used for comparing all groups with each other. Cluster analysis was carried out using a mixture modelling statistical framework in SPSS.[255] The two-step cluster analysis method was used to test the number of clusters present in each iteration across the three dimensional multivariate space. The cluster algorithm worked by finding the split of the data that would best fit the data for the number of clusters specified. The best fitting model and, thus, the number of clusters was determined by calculating the Bayesian Information Criterion. This form of test for model fitting uses both the fit of the model as well as the number of parameters used to determine the best fitting model. Overall, data from more than 125 computational iterations were analysed and are discussed in this chapter. [xx]

4.4 RESULTS

4.4.1 3D AGENT-BASED MODEL OF *IN VITRO* OSTEOGENESIS

Figures 4.5 and 4.6 display the proliferation and spatiotemporal transformation of the precursor (colony forming) mesenchymal cells into a condensation, followed by the deposition and mineralisation of osteoid (via hypothesis #3). These precursor cells proliferate *in virtuo* in a cuboidal Petri dish, the geometry and shape of which becomes apparent by the fifth frame in Figure 4.5A when cells have completely occupied the entire area. As the cells approach confluence, certain stochastically determined cells differentiate

[xx] The statistical tests and analyses reported in this chapter were conducted by the author and Dr Christopher Newby (University of Leicester). Statistical results were analysed and extended by the author in consultation with Prof Brian Hall, Dr Chris Newby, and Prof Yiannis Ventikos

into pre-osteoblasts (shown in orange, Figure 4.5B) and begin migrating in a bid to aggregate at the site of condensation formation.

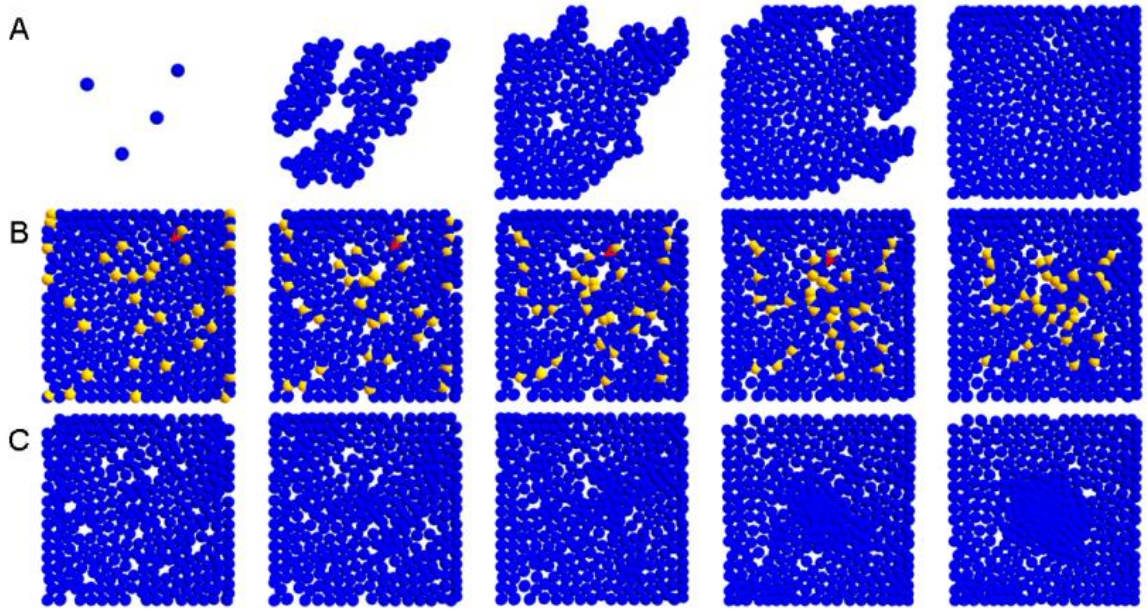

Figure 4. 5: Confluence, migration, and aggregation. The figure shows a series of frames capturing proliferation of the progenitor mesenchymal cells until confluence **(A)** and the migration of pre-osteoblasts to the site of skeletogenesis **(B)**. The largely vacant area begins with five cells that continue to proliferate and fill the entire space. Cells until this time only form a monolayer. They can neither migrate nor grow in the third dimension. The centre of the virtual Petri dish serves as the site of skeletogenesis. Only cells that have acquired a pre-osteoblastic phenotype (orange), unlike the initial fibroblast-like cells (blue), migrate towards the centre. The direction of one of these pre-osteoblasts has been indicated using the red arrow-head. **(C)** displays progression in terms of cellular aggregation. Aggregation can be easily visualised in the final two frames of **(C)**, which show a ventral view of the monolayer after the pre-osteoblastic cells have triggered condensation initiation at the top. As the frames move towards right, time increases by 6.25 days in **(A)**, 30 hours in **(B)**, and 45 hours in **(C)**.

Although clearly visible only after the third frame in Figure 4.5C, the tight aggregation of pre-osteoblasts in the centre of the presented region, the site of osteogenesis, can be observed, in contrast to their neighbouring progenitors. Finally, in Figure 4.6 (A, B), the emergence of a condensation from the site of cell aggregation at various time steps is shown (as observed from the top and as a cross-section). The condensation, initiated by migration, develops due to proliferation of pre-osteoblasts in the third dimension, which continues until the condensation reaches a height of 90 μm. The differentiation of pre-osteoblasts, located in the middle of the condensation, into osteoblasts (green spheres) begins to occur once the condensation has reached a height of 50 μm.

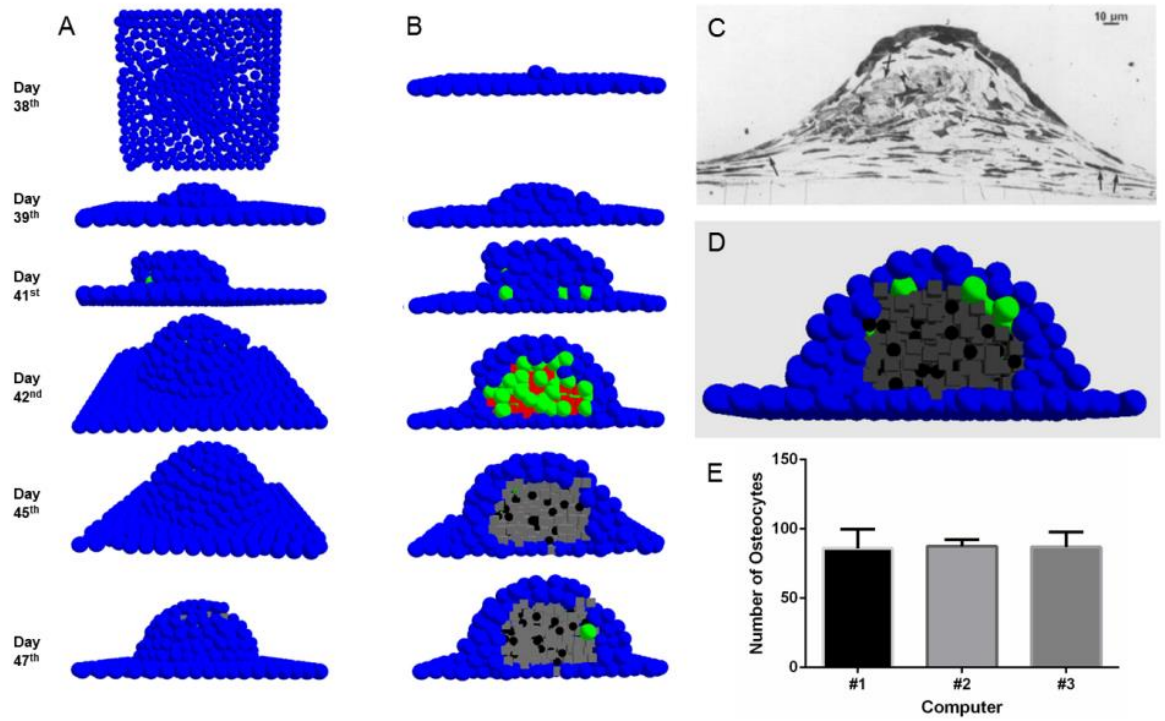

Figure 4. 6: *In virtuo* nodule. The figure displays **(A)** dorsal and **(B)** cross-sectional view of condensation initiation, growth, and mineralisation *in virtuo*. Images in the same row were captured at the same time, also displayed in the figure. As the condensation increases in size, cells in the middle transform into osteoblasts (green) and start depositing matrix (red) instantly. The matrices gradually mineralise (grey) encasing osteoblasts within them, which undergo terminal differentiation into osteocytes (black). **(C, D)** capture the similarities between an *in vitro* developed nodule and its computational counterpart. The basal cells in both cases are fibroblastic and more mesenchymal in nature (blue *in virtuo* and arrows *in vitro*) – they do not participate in bone synthesis. Cells at the top of the nodule, on the other hand, are pre-osteoblastic. The nodules also contain osteoblastic and osteocytic (black *in virtuo* and arrow-heads *in vitro*) cells, the latter embedded within the mineralised matrix (grey *in virtuo* and crossed-arrows *in vitro*). The two nodules differ in their population of osteoblastic cells (higher *in virtuo*), and indicate a difference in their 'age'. **(E)** shows lack of statistical difference in the number of osteocytes produced by the model(s), when run on three different computers. This was done to ensure that the model was not sensitive to stochastic elements within the code. ***(C)** reproduced with kind permission from Ref.* 250 © *(1988) Elsevier*.

Once condensation height increases to 70 µm the osteoblasts start depositing osteoid (red cubes) contributing to further condensation growth as a result of osteoid apposition, which continues until the condensation has reached a height of about 100 µm: commonly attributed as the maximum height achieved by *in vitro* condensations. This is when the deposited osteoid is mineralised (grey cubes). The osteoblasts trapped within the matrix, once the condensation height has reached 100 µm and the cells is in contact with at least 6 mineralised matrix neighbours, eventually transform into osteocytes (black spheres). Condensation growth stops entirely if the condensation grows beyond 110 µm.

A parallel between the computationally generated *in virtuo* condensation and its *in vitro* counterpart is also presented (Figure 4.6C, D). The frame at the top is an electron micrograph montage illustrating the cross-sectional organisation of the mineralising condensation. In this frame, cells at the bottom represent the precursor mesenchymal cells, whereas the top consists of (pre-) osteoblast like cells. Osteocyte-like cells are present within the nodule and are completely surrounded by a dense matrix (arrowheads). The frame below features cross-section of the analogous computational, mineralising condensation possessing similar features. For example, cellular layer at the bottom consists of the precursor cells, while the top consists of pre-osteoblasts. It must be stressed that although both precursor cells and pre-osteoblasts are visualised as blue spheres, they are not treated the same in the model: the former can neither migrate nor proliferate in the third dimension.

The exact moment when a condensation can be categorised as mature is not strictly defined, and could correspond either to the time when osteocytes are first observed within the condensation or, alternatively, when mineralisation is first detected inside the condensation. The author opted to work with the former qualification as it is relatively easier to characterise. The time taken for condensation development can vary even within the same organism. Investigators have reported condensation growth and maturation to take anywhere between 3 – 15 days post-confluence (pc henceforth).[232,249-251] Condensation evolving out of hypothesis #1, #2, and #3 required approximately 9 days pc to achieve maturity, in agreement with empirical observations. Hypothesis #4, however, resulted in condensations that either did not mature at all or required significantly more time to achieve maturation (Kruskal-Wallis test, $p<0.001$). By the end of the simulations, osteocytes constituted the major proportion of cells within the virtual condensation, as has been observed experimentally.[17,256]

4.4.2 CONDENSATION MATURATION DEPENDS UPON OSTEOID SYNTHESIS AND OSTEOBLAST RECRUITMENT

Variables pertaining to cellular interactions, which governed condensation development and osteoblast entrapment, were altered to observe how changes might affect the evolving structure. A total of 8 alterations (refer to Table 4.7) were made from the original model, employing Hypothesis #3 to deposit osteoid (Figure 4.7A-G). The alterations can be categorised as affecting *osteoblast recruitment* (*S1*, *S2*, *S3*), *matrix neighbours* required for differentiation (*S4*), *osteoid synthesis* (*S5*, *S6*, *S7*), and both *osteoblast recruitment and osteoid synthesis* (*S8*). The alterations were found significantly different ($p<0.001$) using a two-way ANOVA with time as covariate and the alterations as the group variable. When compared individually against the original model (hypothesis #3), employing Dunn's post hoc test for multiple comparisons, only the following simulations showed significant difference from hypothesis #3: *S3* ($p<0.001$), *S6* ($p=0.001$), *S7* ($p=0.001$), and *S8* ($p<0.001$) (Figure 4.7H-K). This indicated that the model was generally insensitive to minor stochastic alterations in parameters regulating the spatiotemporal evolution of condensations. For example, employing pre-osteoblast division frequency of 12 (hypothesis #3); 12±3 (*S1*); and 12±1 (*S2*) hours resulted in statistically similar condensations, $p>0.05$ for *S1* and *S2* compared with the original. The post hoc comparison to the standard (hypothesis #3), however, suggested that the model is dependent upon osteoid deposition rate as well as osteoblast recruitment.

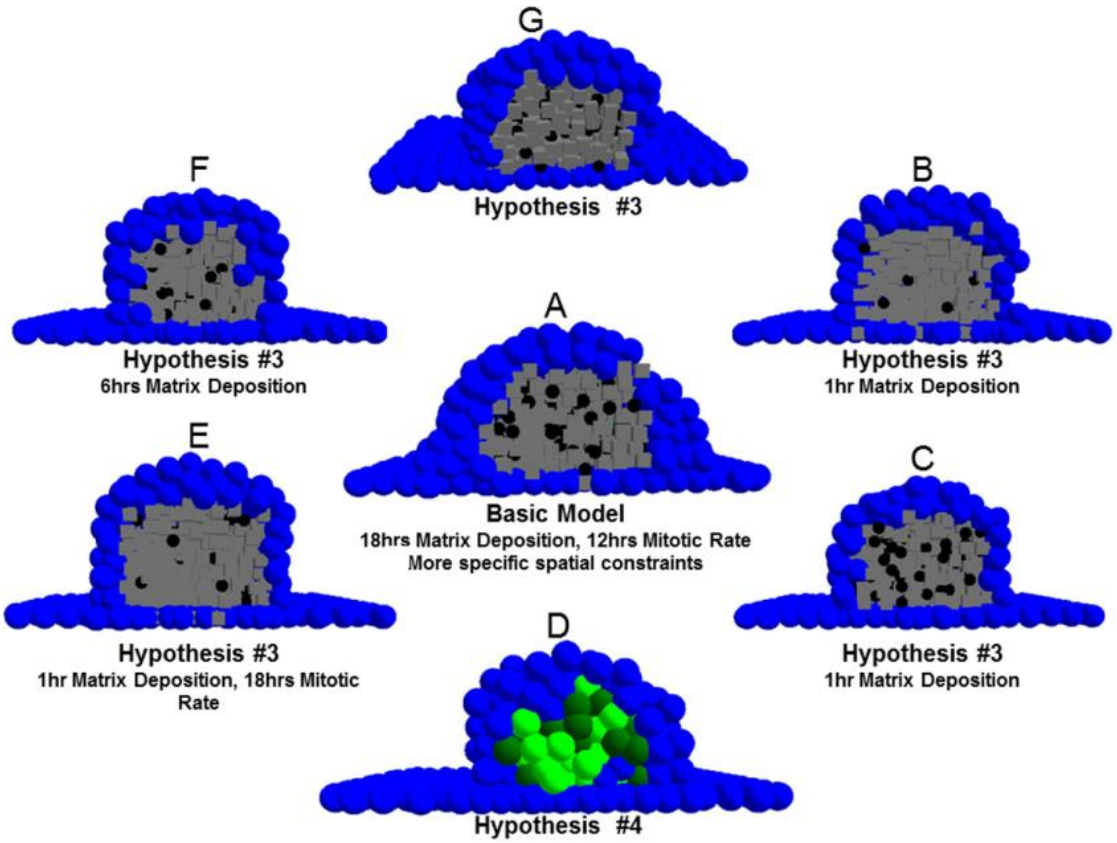

h

Alteration	Mean difference from Hyp #3	Std Error	p-value
S1	-13.06	5.14	0.074
S2	-2.94	5.14	0.995
S3	39.33	5.14	<0.001
S4	3.94	5.14	0.970
S5	0.39	5.14	1.000
S6	-19.78	5.14	0.001
S7	-21.28	5.14	0.001
S8	-40.44	5.14	<0.001

i

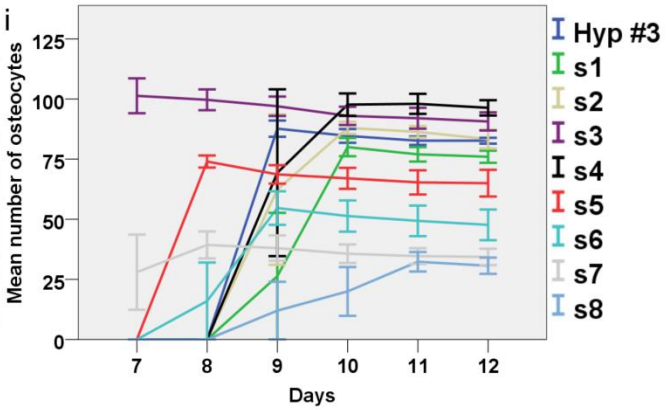

j

Alteration	Mean difference from Hyp #3	Std Error	p-value
Deposition and Recruitment	-40.44	8.55	<0.001
Neighbours for Differentiation	3.94	8.55	0.963
Osteoid Deposition	-13.56	8.55	0.151
Osteoblast Recruitment	7.78	8.55	0.584

k

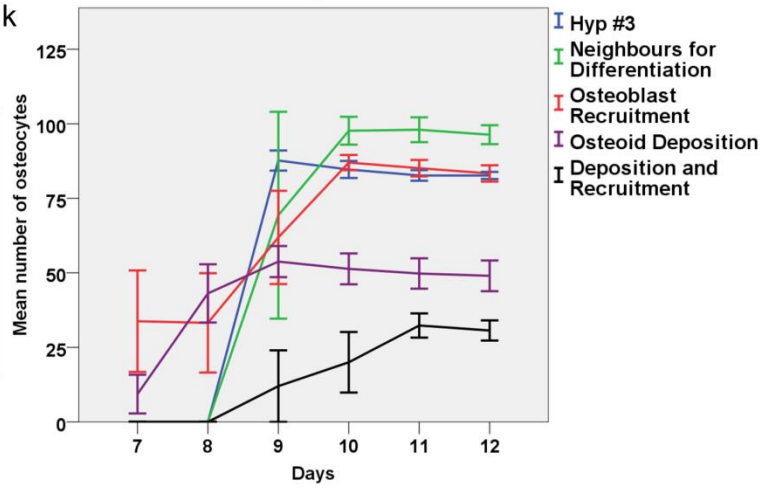

Figure 4. 7: **Model sensitivity to parametric alterations.** In order to test the basic model's **(A)** sensitivity to parameters regulating the spatiotemporal development of condensations the following variables were varied: osteoid deposition **(B)**, osteoblast recruitment (in terms of pre-osteoblast proliferation) **(C)**, or both (indicated in the figure) **(D, E, F)**. More robust boundary conditions pertaining to the spatial aspect of condensation development led to a very realistic condensation structure **(A)**. Extreme increase in the matrix deposition rate of osteoblasts resulted in very few osteocytes being formed **(B, E)**, whereas adding the switching-off gene resulted in stunted condensation growth as can be observed due to absence of osteocytes **(D)**. The images correspond to condensation on day 12 pc. The analysis revealed the dependence of condensation development in the model on two features acting synchronously: osteoid deposition and osteoblast recruitment, which is empirically known. The data presented in tabulated and graphed form demonstrates this quantitatively. In **(H, I)**, comparison of the altered parameters (i.e. matrix deposition rate = 6 hours, etc.) with the hypothesis #3 is presented, whereas **(J, K)** display the comparison of categories (i.e. osteoblast recruitment, etc.) with hypothesis #3. Notice the significant difference only when both osteoblast recruitment and osteoid deposition are co-varied.

For example, increasing pre-osteoblast proliferation (index of osteoblast recruitment) frequency by 50% (i.e. division every 8 hours instead of 12 hours) led to early formation ($p<0.001$) of osteocytes, (day 7 post-confluence compared to day 9 post-confluence from the original case). Similarly, increasing osteoid deposition rate by three times (every 6 hours instead of 18 hours) also increased osteocyte formation rate. Increasing matrix deposition rate by a factor of eighteen, however, even though it led to an increased rate of osteocyte formation (day 7 post-confluence), resulted in significantly few osteocytes in *S7* ($p=0.001$). On a similar note, increasing osteoid deposition frequency to every one hour but decreasing proliferation rate by a half (18 hours), *S8*, resulted in delayed condensation maturation, along with the formation of fewer osteocytes. These results have been summarised in Table 4.7. However, comparison of simulation *categories* against the original model; e.g. osteoblast recruitment (*S1*, *S2*, *S3*) vs. original (instead of hypothesis #3 vs. *S2*); only the case where both osteoid synthesis and osteoblast recruitment were altered simultaneously (*S8*) showed significant difference ($p<0.001$). The comparison was made using two-way ANOVA and Dunn's post hoc test for multiple comparisons. This was an important finding, for it suggested that the development and maturation of the virtual condensation relied on *both* osteoid deposition rate and osteoblast recruitment acting synchronously. This is known to be the case *in vitro* and *in vivo*,[17,232,249,251,256-261] where

abnormal alterations to either are known to cause pathological eventualities. This is better contextualised by data presented for hypothesis #4 where a minor alteration in osteoid depositing capacity of osteoblasts resulted in abnormal condensation development, even though the pre-osteoblast proliferation rate (or osteoblast recruitment) was the same as for other hypotheses. That the model captures certain governing principles of osteogenesis reasonably accurately is, therefore, quantitatively validated by this analysis.

Case	Parameter	Variation	Original	Result	Maturation	Average Osteocytes
h3	Hypothesis #3	Original	Original	Osteocytes observed on day 9 pc; Osteocyte number roughly equal to 86±5	day 9	86±5
S1	Pre-osteoblast proliferation	12±3 hours	12 hours	Delay observed in condensation formation (day 10pc); number of osteocytes roughly the same (83±3)	day 10	83±3
S2	Pre-osteoblast proliferation	12±1 hours	12 hours	Similar to the original in terms of condensation formation rate (day 9pc) and number of osteocytes formed (84±5)	day 9	84±5
S3	Pre-osteoblast proliferation	8 hours	12 hours	Earliest condensation and osteocyte formation observed (day 7pc); number of osteocytes relatively unaffected (96±5)	day 7	96±5
S4	Matrix surrounding Osteoblasts	4 neighbours	6 neighbours	Similar in terms of condensation formation (day 9pc); but relatively higher number of osteocytes observed (101±3)	day 9	101±3
S5	Matrix deposition rate	6 hours	18 hours	Early condensation formation observed (day 8pc); relatively similar number of osteocytes (76±1)	day 8	76±1
S6	Matrix deposition rate	18±3 hours	18 hours	Similar to the original in terms of condensation formation rate (day 9pc) but fewer osteocytes (53±5)	day 9	53±5
S7	Matrix deposition rate	1 hour	18 hours	Condensation formation earliest (day 7pc); but very few osteocytes observed (30±0)	day 7	30±0
S8	Matrix deposition rate/Pre-osteoblast proliferation	1 hour/18 hours	18 hours/ 12 hours	Lack of enough osteoblasts (37±3) as well as extremely delayed condensation formation (day 11 pc)	day 11	37±3

Table 4. 7: A summary of the sensitivity analysis. Simulations conducted to test model's sensitivity to various parameters governing condensation development, as well as a summary of results from each test case (n=3) are provided. To contextualise the analysis, condensation maturation time and average osteocyte population on day 12 p.c. is also given.

4.4.3 OSTEOBLAST POLARITY DICTATES THE ARRANGEMENT OF OSTEOCYTES WITHIN CONDENSATIONS

Following basic model development, the strong-inference approach[262] was used to test the proposed mechanisms. Figure 4.8 (A-D) displays the process of bone deposition and the transformation of osteoblasts into osteocytes governed by the four hypotheses. Hypotheses #1 – 3 do not show significant differences between the structure and number of osteoblasts (Kruskal-Wallis, p=0.095) that form at a given time. Furthermore, the processes of condensation initiation and growth, differentiation of the initial progenitor-cells into osteoblasts, matrix deposition, mineralisation, and osteocyte formation occur approximately at the same time.

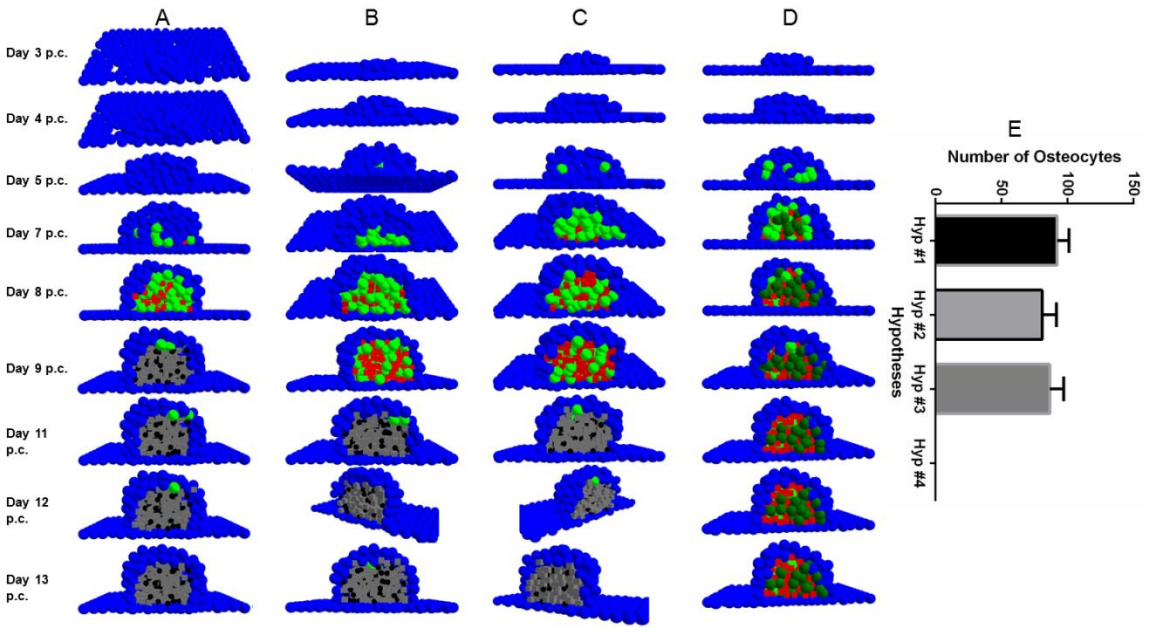

Figure 4. 8: Transformation of osteoblasts to osteocytes according to the proposed hypotheses. The figure shows cross-sectional view of the nodules capturing the transformation of osteoblasts (green) to osteocytes (black). Hypotheses #1-3, displayed by **(A – C)** respectively, roughly yield similar transformation patterns within similar time frames. Hypothesis #4 **(D)**, however, underperforms substantially being unable to either allow the condensation to achieve the right size or osteocytic transformation. This observation is statistically represented in **(E)**, which shows lack of osteocytes in nodules employing hypothesis #4 for condensation development and maturation 12 days post-confluence and similar values of osteocytes produced by hypotheses #1-3.

Hypothesis #4, however, substantially underperforms under this criterion producing, for the dominant majority of simulations, no osteocytes even after 30 days pc (Kruskal-

Wallis, $p<0.001$). The results were consistent when gathered from simulations conducted across three different work stations (Kruskal-Wallis, $p=0.788$). This was done to ensure code insensitivity to random elements within the code, which were used to account for biological stochasticity, and achieved by employing random number generation, which tends to vary between different workstations.

The sequence of events encountered in Figure 4.8 is shown without the precursor/pre-osteoblastic cell cover in Figure 4.9. The inadequacy of hypothesis #4 is further exposed here. However, a more noteworthy observation becomes apparent. The differentiated osteocytes emerging from hypothesis #3 seem well sequestered from each other by the matrix in which they are embedded and are more regularly arranged as compared to hypotheses #1 and #2. In order to quantify this visual observation, a cluster analysis was conducted on data collected for hypotheses #1, #2, and #3. Despite lack of significant structural differences between condensations formed using the three hypotheses, the analysis revealed hypothesis #3 formed the most consistent number of clusters across iterations, resulting in more ordered and consistent arrangement of osteocytes over iterations. Hypotheses #1 and #2, though, showed more variation in the number of clusters formed, and so resulted in cells that were irregularly arranged over iterations owing, perhaps, to the varying polarity exhibited by the osteoblasts.

Non-selective osteoid deposition (#1 and #2) was, therefore, observed to cause irregular, non-homogeneous arrangement of osteocytes with certain condensation zones being heavily populated and certain others entirely devoid of osteocytes. This observation deserves a special mention, for not only does it have experimental basis; it also underscores the ability of ABM in capturing emergent behaviour. Ferretti *et al*. (2002)[226] reported evidence for irregular arrangement of osteocytes with arbitrary polarities that form due to self-entrapment of osteoblasts.

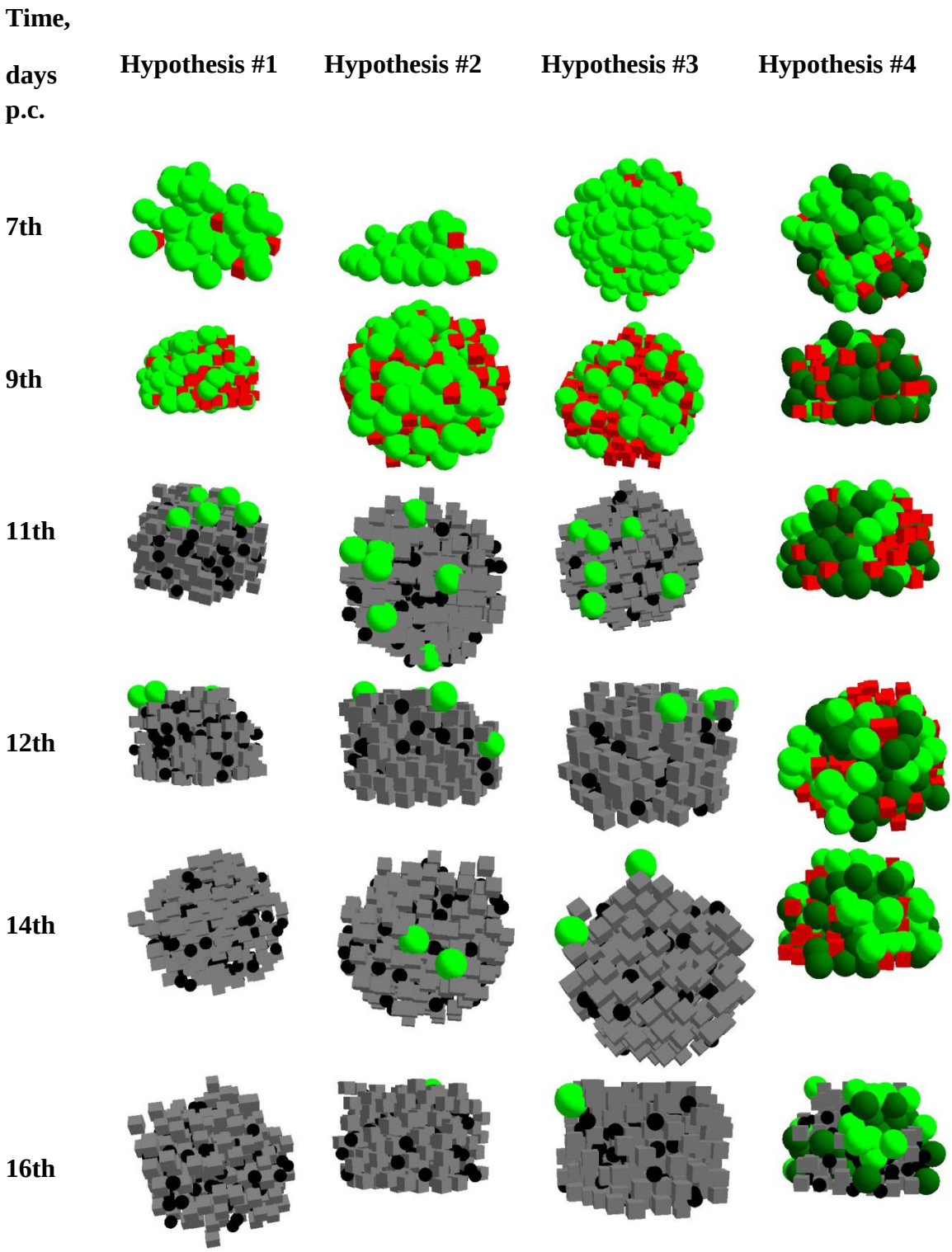

Figure 4. 9: Osteoblastic transformation into osteocytes without Mesenchymal cells. The figure captures the spatiotemporal development of the condensation in terms of matrix deposition, its mineralisation, and the terminal differentiation of osteoblasts into osteocytes. Frames presented in this figure were captured from various angles. A couple of conclusions can be easily drawn from the frames presented in this figure: condensation growing per hypothesis #4 fails to achieve the requisite condensation size and therefore osteoblast differentiation; and matrix deposition occurs in the most ordered manner governed by hypothesis #3.

In comparison, osteocytes formed due to entrapment from neighbouring cells showed more regular arrangement as well as collective polarity. The model captured both phenomena: self-entrapment represented by hypothesis #1 and #2 resulted in irregular osteocyte arrangement, whereas entrapment represented by hypothesis #3 formed regularly arranged osteocytes. It needs to be emphasised that the resulting observed osteocyte arrangement was neither coded for in the models, nor alluded to as part of initial and/or boundary conditions. It emerged from polarity acquired by osteoblasts dynamically during model run time.

The cluster analysis, furthermore, revealed that hypothesis #2 showed more variation in the number of clusters formed (though it resulted in two clusters more consistently than hypothesis #1). Hypothesis #2 can, thus, be concluded to result in an irregular arrangement of osteocytes, in comparison with hypothesis #1, and hence the mechanism contributing to static bone formation. However, as little is known about the source of irregularity in static bone formation, disproving one of the two mechanisms represented by hypotheses #1 and #2 will require more detailed computational analyses. The best fitting number of clusters per iteration is displayed in Table 4.8 for each hypothesis.

4.4.4 OSTEOBLASTS DO NOT SWITCH-OFF OSTEOID DEPOSITION

Hypothesis #4, similar to hypothesis #3 in terms of osteoblast polarity, suggested that certain osteoblasts terminate or slow-down osteoid synthesis and end up getting buried by neighbouring osteoblasts. In the initial model, the population fraction that turned-off its 'genes' was set to 30%. The period over which termination occurred was indefinite. This combination produced no osteocytes during the periods where other hypotheses resulted in normal condensations. This remained the case when the termination period was decreased to 2 days and 1 day. No differences were observed upon setting the population fraction to

10% (indefinite, 2 days, and 1 day switch-off periods) and 2% (indefinite and 2 days switch-off periods). Only one case from the set of simulations conducted with the 2% and 2 days combination produced osteocytes (Figure 4.10) but the mechanism failed to capture other events in the same time frame as the other hypotheses; so much so that the differentiation of osteoblasts into osteocytes was not fully observed until the end of majority of the simulations. Two problems were identified with this hypothesis: (i) the condensation fails to develop normally in size, which in turn is the cause of many anatomical complications and malformations[263], and (ii) 'burial' of osteoblasts cannot occur properly as there is not enough matrix to properly embed osteoblasts, which, therefore, fail to differentiate into osteocytes. If the deposition of osteoid can indeed be considered *the* most significant reason behind condensation maturation and the differentiation of osteoblasts into osteocytes, hypothesis #4 seems untenable.

Number of clusters detected			
Iteration #	**Hypothesis #1**	**Hypothesis #2**	**Hypothesis #3**
1	2	2	2
2	2	3	2
3	3	2	2
4	2	1	2
5	2	2	2
6	3	2	3
7	2	2	2
8	3	3	2
9	2	2	2
10	3	2	2
11	3	2	3

Table 4. 8: Number of osteocyte clusters per hypothesis. The table lists the number of osteocyte clusters observed for simulations conducted employing hypotheses #1-3. Data from 11 simulations conducted on three different computers (5-3-3) are shown. Inconsistency in cluster formation when employing hypothesis #2 can be observed by the variation in the number of clusters that can form (three as opposed to two for hypothesis #1). Osteocytes were not observed in simulations employing hypothesis #4 during normal time frame and, therefore, were not included in this analysis.

Hypothesis #4 only produced osteocytes when, for the population fraction of 2%, the termination period was decreased to 1 day (1.5% of the simulation time). However, this behaviour was critically contingent on the moment when the termination period was applied.

If the 'switch-off' was imposed too early, a reasonable number of osteocytes resulted. Delayed application of this condition, though, led to inconsistent results. Kruskal-Wallis test conducted on simulations with population fraction and switch off period as 2% and 1 day respectively showed lack of significant difference (p=0.638) amongst each other (in terms of number of osteocytes observed). While this analysis points to inconsistent performance of hypothesis #4, even when mild limitations regarding population fraction and termination period are imposed, a pattern can be clearly identified. As hypothesis #4 approaches hypothesis #3, i.e. as the effect of population fraction and switch-off period are removed, it starts to produce condensations more consistently. This suggested that hypothesis #4, quite possibly, embodies a pathological departure from hypothesis #3 – a conjecture that required further probing.

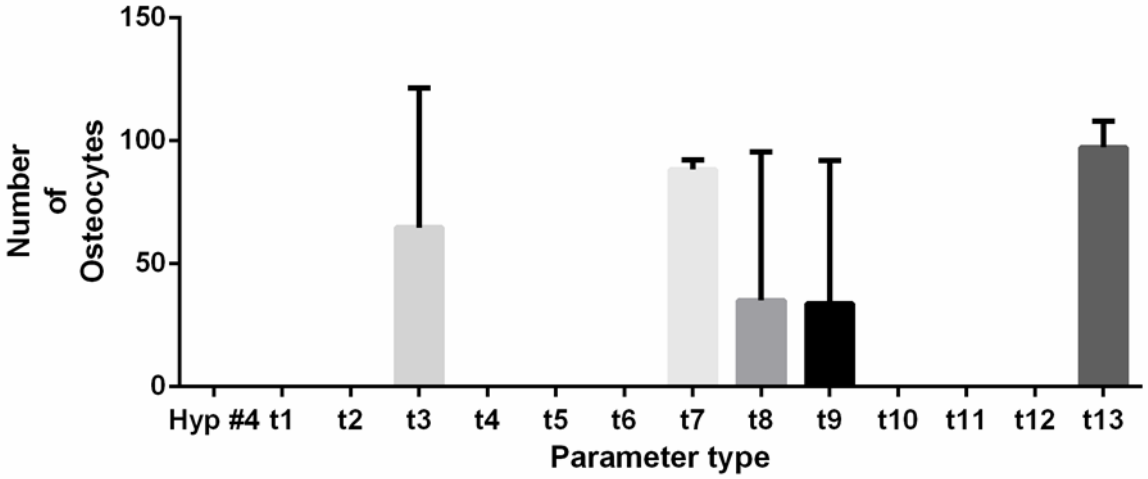

Figure 4. 10: Sensitivity analysis of hypothesis #4 as the mechanism governing condensation development. The graph represents the number of osteocytes obtained when parameters regarding osteoid 'switch-off' were altered. Parameters altered included the percentage frequency of osteoblasts switching off their osteoid deposition genes (30%, 10%, 2%), the amount of time during which this decision was made (indefinite, 2 days, 1 day), and the moment during simulation when this behaviour was allowed (early vs late). Osteocytes were only observed when the population switching-off osteoid deposition was reduced to 2%, the period to 1 day, and when this condition was imposed quite early during simulation. This indicated that normal osteocyte population can be observed as hypothesis #4 approaches hypothesis #3. Please refer to *Materials and Methods* for details regarding the analysis.

4.4.5 ABNORMALITIES IN OSTEOBLAST RECRUITMENT AND OSTEOID DEPOSITION RATE ARE LINKED TO BONE-RELATED PATHOLOGIES

Identification of a defect forms the first step towards its correction. Whether *in vitro* or *in silico*, a model of osteogenesis must be dynamic enough to identify a defect and initiate corrective measures. As such, the ability of the model to initiate remodelling and the effectiveness of various hypotheses to govern this remodelling were investigated. Normally developed condensations (via hypothesis #3) were compromised by 'resorbing' a significant amount of mineralised osteoid and necrosing a substantial number of osteocytic, osteoblastic, and pre-osteoblastic populations (Figure 4.11A). The author expected the model to initiate osteoblastic recruitment followed by osteoid synthesis to recreate the condensation. This is exactly what was observed, albeit with the difference that remaining pre-osteoblasts initiated proliferation (index of *osteoblast recruitment* for *in vitro* cases) and differentiated into osteoblasts, which subsequently produced matrix (index of *osteoblast vigour*) that mineralised and aided the differentiation of osteoblasts into osteocytes.

In concurrence with the aforementioned results, hypotheses #1, #2, and #3 resulted in normal condensations, similar to each other (two-way ANOVA for n=3, $p=0.102$). Hypothesis #4, quite obviously, underperformed, resulting in subnormal condensations with sub-optimal amount of matrix and fewer osteocytes, especially in comparison to hypothesis #3 (two-way ANOVA, $p<0.001$ for n=3; Figure 4.11 B, C, F, G). This underperformance was attributed to low osteoblast vigour. In order to test this conjecture further, hypothesis #3 was modified to (r1) over produce matrix and (r2) suppress osteoblast recruitment and osteoid production (low osteoblast vigour) (n=3, for both cases), the latter affecting the condensation by depositing less osteoid than needed. Both modifications failed to result in normal condensations (Figure 4.11 D, E, H, I), two-way ANOVA ($p<0.001$), showing a significant deviation from hypothesis #3 (Bonferroni multiple comparison, $p<0.001$ for r1,

and p=0.001 for r2; Figure 4.11J) but similarity with results obtained using hypothesis #4 (p>0.05 for both; Figure 4.11J).

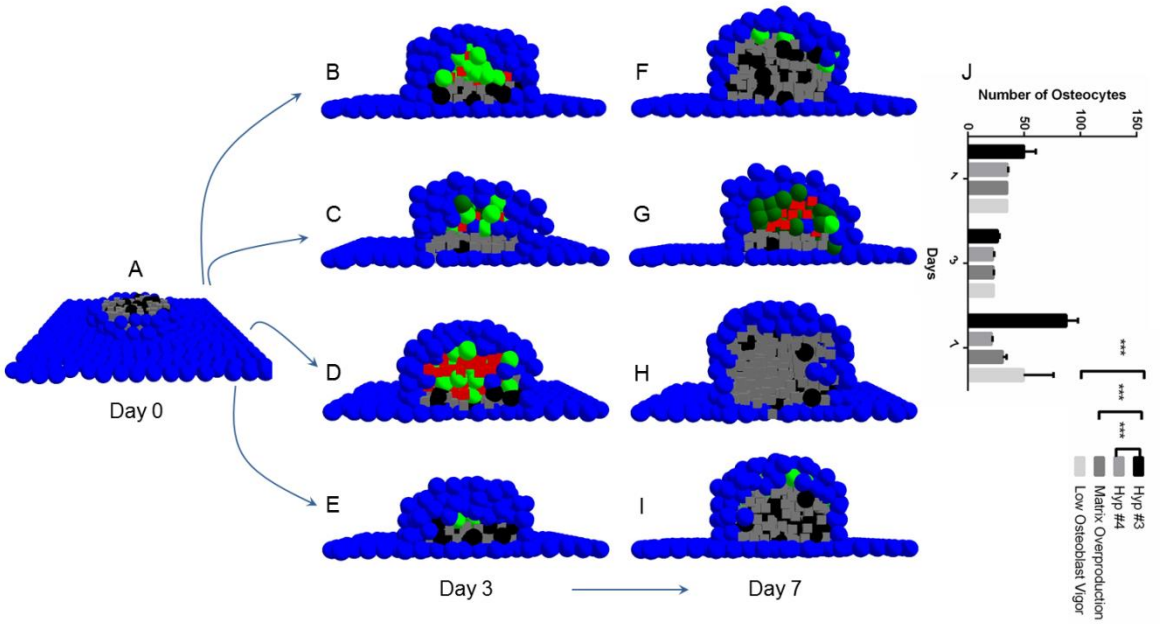

Figure 4. 11: Nodule remodelling following the 'resorption' challenge. The figure captures the spatiotemporal development of the condensation following a challenge in the form of bone resorption. As part of the challenge, mineralised matrix of a normal condensation was 'resorbed' and the osteocytes necrosed **(A)**. The recovery of this nodule was observed by employing four mechanisms: hypothesis #3 **(B, F)**, hypothesis #4 **(C, G)**, matrix overproduction **(D, H)**, and low osteoblast vigour **(E, I)**. The two frames were taken on days 3 and 7. Nodule remodelling under hypothesis #3 recovered normally producing osteocyte population that was statistically similar to the original, mature condensation. Hypothesis #4 failed to produce a normal condensation in size, osteoid production, as well as osteocyte population. While matrix overproduction did result in a remodelled condensation that resembled the original condensation in size, it had considerably less osteocyte population: a sign of skeletal abnormality. Finally, the condensation that recovered via low osteoblast vigour fared better than the previous two mechanisms, the amount of osteocytes observed were not statistically similar to the ones observed for the normal, mature condensation, indicating skeletal abnormality. In **(J)**, this information is represented statistically. $***p < 0.001$.

This indicated the mechanism encoded in hypothesis #4 was similar to that obtained using the modified (abnormal) hypothesis #3. It, therefore, seems quite likely that mechanisms represented as hypothesis #4 actually result in pathological bone structures and are, thus, less likely to play any role in normal differentiation of osteoblasts into osteocytes. Furthermore, the investigation also revealed the manner in which matrix overproduction, out of sync with available osteoblast numbers, results in fewer osteocytes due to accelerated condensation growth as a result of enhanced osteoid apposition, which fails to trap enough

osteoblasts. In animal models, while underproduction of osteoid is linked to *osteoporosis*, overproduction is usually associated with *hyperparathyroidism* and *osteitis fibrosa*.

4.5 DISCUSSION

In order to validate the model, the maturation time of the virtual condensations was compared with their *in vitro* counterparts. Hypotheses #1, #2, and #3 produced condensations that matured within the empirically observed range of 3 – 12 days pc. Moreover, all normal condensations (refer to the sensitivity analysis conducted on hypothesis #3) matured within this time frame as well. Secondly, the number of cells within a nodule was quantified by Bellows and Aubin[264] (also discussed by Beresford et al.(1993)[249]) to be ~100. Moreover, it is also known that there are about 10 times as many osteocytes as osteoblasts.[17] Considering these two empirical data points, one can conclude that the number of osteocytes within a mineralised nodule should be close to 90. This formed a crucial piece of validation for the model as well as the underlying rules and boundary conditions, for all *normal* condensations (i.e. hypotheses #1, #2, and #3) produced osteocytes – 87±11 (mean ± standard deviation) – in agreement with the known empirical figure (especially 90 osteocytes). Simulations that produced ~35 osteocytes were statistically different from the *normal* condensations (as pointed in the analyses). Hypothesis #4, though, failed on both accounts. Furthermore, in addition to these two *explicit* comparisons another *explicit* comparison was presented: *in virtuo* nodule structure in comparison with *in vitro* nodule structure. The spatial arrangement of cells and mineralised matrix, as well as nodule height, reproduced cleanly the *in vitro* observations, which further validates the model as well as the underlying rules.

The model, relying purely on initial and boundary conditions (the latter in terms of spatial limits), presence or absence of neighbours (cells or matrix), instructional relationship

between the various agents (cells/matrix), and certain stochastic variables (refer to *Methods*), faithfully reproduced the template observed during nodule formation as first proposed by Hall and Miyake,[263] as follows: epithelial-mesenchymal interactions → differentiation → condensation formation → deposition of extra-cellular matrix → terminal differentiation (including mineralisation). There were two chief reasons behind simulating the process *in vitro*: (i) the situation provides a realistic representation of what happens *in vivo,* (ii) uncomplicated by extraneous factors such as hormones, mechanical conditions, vascularity, and so forth. The first reason is justified as the *in vitro* mineralised nodules have been demonstrated to resemble true bone.[250] Furthermore, agreement amongst several authors that "*[…] mineralised nodules in vitro closely resemble the embryonic/woven bone that is formed in vivo*"[249,250,252,265-267] points to similarity between mechanisms that produce morphologically similar skeletogenic structures *in vitro* as well as *in vivo*.

However, it was felt that these comparisons though useful were not sufficient and, as such, additional *semi-explicit* comparisons were made. These included comparing: (i) factors that regulate condensation development (*in vitro* and *in vivo*); (ii) arrangement of osteocytes within condensations; (iii) impact of osteoblast polarity on osteocyte arrangement; (iv) impact of osteoblast polarity on osteoblast entrapment; and (v) condensation recovery under pathological conditions. Analyses conducted herein reveal that (i) both[221,249,250,256] osteoblast recruitment – captured in the *in vitro* model by pre-osteoblast proliferation – and osteoid deposition must act normally for normal condensation development: failure in even one can result in abnormal condensations (e.g. hypothesis #4 and simulations r1 and r2); (ii) models produce both irregularly (hypothesis #2) and regularly (hypothesis #3) arranged osteocytes, which can be employed during osteogenesis; (iii) osteoblasts polarised as a layer produce regularly arranged osteocytes whereas osteoblasts with individual polarity give rise to irregularly arranged osteocytes (which

happens to be an empirical observation[226]); (iv) osteoblast that act as layers (hypothesis #3) bury neighbouring osteoblasts whereas those that are individually polarised undergo self-burial (hypothesis #2)[226]: the cluster analysis revealed the latter to be producing irregularly organised osteocytes, but was additionally validated by the observation[226] that those cells that acquire an orientation initially and deposit matrix in that direction throughout their life produce irregular arrangement of osteocytes (we computationally captured that conjecture); and, finally, (v) even normally developed condensations can display poor recovery in case pathological mechanisms (i.e. slow osteoblast vigour/recruitment and abnormal osteoid deposition) become operational during recuperation.[256]

In the biological context, these results refute the view proposed by Palumbo *et al*.[229] and Nefussi *et al*.[230] that those osteoblasts that switch off their osteoid deposition capacity are transformed into osteocytes. While termination of osteoid deposition will inevitably accompany osteoblast differentiation, a certain case of correlation, it cannot be attributed causality over the event. Furthermore, attributing to a cell this additional event of 'terminating' a particular behaviour based on the amount of matrix in its immediate environment is tantamount to adding a layer of complication (rather than complexity) that might be difficult to justify and explain in terms of intra- and extra-cellular features that will additionally come into play if the cells are assumed to display such sensibility and control. The results presented here promote and reinforce Romer's[227] as well as Windle & Nonidez's[228] view that polarised osteoblasts act synchronously to deposit bone. Contrary to this is the view proposed by Ham & Cormack,[224] Bloom & Fawcett,[225] and Ferretti *et al*.[226] that treats acquisition of polarity to be self-regulated. This allows discrete and seemingly random distribution of polarity within a given osteoblast population and, thereby, non-selective deposition of osteoid, which our results indicate lead to clustered and inconsistent osteocyte formation. The analysis also supports the evidence for this behaviour, reported by

Ferretti *et al.*[226], suggesting that the direction of osteoid deposition does not alter significantly through an osteoblast lifetime, and rules out Ham & Cormack's[224] view that osteoblasts deposit osteoid randomly throughout their lives.

The analyses, furthermore, provide computational evidence for the view that ossification can employ multiple osteogenic strategies, which Ferretti *et al.*[226] refer to as static and dynamic bone formation. Whereas static bone formation employs self-burial, hypothesis #2; dynamic bone formation occurs by entrapment due to neighbouring cell activity, hypothesis #3. The implication is that osteoblasts acquire polarity influenced by their environment rather than by their genomic content alone. The environmental variables can include presence of biological structures or gradients of a chemokine or morphogen, amongst others. Whichever case it may be, the environmental impact will be continuous, and, therefore, it can be argued, most cells within a population would be influenced collectively, rather than individually. For example, if gradient of a particular solute is assumed to contribute to polarity, it is logical to conclude that a collection, or layer, of cells, rather than one cell, would be affected. This layer of cells will then act in alignment to carry out functions influenced by their polarity; such as, deposition of osteoid and, in turn, the burial of neighbouring (arguably, layer of) osteoblasts. This is perhaps the reason why the static mechanism (hypothesis #2) mainly contributes to the formation of the core of intramembranous bone structures, such as the primary trabeculae, which form around the vascular framework where gradients will be low owing to presence of high solute concentration (hence little impact on polarity); whereas the dynamic mechanism (hypothesis #3) seem to be mainly involved in bone compaction, at sites away from the vasculature where solute gradients will become more appreciable.

A significant feature of this investigation remains the fact that the agent-based approach enabled the observation of the development of abnormal nodules (hypothesis #4),

and allowed the author to investigate parameters that are linked to bone pathology. Additionally, the model, being inherently dynamic in nature, provided a novel foray into the mechanics of bone remodelling (*sans* osteoid resorption), both normal and pathological. For example, the model suggested both under- and over-production of osteoid (index of osteoblast vigour) as well as low and high pre-osteoblast proliferation (index of osteoblast recruitment) to contribute towards abnormal condensation development. This has implications in studying bone defects such as *osteoporosis*, where the model, following the incorporation of *osteoclasts* as bone resorbing agents, can be employed to better understand the role of aforementioned parameters in causing low bone density, as well as cases where bone deposition seem to be amplified (e.g. *osteitis fibrosa*). Furthermore, by introducing into the model interactions between a drug molecule and the targeted 'agent', usually osteoblasts, the efficacy and impact of the given drug on osteoblast activity or recruitment can be evaluated. The model can, therefore, be used to optimise drug development. The fact that the author was able to analyse parameters that caused abnormality and, more importantly, optimise them to lead to normal condensation development constitutes the principal beauty of the agent-based paradigm.

The model relied on cellular migration as the initiator of condensations. *In vivo,* mesenchyme close to the site of skeletogenesis helps furnish condensations with cells, which migrate to the relevant site, as indicated by Jabalee *et al*. (2013)[221] The conclusions of our model, therefore, with respect to osteoblast differentiation, apply equally to *in vivo* cases, especially considering that osteoid deposition occurs after migration and differentiation of pre-osteoblasts (in addition to the fact that the orthopaedic community agrees that mineralised nodules resemble true bone). Furthermore, the model assumed optimal nutrient and morphogen concentrations, which are only justifiable for *in vitro* studies. Similarly, polarity, even though acquired dynamically by osteoblasts during development as well as

remodelling in this investigation, had a purely spatial character. *In vivo*, this will not be the case, for the chemical and mechanical environment of osteoblasts will also influence polarity. The two assumptions, however, will not alter these conclusions as the aim of this investigation was to compare the performance of the proposed differentiation mechanisms under normal circumstances. Moreover, the agent morphology employed in the model was idealised, though it would not upset the conclusions as agent morphology was not considered to play any role in influencing either osteoblast polarity or its differentiation. Finally, in this investigation, growth and maturation of only one condensation/nodule was considered, but, once again, the conclusions can be extended to *in vitro* cultures with multiple condensations/nodules without any loss of generality.

Furthermore, while osteoblasts display directional sensitivity to mechanical stimuli,[268,269] the impact external mechanical loading can have on osteoblast activity, as well as polarity, is undeniable. In hypotheses #3 and #4, a key factor is the synchronised acquisition of polarity by the osteoblast agents. In reality, this is a result of integration of environmental physical and chemical cues along with the genetic content of the osteoblasts. However, as the model did not consider physical or chemical cues, this was achieved simplistically. Space in the z-dimension was distributed into regions alternating in polarity. The regions were determined probabilistically in each simulation. While the cells acquire polarity dynamically within the model (a. cells were not assigned pre-determined polarity, and b. polarity itself was decided during run time), this remains a limitation of the model, as it does not consider the gradients that play the role in informing cell polarity. This aspect shall be advanced in the forthcoming version of the model. Furthermore, this dynamic acquisition of polarity was achieved by introducing a global rule in the model, which led to an increase in the computing time (refer to §2.3.2 for a discussion on the impact of global on computational complexity). However, adding this global rule was, in the absence of

physicochemical cues, the only manner in which the osteoblasts could have acquired polarity dynamically during run time.

The process of cell condensation emerges as a result of factors, which include: changes in cell proliferation,[220] alteration in cell-cell and/or cell-ECM interactions that prevent movement of cells away from a centre,[270] local deposition of ECM components,[270,271] haptotaxis influenced by spatiotemporal patterns of ECM production,[272] and patterns of diffusible morphogens.[273,274] However, the actual mechanism(s) informing mesenchymal cell condensation still remains unknown.[275] Previously, this has been captured by employing reaction-diffusion equations where condensation patterns emerge as a result of interactions between two morphogens (an activator and inhibitor) and the cellular response to these interactions, which is a more complete and robust way of capturing the process. CPM oriented standalone models have achieved this by adding a term to the *Hamiltonian* to capture preferential attachment of cells to the matrix. In the presented model, cells, in the absence of chemical and mechanical stimuli, condense by migrating along an arbitrary gradient towards the centre of the field. While the model can support condensation anywhere within the virtual field, the only reason the centre of the field was chosen as the desired spot for condensation was to ensure full visibility of the resulting nodular structure as the field boundary was not periodic. This was permitted by the lack of underlying reaction-diffusion equations, but remains a limitation of the model. However, the modularity of the code, which allows easy incorporation of reaction-diffusion equations or indeed the transport equation, means that this limitation can be easily mitigated (to be addressed in the sequel to this model).

Besides aiding our fundamental understanding of a significant biological event, results from this investigation display how computations can serve as efficacious supplements to experiments. As the philosophy behind the use of computational strategies

is to condense the lab into the computer, and the experiment into the code, the model's sensitivity to stochastic variables within the code as well as result reproducibility across various computer systems was also tested. This was achieved by running models (employing the four hypotheses) on separate workstations. Simulations resulted in similar condensation structures with similar osteocyte populations within the same time frame. The fact that statistically similar results were reproduced on more than one machine means that our model (code available under Creative Commons Attribution License) as well as results can be reproduced and modified by anyone anywhere, and further used for hypothesis testing of any kind. In particular, this investigation underscores how the discrete mathematical approaches, specifically, agent-based modelling can be applied to recreate experiments that for a variety of reasons may be difficult to design and execute. It must be reiterated that these hypotheses could not have been tested experimentally, especially in the detail presented here. The mechanism(s) governing osteoblast differentiation being unknown, it is immensely challenging, if not outright impossible, to engineer a cellular population that can obey *in vitro*, and most certainly *in vivo*, mechanisms represented by the four hypotheses. Moreover, despite the availability of mutated osteoblasts, which display abnormal osteoid deposition, it must be kept in mind that the experiments evaluating these hypotheses require precursor cells to undergo two degrees of differentiation to form osteoblasts, which can subsequently display abnormal osteoid deposition or randomly acquired polarity. Currently, this can only be achieved *in virtuo*. However, mutated osteoblasts can be employed *in vitro* to quantify the contribution of hypothesis #4 in causing bone related pathologies – an investigation the author intends to undertake next.

Furthermore, agent-based modelling, in offering a fresh perspective to investigators interested in exploring the impact of activity of a collection of entities (enzyme, cell, extracellular-matrix, etc.) on global observables, opens up previously inaccessible data.

Finally, the fact that the model was able to capture differences in condensation maturation that emerged due to the differences in the hypotheses tested as well structural features not explicitly included within the code, points to the robustness of the technique as a hypothesis testing tool. Given that agent-based modelling is the most intuitive way of simulating biological systems, the author hopes that results from this investigation shall encourage biologists to pick up this methodology to investigate questions that have proved challenging to explore due to lack of suitable apparatuses and/or techniques, or other logistical or ethical issues.

4.6 SUMMARY

A key conclusion to take away from the results presented in this chapter is that any modelling approach required to simulate biological complexity must possess certain features, which include: the ability of the approach to simulate non-linear and dynamic behaviour, synthesise relevant "constituent-constituent" and "constituent-environment" interactions, track the evolution of various constituents that are heterogeneous in nature, develop memory of various prior constituent interactions, adapt to the external environment, and permit visualisation of emergent phenomena that will result from the combined interactions of system constituents. Continuum models alone cannot fulfil all these criteria and hence a different methodology to model interaction-reliant progression and emergent character of most morphogenetic processes was presented in this chapter – that of ABM. The series of discussions undertaken in this chapter were motivated by this objective.

ABM was used to simulate *in vitro* intramembranous osteogenesis. The model was based on spatial restrictions, instructional relationship between cells, and a cell's ability to sense its environment, and reinforced by a range of sensitivity tests and evaluation of model output following a physiologically relevant challenge (bone resorption). The model, capable

of capturing empirically observed emergent behaviour during osteogenesis, revealed two aspects of osteogenic differentiation that were completely unknown, are counter-intuitive, but provide novel insights into this hitherto unexplained process: osteoblasts display polarised behaviour, and they do not, under normal development, switch off their matrix deposition genes. These findings effectively discount two major current hypotheses and illustrate the developmental relevance of this model. Moreover, Figures 4.6 and 4.8 serve as excellent exemplars for the power of abstraction and conceptualisation that this approach offers, illustrating in a visually compact manner the processes that were investigated and the message that, in osteogenesis, multiple mechanisms are at play; an empirically verified fact.[226] The versatility of the agent-based approach makes it a particularly appealing modelling framework to analyse complex systems. However, the approach on its own cannot be employed to capture the continuous features of a biological system and, as such, cannot display the ability to assimilate information dynamically. A hybrid approach, as has been hinted thus far, is best suited to capturing biocomplexity with greater resolution and clarity – an argument that was explored in Chapter 2. In the next chapter, a multi-paradigm, transport-agent coupled, hybrid framework is presented, which enriches the existing landscape of hybrid computational approaches that are available to simulate biological phenomena.

A Multi-Paradigm Modelling Framework to simulating Dynamic Reciprocity

CHAPTER 5

In the preceding chapters we analysed the utility of Computational Fluid Dynamics as well as Agent-based Modelling as suitable mathematical approaches to simulating bulk and emergent behaviour, respectively. However, due to restrictions applicable to each, pointed out in previous chapters, neither obeys dynamic assimilation, as discussed in §2.7, in full. Therefore, there still remains an absence of a suitable modelling paradigm that can truly capture biocomplexity and the dynamism that exists in biological systems. This chapter addresses the overarching aim of this thesis: Develop a framework that can capture biocomplexity, especially in the TERM context, in 3D; and discusses the development and validation of a computational framework that can be used to simulate biological phenomena in most, if not all, TERM related systems. Results displaying the capability of the framework to capture dynamic reciprocity as well as dynamic assimilation, and its validation are presented. Images and certain sections have been reused under the ***Open-Access License.***[xxi]

5.1 INTRODUCTION

A recurrent message in this thesis concerns the importance of synthetically generated autologous substitutes[276,277] towards the treatment of the diseases of *cellular deficiency*;[19] situations where populations of crucial cells are permanently lost. Given that certain adult human tissues lose their capacity to regenerate,[21] they rely exclusively, in case of a critical injury, on functionally similar substitutes.[21,278-280] As was suggested in previous chapters the principles of tissue engineering can be employed to develop such biological substitutes, with remarkably similar properties as those of the host tissues, *in vitro*.[21,22,279-281] This, however, requires tight control over the artificial growth environment,[28,277,280] which can be achieved by using bioreactors that in addition to providing an optimal growth environment for cells, are also used to ensure effective mass transport (as demonstrated in Chapter 3). Bioreactors have evolved significantly in both their

[xxi] *The work presented in this chapter appeared as: Kaul H, Cui ZF, Ventikos Y (2013). A Multi-Paradigm Modeling Framework to Simulate Dynamic Reciprocity in a Bioreactor.* ***PLoS One*** *8(3):e59671.*

complexity and functionality over the last two decades.[28,276,277] Subsequent to their primary design objectives: regulating the cellular microenvironment to support cell viability, promoting their 3D organisation and providing the cells with spatiotemporally controlled signals; their design has been modified to offer the user the possibility to seed cells dynamically within 3D matrices, overcome the constraints inherent to static cultures, and stimulate the developing constructs physically.[28,277]

Despite the technological advances that have been made in the sector of regenerative medicine and, in particular, bioreactor technology, there is still a pressing need for safe and clinically efficacious autologous substitutes.[277] Furthermore, translating regenerative medicine from bench to bed-side would not only require a good product but also robust, controllable and cost-effective manufacturing bioprocesses that are compliant with the evolving regulatory frameworks.[53,277] As automated devices, bioreactors serve ideally towards this end, for they are the key element in the development of standardised, traceable, cost-effective and safe manufacturing processes for engineered tissues for clinical applications.[277]

However, they too, like most biological systems, are utilised primarily as black boxes, where trial and error eventually leads to the desirable cellular outcome.[55,277] It should, therefore, come as little surprise that their yields remain qualitatively poor and the process of cell expansion almost non-reproducible.[29,277] The problem, once again, stems from the fact that little is known about the impact of specific bioreactor mass transport characteristics and features on the expansion and growth of cells within the device. Investigators in recent years have begun utilising computational tools (reviewed in Chapters 2 and 3, and elsewhere[55,57]) to study mass transport inside bioreactors (a critical feature of this thesis as well) and how that may influence cellular dynamics, but this extremely complex interplay has thus far proven elusive.

Analyses based on tackling directly the differential equations governing transport have in addition to being successful in quantifying mass transport and hydrodynamics inside bioreactors; have been extended to, given certain assumptions, studying cellular dynamics as well.[55,282] Such models usually either assume absence of neo-tissue within the interconnected pore space in a scaffold or cell attachment only along the surfaces of the scaffold.[55] The differential approach models the cell population, the surrounding extra-cellular framework and nutrients as distributed continua.[282] The matrix in which the cells grow can be treated as a porous medium[282] and one can utilise a wide variety of available computational methods to quantify the distribution of any number of substances being transported and diffusing inside it. Whereas the continuum approach captures transport quite accurately, the fact that it investigates biological phenomena at cell *population* level, disregarding entirely the cellular heterogeneity – central to biological function[13,282] – and the low-level system details,[12] hinders accurate analyses of cellular dynamics, as the continuum approach captures averaged responses. The averaged response exhibits large variability between experimental models, especially when small number of cells are being utilised. This is usually mitigated by employing stochastic elements within population-based models, which makes them useful in explaining the modelled phenomenon, but not while making experimental predictions.[53] Secondly, population-based models do not allow for tracking of individual cells and cell properties (as the microscopic details are abstracted away), which leads to a loss of realism.[151] Similarly, continuum formulations do not consider the history of individual cells while simulating cell behaviour.[283] Collectively, this makes quantification of cellular dynamics less precise and rather difficult.

In order to understand the impact of cell level behaviour on the overall cell population, discrete models can be employed[12,13,151,282] – a conclusion argued for in Chapter 4. The cellular automata approach, one of the many discrete approaches, has been used

extensively to trace the microscopic details of cellular dynamics more directly and accurately by attributing a set of evolution/transition rules to the computational grids that can represent biological entities such as the cell or the physical microenvironment.[5,282] The models that have been tried using this approach usually assume a constant supply of nutrients, which is not fully reflective of the actual conditions, even under carefully designed experiments.[13,284] Furthermore, the discrete models available in the literature, despite capturing processes such as contact inhibition, persistent random walk and cell division with marked accuracy, do not consider the impact of chemotaxis and apoptosis on the overall growth dynamics of a cellular colony.[13,284]

Both the continuum and discrete formulations have advantages as well as disadvantages, which were outlined in §2.4. More recently, hybrid models, which are a combination of the continuum and discrete approaches, have been utilised to study the evolution of biological systems through intercellular and cell-environmental interactions[12,105,282,285-287] especially within bioreactors.[14,15,288-290] This, arguably, is a better approach, compared with either continuum or discrete formulations, to quantify biocomplexity, as it provides sufficient resolution to analyse both the cellular and environmental heterogeneity.[288] Furthermore, especially within the TERM context, this approach is particularly suited to investigate the impact of drug or non-drug based interventions on cellular activity, considering that the continuum module can be utilised to model distribution of the therapeutic agent and the discrete module to simulate the cellular interaction with it. Moreover, bioreactor functionality and design can be enhanced through this approach, where the continuous PDEs can be employed to capture transport, hydrodynamics, and mechanical stimulation and the discrete equations/rules to capture how these physical forces impact biological growth, and vice versa.

The hybrid approach, based on the formulation capturing cellular behaviours, can be broadly divided into two categories: *on-lattice* and *off-lattice* models. As the title suggests, on-lattice hybrid models employ a lattice-structure, which is utilised to represent the biological space, and where each cell is represented by a single point on the lattice[11,291] (though multiple sites can be employed to represent a complex cell shape). Off-lattice hybrid models, on the other hand, employ continuous space to encapsulate cells within. Each approach has advantages and limitations, which are briefly addressed along with a review of existing hybrid models in the following sections.

5.1.1 ON-LATTICE HYBRID MODELS

Two of the most-commonly employed on-lattice approaches simulate cellular activity via either the cellular automata (CA) or the cellular potts modelling (CPM) paradigm. The reader came across some of these hybrid, on-lattice models in Chapter 4 where formulations capturing mesenchymal condensation, osteogenesis, and even limb-bud formation were presented. These include the hybrid model of chondrogenic condensations proposed by Kiskowski *et al.* (2004)[210] integrating reaction-diffusion equations, which captured interactions between an activator morphogen and its inhibitor, with a stochastic lattice-based model, which captured migration, morphogen secretion, and production of an adhesion molecule. An advance on this model was proposed by Christley *et al*. (2007)[235] who incorporated substrate adhesion within the model, ability of cells to change shape (during condensation), and simulated cellular behaviour and molecular dynamics of the morphogen at different spatial scales. The investigators identified two distinct regimes of reaction rates that impact cell behaviour: slow reaction rates leading to stable morphogen peaks and fast rates leading to oscillatory peaks. Checa & Prendergrast (2009)[209] also integrated a stochastic-lattice with a previously developed mechanical algorithm.[97] The investigators employed the finite-element model to capture mechanical stimuli and used the

discrete model to account for migration, proliferation, differentiation, apoptosis, and capillary network formation to generate a range of biomechanochemical cues to inform osteogenesis. Chaturvedi *et al*. (2005)[115] coupled a discrete stochastic CPM with reaction-diffusion equations to capture limb bud formation. The hybrid model was able to successfully capture normal and abnormal limb bud development.

On-lattice hybrid models have been also utilised to simulate tumourigenesis. Jiang *et al*. (2005)[292] developed a multi-scale, hybrid model of tumour formation by integrating approaches that captured sub-cellular, cellular, and environmental dynamics. They utilised the Boolean network approach to regulate the expression of proteins that controlled cell cycle, and reaction-diffusion-consumption PDEs (i.e. reaction-diffusion equations with a *sink* term) to account for chemical dynamics at the extra-cellular level. CPM was utilised to capture cell proliferation, adhesion, and necrosis. The extracellular microenvironment included oxygen and glucose as nutrients, lactate as metabolic waste, and growth activators and inhibitors. The (sub-cellular) progression of cells through their cell-cycle was also governed by local concentrations of growth activators and inhibitors. The model replicated the development of avascular tumours both qualitatively (i.e. a necrotic core at the centre, and proliferating and quiescent cells at the surface and intermediate layer) and quantitatively (in terms of tumour volume, cell number growth, growth curves when nutrient concentrations were varied) rather well; and predicted that proliferation within the tumour is regulated by a combination of limited growth promoters and internally produced growth inhibitors, as has been observed experimentally. Gatenby *et al*. (2007)[293] integrated a model capturing reaction-diffusion equations to account for gradients of oxygen, glucose, and H^+ with a cellular automata model simulating cellular activity, which allowed the investigators to generate continuously varying local maps of the aforementioned molecules/ions. The investigators wished to probe the hypothesis that adaptation of hypoxia and acidosis are key

in the later phases of carcinogenesis, and developed an *in vitro* model of multi-cellular spheroids to test the conclusions drawn from the computational model. Starting from a normal cell population, the cells underwent random heritable changes due to mutation or epigenetic changes that resulted in *proliferative* (proliferation even under sub-optimal conditions, i.e. hypoxia, acidosis, lack of contact with the basement membrane), *glycolytic* (constitutive up-regulation of glycolysis even under normoxic conditions), and *acid resistant* (proliferation under apoptotic pH) cells. Simulations led to observation of multiple adaptations to hypoxia and acidosis, which converged to the final phenotype with constitutive upregulation of glycolysis and resistance to acid-induced toxicity. Such cells would invade into normoxic regions, lowering its pH due to upregulated glycolysis, which is toxic to normal cells. This, inevitably, assists in late stages of carcinogenesis as it confers a proliferative advantage enhancing invasiveness.

Bailey *et al*. (2007)[294] developed a hybrid model underpinned by a blood flow network simulation to dynamically track inflammatory cell navigation through microvasculature to a simulated skeletal muscle capillary bed via interactions with the endothelium. The microvascular network was derived from mouse spinotrapezius muscle, and combined with a network flow model designed to calculate haemodynamic parameters (such as fluid flow and wall shear stress) throughout the simulated microvascular network. The investigation yielded results consistent with literature data, including monocyte migration occurring primarily in the venules (even though differences in endothelial cell phenotype were not explicitly accounted for in the model) and low dependence of monocytes on *selectins* for firm adhesion (a non-intuitive result).[294]

Cheng *et al*. (2009)[12] utilised the continuum-discrete approach to model the complex interplay that exist between cell populations and mass transport dynamics. Cell interactions were modelled using the discrete CA approach whereas diffusion and consumption of

nutrients were based on a transient PDE approach. The dependence of cell division and cell migration on nutrient concentration, which is not to be confused with chemotaxis, was also accounted for. As migration speed was proportional to nutrient concentration, lower nutrient concentration meant lower migration speed.

In order to simulate patterns observed during *in vitro vasculogenesis*, defined as the *de novo* formation of the primary vascular network from the initial endothelial cells, Merks *et al*. (2006)[295] integrated a PDE model to account for diffusion and secretion of chemoattractant with a CPM simulating endothelial cell behaviour. The investigators aimed to study "*how the phenomenology of endothelial cells drives tissue-level dynamics*". The model assumed endothelial cells to acquire an elongated shape due to cytoskeleton remodelling; secrete a chemoattractant, which diffuses into the ECM and slowly decays producing gradients; move up this chemoattractant gradient. In order to mimic cell elongation, a *cell-length* and *connectivity* constraint was added to the *Hamiltonian*, refer to (2.55). The connectivity constraint was added to eliminate artefacts introduced by the cell-length constraint. The PDE capturing diffusion and secretion of the chemoattractant was discretised by employing the finite-difference method. The model demonstrated the importance of endothelial cell shape, i.e. elongation, to the formation of vascular-like morphologies, in conjunction with autocrine secretions. The model also predicted that Vascular Endothelial Growth Factor$_{165}$ (VEGF) is less likely to be the signalling molecule essential for vasculogenesis, and that a less diffusive growth factor, such as one of the ECM-bound VEGF$_{189}$ or VEGF$_{206}$ isoforms, is probably the key signalling molecule.

The models proposed by Picioreanu and co-workers[14,15,296-299] utilise a differential-discrete approach to model biofilm growth as a result of substrate gradients. Biofilms are heterogeneous systems comprising microbial cells (distributed in a non-uniform manner) and polymers, creating a chemically distinct microenvironment.[14,299] Understanding the

factors that influence biofilm development is essential to designing membrane systems more immune to biofouling.[15] The computational approach entailed quantifying the role of soluble components (such as substrate concentrations, fluid flow, etc.) by the continuum approach and utilising the discrete approach to simulate solid components (i.e. the biomass: bacteria, matrix, etc.). The approach was motivated by the, proven and quantified, structural heterogeneity of biofilms, which informs its development.[296] The underlying idea was to predict biofilm structure coupled with "*correct time evolution of concentrations, fluxes, and conversion rates*".[296]

A case in point is an earlier version[14] of their approach where spatial distribution of the substrate is determined by applying relaxation methods to the reaction-diffusion mass balance (the latter approximated using the finite-difference method). Biomass growth was assumed to be a direct result of nutrient consumption (oxygen). Here, biomass spreading was modelled using a CA algorithm, whereby the CA grids were identified as either *fluid* (representing nutrient reservoir), *land* (the biofilm), and *lakes* (pores and voids within the biofilm). The biofilm front in the model was governed by the following rule: "*each particle of the hull has at least one "fluid" (external) nearest or next-nearest neighbour*".[14] Biomass growth was implemented in CA by a rule-set whereby a newly formed biomass "pushed" its neighbours to an adjacent, unoccupied site to make a place for itself.[296] The model assumed microbial growth in static liquid and investigated the influence of substrate transport rate on biomass growth. The investigation, relying on a variety of statistical variables (biofilm surface shape, roughness coefficient, and fractal dimension) and dimensionless numbers proposed in the article, concluded that high substrate transfer rates resulted in compact and dense biofilms. In another version of the model, which simulated immobilised microbial growth,[296] good qualitative and quantitative agreement was obtained when computed

oxygen uptake rates, oxygen concentration profiles, and biomass size were compared against empirical data.[296]

In incorporating the impact of hydrodynamics on biofilm development these models were further extended by Picioreanu *et al*. (2009)[15] to simulate biomass growth under perfused conditions. The extended model was developed to investigate biofouling, i.e. the process of biofilm growth, in membrane system (reverse osmosis, nanofiltration, etc.) modules. The investigators coupled fluid dynamics, solute transport, and biofilm formation. The model was developed to facilitate understanding of parameters that influence biomass development and, consequently, increase in pressure-drop inside membrane systems to design better membrane systems with higher immunity to biofouling. The feed channel of spiral-wound nanofiltration and reverse osmosis membrane devices containing *feed spacers* was modelled in this investigation. Feed spacers create an intricate flow pattern within the device, which is influenced by the heterogeneous biofilm growth in the feed channel. Membrane system hydrodynamics were modelled by the incompressible laminar Navier-Stokes equations, which were discretised using the finite-element approach. Oxygen transport alone was considered the limiting nutrient. The spatial distribution of oxygen concentration was determined from the transport equation. The computational space was divided into 3D cubic elements, which were categorised based on the presence or absence of biomass. Biomass growth was solved in the CA representation. In addition to demonstrating the capacity of 3D models to more accurately capture the complexity of flow-patterns in 3D arbitrary geometries, simulations showed formation of preferential flow channels and a heterogeneous flow pattern. The investigators concluded that biofouling in membrane systems leads to quasi-stagnant zones and an increase in the dispersion of the residence time distribution.

5.1.2 OFF-LATTICE HYBRID MODELS

The other set of hybrid approach include off-lattice models, which as the title indicates do not require an underlying, fixed grid. Off-lattice models, cells are assumed to exist in continuum space and possess a defined location and volume within this space. This allows the cells to exhibit uninhibited movement in three dimensions. Galbusera *et al.* (2008)[286] adopted this strategy to create a software framework for computational modelling of tissue engineering experiments. Cell population in this framework is modelled using the 'discrete cells in a continuum space' approach.[286] The finite element approach was used to model the cell environment. The group presents a 3D microscopic model but only a 2D macroscopic model. Michaelis-Menten kinetics were used to calculate oxygen consumption by the cells (which makes oxygen consumption a population-level behaviour). Furthermore, the model considers necrosis, due to lack of oxygen, occurring when the oxygen concentration falls to less than 50% of the initial value. The model did not consider chemotaxis.

Adra et al [245] integrated Flexible Large-scale Agent-based Modelling Environment (FLAME) with COmplex PAthway SImulator (COPASI) and a physical numerical solver [123] to develop a 3D multi-scale model to grow a virtual piece of epidermis from a collection of stem cells and derive a set of biological rules for TGF-β1 (cytokine) during epidermal wound healing. In this investigation, the agent-based model was used to capture biological rules governing intercellular interactions in the human epidermis; COPASI was used to simulate the expression and signalling of TGF-β1 at the intracellular level; and the physical solver was used at the continual level to resolve forces exerted between cells. The model was able to successfully simulate many described keratinocyte behaviours and TGF-β1 intracellular mechanisms. Sun et al [300] utilised the same approach to develop a 3D multi-scale model of the formation of skin epithelium based on rule-sets involving TGF-β1 to test

the role TGF-β1 plays in wound healing. Wounds were introduced into the model, which was then used to observe keratinocyte behaviour during healing and explore various hypotheses concerning the role of TGF-β1 by manipulating the rule-set associated with the cytokine. The model supported the *in vivo/in vitro* observation that TGF-β1 maintains a balance between keratinocyte proliferation and differentiation during wound healing, and further indicated that disruption of TGF-β1 expression or signalling could impact the healing process.

Solovyev et al [301] constructed a hybrid model of ischaemia-induced hyperemia (sudden increase in skin blood flow following ischaemia) and pressure ulcer formation by combining an ODE model of blood flow and reactive hyperemia, and ABM of skin injury, inflammation and ulcer formation. Their primary objective was to gain useful insights into post-spinal cord injury (SCI) pressure ulcers, which may result from prolonged tissue ischaemia. The agent-based aspect of the model simulated injury, inflammation and ulcer formation by capturing interactions between oxygen, pro-inflammatory elements, anti-inflammatory elements and skin damage (agents used in the model). Experimental data from human subjects (six SCI patients and six non-injured subjects) was used to calibrate the ODEs used in the model. The model suggested a higher propensity for ulceration in the patients compared to the subjects. Despite certain limitations identified by the authors themselves, the model can be employed as a diagnostic platform for post-SCI ulcer formation.

Off-lattice hybrid models, just like their on-lattice counterparts, have also been utilised to study tumourigenesis. Drasdo & Hohme (2005)[302] compared growth of tumour monolayers and spheroids by integrating an individual cell-based model with reaction-diffusion equations capturing local alterations in glucose concentration. Each cell in the

model was considered a sticky, elastic sphere[xxii] of limited compressibility and deformability, which could migrate, grow, and proliferate. Cellular activity was modelled using the standard Metropolis algorithm (refer to §2.3.2.2). Mechanical interactions between cells (elastic, isotopic, adhesive spheres) were measured by employing the Johnson-Kendall-Roberts (JKR) model of elastic contact, which assumes that spheres are able to deform as a result of adhesion. The simulations suggested that within monolayers with sufficient nutrients the shift from exponential to linear growth can be a result of cell-cell contact-mediated growth inhibition and that growth of cells in the interior of monolayers is inhibited as they are sufficiently compressed. Rejniak (2005),[303] in order to simulate the formation of tumour micro-regions, developed a hybrid 2D model where cells were described as a set of discrete points connected to each other by elastic springs, and the entire ensemble of points and springs immersed in a viscous, incompressible fluid that captured the material properties of the cells as well as the intercellular space. Oxygen was modelled as the limiting nutrient, and its concentration profile changed as a result of its diffusion within the fluid and consumption by cells for which the reaction-diffusion paradigm was utilised. The model showed biological adequacy and relevance in capturing the emergence of tumour cell sub-populations, spatiotemporal evolution of tumour micro-regions and concentration-profile of oxygen, and tumour aggressiveness (in terms of invasiveness).

Kim *et al*. (2007),[304] similarly, integrated reaction-diffusion equations to account for the transport and consumption of oxygen and glucose with a pseudo-discrete representation of cellular behaviour to model growth of tumour spheroids. Cellular behaviour was pseudo-discrete as the investigators utilised a discrete formulation to account for cell migration and proliferation for cells at the periphery of the tumour while a continuum formulation was utilised for the quiescent cellular zone, necrotic core of the tumour as well as the ECM. The

[xxii] Cells acquired a dumb-bell shaped during mitosis

investigators used this approach to model growth of tumour spheroids in suspension and agarose gel. The simulations showed the tumours to develop asymmetrically as a result of variable proliferative activity of cells and that tumour growth settles into a quasi-static regime, subsequent to which the thickness of the viable region (i.e. the proliferative region) remains constant. Finally, the simulations revealed that increase in gel stiffness and, therefore, stress exerted by the gel on the tumour, results in slower growth rates.

Lapin *et al*. (2004, 2006, 2010) [288-290] modelled microorganism population behaviour in bioreactors by opting for an *individual-based approach*[288-290] whereby the dynamic behaviour of the system as a whole can be traced to the behaviour of individual organisms. Their initial model[288,290] focused on simulating temporal and spatial behaviour of a population of oscillating yeast cells based on glucose concentration fields in a bioreactor. In order to achieve this, computational fluid dynamics (CFD) – modelling the turbulent flow fields in the bioreactor – was coupled with an Eulerian-Lagrangian representation of the system, where the extracellular environment was based on the Eulerian approach and the distributed biophase was characterised by a discrete cell ensemble (Lagrangian) approach. The model considers cell migration by superimposing random movement due to turbulent dispersion on the convective flow. The cell in this instance, however, does not mean a 'real' living cell, rather a computational element that represents a large collective of real cells. In its advanced form[289,290] the model was extended to simulate E. coli population dynamics in a stirred-tank bioreactor with non-ideal mixing. In particular, Lapin *et al*. (2006, 2010) modelled glucose uptake by the bacteria, which depends on a combination of the extracellular glucose as well as intracellular metabolite concentrations. The investigators observed distinct differences in cell viability at various scales of operation. The novelty of the model lies in its strategy to trace population behaviour by considering the individual cell response as a result of key reactions of the central metabolism, which the author feels is a

more mature way of approaching biological complexity. Certain assumptions of this model are worth highlighting here: firstly, the Lagrangian representation of the model is pseudo-discrete. Each computational element represents a population of physical cells. It can be argued that this makes the simulation computationally economical but has the disadvantage of ignoring various individual-level details.

Lapin and co-workers worked with the assumption that quantitative description of a biological phenomenon requires an understanding of the intracellular reaction rates and regulatory responses of intracellular networks to environmental changes as well as spatiotemporal variations in the structure of the extracellular abiotic phase. Furthermore, working with the no-slip assumption (between the fluid and corpuscular phase) and ignoring momentum transfer between the particles and fluid phase the investigators concluded that the Euler-Lagrange strategy delivers more accurate results (i.e. in agreement with experimental data) compared with the standalone Euler approach (i.e. both fluid and bio-phase represented by Eulerian formulation) and that the Euler-Lagrange method permits analysis of the lifelines of individual cells in space and time (evidenced by the ability of the model to predict synchronisation of autonomous glycolytic oscillations in yeast cells at the population level and to account for activity of E. coli within a fed-batch culture). The investigators finally concluded, from this, that the approach is ideal to capture heterogeneity present in real reactors in both fluid and cellular phases and is a potent simulation strategy for the design and operation, particularly for cases where fate of individual cells is of interest.

The environment and phenomenon (cells within a bioreactor) investigated by Lapin and co-workers (presented in the previous paragraph) were closest in the literature to the phenomenon presented in this chapter (despite differences in methodology). However, the computational approach utilised to develop the platform to be presented in this chapter finds, amongst parallels discussed above, models developed by Picioreanu and co-workers[14,15,296-

[299] mirroring it closely. The models by Picioreanu and co-workers presented in §5.1.1, entitled biomass-based models (BBM), were pseudo-discrete, for each grid in the CA platform represented *biomass* (collection of microbes and polymers), instead of individual cells. These models were followed by a hybrid, individual-based model (IBM) of biofilms.[299] This model simulated a nitrifying biofilm with multiple bacterial species. Unlike the BBM, this model was truly individual as each discrete particle accounted for individual bacterial cells, and more realistic. Each of these bacterial cells were assumed to be non-deformable spherical shells occupying continuum space. The IBM constituted of two modules: one simulating substrate and product diffusion and reaction, whereas the other simulating bacterial dynamics. Substrate concentration was determined from a solution of their mass balance. The model, like the two BBMs, only considered diffusion, with the diffusion-reaction equation solved for the steady-state solution using the finite-difference scheme. However, unlike the BBM where biomass growth was simulated computationally (employing CA rules), bacterial dynamics in this case were numerically (employing differential equations) simulated. The model assumed dependence of biofilm growth on diffusion, reaction, growth (like the BBMs) and a stochastic element. Each bacterium could consume nitrogen, grow in size, and exert intercellular force on neighbouring bacteria. Biomass spread was simulated by maintaining a minimum distance between neighbouring cells. This was achieved by calculating the vector sum of all positive radii with neighbouring cells and shifting the cell in the direction opposite to the vector. In terms of the overall biofilm growth, results from the model were in agreement with those from the BBM as the same diffusion-reaction process was modelled similarly in both cases. However, the IBM resulted in a smoother, confluent, and compact biofilm shape due to the underlying 'spreading' (deterministic overlap correction) mechanism used in this case. The two models, even though they produced results that macroscopically were in agreement, differed in the

details of biofilm shape and growth, which is expected due to the truly discrete, high spatial resolution[xxiii] of the IBM.

From a computational point of view also, the BBM reviewed above are pseudo-discrete, which means that each discrete entity in the model represents a multiplicity of cells and biomass. The only model[299] where a discrete entity corresponded to single cell simulated the dynamics numerically, i.e. by relying on mathematical equations, thus treating each cell homogeneously. However, the advantage of employing this individual-based computational model includes achieving greater spatial resolution and understanding the role of heterogeneity (concentration-, stress-, or cell-related) in system development, but only in comparison with classical continuum models. The models proposed by Picioreanu and co-workers represent the first step towards capturing computationally the dynamic feedback observed in biological systems. This can be observed in their model where biofilm growth causes alteration in pressure drop, and flow-pattern is in turn influenced by it.

5.1.3 OBJECTIVE

The hybrid approach of simulating biological behaviour, as evident through the review conducted above, is gaining popularity within the computational community. Whether achieved via an off-lattice or on-lattice discrete framework, the hybrid approach allows the user to account for most data-structures that can be exploited, in the form of cell behaviour regulating physical stimuli, during experimentation and offers better resolution towards the investigation of biological phenomena compared with either of the two parent approaches (continuum and discrete) by themselves.

[xxiii] IBM, as compared to the BBM, possessed higher resolution as the discrete entities representing the bacteria were all 1 μm in diameter, as oppose to the BBM, where the discrete entities represented an aggregation of microbes and other polymers.

On-lattice hybrid models are simpler to learn, develop, and implement. The fact that they possess an underlying grid is especially conducive to developing hybrid models for two reasons. Firstly, the presence of the grid means that the cell neighbourhood relation is defined, which immensely simplifies the search for cell-neighbours (while determining adhesion, migration, proliferation, etc.) as no additional algorithms (such as collision detection and correction) need to be incorporated. Secondly, the presence of the grid also provides a template on which meshes/elements, which are needed to calculate continuous fields (flow, concentrations, etc.), can be based. This is especially amenable to integrating the two formulations. The on-lattice approach, furthermore, is less expensive computationally, as the presence of the underlying grid reduces sampling of the environment to sampling of the adjacent lattice sites. The common underlying grid between the continuum and discrete modules, however, implies that the chemical fields are determined at the cell scale. As such, the 'jumps' in the values may not fully reflect the smooth transition in chemical gradients.[291] Furthermore, on-lattice models typically offer a limited number of directions in which cells can move. Similarly, the movement itself is restricted to the underlying pre-defined lattice-points.

Off-lattice formulations, which model cells as discrete entities within continuous space, allow for more realistic representation of cell spatial location and movement. The approach allows the user the freedom to incorporate a complex array of shapes into the model. This means that one agent of arbitrary shape in the model can correspond to one physical cell. On the contrary, in lattice-based models a complex shape is generally achieved by representing one cell as a collection of lattice sites. Secondly, the absence of an underlying grid also gives the user the freedom to customise the representation of the continuous fields (allowing for smoother transitions in relevant continuous gradients). These formulations can easily account for global behaviour and allow greater freedom for detail

and complexity – as such; they can potentially be fully mechanistic. However, off-lattice models require more time commitment from the user and are not very straightforward to implement. Modelling something as simple as cell placement (during mitosis or migration) require additional algorithms that can detect (and correct) spatial overlap between the discrete entities. Furthermore, their major advantage – allowing freedom of movement – can potentially be a risk, in case the discrete time step is not appropriately chosen, which may result in cell collisions, especially if the domain is densely packed.[291] This can of course be mitigated by selecting a shorter time step, but leads to an increase in computing time. The approach, moreover, is more computationally expensive than its on-lattice counterpart.

Despite its disadvantages, the off-lattice approach allows the user to represent a biological system more completely, investigate the impact of both local and global variables on the spatiotemporal evolution of the system, customise the continuous mesh to ensure appropriate resolution (and not be constrained by the lattice that cannot be divorced from the discrete model), and, therefore, capture behaviour of arbitrary complexity. The aim of this chapter is to develop a hybrid, multi-paradigm, off-lattice 'transport-agent' framework, capable of predicting the impact of mass transport and hydrodynamics on the growth dynamics of cells and vice versa, and provide proof-of-principle that it can achieve the aforementioned, based on appropriate combinations of logical, algebraic, stochastic, and differential rules. As this thesis is directed towards TERM, evolution of cellular colonies inside a perfusion bioreactor was investigated. Furthermore, as an intention of this chapter, and thesis, is to illustrate the potential of the developed framework, the process selected for simulation was only tangentially relevant to the more practical bioprocess of cell expansion within a microbioreactor. However, the model presented here is meant to serve as a stepping stone to framework development and the more realistic case of capturing cellular activity as a function of flow within microfluidic devices (a desirable advancement of the model). This

framework is ideally positioned in the domain of off-lattice hybrid platforms and complements the research that is both ongoing and has been conducted towards the development of off-lattice hybrid models. Through the platform the hypothesis that bioreactor geometries, bioreactor variables and initial conditions are crucial to histogenesis and that the integrated framework could be used to capture that and optimise bioreactor design was tested.

5.2 METHODS

5.2.1 THE TRANSPORT-AGENT FRAMEWORK

To achieve the objectives set out in this thesis, tight coupling of two mature modelling platforms was pursued; first, the Flexible Large-scale Agent Modelling Framework (FLAME),[8,64,245,300,305] an agent-based system (introduced in Chapter 4), together with a computational multi-physics transport phenomena platform (CFD-ACE+, ESI Group, Paris, France), introduced in Chapter 3. As discussed, CFD-ACE+ is a multi-physics computational tool that allows easy interfacing with external modules, thus incorporating additional physics (for example, the effect of electrical or magnetic fields, temperature or deformable substrates on cells). Whereas FLAME captured the rules governing cell growth and proliferation, CFD-ACE+ was employed to simulate bioreactor hydrodynamics, mass transport processes and other biomechanical effects (for example, shear or strain triggered cellular responses). The platform considers cellular behaviour in 3D. The bioreactor models considered were relatively simple, although the platform has the capability to deal with geometries, perfusion/stimuli characteristics and cellular populations of arbitrary complexity. Conclusions from this analysis could be easily extended to living structures, for bioreactors are primarily designed to replicate the dynamic environment provided by these structures *ex vivo*.

This natural decoupling of environmental vs. cellular processes due to the application of two disparate continuum and discrete modules is actually beneficial, and justified, due to differences in time scales between processes such as convection, diffusion, chemical reaction (fast) and growth, proliferation, differentiation (slow) of the cellular colony. While the equations capturing the environmental processes were solved in their full transient form, they can be simulated assuming the cellular processes to be frozen. The continuum modality provides a 3D continuous space, which is discretised into finite-volumes (or control volumes, refer to Chapter 3) where the relevant variables are defined and fluxes calculated. The continuum modality computes the relevant concentrations, gradients, fields from a solution of mass balance of the relevant species, including transport and reaction terms. The agent-based modality allows the user to superimpose agents on the same 3D geometry, created by the continuum modality. These agents themselves can be 2- or 3-dimensional and of arbitrary shape. The agents are able to move throughout this 3D space. Agents interact with each other based on information protocols defined in the model and memory of their previous history. Communication between agents and their environment is achieved by apportioning the agent's attributes (such as stimulus, consumption, secretion, detection, etc.) into the control volume that the agent is in, which act as sources or sinks as desired by the model. The location of each agent is stored and fed into the continuum model; similarly, the relevant quantities are derived from the continuum modality and fed to the agent-based modality, where the agents identify the control volume they are occupying and respond according to the local concentrations, gradients, fields, etc.

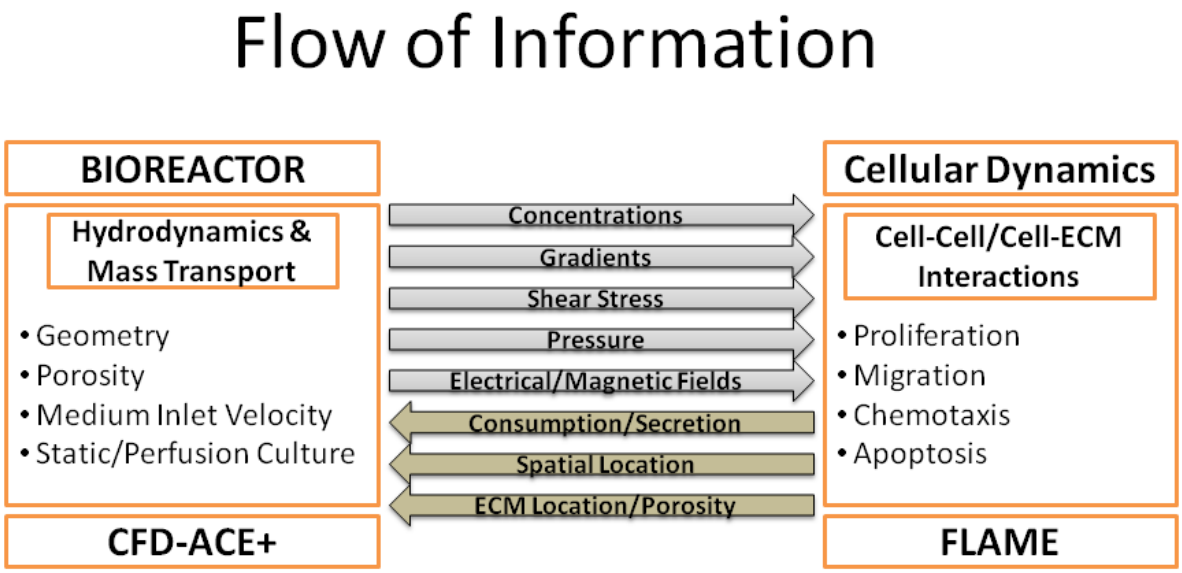

Figure 5. 1: Flow of Information in the modelling framework. The figure shows the communication between the transport-phenomena and agent-based modules that is at the heart of the modelling platform. Information relevant to bioreactor hydrodynamics and mass transport is communicated from the transport-phenomena module to the agent-based module where cells, modelled as agents, detect the local concentrations (and other continuum variables) and act based on the rules attributed to them. The cellular information is then relayed back to the transport-phenomena module to complete the circuit.

The option of introducing user-defined sub-routines to the continuum modality as well as user-defined data-structures to the agent-based modality enables the framework to deal with biological systems of arbitrary complexity. As indicated earlier, the continuum modality solves the relevant equations assuming the cellular processes are frozen for a certain period of time, at the end of which results from the continuum modality is passed on to the agent-based modality to simulate the cellular process(es). The agent-based model is run for the same period as the continuum model, at the end of which data from the agent-based modality is passed on to the continuum modality. This way the disparity of time scales is bridged in a simple multiscale modelling manner. Numeric details specific to the simulations conducted to demonstrate proof-of-principle are presented next. Figure 5.1 shows the exchange of information between the agent-based and the transport modalities that is at the heart of this hybrid platform.

5.2.2.1 OXYGEN TRANSPORT AND CONSUMPTION

The cells were assumed to be seeded in a porous scaffold inside the bioreactors and were supported by the influx of oxygenated medium. Two virtual bioreactors of different geometries but same volume were constructed. The two bioreactor geometries can be seen in Figure 5.2. The dimensions of the bioreactors as well as bioreactor variables are listed in Table 5.1.

Bioreactor Variables		
Geometries		2
Scalar		Oxygen
Initial Concentration14		0.21 mol m^{-3}
Scalar Diffusivity in the Media14		10^{-5} m^2/h
Scaffold Porosity		75%
Scaffold Permeability		10^{-10} m^2
Medium Density		1000 kg/m^3
Medium Viscosity		0.001 kg/m-s
Medium Inlet Velocity		0.001 m/s, 0.01 m/s
Bioreactor Dimensions	Length	1 mm
	Width	1 mm
	Depth	0.2 mm

Table 5. 1: Bioreactor Variables. The table lists various volume, boundary, and initial conditions applied to compute mass transport inside the bioreactors. The dynamic relationship between cell proliferation and mass transport of oxygen was investigated in two bioreactors of same volume but different geometries (shown in Figure 5.2). Oxygenated medium was introduced at two different velocities: 0.001 m/s and 0.01 m/s.

Bioreactor construction was followed by a grid independence analysis, which was conducted on one of the bioreactors (geometry A). The bioreactor was tested with structured (50,000; 100,000; 200,000 and 400,000 elements) as well as unstructured (100,000 and 400,000 elements) grids. The results indicated no appreciable difference between a bioreactor with a 100,000 element structured grid and a bioreactor with a 400,000 element unstructured grid. As a result, to strike a balance between result accuracy and computational time, the bioreactors were solved using 100,000 elements structured grids. Furthermore, the scaffolds were assigned constant isotropic porosity and permeability (75% and 10^{-10} m^2

respectively) and tested for medium inlet velocities of 0.01 m/s and 0.001 m/s. Please refer to Table 5.2 for a description of different test cases.

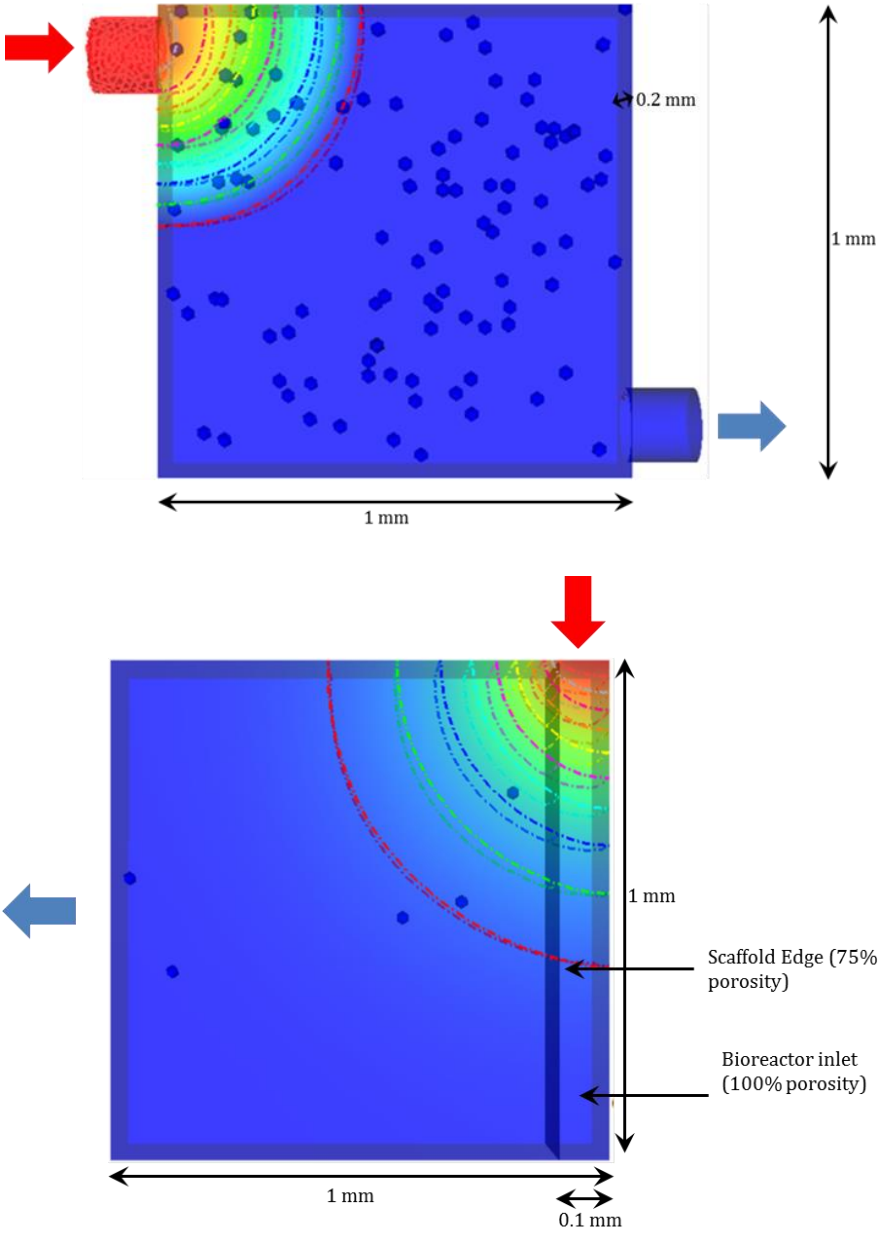

Figure 5. 2: Bioreactor configurations utilised in this investigation. The figure shows the two bioreactor configurations used in this study. Each bioreactor was 1mm×1mm×0.2mm in dimensions (irrespective of the ports, which were approximately 0.1mm in radius). The geometry on the top consists of two cylindrical ports situated at diagonally opposite ends of the bioreactor. The scaffold inside the bioreactor was assumed to cover most of its internal space. In the geometry shown at the bottom, the top right side of the bioreactor served as the inlet, whereas the left edge served as the outlet. The scaffold in this bioreactor was only assumed to extend to 0.9 mm of the bioreactor length leaving a volume of 0.1mm×1mm×0.2mm with no porous-medium resistance to incoming flow. This space can be observed on the right side of the column marked as scaffold edge. Scaffolds in both geometries were assigned a porosity of 75%. Solid arrows indicate the direction of medium flow, with the colour indicating concentration of dissolved oxygen (red: high; blue: low – refer to Table 5 for relevant values).

Concentration gradient of oxygen is known to affect tissue-growth rate in bio-artificial scaffolds.[12] Therefore, the model was designed to study cell growth in a continuous medium perfusion system with oxygen being the limiting nutrient. After the bioreactor-scaffold complex was suffused with virtual cells, oxygenated medium was pumped in at the velocities (and corresponding flow rates) listed in Table 5.2. Oxygen transport inside the bioreactor occurred by convective as well as diffusive processes. The diffusivity of oxygen in the medium was taken as 10^{-5} m^2/hr.[282] The medium supplied to the bioreactors was assumed to be carrying oxygen at a concentration of 0.21 mol/m^3.[282] Oxygen consumption was modelled using cells as proliferating and migrating non-zero sinks consuming oxygen at 3.39 mol kg m^{-3} s^{-1}.[282] In the agent-based component this amounts to oxygen consumption by each cell at a rate of 12.2 mol m^{-3} hr^{-1}.

Case	Bioreactor Geometry	Initial Cell Density	Medium Inlet Velocity (m/s)	Flow Rate (µL/min)	Relevant Figures
Case 1	A	100	0.001	1.88	Fig 5.3
Case 2	A	100	0.01	0.188	Fig 5.4/5.7/5.8
Case 3	B	5	0.001	2.4	Fig 5.5/5.6
Case 4	B	5	0.01	0.24	Fig 5.6

Table 5. 2: **Test Cases.** The table lists various test cases simulated for the purposes of this investigation and relevant parameters, such as medium flow rate, and relevant figures and supplementary material.

Oxygen (or any other substance) consumption (or secretion), modelled as an individual-level event, was accounted by the source term represented as S_Φ in (2.20).

$$\frac{\partial}{\partial t}(\rho\Phi) + \nabla.(\rho U\Phi) - \nabla.(\Gamma_\Phi \nabla\Phi) = S_\Phi \qquad (2.20)$$

The equation was implemented with migrating non-zero sinks (positioned where the cells are found). Oxygen concentration in this model is assumed to vary based on the bioreactor hydrodynamics, mass transport and cell proliferation. Dirichlet and Neumann boundary conditions were applied as needed. Oxygen transport and consumption, in sync with cellular proliferation and migration, was calculated for periods of four to six days depending on the case and the fate of the cells in the virtual bioreactors. In the current state of development,

absence of neo-tissue within the interconnected pore space was assumed. To keep this initial attempt at framework development simple, co-transport of oxygen and glucose and momentum exchange between cells and the fluid phase were not considered.

Behaviour	Rule
Proliferation	Cell proliferation occurs until confluence as per assigned probabilities (Table 5.5)
Migration	Migration occurs either via persistent random walk (under normoxic conditions) or chemotaxis (under hypoxic conditions)
	If local oxygen concentration > 0.0672mol/m^3, cells display persistent random walk
	Cell speed during persistent random walk = 10μm/hr
	If local oxygen concentration < 0.0672mol/m^3, chemotaxis begins
	Chemotaxis speed = 20μm/hr
Apoptosis	If a cell experiences hypoxia for more than 15 hours, it dies of hypoxia-induced apoptosis
	If, while performing chemotaxis, a cell ends up in a region rich in oxygen, it goes back to display persistent random walk

Table 5. 3: **Rules.** The table summarises the rules used to simulate cellular dynamics.

5.2.2.2 CELL POPULATION DYNAMICS

The platform is designed to incorporate a variety of behaviours displayed by cells: migration, proliferation, differentiation, chemotaxis, apoptosis, necrosis and other processes as needed. Differentiation was not considered in the cases tested in this chapter. The biological rules governing the virtual cells, listed in Table 5.3, are controlled by constants, for example cell cycle, as well as variables – which in turn emerge from the transport phenomena component – such as oxygen concentration gradients.

The cells were assumed to be non-deformable spheres of radius 10 μm each and capable of consuming oxygen at a rate of 12.2 mol m^{-3} hr^{-1} $cell^{-1}$ when available. Initial cell placement inside the bioreactor-scaffold complex was random. Forces between the agents were resolved using the explicit overlap detection and correction scheme discussed in Chapter 4. While the equations are being presented here again, refer to §4.3.4.1 for the relevant explanation.

$$F_{c,ij} = s_{ij} O_{ij} c_{c,i} \tag{4.19}$$

$$O_{ij} = \sqrt{\left(x_i - x_j\right)^2 + \left(y_i - y_j\right)^2 + \left(z_i - z_j\right)^2} - \left(r_i + r_j\right) \quad (4.20)$$

$$s_{ij} = 1 \Big/ \sqrt{\left(x_i - x_j\right)^2 + \left(y_i - y_j\right)^2 + \left(z_i - z_j\right)^2} \quad (4.21)$$

$$c_{x,i} = \left(x_j - x_i\right)\alpha \quad (4.22.1)$$

$$c_{y,i} = \left(y_j - y_i\right)\alpha \quad (4.22.2)$$

$$c_{z,i} = \left(z_j - z_i\right)\alpha \quad (4.22.3)$$

$$x_{i,t} = x_{i,0} + F_{x,ij} \quad (4.23.1)$$

$$y_{i,t} = y_{i,0} + F_{y,ij} \quad (4.23.2)$$

$$z_{i,t} = z_{i,0} + F_{z,ij} \quad (4.23.3)$$

The cells could migrate by choosing either a persistent random walk or chemotaxis. The cells displayed persistent random walk[12,13,284] if the local oxygen concentration > 0.0672 mol/m^3. If, however, the local oxygen concentration dropped below 0.0672 mol/m^3, the cells began to display chemotaxis in a bid to move to an oxygen-rich region. This value is equal to 0.3% of the initial oxygen concentration, and was decided upon after reviewing the work of Liu *et al*. (2007)[306] who reported induction of hypoxia at oxygen concentration of 0.3% in HCT 116 colon carcinoma cells. The cells were assumed to divide until confluence or until the point where there was not enough oxygen available to them. Confluence, or the point where the bioreactor is completely filled with cells, was achieved when each cell was bonded to at least four other cells. The cells divided based on a division probability assigned to them: 64% of the cells divided by eighteen hours, 32% by twenty four hours and the remaining 4% by thirty hours.[307] The daughter cell is positioned at a random orientation relating to the coordinates of the parent cell, and in the immediate vicinity of the parent cell.

Another feature this platform has to offer is that it takes into account cell apoptosis that may occur due to cells experiencing hypoxia in oxygen deficient areas created in the bioreactor due to cell growth or other factors such as low medium inlet rate or deficient mixing. If the local oxygen concentration dropped below 0.0672 mol/m^3, the cells began to

express apoptotic proteins. If a cell stayed under the hypoxic condition for more than 15 hours, it died of hypoxia-induced apoptosis. The cells were assumed to exert a repulsive force on each other in case of contact, which was taken from a model developed by Tao *et al*. (2007)[305]. Although the nature of mechanical forces that cells exert on each other is quite complex, the physical forces were resolved using constants instead of variables as the primary objective was to display the platform's capability to handle such occurrences and to accommodate any such sub-model when available.

5.2.2.3 CELL MIGRATION

The extracellular environment and cell type affect and dynamically modulate[12] a cell's speed and its persistent time,[13] with prostate cancer cells displaying speeds of 8-15 μm/hr in 3D collagen matrices and melanoma cells 20-40 μm/hr in 3D collagen matrices modified with RGD proteins.[13,308,309] The scaffold in our case was assumed to have no restraining effect on cell migration. Therefore, despite their presence in a porous scaffold, the cells could move freely in all (three-dimensional) directions.

A migration speed was assigned to each cell. As long as the cell displayed persistent random walk, it could acquire a maximum speed of 10 μm/hr. The cell continued moving in a particular direction for two hours after which, based on the availability of space, the cell assumed a new randomly chosen direction, in agreement with existing literature.[12,13,282,284,307] If, while migrating, a cell came in contact with another cell or the bioreactor boundary, it stopped for an hour, in agreement with existing literature,[12,13,282,284,307] before changing its direction and continuing migrating in a randomly chosen direction. The cells stopped moving prior to dividing and, along with the daughter cell, remained at rest for about an hour after division.[284] While displaying chemotaxis, the speed and direction attributed to the cells were based on the local concentration gradients. Under chemotaxis the cells were assumed to display a set migration speed of 20 μm/hr. If,

while performing chemotaxis, a cell ended up in a region rich in oxygen, it went back to displaying the persistent random walk; if not, then the cell moved under the influence of the concentration gradient until it either ended up in an oxygen rich area or it died. The algorithms for persistent random walk and chemotaxis have been summarised in Table 5.4.

Migration Algorithm	**If** Oxygen concentration ≥ 0.0672 mol/m^3	**Then** initiate **Persistent Random Walk**	i. (at t=0) acquire a random direction	
			ii. Traverse in that direction at 10 μm/hr	
			iii. Continue moving in that direction for 2 hours	
			iv. After two hours: stop, and remain at rest for an hour	
			v. Repeat steps i-iv	
			If in contact with another cell (due to cell-cell collision) or environment boundary, **Then**	vi. Stop, and remain at rest for an hour
				vii. Acquire a random direction
				viii. Repeat steps i-iv
			If about to divide, **Then**	ix. Stop
				x. Divide
				xi. Remain at rest (along with the daughter cell) for an hour after division
				xii. After one hour, repeat steps i-iv
	Else if Oxygen concentration ≤ 0.0672 mol/m^3	**Then** initiate **Chemotaxis**	a. Access oxygen concentration gradient obtain from the transport equation	
			b. Locate the closest computational 'cell'	
			c. Align direction in terms of the gradient	
			d. Traverse in the direction of the gradient at a speed of 20 μm/hr	
			e. Continue chemotaxing until in a normoxic region (i.e. Oxygen concentration ≥ 0.0672 mol/m^3)	
			If in a normoxic region	**Then** Initiate **Persistent Random Walk**
				Repeat steps i-xii

Table 5. 4: Migration algorithms for persistent random walk and chemotaxis. The table lists the oxygen requirements that influence the migratory pattern of cells, along with the set of steps that cells follow while displaying either kind of migration.

Apoptotic trigger was initiated if the local oxygen concentration dropped below 0.0672 mol/m^3. If a cell remained in an oxygen-deficient region for more than 7 hours, it changed its state (and its colour in the visualisation platform used to analyse the results of

the simulations) indicating that the apoptotic mechanism, physically represented by formation of apoptotic proteins in the cells that lead to cell death, has been triggered. If the cell, in chemotaxis mode at this point, was successfully able to move to an oxygen rich region it survived; otherwise if it remained in a hypoxic environment for more than 15 hours since the start of the apoptotic mechanism, it died.

Cellular Variables	
Persistence Time[14-16, 20, 53]	2 hours
Post Collision, pre-Division Stationary Phase[20]	1 hour
Cell Cycle & Division Probability of Cell Population[53]	18 hours (64%)
	24 hours (32%)
	32 hours (4%)
Maximum Random Speed	10 μm/hr
Cell speed during Chemotaxis	20 μm/hr
Oxygen Consumption Rate[14]	3.39 mol kg m^{-3} s^{-1}
Chemotaxis Ensues at Scalar Concentration[52]	0.0672 mol m^{-3}
Hypoxia-induced Apoptosis	15 hours
Cell Density in Bioreactors	100, 5

Table 5. 5: Cellular Variables and Rules. The table lists parameters pertinent to the cells as well as rules the cells followed during the computation. For example, under normoxic condition cells displayed persistent random walk changing direction once every two hours. Cells would only stop if it is in contact with another cell or about to undergo mitosis. Furthermore, chemotaxis ensues if a cell experiences local oxygen concentration of less than 0.0672 mol m^{-3}. Failure to move to a normoxic region within 15 hours since the inception of chemotaxis leads to hypoxia-induced apoptosis.

The time advancement of the system was organised around computing cycles, usually referred to as *iterations* in agent-based modelling. Since this term has a different meaning in transport phenomena implicit solvers, the author shall refrain from using the term – it suffices to say that each computing cycle or iteration (in FLAME) was set to 15 minutes and this value sufficiently captured the fine features of the system, while leading to reasonable computational time requirements. Please refer to Table 5.5 for a summary of the cellular variables utilised in this investigation. Transport processes, however, occur at a much faster rate compared to the time scales observed for cellular dynamics. The solution of transport equation was, therefore, decoupled from the solution of cellular evolution. As

such, the two models were executed with different time-step characteristics, as explained in the pseudocode below.

Set initial conditions for bioreactor hydrodynamics
Set initial conditions for cellular behaviour
Time-march continuum mechanics assuming cellular population is frozen
I. Bioreactor Hydrodynamics
- *a. Solutions for flow*
- *b. Solution for concentration*
- *c. Calculation of gradients*

Time-march cellular population
II. Cellular Dynamics
- *d. Sense Oxygen concentration*
- *e. Sense Oxygen gradient*
- *f. Intercellular Forces*
- *g. Migration (Persistent Random Walk Or Chemotaxis)*
- *h. Proliferation*
- *i. Apoptosis*

Time Step, $t \leftarrow t + \Delta t$
repeat until desired time interval is simulated

Box 5. 1: Pseudocode employed to execute the continuum and discrete models.

5.2.3 EXPERIMENTAL VALIDATION

In order to experimentally validate the platform cellular chemotaxis was simulated in a direct visualisation chamber. To achieve this a virtual analogue of the *Insall Chamber*[310] was created. The Insall chamber is a direct visualisation chamber developed by *Muinonen-Martin et al*. (2010)[310] to study chemotaxis using high numerical aperture (NA) oil immersion lenses, which was not possible with other visualisation chambers. The Insall chamber consists of an inside well containing the control and an outside well (enclosing the inner well) containing the chemoattractant. The investigators analysed chemotaxis of MV3 melanoma cells based on linear concentration gradients of Foetal Bovine Serum (FBS). Details regarding the chamber and the experiment can be found here.[310]

A virtual Insall chamber was constructed, based on the exact dimensions and specifications of the experimental setup, as obtained directly via private communication[311,312] with the developers. To ensure consistency between the simulation and

experiment, diffusion of FBS was modelled in the half of chamber containing the 0.5 mm bridge as shown in Figure 5.9. The geometry was discretised using structured grids (approximately 150,000 cells ensured grid independence). The diffusivity of FBS considered in the model was derived from the *Svedberg*[313] equation and calculated to be 8.705×10^{-11} m^2/s. Virtual MV3 melanoma cells were modelled as spheres chemotaxing at a speed of 8 μm/hr after sensing a critical FBS concentration (30% of the initial FBS concentration in the outer well). In the absence of the gradient, or in case the local gradient < 30% FBS, cells migrated by displaying the persistent random walk. Cellular migration coupled to FBS transport in the virtual *Insall* chamber was modelled for a period of 25 physical hours. As a control, MV3 melanoma cell migration was modelled in the absence of FBS. Statistical[xxiv] significance was determined by conducting two-way ANOVA with time and coordinates as discrete outcomes. $p<0.05$ was interpreted as significant. In order to conduct the analysis, the *x* and *y* coordinates of cells were averaged at each time step.

Furthermore, conclusions from the virtual assay were compared against a separate (real) chemotaxis assay where the Insall chamber was used to observe migration of melanoma cells in the presence and absence of FBS.[314] In this experiment, melanoma cells were seeded within the Insall chamber. They were spread homogeneously in order to avoid bias in migration due to contact inhibition. The cells were loaded inside the chamber in complete medium that had been conditioned previously for 48 hours by melanoma cells. One of the wells was subsequently replaced with medium containing 10% FBS (the concentration utilised in the virtual assay). The investigators recorded images capturing cell migration through an inverted time-lapse microscope, which (following processing) were used to track cell trajectories via *MtrackJ*

[xxiv] The author acknowledges technical support from Dr Chris Newby (University of Leicester) in conducting the Two-way ANOVA

(www.imagescience.org/meijering/software/mtrackj/). This data was employed to create spider plots (using the data processing toolbox in MATLAB referred to as *Circstat*[315]) and to calculate the *chemotaxis index*: cosine of the angle between a line that connects a cell's start point to its end point and one that is directly up the gradient.[316] The plots displaying chemotaxis index are presented as mean ± standard error of the mean.[314] The chemotaxis index provided a direct way of comparing the virtual data against its empirical counterpart. For the computational case, obtaining cell coordinates for each cell at the end of each iteration was relatively straightforward, as this was part of model output. In summary, every effort was made to match experimental and virtual conditions and parameters as much as possible, within the limitations of model assumptions as well as available experimental/data-processing details. For more details the interested reader is referred to the original article.[314]

5.3 RESULTS

Figure 5.3 shows the oxygen concentration contour plot as well as cell distribution inside one of the two different types of bioreactors, at different time instances. The bioreactor is a rectangular prism in shape with two ports: one serving as an inlet (top left) and the other as an outlet (bottom right). Initially, the bioreactor was seeded with one hundred cells. The figures capture the interplay between cell population dynamics and the overall mass transport at various time steps – the final step was recorded at 4 physical days. The migration of cells from the relatively deoxygenated region (bottom right) of the bioreactor to top left can be observed.

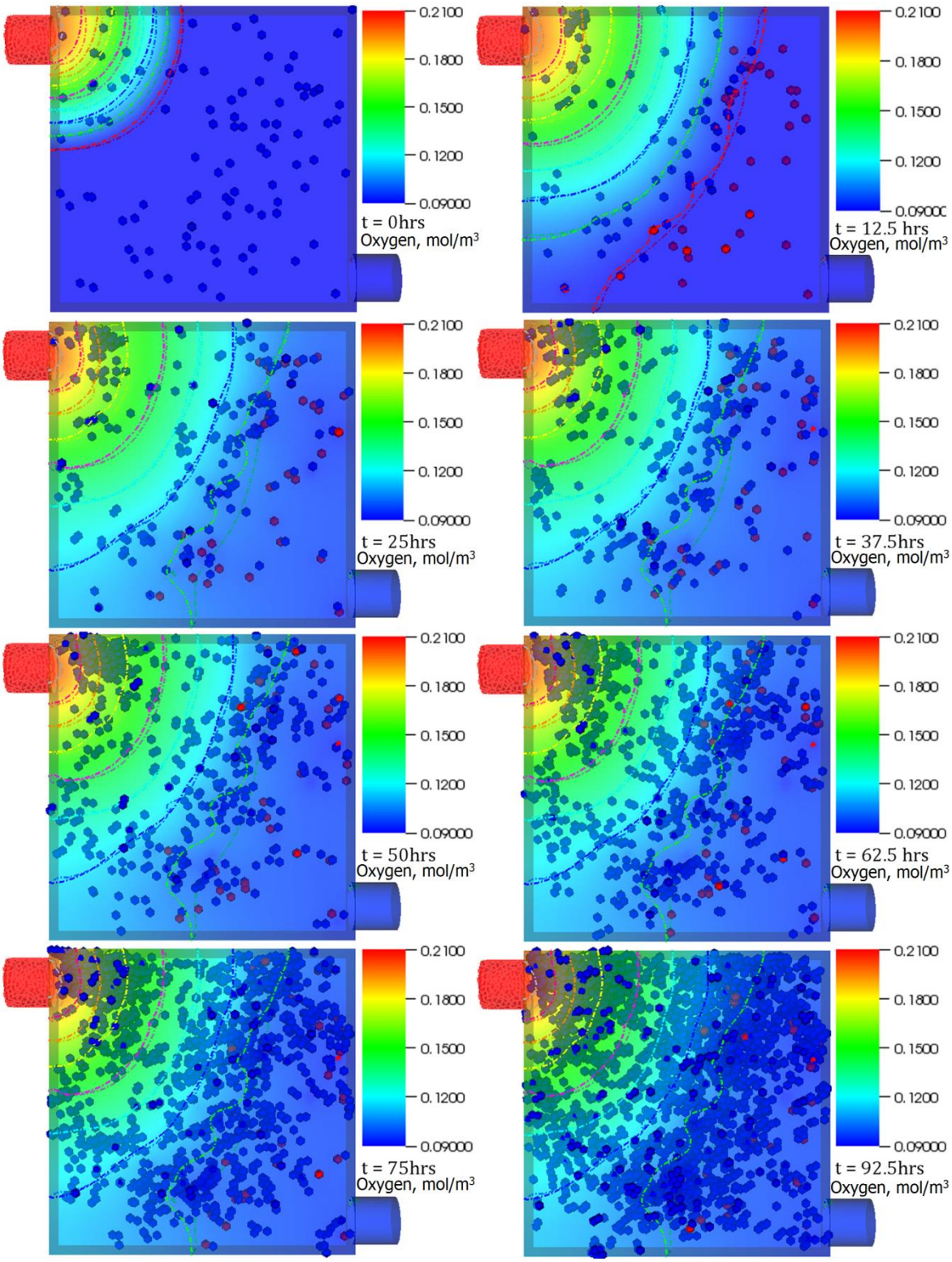

Figure 5. 3: **Case 1 results**. Temporal evolution of cell population and nutrient concentration inside a bioreactor (geometry A) with a medium inlet velocity of 0.01m/s. The final frame captures cell distribution at the end of 4 (physical) days – the time interval between snapshots (left to right) is 12.5 hours. The initial cell density was 100. The concentration contours can be observed to change continuously throughout the simulation. This is in contrast with physical systems with no cells inside where such behaviour would not be possible after the flow becomes stationary beyond initial transients. This demonstrates the platform's ability capture dynamic reciprocity.

The dynamic nature of the relationship is best evident by the change in oxygen concentration close to the inlet port – it decreases in intensity in the subsequent time frames, corresponding to a decrease in concentration due to cellular proliferation and resulting increased consumption. Cell division in the region close to the inlet port was initially higher as compared to the rest of the reactor. This propensity of cells to divide closer to the inlet port where Oxygen concentration is relatively high is behaviour one would normally expect in reality.

It must be stressed that this feature was not explicitly coded in the model but, it seems, emerged from the integration of the rule-set with underlying transport phenomena. Widespread proliferation is observed towards the end of the simulation as oxygen concentration exceeds the threshold value throughout the bioreactor. An interesting observation remains the preference the cells show in aligning themselves to the contour curves; thus resulting in an emergent banded distribution pattern – most evident in the second, third and fourth time frames.

Figure 5.4 shows the temporal evolution of cell population and nutrient concentration in a bioreactor (same as Figure 5.3) but with a medium inlet velocity (0.01 m/s), an order of magnitude higher than Case 1. As was the case in Figure 5.3, the cells tend to migrate away from the oxygen deficient region: chemotaxis. The top left region remains an area of high cell division during the initial stages. An important observation is the constant translation of the oxygen concentration contours. It is of interest to note that the banding pattern is significantly less pronounced in this case, and of a different shape than that observed in the previous virtual experiment most probably due to higher oxygen concentration relative to Case I. This behaviour merits further investigation as it resonates, albeit modestly, with self-organisation observed in biological systems. In effect, the continuous supply of oxygen on one hand and the very random and unpredictable

consumption on the other led to a non-intuitive pattern formation, which spatially does not correspond to where the pure transport solution of the system would place the oxygen threshold iso-contour. Part of this emergent effect comes from the randomness inherent in cell (and agent) migration, but the most significant portion comes from the interplay of these two profoundly different mechanisms that such a hybrid methodology is well-positioned to capture.

It must be noted that no matter which threshold is selected (within reasonable and biologically meaningful limits) the pattern formation is persistent in structure (of course varying slightly in exact position and formation) and thus clearly a feature of the coupled system. This very interesting and exciting emergent theme was observed in every simulation. Such behaviour can be exploited to create multiple mono-layers of defined thicknesses or bi-layers where cells towards the more deprived region of the bioreactor can act as an interface (as in a bone-cartilage hybrid structure).

Figure 5.5 examines a different bioreactor setup. The top right end of the bioreactor serves as the inlet whereas the entire left as well as bottom ends of the bioreactor serve as the outlet. The medium inlet velocity in this case was 0.001 m/s. The bioreactor was randomly seeded with 5 cells. The simulation was run for a total of 6 physical days. By the second frame (17.5 hours), most of the cells in the deoxygenated region have died – a result of hypoxia-induced apoptosis. The cluster of cells formed by the final frame is a result of the *single* cell that was able to move and begin proliferating in the oxygen rich zone. When the medium inlet velocity was increased to 0.01 m/s, more cells survived which in turn aided in the colonisation of the bioreactor.

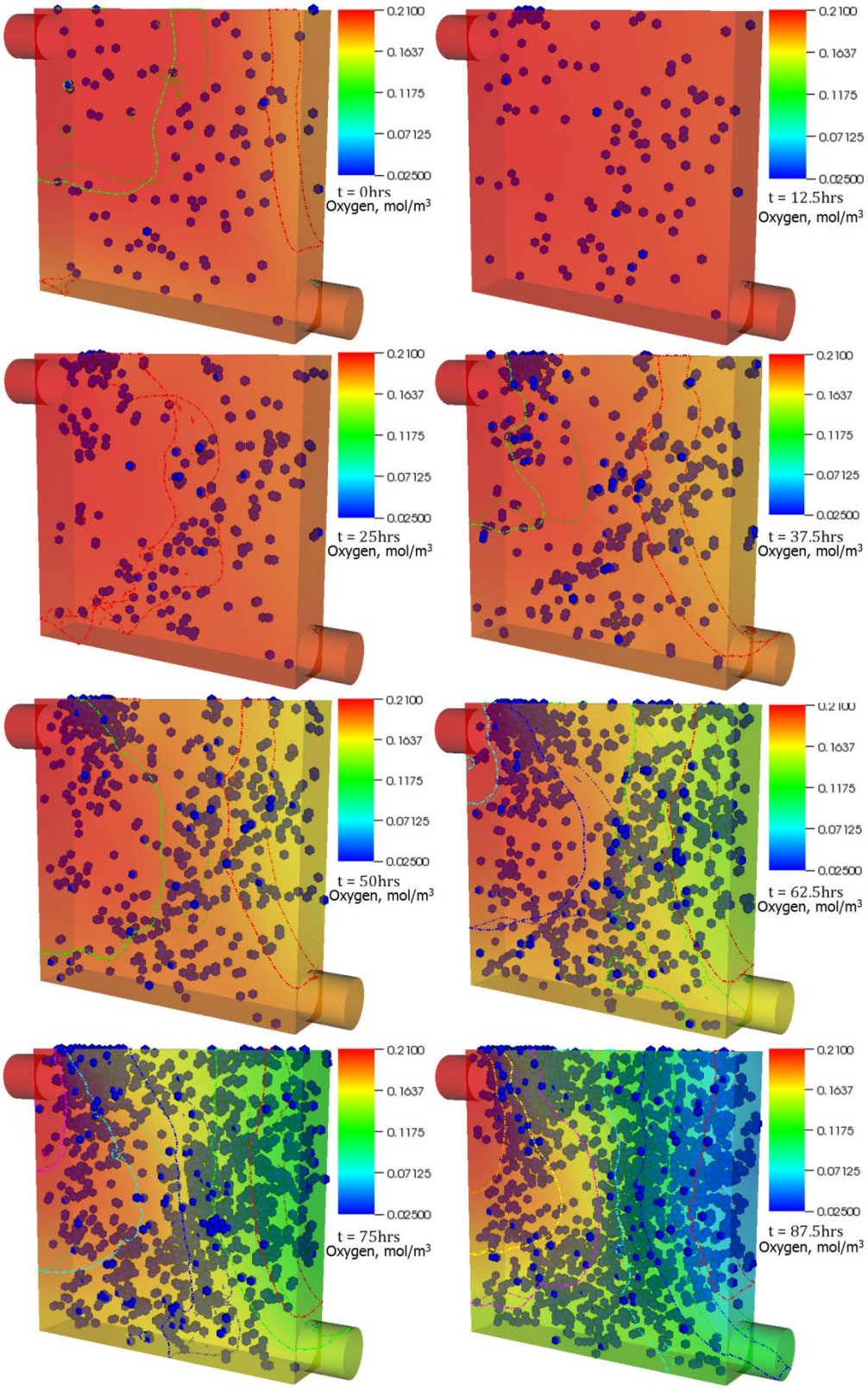

Figure 5. 4: **Case 2 results**. Temporal evolution of cell population and nutrient concentration inside a bioreactor (geometry A) with a medium inlet velocity of 0.01m/s. The final frame captures cell distribution at the end of 4 (physical) days – the time interval between snapshots (left to right) is 12.5 hours. The initial cell density was 100. The concentration contours can be observed to change continuously throughout the simulation. This is in contrast with physical systems with no cells inside

where such behaviour would not be possible after the flow becomes stationary beyond initial transients. This demonstrates the platform's ability capture dynamic reciprocity.

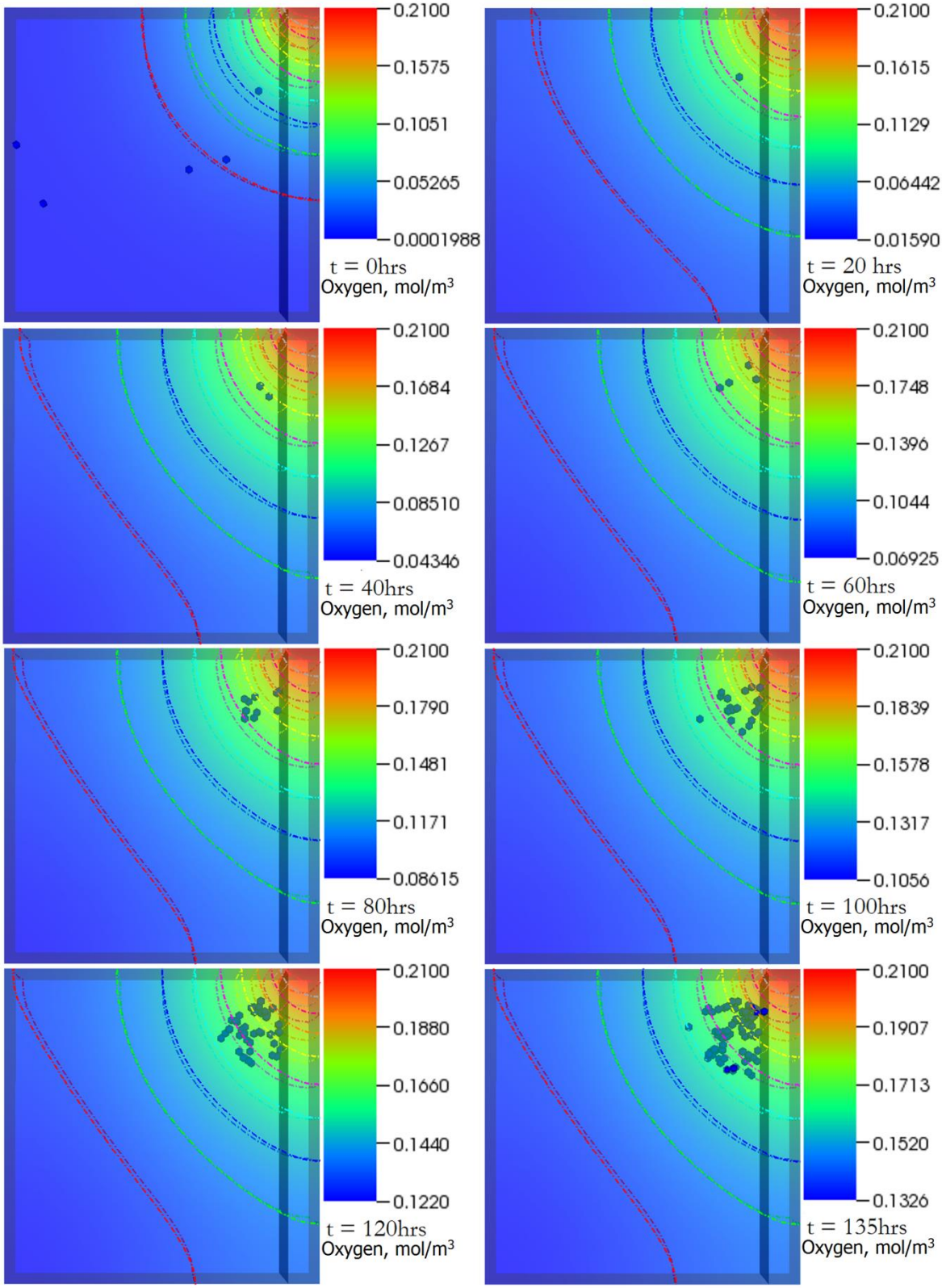

Figure 5. 5: Case 3 results. The figure shows temporal evolution of cell population and nutrient concentration inside a bioreactor (geometry B) with a medium inlet velocity of 0.001m/s. The top right end of the bioreactor serves as the inlet whereas the entire left as well as bottom ends of the bioreactor serve as outlet. The initial cell density was 5. The time interval between snapshots (left to right) is 20 hours. The final frame captures cell distribution at the end of 6 (physical) days.

In comparison (Figure 5.6), the bioreactor with the higher inlet velocity by the final frame ends up with considerably higher number of cells and a distinct growth pattern (resembling the banding arrangement observed in the first case) – once again displaying not only the dynamic nature of the system but the dependence of the spatiotemporal evolution of the system on processes such as chemotaxis and apoptosis. It must be noted that, in some frames (in Figure 5.3), a few cells still appear 'red' despite the local oxygen concentration being higher than the threshold. This is not connected with the simulation itself, but it is rather a visualisation effect, utilised to highlight the hypoxic **history** of the relevant cells. The cells are no longer hypoxic and continue to grow as any other normoxic cell.

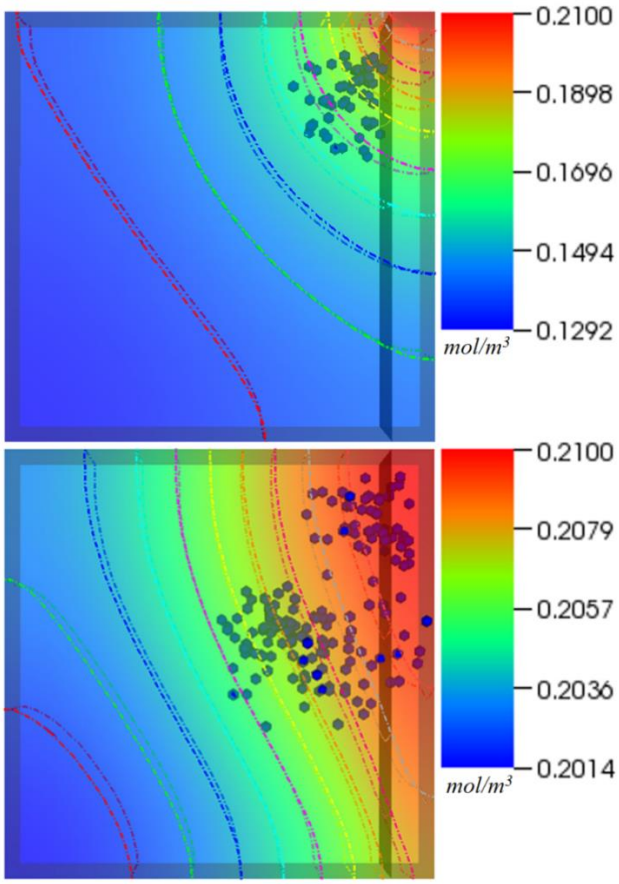

Figure 5. 6: Different boundary conditions lead to different output. The figure shows temporal evolution of cell population and nutrient concentration in the same bioreactor set at different medium inlet velocities; 0.001m/s (top) and 0.01m/s (bottom). The bioreactor on the right ends up with considerably higher number of cells and a distinct growth pattern. This displays the dynamic nature of the system and the dependence of the spatiotemporal evolution of the system on processes such as chemotaxis and apoptosis. The frames were recorded at 5.5 days.

Figure 5.7 provides a comparison in performance of the hybrid framework (with agents) against the (transport only, agent-less) continuum method (outlined in Chapter 3) within the context of evaluating oxygen concentration in the bioreactor with initial and boundary conditions utilised in Case II.

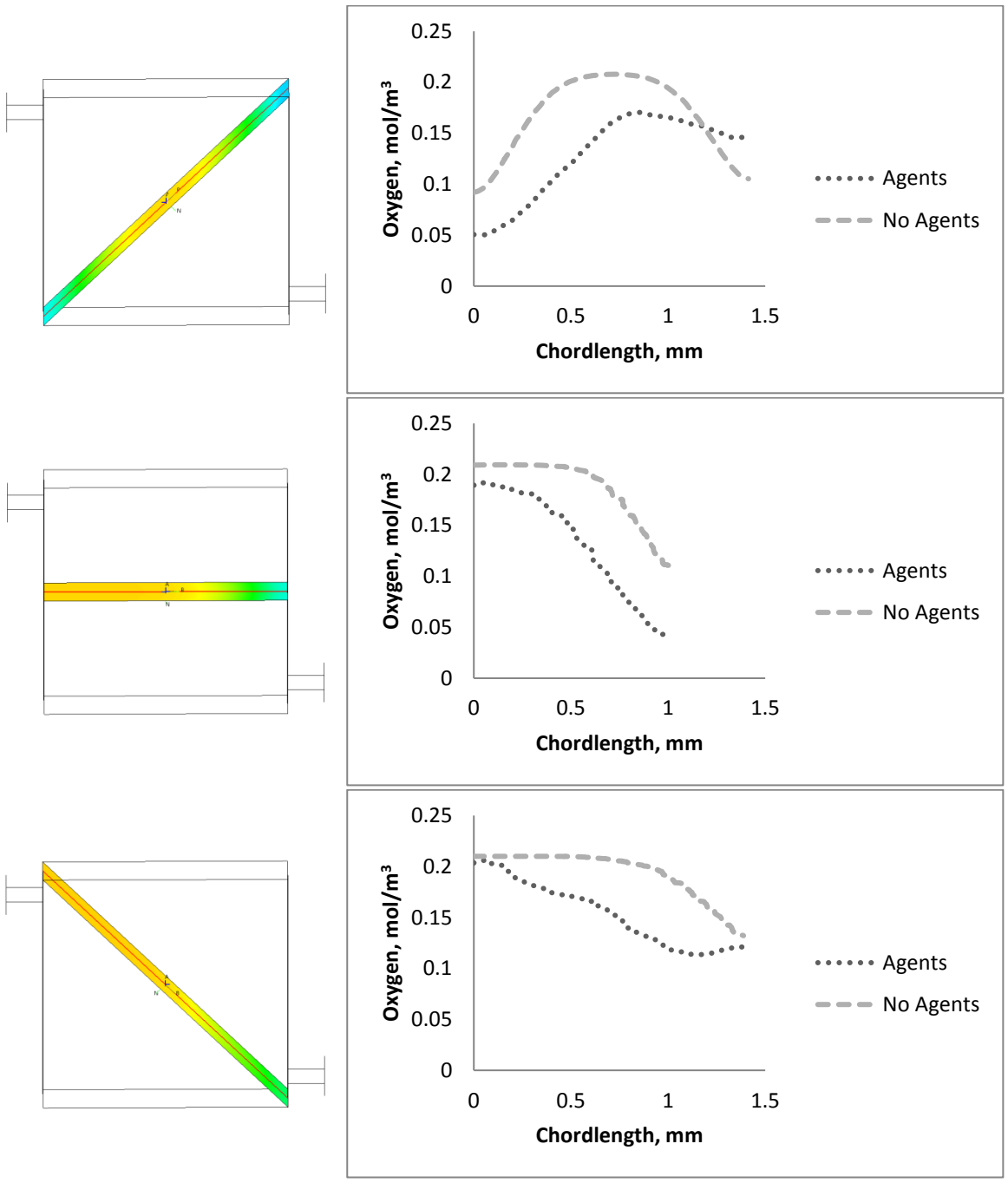

Figure 5. 7: Comparison of the hybrid approach against the continuum approach (without agents). Major differences in oxygen concentration can be observed within the bioreactor. Clearly, in the absence of mobile agents, which can represent cellular behaviour, a standalone continuum methodology will not be most the most efficient tool in optimising bioreactor design.

In order to compare oxygen concentrations within the two cases, three (red coloured, refer to Figure 5.7) chords (~1 mm) were drawn within the bioreactor (two diagonal and one horizontal). The concentration was computed along the length of these chords. The data for the hybrid model represent the state of the bioreactor on the 5th day whereas data for the agent-less model represent conditions within the bioreactor at steady state. There is an appreciable difference in concentrations across the three cuts. The benefit of using the hybrid approach in bioreactor design becomes evident when one considers the fact that this difference surfaces with the hybrid bioreactor case (with agents) containing ~1800 agents only (at the end of day 5), which is nowhere near the realistic scenario of 1 million cells/mL of cell suspension (the figure utilised in Chapter 3).

Furthermore, Figure 5.8 shows flow vectors and streamlines for the agent-rich as well as agent-less cases. Flow in both cases is almost identical due, again, to lack of explicit treatment of momentum exchange. The flow, with *Re* = 20, is laminar and fully developed.

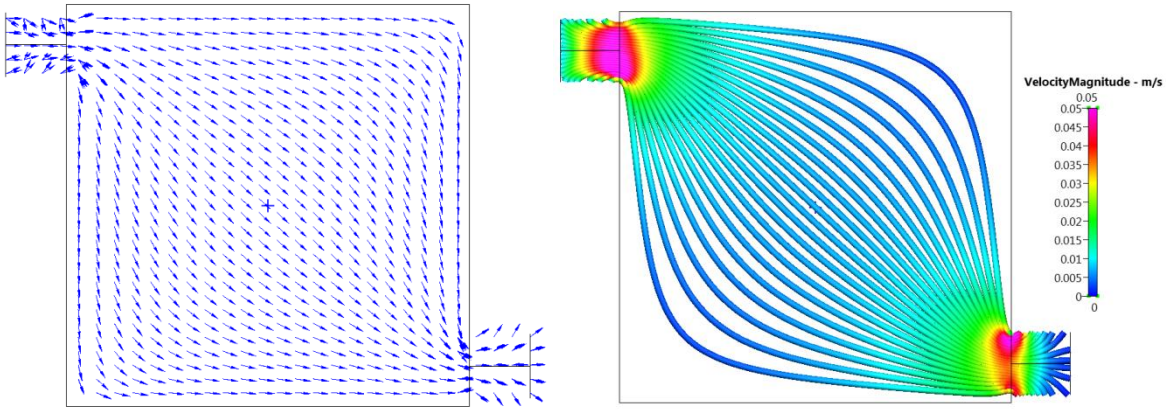

Figure 5. 8: Flow within the bioreactor. Identical flow was observed in agent-rich and agent-less bioreactors. As can be observed, the flow is well developed and laminar.

Figure 5.9 shows the evolution of FBS concentration gradient across the bridge and the cells' migration response to the gradient over a period of 25 hours. Cell chemotaxis can be easily observed with the increase in FBS gradient towards the inner chamber. However, few cells that have not committed to chemotaxing can be observed at the end of the simulation on the left hand side of the bridge, but that is because these cells have not yet

sensed the critical FBS concentration (30% of the initial concentration in the outer well). This time-lag between the moment when cells supplied with FBS stop moving randomly (as they have not sensed the critical concentration yet) and start chemotaxing can be better observed in Figure 5.10, which plots the averaged x-coordinates of both randomly migrating and chemotaxing cells, as a factor of time.

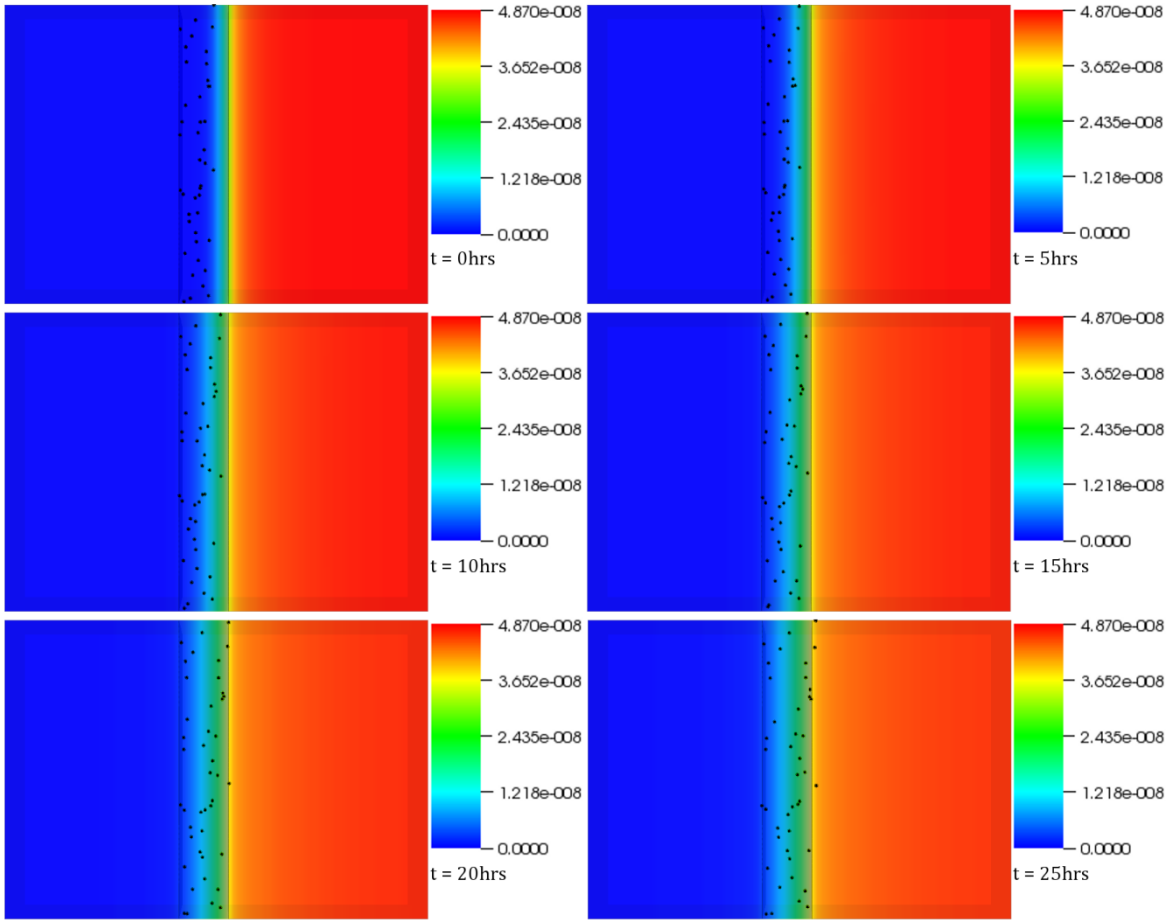

Figure 5. 9: **Experimental Validation of the platform**. The figure shows migration response of MV3 melanoma cells based on FBS concentration gradient inside the Insall chemotaxis chamber. The Insall chamber consists of two wells, one of which is filled with buffer solution (left) and the other with the chemoattractant (right). Cells are seeded in the middle of the two wells, which upon sensing the chemoattractant gradient resort to chemotaxis to move towards the well containing the chemoattractant. In this case, the MV3 melanoma cells, displaying persistent random walk in the absence of FBS gradient, move towards the right well on sensing FBS concentration. Notice the right-bound migration of cells that have sensed the critical FBS concentration (roughly 1.218×10^{-8} **kM**). Only the cells (on the far left) not in contact with the critical amount are yet to display chemotactic movement towards the well containing FBS. These chemotaxis results, when compared to similarly acquired ones but in the absence of the chemoattractant (i.e. in the Insall chamber with both wells containing the buffer solution), confirm the capability of the simulation platform to capture such behaviours (refer to Figure 5.10). The time interval between snapshots (left to right) is 5 hours. The final frame captures cell distribution at the end of 25 (physical) hours.

Two-way ANOVA revealed this deviation to be significantly different ($p<0.05$) from the migration of randomly moving cells. Furthermore, the analysis revealed significant difference ($p<0.001$) when the two data-sets were compared. The computational results met expectations, both qualitatively and quantitatively, and were in statistical agreement with the experiment conducted by Muinonen-Martin *et al*. (2010)[310], where the melanoma cells were observed to migrate towards the outer well in a comparable manner.

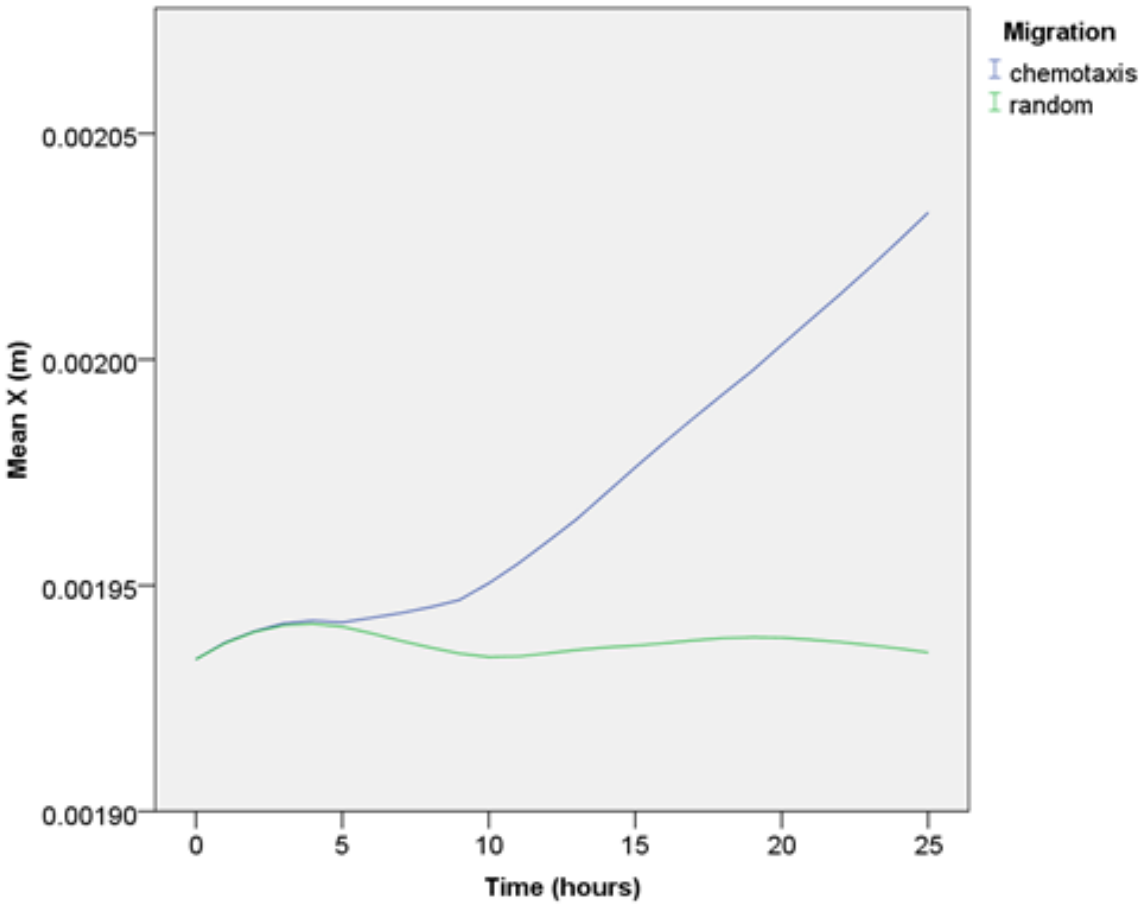

Figure 5. 10: Migratory paths acquired by the chemotaxing vs randomly migrating cells. The plot shows averaged x-coordinates of both randomly migrating and chemotaxing cells within the Insall Chamber, as a factor of time. Notice the significant deviation ($p<0.001$) between the x-coordinates of the two systems (blue: under the influence of the chemoattractant FBS, and green: in the absence of a chemoattractant). Cells only migrate in the x-direction, as can be observed in Figure 5.9, due to the concentration gradient established in the x-coordinate (by virtue of device design). Deviation in the y-axis, though appreciable, was not significant (and, therefore, not shown). Each time step is equal to 5 physical minutes.

The practical applicability of these observations was further confirmed in Figure 5.11, which compares spider plots tracking individual cell trajectories and the chemotaxis

indices in the absence and presence of the chemoattractant for the real (Figure 5.11 A) and virtual (Figure 5.11 B,C) cases. There seem to be slight differences in cell trajectories, which are inevitable given this comparison was conducted post-hoc and the fact that the two assays were not developed in conjunction. However, there are similarities too. The paths the cells followed in both experimental and computational setup displayed a strong bias for migration in the direction of the chemoattractant (towards the right). This directionality was not observed in either case in the absence of the chemoattractant.

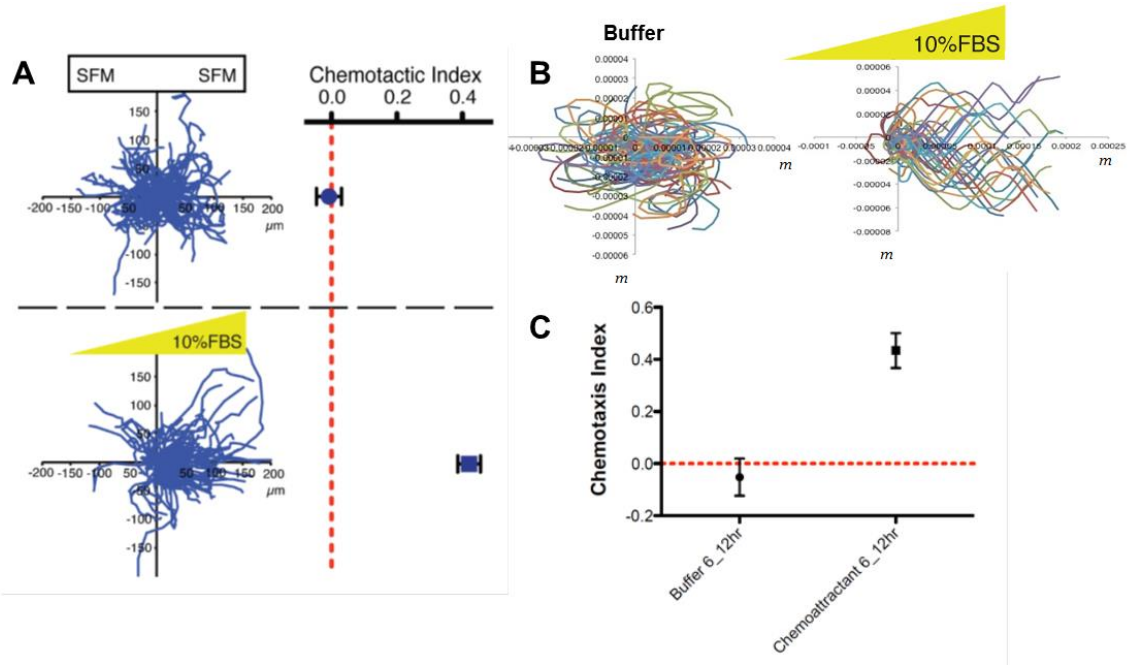

Figure 5. 11: Chemotaxis Comparison. The figure presents spider plots tracking paths of individual cells in the real (**A**) and virtual (**B**) assays, as well as the plots of chemotaxis index plotted for the real (**A**) and virtual (**C**) assays. Both experimental and computational data suggest non-directional migration in case of the assay conducted using buffer solution, and a strong bias in migration towards the chemoattractant observed as the shift towards the right (in the real and virtual cases). The plot also shows chemotaxis indices calculated for migration of cells in the presence and absence of the chemoattractant (for the real and virtual cases). As indicated in the plot, cells migrating non-directionally produced a chemotaxis index of ~0.0, whereas migration under the influence of chemoattractant gradient displayed index of ~0.4 (in both the real and virtual cases). The author gratefully acknowledges the support of **Andrew Muinonen-Martin** in determining and plotting the chemotaxis index and creating the Spider plots for the virtual data. Experimental graphs (**A**) have been printed under the ***Open-Access License*** and first appeared in *Ref. 314*.

One difference that is easily identifiable is that the trajectories observed in the computational data were a lot smoother than their experimental counterpart. This discrepancy can be addressed possibly by altering the step-to-step random component of the

cell migration rule. An additional difference is that in the experimental study, there are clearly a few cells that move *against* the chemotactic gradient. This cellular variability has not been incorporated as a rule in the agent model, since the mechanism governing it is not understood. Nevertheless, the overall similarity between the two sets of results was not compromised due to this – moreover an effort to provide quantitative comparison is reflected by the chemotaxis index.[xxv] Both the real and virtual assays revealed a chemotaxis index of ~0.0 for the control and ~0.4 for the case with the chemoattractant.

5.4 DISCUSSION

The coupled platform presented in this manuscript was created keeping bioreactors in view where the concentration gradients, shear and flow profiles etc., influenced initially by the geometry of the bioreactor and, later, by cellular activity, play a pivotal role in the synthesis of the autologous substitutes required for regenerative medicine. The modelling platform is composed of two working elements: *continuum* – transport phenomena capturing – and *discrete* – cellular behaviour capturing. The greatest advantage of the platform, however, remains the fact that it can capture emergent phenomena – a benefit extending from the agent-based side of the platform (as demonstrated in Chapter 4). As such, the platform can not only help explain non-intuitive observations but has the potential to reveal processes and mechanisms not expected to emerge *a priori*, like the cell band formations shown in *Results*.

Simulation results presented in this chapter are in agreement with those from other models that were discussed in previous pages. Cheng *et al*. (2009)[12] suggested that the hydrodynamic conditions affect not only the rate, but the pattern, of tissue growth as well:

[xxv] The author is grateful to Andrew Muinonen-Martin (Beatson Institute for Cancer Research) for creating the spider plots and calculating the Chemotaxis Index for the validation case.

something demonstrated in the results. One can easily observe (in Figure 5.6) the way transport limitations affect spatial distribution of cells, also reported by Cheng and co-workers.[12] Furthermore, according to Cheng *et al*. (2006)[13], by inducing a preferential migration direction oxygen concentration gradients influence cell migration. The platform captured that behaviour evident in any of the figures. Moreover, the impact of the altered boundary conditions on cell proliferation can be also observed, especially in Figure 5.6 where Case IV results in a richer cell growth pattern compared with Case III, which had lower (by an order of magnitude) media flow rate. This mirrored the observations of Grayson *et al*. (2008), who developed a bioreactor with perfusion and imaging capability to bioengineer bone formation and reported that a higher flow rate supports higher cell densities within the constructs due to more efficient nutrient transport.

The presented simulations also recapitulated numerical and experimental observations reported elsewhere. Lapin and co-workers[289] had observed cellular activity to be higher in regions of high glucose concentration (i.e. close to the source). Similarly, Grayson *et al*. (2008)[317] reported higher cell density near the inlet of their bioreactor. Auniņš *et al*. (2008),[318] furthermore, who utilised a diamond shaped bioreactor referred to as *CellCube*, very close to the morphology of bioreactors utilised in this investigation – particularly Cases I and II, also observed higher cell density in the half of the bioreactor close to the inlet. Auniņš and co-workers followed this observation with a computational analysis of flow and transport within the bioreactor, and concluded this to be dependent on "*good cell nutrition*" in this area (amongst other factors). The same can be observed in Figures 5.3 – 5.6, where increased proliferative activity is observed closest to the media inlet port, resulting in the highest density of cell population in that region within the bioreactor.

Furthermore, a comparison of results against those reported by Picioreanu et al. (2009)[15] also reveal similar qualitative performance. Picioreanu and co-workers reported a

higher pressure-drop in reactors as a result of biofouling (against those without the biomass). Similarly, the simulations presented here reveal an increased drop in concentration in the bioreactors containing cells compared with the same bioreactor containing no cells (refer to Figure 5.7). Furthermore, the investigators also reported formation of quasi-stagnant zones, much like the bands observed in this investigation. Similarly, when Picioreanu and co-workers[14] modelled the impact of high substrate transport on microbial growth, they concluded that higher transport results in more dense biofilms. The results presented in this investigation show a similar trend. For example, the two bioreactors displayed in Figure 5.6 differ in the boundary condition that the media flow rate in Case IV (bottom in the figure) is an order of magnitude higher than Case III (top). The higher density of cells within the bioreactor with richer transport can be easily appreciated.

Picioreanu et al. (2009)[15] reported pressure drop and altered flow in their investigation, which the current model could not, because they explicitly tied momentum exchange between the fluid phase and biomass accumulation. In this investigation, momentum exchange between cells and the fluid phase was not explicitly considered as was the case in investigations conducted by Lapin and co-workers.[288-290] This worked for Lapin and co-workers and the model presented here because each agent represented a single cell whereas the *biomass* of Picioreanu and co-workers, represented a collection of cells as well as polymeric matrix secreted by those cells. This feature can be incorporated within the model by introducing cells as momentum sinks in the Navier-Stokes equations. The current framework can, therefore, handle momentum (and energy) exchange as well as its impact on the spatiotemporal evolution of cellular systems, for the continuum module solves the transport equation (2.20), which allows incorporation of momentum and energy sinks/sources. As the endeavour reported in this thesis marked the initial step in the development of the multi-paradigm framework, to keep things simple and generate efficient

and exploitable coupling between the continuum and discrete modules, momentum exchange between the cellular and fluid phase was not considered here.

Moreover, cell alignment normal to the oxygen gradient was not a part of the rule-set attributed to the cells but emerged from it. The formation of similar cell bands or patterns within bioreactors, as a result of the cellular interaction with nutrient gradients, qualitatively agrees with similar theoretical predictions[105,287] and experimental observations[318] reported previously. Auniņš and co-workers,[318] utilising a similar bioreactor morphology to what was utilised in this investigation, implicated nutrient delivery as a factor responsible for cell patterns observed within their bioreactor. The current investigation certainly supports their view. Such patterns can be exploited within the bioreactor to develop tissue and organ structures that display zonal variation within their structure, such as articular cartilage.[319] The presented framework in enabling visualisation of such patterns, by quantifying location of cells that form the various zones/bands as well concentration profile of the nutrients in and around these zones/bands, is ideally suited to optimise this type of exploitation. A quantitative comparison between the bands formed in this investigation and others was not made due to differences in the model (i.e. nutrient utilised, media inlet velocity, cellular characteristics, etc.) and the comparison being outside the remit of the objective of the chapter. This, however, shall be pursued in the future. Moreover, in Figures 5.3 and 5.4 – especially in Figure 5.4 –, the concentration contours change continuously, proving the effectiveness of the platform in capturing dynamic reciprocity (as explored later). A physical system with either no cells or constant number of cells inside would not show such behaviour after the flow becomes stationary, beyond initial transients. The latter can be observed in Figures 3.5 and 5.7, which further puts into perspective the advance achieved by integrating the continuum and discrete approaches.

Finally, the virtual chemotaxis assay, where the virtual Insall chamber was seeded with melanoma cells that could migrate under a FBS gradient, conducted to provide validation, delivered a similar qualitative and quantitative performance as the actual experiments.[310,314] The fact that the chemotaxis index, presented as a mean of the population, for both the buffered and chemoattractant simulation matched their experimental counterparts lends some confidence regarding the capacity of the framework to capture cellular behaviour for a population of cells within artificial devices. Despite this similarity, however, the statistical comparison between the trajectory of individual cells in the real and virtual cases must be pursued. This was not possible in the current investigation as the comparison against real data was conducted *post-hoc*. This also means that the 'critical' concentration assumed to trigger chemotaxis could not be tested, though the very similar chemotaxis indices support the values utilised herein. Still, this remains an indirect comparison and a more direct comparison against physical data needs to be pursued as part of developing the next version of the model/framework.

The 'cells inside the bioreactor' model was chosen solely to illustrate the potential of the transport-agent approach in capturing biocomplexity (especially within the TERM paradigm) as well as to highlight the potential contribution the framework can make as a design optimisation tool towards bioreactor development. The author, however, is aware that the current model bears a tangential relevance to practical bioprocesses, and aims, as the next step, to apply the framework and the approach to simulate the closely related and practically more relevant case of cellular activity within microfluidic devices. Still, the model offered useful insights into how coupling cellular activity with transport resulted in the emergence of patterns that have been predicted and observed previously,[76,287,318] and in illustrating how the continuum approach alone cannot robustly guide the development of bioreactors. The model, however, has certain limitations. For example, it did not consider

cell aggregation and matrix synthesis, unlike the model proposed by Picioreanu and co-workers,[15] which allowed the investigators to tie the growth of the 'biomass' to fluid mechanics. This segues into the second limitation of the model: it does not consider momentum exchange, which can be accounted for through (a decrease in) the permeability of the system (with increased deposition of the ECM) or the emergence of cell colonies (cells and the matrix) acting as sinks to momentum transport. Furthermore, the model, as well as the framework, does not deal with mechanical cues. As such, the mechanical impact of the scaffold on cells was not considered. This is a non-trivial task and will require coupling of the framework with the finite element paradigm. Moreover, the model, while it displayed 'differentiation' of cells into an apoptotic phenotype, did not consider differentiation of the cells into either chondrocytes or osteocytes as a function of oxygen gradient. This was done to keep this first attempt towards the development of the transport-agent framework simple. Furthermore, at the moment, just as was the case with the model presented in Chapter 3, consumption of oxygen (glucose in Chapter 3) by cells occurred at a constant rate. A limitation of the chemotaxis assay was that cellular migration under chemotaxis had no stochastic element, though while displaying persistent random walk in the absence of the chemoattractant the cells could alter their direction randomly. This shall form part of the next step in framework development and optimisation.

Additionally, the model as it currently stands is, computationally speaking, very expensive. As such, its performance against the Euler-Lagrange and continuum-CA approach approach, by Lapin & co-workers[288,289] and Picioreanu & co-workers,[14,15,296,298,299] which can easily accommodate 100,000 cells, is rather limited. This can be mitigated by compartmentalising the geometry and running the compartments on a cluster set-up – both modules of the framework can be parallelised. However, this particular limitation is inherent to the framework, as the agent-based paradigm is computationally expensive. The user,

however, can potentially optimise the speed by conducting a grid independence analysis and opt for a balance between the mesh size and number of agents to be modelled. The framework can be currently run on Windows and Linux. The framework, for the purposes of this thesis, was run on a 32-bit Windows XP workstation fitted with 2.80 GHz Xeon™ processor and 3GB RAM. While simulation speed will vary between computations depending upon the number (and type) of meshes employed by the continuum module and number of agents in the discrete module, the framework running on the aforementioned system could easily handle any arbitrary geometry containing a collection of few hundred thousand structured mesh elements and thousands of agents.

There is, finally, the question of the role of stochastic elements within the model. This was not attempted due to logistical reasons and the fact that this question was rigorously pursued in Chapter 4, where the model – following analysis of data gathered from over 125 simulations – was found to be relatively insensitive to (reasonable) stochastic perturbations. That modules of the osteogenesis model formed the foundation of the agent-based model utilised in this chapter (which was coupled with the continuum model of Chapter 3). Furthermore, despite the aforementioned limitations, the reader may appreciate that the model consistently displayed certain features throughout the four test cases despite variations in boundary conditions, including the fact that two different bioreactor formulations were utilised. These include enhanced cellular activity near the source (also reported elsewhere[289,317,318]), formation of band patterns (predicted[105,287] and reported[15,318] elsewhere), and a more accurate and dynamic relationship between transport and cell locations (as reported elsewhere[12,14,15,289,317]). Given the question that was being investigated through the model – whether the framework can capture difference/similarity in growth patterns as a result of varying boundary conditions – this, in effect, points to 4 different cases of numerical experiments (n=4). The author is aware that this remains a limitation of the

model. However, the model in its current state was only meant to illustrate the potential of the framework. The author aims to mitigate this in the next version of the model, which will target a more realistic set-up.

In terms of capabilities, the off-lattice transport-agents framework presented herein complements the hybrid landscape that was elaborated in §5.1 and Figure 2.14. Based on the results, it can be concluded that the methodology is robust and more accurate compared with standalone continuum and discrete formulations in capturing system-relevant details and data structures. This is a result of the type of agent-based modality used in this thesis, which allows its user the option to incorporate user-defined data structures as well as the flexibility to work with cell shapes of arbitrary complexity (instead of just spheres, CA-lattices, or polygons). The hybrid framework presented in this thesis, therefore, enables modelling of most observed cellular behaviours: proliferation, differentiation, migration, chemotaxis, aggregation, necrosis, and apoptosis; all in 3D, as have been simulated in the two models presented in Chapters 4 and 5.

In comparison with *standalone* discrete, agent-based modelling platforms such as FLAME and NetLogo the current framework offers the ability to simulate microenvironmental variables for a multi-cellular structure. The two platforms, including other standalone discrete platforms, will simply not be able to simulate hydrodynamics and transport within *in vitro* environments, such as the bioreactors utilised in Chapters 3 and 5. Another advantage that the platform has over NetLogo is the fact that the platform models a system in continuous space, unlike NetLogo, which is lattice based and 2D. The same applies to the commercially available rule-based platform for complex system known as *Complex Systems Modeling*. Along similar lines, continuum methodologies such as CFD-ACE+, FLUENT, etc., will not be able to capture dynamics at the cellular level, due to the homogeneity assumption. It would not be feasible to observe development of the emergent

patterns via the use of any of the standalone continuum methodologies. The same arguments can be extended while comparing the presented framework against any wholly continuum or discrete methodology.

Comparison, however, needs to be made against currently existing virtual, hybrid platforms such as CC3D and CHASTE, which, like the framework presented herein, by accounting for a variety of data structures, display the property of dynamic assimilation, as defined in §2.5. The two software platforms are relatively mature and offer the user the ability to code, simulate, and visualise – much like the presented framework. These two platforms have, in particular, achieved sufficient efficiency to allow simulation of a variety of biocomplex phenomena and represent the state-of-the-art in multi-scalar, multi-paradigm modelling software.

CC3D, as discussed in §2.3.3, is based on the *Glazier-Graner-Hogeweg* (*GGH*) approach, which facilitates multi-scale simulations by defining spatially-extended generalised cells, thereby allowing tuning of the level of detail from intracellular to continuum without switching simulation framework. This is an architectural advantage that CC3D currently possesses over the presented framework. However, it is precisely the fact that the presented framework is composed of multiple simulation modalities that makes it more desirable, as discussed shortly. In terms of implementation, behaviours and interactions in CC3D are embodied in the effective energy, which determines cellular parameters (such as shape, motility, adhesion, etc.). While the biochemical behaviour can be represented through a variety of differential equations, the cell lattice evolves probabilistically. The current framework, in comparison, offers a more realistic ontology to represent both the cells as well as the evolving microenvironment, especially in terms of continuous space. Furthermore, the framework presented in this thesis, can capture physical phenomena such as flow, transport, and shear in addition to chemical processes such as

secretion, consumption, and reactions. Moreover, the platform allows the user, through a CAD program, to develop a physical domain of arbitrary geometry, which is especially beneficial towards the generation of *in vitro* environments such as Petri-dish, bioreactors, lab-on-a-chip devices, where the contribution of domain morphology is of utmost importance. Additionally, the presented platform relies on the finite-volume formulation, which is more intuitive to follow (as discussed in Chapter 2) over the finite-difference scheme typically employed to solve diffusive equations within CC3D. Finally, the fact that the continuum methodology can handle moving boundary problems, electric as well as magnetic effects, transfer of heat (to account for heat based interventions, such as bronchial thermoplasty) and the ability to generate geometries of arbitrary complexity are some of the advantages of the transport-agent framework. However, CC3D is simpler and more flexible to implement. Furthermore, as it is based on a lattice-grid, this really simplifies implementation of intercellular and cell-environmental interactions. Secondly, it requires a relatively short time commitment in terms of acquiring working knowledge of the platform. This is certainly not the case with the framework, for which a working knowledge of object-oriented programming and FORTRAN is essential. Thirdly, CC3D is especially suited to systems where differential adhesion is essential. Another advantage of CC3D is that it offers faster computations in comparison to the current framework, which can be a crucial component in the decision-making process to opt for a certain methodology. Finally, in practical terms, CC3D has a wealth of relevant models and documents available that provide guidance on *getting started* as well as model development, which gives it a clear edge over the presented framework. This, however, remains a "work in progress" for the author.

CHASTE, on the other hand, is perhaps the most mature hybrid platform currently available.[xxvi] The features that CHASTE carries certainly confer to it a lot more range, in terms of the options for the users, than the multi-paradigm framework presented here. The code includes (i) global component for basic mathematics; (ii) input-output code for reading, writing, and converting various files; (iii) the capability to generate meshes; (iv) code to conduct vector and matrix operations, (v) codes for defining and solving ODEs and PDEs, as well as (vi) the capacity to solve compressible and incompressible general non-elasticity problems[129]. The presented framework also includes features (i)-(v) and, thus, offers the user the same applications as CHASTE. However, the advantage CHASTE offers its users is the fact that it can currently deal with solid mechanics more robustly, which is a limitation of the presented framework. Furthermore, CHASTE's range is put into perspective when one considers the fact that it offers the user the option to use both lattice-based and non-lattice-based representation of cells. On-lattice models utilise the CA and/or CPM frameworks, whereas off-lattice models define cells spatially either by their centres (connectivity defined either by Voronoi tessellation or 'overlapping spheres') or vertices (cells assumed polygonal whose vertices move in response to forces). This is where the presented framework's advantages become apparent. While the on-lattice representation of cells in CHASTE can be argued to be a better ontology than its off-lattice counterpart, the lattice-based approaches in CHASTE are not as realistic as the off-lattice approach offered by the presented platform. Secondly, the off-lattice modules in CHASTE do not capture the algorithmic behaviour of cells, as it is not based on a global/local interaction reliant protocol, which is precisely the sort of strategy needed to allow emergence of patterns from underlying rule-set. This is a key advantage that the presented framework possesses over CHASTE. In its sophistication

[xxvi] The current avatar of CHASTE and the multi-paradigm framework reported in this thesis were published in the same month by the PLoS group of journals.

and ability, however, CHASTE is perhaps the most complete and mature to simulate models with developmental, clinical, and commercial significance. However, a limitation of CHASTE is that currently it can only be run on Linux, while the presented framework can be run on Windows and Linux operating systems. Finally, the set of documentation available on CHASTE gives it an additional edge over the presented platform.

Where CC3D lacks an in built mechanical and flow solver and is lattice-based, CHASTE only simulates mechanical interactions between cells. The presented framework complements the existing landscape by offering a coupled approach with a module that can solve for flow and a module that can capture the spatiotemporal evolution of cellular populations via an interaction-reliant strategy, which, arguably, is a more realistic representational formalism to capture the algorithmic nature of cell decision-making. Along with CHASTE and CC3D, the presented framework forms part of those computational methodologies that can capture the impact of the cellular microenvironment to tissue development. This bi-directional relationship was captured by the principle of *dynamic reciprocity*,[18] which suggested that "*the ECM affects the cell which in turn responds by synthetic and degradative processes causing the composition and the structure of ECM to change which in turn influences the cell and so forth"*.[18] This principle, however, limited the role of the microenvironment to the 'material' aspect of the systems, i.e. the ECM, and lacked an essential component: local transport phenomena. However, there has been, for a while now, increasing evidence implicating flow and transport on tissue development, in addition to the ECM. [xxvii] The principle can, therefore, be more inclusively stated as follows: *the cellular microenvironment – which includes the cells, ECM, and local transport processes – affects the cell which in turn responds by synthetic or degradative processes*

[xxvii] *These examples, in addition to the amendment to the definition of Dynamic Reciprocity, form the basis of a 'Letter-to-the-Editor' that was published as follows: Kaul H and Ventikos Y (2015). Dynamic Reciprocity Revisited.* ***Journal of Theoretical Biology*** *370:205-208.*

causing the composition and the structure of ECM, and therefore the local transport processes, to change which in (a coupled) turn influence the cell and so forth.

One can understand the absence of transport from the original definition for it is easy to overlook, in the absence of suitable experimental methodologies, which can visualise flow fields, and thereby gradients, the vital role played by transport processes in the evolution of biological systems. However, whether it is the diffusion dependent transport within a tissue or convection-diffusion-reliant transport occurring within a perfusion bioreactor, the role of transport processes cannot be neglected. After all, cellular proliferation, stimulated by optimal mass transport, begins to influence local concentration gradients as well as flow profiles, due to consumption/secretion of entities or secretion of matrix that alters the local permeability, thereby non-linearly affecting the overall cell growth. With the rapidly burgeoning state-of-the-art in hybrid models and platforms, which particularly focus on the impact of flow and transport on cell behaviour, and vice versa, including those reviewed in this chapter, we can finally begin to evaluate this relationship as well as the underlying mechanisms in a more quantitative manner.

5.5 SUMMARY

Through the investigations reported in this chapter the overarching aim of this thesis was successfully addressed. A novel multi-paradigm approach as well as a framework was presented that can capture biocomplexity *in vitro* and, given accurate boundary and initial conditions, even *in vivo* (subject of future investigation). The presented framework does not only capture the principle of dynamic reciprocity but in handling various data structures, dynamically integrating information from both environment and cellular structures, and offering the user the freedom to simulate processes in 3D also display dynamic assimilation. Simulation data are in agreement with those obtained using models of similar

purpose;[12,13,285,286] in addition to showing behaviour that may be emergent as has been predicted and observed elsewhere. The platform was validated by simulating melanoma chemotaxis in the Insall chamber. Reasonable agreement was observed between the experimentally and computationally gathered data, further proving the utility of this modelling platform to artificial devices that are employed to grow, differentiate, or exploit the cellular potential. The chapter marks the end of the computational investigations conducted to meet the intended objectives of this thesis.

6 CHAPTER Conclusions

"In order to simulate the complex behaviour of any biological system – whether it is a collection of proliferating cells in a Petri dish, polymeric scaffold, or uterus – the applied computational paradigm must be able to faithfully capture the dynamic interactions between cells and their microenvironment: encapsulated by the dynamic reciprocity principle"

...

"The cellular microenvironment – which includes the cells, ECM, and local transport processes – affects the cell which in turn responds by synthetic or degradative processes causing the composition and the structure of ECM, and therefore the local transport processes, to change which in (a coupled)sense influence the cell and so forth"

...

"Dynamic assimilation is the act of receiving diverse structures of data, which could be continuous, discrete, binary etcetera in nature; integrating them with equally diverse sets of information from either sub-components or individuals existing in the same microcosm; processing the information to pursue a set of (design) objectives; and, finally, the iteration of this process as many times as desired"

6.1 SUMMARY

The first sentence listed in the box above was presented, in Chapter 1, as one of the reasons capturing biocomplexity has proven challenging. In the introductory chapters we find how computational approaches of the continuum variety struggle to provide adequate representational formalisms for biological entities, thereby offering little beyond qualitative similarity while simulating biocomplexity. We saw that discrete approaches, on the other hand, while closer to capturing the dynamic relationship between biological structures and their (micro)environment, being computationally expensive, cannot be employed to capture the bulk phenomena that are crucial, as suggested by the extended definition of dynamic reciprocity (presented in Chapter 5 and listed as the second statement in the box above), to the time evolution of biological structures. Furthermore, computational frameworks that cannot deal with a diversity of data structures

(whether *continuous*: concentration gradient of a morphogen, *discrete*: phenotype of a cell, *binary*: 'on-off' switch of a bioreactor, *topological*: 3D configuration of enzymes, for example) also find it difficult to capture the relevant details that may influence the spatiotemporal evolution of cellular systems. Finally, we realised that there is a gap within the existing landscape of computational frameworks, refer to Figure 2.14, which can address some of these issues and quantify the seemingly irreducible organisation of biological systems.

In the chapters that followed, the reader was acquainted with the methodology, strengths, and weaknesses of two major computational approaches, evident from their pervasive use in bio-computational literature, before the two were integrated to create a coupled transport-agents multi-paradigm framework that can capture not only the relevant physicochemical environmental details but the individual-level cellular behaviour as well. Furthermore, being able to handle the three-dimensional aspect of cellular environments as well as a wide variety of data structures, the hybrid framework displays the concept of dynamic assimilation, as stated in Chapter 2 and listed at the beginning of this chapter.

6.2 CONCLUSIONS AND IMPLICATIONS

6.2.1 CONCLUSIONS

The major conclusions, and the contributions, of the work presented within this thesis are as follows:

- The extended definition of *dynamic reciprocity* suggests a modified perspective to the cellular microenvironment emphasising the collective roles that cells, material environment, and local transport processes play in the spatiotemporal evolution of cellular systems both *in vitro* and *in vivo*

- A novel computational framework capable of capturing the principle of dynamic reciprocity and displaying dynamic assimilation is presented
- The framework can simulate a broad array of biocomplex phenomena *in vitro*. Its usage, furthermore, extends beyond the domain of TERM
- The framework can capture emergent phenomena (discussed in Chapters 4 and 5)

More specifically,

- results presented in Chapter 3 validate the potential of Computational Fluid Dynamics as a design optimisation tool,
- these results, furthermore, demonstrated the capability of the default operational parameters of the TissueFlex® in sustaining growth and expansion of hMSCs,
- the '*top-inout*' morphology tested in the investigation is being developed for commercial exploitation,
- the 3D agent-based model of *in vitro* osteogenesis, in capturing the emergent behaviour of maturing osteogenic nodules, shed light on the mechanics of static and dynamic bone formation, and
- the model suggested that osteoblasts do not 'switch-off' their matrix deposition capability during the process of osteoblast transformation into osteocytes, and that acquisition of polarity in osteoblasts does not seem to be a random event.

The implications of the foregoing conclusions are discussed in the following section.

6.2.2 IMPLICATIONS

6.2.2.1 CAPTURING DYNAMIC RECIPROCITY

A distinct advantage of CFD is that it allows for intuitive evaluation of flow fields, especially in the microscopic recesses that may be harbouring the evolving tissue structure, as well as variations that these flow fields undergo with the development of these structures:

insight that is extremely difficult if not outright impossible to attain experimentally. Using a computational framework that makes use of CFD, therefore, allows the user to map the evolving transport needs of a system, which would previously not be possible. This is of marked commercial value, while designing bioreactors or scaffolds to support cell expansion and differentiation, for quantifying the transport demands of cells growing in an automated device will help in designing devices that can meet not only the initial but also the evolving demands of this system with relevant cost implications. However, CFD itself finds challenges in capturing the dynamically changing flow fields or concentration gradients of a system if employed to model the cellular phase as well. This becomes apparent when conclusions from chapters 3 and 5 are considered in tandem. In Chapter 3, the system: hMSCs consuming glucose, achieves steady state, as can be seen in Figure 3.5, and no change is observed in the concentration contours beyond those initial transients. Compare that to Figures 5.3 – 5.6 where the concentration gradients are constantly evolving, and are captured doing so by the presented framework. Refer also to Figure 5.7, where the boundary and initial conditions utilised in Case II (refer to Table 5.1) are employed to compare Case II with and without agents. There is an appreciable difference in oxygen concentration. This reflects the benefit of using the hybrid approach as a design tool, especially considering the fact the fact that this difference in concentration emerges in the hybrid bioreactor case (with agents) containing ~1800 agents only (at the end of day 5), which is nowhere near the realistic scenario of 1 million cells/mL of cell suspension (the figure utilised in Chapter 3). This, furthermore, offers proof-of-principle that the framework can simulate the extended definition of dynamic reciprocity.

6.2.2.2 DYNAMIC ASSIMILATION

At the end of Chapter 4, the following features were identified as being essential for a modelling approach to simulate biological complexity: the ability to simulate non-linear

and dynamic behaviour, synthesise relevant "constituent-constituent" and "constituent-environment" interactions, track the evolution of various constituents that are heterogeneous in nature, develop memory of various prior constituent interactions, adapt to the external environment, and permit visualisation of emergent phenomena that will result from the combined interactions of system constituents. This is, however, not possible until the modelling approach considers the process in appropriate dimensions, possess the capability to handle a variety of data structures, and is able to consider information that may dynamically emerge during simulation. This forms the crux of *dynamic assimilation*.

Comparison of the coupled CFD-transport model with the models presented in Chapters 3 and 4 will put this into perspective. Neither of the standalone models can lay claim to be dynamically assimilating methodologies. The CFD-based model presented in Chapter 3 deals neither with discrete data nor captures emergence. In comparison, the model presented in Chapter 4 assumes idealised conditions in terms of continuous system characteristics. However, an integration of the two approaches, presented in Chapter 5, displays most, if not all, features mentioned in the paragraph above, and in its ability to consider a variety of data structures, satisfies the dynamic assimilation condition.

Figures 5.3 – 5.6 validate the aforementioned point. In terms of the concept presented above, the figures display the framework's ability to: capture the evolution of a system based on component-component and component-environment interactions, which occurs due to the rule-based modality of the framework; track the evolution of various constituents that are heterogeneous and develop memory of previous interactions, proven by the fact that the history of any of the two kinds of agents (hypoxic and normoxic) can be reviewed easily; visualise emergent behaviour, as it occurs in the formation of a belt at the normoxic-hypoxic interface; deal with a variety of data structures – continuous (oxygen concentration), discrete (cellular phenotype), and binary (available or blocked active site of an enzyme); all in three-

dimensions. This is a robust paradigm of simulating biocomplexity, with the principle itself serving as a rather systematic touchstone for computational frameworks. It must, however, be stated that the presented framework is not the only one to possess the ability to dynamically assimilate. CHASTE and CC3D, which were discussed in the previous chapter, for example, are other modelling frameworks that can dynamically assimilate information, which, the author feels, is the chief reason behind their versatility and wide-ranging application as computational platforms utilised to model biocomplexity. The presented modelling framework is, therefore, an addition to the list of software that can dynamically assimilate information.

6.2.2.3 DYNAMICALLY ASSIMILATING FRAMEWORK

The investigations conducted as part of this thesis aimed to develop a computational framework that can capture biocomplexity as well as the emergent behaviour of biological systems. In essence, this was an exercise in creating a computational scheme that displays dynamic assimilation. Towards the end of this thesis, a dynamically assimilating, experimentally validated framework, created by integrating an agent-based platform with a transport phenomena solver, was presented. The framework can combine the various elements of a cellular microenvironment to simulate the spatiotemporal evolution of the entire system. The most promising aspect of the framework, however, is its capacity to capture emergent phenomena, presented and discussed in Chapter 5, which makes it possible for the framework to present not only counterfacts but also *unknown unknowns*.

6.2.2.4 CFD & ABM MODELS

6.2.2.4.1 CFD

The methodology presented in Chapter 3 was used to determine whether the default configuration and standard operating parameters for TissueFlex® were optimal to support the expansion of hMSCs seeded inside alginate scaffolds. The two significant aspects of this

investigation were the use of dimensional analysis and the evaluation of CFD as a design optimisation tool. While TissueFlex®'s default operating parameters were computationally validated to support hMSC expansion – a conclusion of high commercial worth; that the investigation, in showing how slight modification in bioreactor geometry can increase the shear experienced by the scaffold, validated CFD's efficacy as a robust design optimisation tool is a conclusion of higher significance. The observation, in itself, also demonstrated how bioreactor initial and boundary conditions can be altered (by exposing cells to high/low shear levels or hypoxic/normoxic environments) to manipulate cellular phenotype. This also provides credence to the claim that the modelling platform presented in this thesis, as it comprises of the CFD modality, can be used as a design optimisation tool during the concept selection phase of biotechnology devices.[xxviii] Finally, the dimensional analysis[xxix] used in this thesis can be employed by other investigators in the community to determine the efficacy of a bioreactor, or any other perfusion device for that matter, in supporting cellular growth.

6.2.2.4.2 ABM

Agent-based modelling was employed to model *in vitro* osteogenesis. The model, due to its interaction based approach, can accurately capture the processes observed during osteogenesis with high fidelity, as discussed in Chapter 4. The model suggested that the premise that osteoblasts 'switching-off' their capability to synthesise matrix is, from a spatial perspective, untenable; and that osteoblasts acquiring polarity seems to be a non-random event. While the latter confirms what probably is common knowledge amongst biologists examining a cell's ability to acquire polarity (though in itself slightly remarkable), the initial finding, at least, rules out one hypothesis (#4) considered to play a role in the

[xxviii] The '*top-inout*' bioreactor geometry is currently under development for commercial exploitation.
[xxix] The dimensionless numbers employed in this investigation were not developed by the author

transformation of osteoblasts into osteocytes. At most, it identifies two hypotheses (#2 and #3) as serious contenders of matrix deposition. In either case this is a helpful contribution, since experimental work can be focused to better analyse the process from the perspective of hypothesis #3. The results presented herein open the path for the development of novel therapeutics aimed to treat skeletal defects of development and remodelling. The model itself can play an important role towards the design, optimisation, and testing of novel/pre-existing orthopaedic drugs.

6.3 LIMITATIONS & FUTURE

6.3.1 MODELS

6.3.1.1 CFD

While the continuum model presented in Chapter 3 was able to suggest why the default operational parameters of the commercial TissueFlex® micro-bioreactor is able to support cell growth and laid the foundation towards the design and development of a new commercial bioreactor morphology, it was not without limitations. Firstly, in the model only the transport of glucose was considered. The model can be made more accurate and relevant if the transport of oxygen is also considered in parallel with the transport of glucose, which was avoided here due to computational limitations (refer to §3.4). Furthermore, the consumption of glucose by cells was assumed to follow zero-order kinetics, with the consumption rate itself being a constant, which is not the case physically (refer to Table 3.3) as cells tend to show variability in consumption of nutrients (though this did not impact on the conclusions of the investigation). Secondly, the model assumed a confluent culture, and, hence, it did not account for proliferation, migration, differentiation, or necrosis. As such, the results are not fully reflective of the changes in concentration gradients of glucose, which will occur if the initial cell population was to undergo proliferation within the bioreactor,

and only represents the concentration profile when the cell population is fully confluent. The model can be made more realistic, and perhaps a true indicator of the bioreactor's ability to sustain cell growth, if proliferation and necrosis are also considered. Finally, the assumption of fixed permeability and porosity in the model, which will not be the case physically as both will vary due to scaffold degradation and deposition of matrix by the growing cell population, is another limitation. This is, however, a non-trivial set of processes to incorporate within any model. Scaffold degradation and matrix deposition will have opposing impact on permeability, which needs to be experimentally evaluated before the relevant constitutive equations are added to the model. The forthcoming versions of the model will address these limitations.

6.3.1.2 ABM

The agent-based model presented in Chapter 4 provided novel insights into the mechanisms governing the transition of osteoblasts into osteocytes. However, the model, being standalone agent-based only, is highly idealised. Firstly, the model assumed presence of optimal nutrient as well as morphogen concentrations. As such, the model did not utilise reaction-diffusion equations to account for the formation of osteogenic condensation, which are more sophisticated than the algorithm utilised to model condensation in the current model. Similarly, a cell's acquisition of polarity is modelled as a stochastic event, and independent of gradients of physicochemical signals. Secondly, as the role of apoptosis and migration in the formation of osteogenic condensations is poorly understood, and although the model has raised a few questions that may guide experimental efforts towards a better elucidation of these mechanisms, the model remains subject to revisions on those fronts. Thirdly, the model did not account for the presence of mechanical stimuli that influence osteogenesis, which have been utilised in previous models, especially the ones that employ the finite-element formulation. Fourthly, the agent morphology employed in the model was

idealised. For example, all agents were spherical. While this is not realistic, it would not upset the conclusions as agent morphology was not considered to play any role in influencing either osteoblast polarity or its differentiation. Furthermore, in this investigation, growth and maturation of only one condensation/nodule was considered, but, once again, the conclusions can be extended to *in vitro* cultures with multiple condensations/nodules without any loss of generality. Moreover, the model relied on global as well as local rules to capture the spatiotemporal evolution of the mineralising nodules and the transition of osteoblasts into osteocytes. The presence of global rules meant that the computing time was longer in comparison with a model relying solely on local rules. A simulation consisting of 5000 iterations (~70 physical days) required about 48 hours to run, which was sufficiently low to conduct the entire array of sensitivity analyses without having to parallelise the model. However, if more than one nodule is to be considered, the model will need to be parallelised as the computational time will increase quadratically with the inclusion of each new agent. These advancements to the model will be dealt in the future version of the model, which will be extended to simulate osteogenesis *in vivo*.

6.3.2 MULTI-PARADIGM FRAMEWORK

Firstly, in order to demonstrate proof-of-principle and to keep this first attempt to framework development simple, the 'cells in bioreactor' model utilised bore only a tangential relevance to a real bioprocess. Momentum exchange between the cellular and fluid phase was, therefore, not explicitly considered (though the capability to do so exists). This would be tackled in the future version of the model where a more realistic, and computationally tractable, case of a few cells within a microfluidic device will be considered. Here, momentum exchange will also be considered, in addition to mass transport as well as the impact of shear on cell phenotype. Thirdly, the model did not consider cell colonisation (possible through the discrete module) and alterations in permeability as a result

of colony formation by cells (possible through the continuum module). The ‘cells in a microfluidic device’ will feature an initial attempt towards this as well. Furthermore, in comparison to other hybrid approaches, the presented framework, in the absence of a way to parallelise the model, can only tackle about tens of thousands of cells. While the user can strike a balance between the quality of mesh and number of agents, mitigating this limitation ideally requires a way to run the model in parallel, which is part of the greater plan to make the framework commercially exploitable. Furthermore, the framework currently lacks a formulation to treat solid mechanics as effectively as the finite-element approach. The incorporation of a similar formulation will probably involve developing a relevant algorithm that can be attached to the framework to simulate processes of solid mechanics. Most importantly, the evolution of this framework into fully capturing dynamic assimilation shall also continue. The introduction of a rule-mining or pattern recognition algorithm will strongly reinforce the ability of the presented framework to assimilate information dynamically. This, however, will require a more rigorous analysis of the underlying computational paradigms as well as the programming capabilities to integrate the two. This integration would entail multiple steps such as identification of a robust rule-mining platform (such as *Weka*: http://www.cs.waikato.ac.nz/ml/weka/); identification of data-sets/-structures generated during computation that would be meaningful for this purpose (i.e. cellular orientation, differentiation patterns, guided migration as well as morphogen concentrations, shear, flow, etc.); generating code to gather and efficiently store this information; and enabling cross-talk between the rule-mining software and the framework. Finally, testing the framework capability to capture biocomplexity *in vivo* shall also be pursued in future.

Additionally, in terms of observations regarding formation of band patterns in simulations presented in Chapter 5, questions such as: did lower oxygen availability in Case

1, refer to Figure 5.3, cause the stressed cells to organise themselves in that manner; if so, can this be extrapolated to other cells, does such behaviour lead to more efficient use of resources; what kind of structure would have evolved if cells were assigned more specific rules that govern colony formation, what would be the functionality of such structure; remain a matter of speculation until investigated more rigorously both computationally as well as empirically. This framework makes the computational investigation of such questions feasible.

6.4 EPILOGUE

The work presented within this thesis was motivated by the absence of a hybrid transport-agent framework that can capture the spatiotemporal evolution of biological systems based on interactions between off-lattice, rule-obeying, cellular components and their microenvironment. To achieve this, a hybrid, multi-paradigm modelling framework that can be applied to optimise design of devices employed to maintain or grow cellular products was created and conceptually validated. The framework, which can quantify the entire biological environment and capture the seemingly non-quantifiable cellular interactions with each other and their environment, offers a novel perspective of examining biological systems. *Novel*, as the environment can be completely parameterised in terms of measurable quantities; even in terms of conformational/spatial cellular interactions. *Novel* also, for the framework makes available previously inaccessible observations, such as the impact of hydrodynamics on cellular interactions and *vice versa*. The platform, therefore, can find relevance in numerous investigations on biocomplex phenomena.

References

1. Semple JL, Woolridge N, Lumsden CJ. In vitro, in vivo, in silico: Computational systems in tissue engineering and regenerative medicine. Tissue Engineering. 2005;11(3-4):341-356.
2. Turner CH, Forwood MR, Otter MW. Mechanotransduction in bone – Do bone-cells act as sensors of fluid-flow. Faseb Journal. 1994;8(11):875-878.
3. Ventikos Y, Holland EC, Bowker TJ, et al. Computational modelling for cerebral aneurysms: risk evaluation and interventional planning. British Journal of Radiology. 2009;82:S62-S71.
4. Priami C. Algorithmic Systems Biology. Communications of the ACM. 2009;52(5):80-88.
5. Chavali AK, Gianchandani EP, Tung KS, Lawrence MB, Peirce SM, Papin JA. Characterizing emergent properties of immunological systems with multi-cellular rule-based computational modeling. Trends in Immunology. 2008;29(12):589-599.
6. Azuaje F. Computational discrete models of tissue growth and regeneration. Briefings in Bioinformatics. 2011;12(1):64-77.
7. Fortuna L, Frasca M, Fiore A, Chua L. The wolfram machine. International Journal of Bifurcation and Chaos. 2010;20(12):3863-3917.
8. Richmond P, Walker D, Coakley S, Romano D. High performance cellular level agent-based simulation with FLAME for the GPU. Briefings in Bioinformatics. 2010;11(3):334-347.
9. Lee D, Yannakakis M. Principles and methods of testing finite state machines - A survey. Proceedings of the IEEE. 1996;84(8):1090-1123.
10. Graner F, Glazier JA. Simulation of biological cell sorting using a 2-dimensional extended potts-model. Physical Review Letters. 1992;69(13):2013-2016.
11. Tamulonis CVT. Cell based models: Wiskunde en Informatica, Universiteit van Amsterdam; 2013.
12. Cheng G, Markenscoff P, Zygourakis K. A 3D Hybrid Model for Tissue Growth: The Interplay between Cell Population and Mass Transport Dynamics. Biophysical Journal. 2009;97(2):401-414.
13. Cheng G, Youssef BB, Markenscoff P, Zygourakis K. Cell population dynamics modulate the rates of tissue growth processes. Biophysical Journal. 2006;90(3):713-724.
14. Picioreanu C, van Loosdrecht MCM, Heijnen JJ. Mathematical modeling of biofilm structure with a hybrid differential-discrete cellular automaton approach. Biotechnology and Bioengineering. 1998;58(1):101-116.
15. Picioreanu C, Vrouwenvelder JS, van Loosdrecht MCM. Three-dimensional modeling of biofouling and fluid dynamics in feed spacer channels of membrane devices. Journal of Membrane Science. 2009;345(1-2):340-354.
16. Laycock G. The Theory and Practice of Specification Based Software Testing [PhD Thesis]. Sheffield: Department of Computer Science, University of Sheffield; 1993.
17. Franz-Odendaal TA, Hall BK, Witten PE. Buried alive: How osteoblasts become osteocytes. Developmental Dynamics. 2006;235(1):176-190.
18. Bissell MJ, Hall HG, Parry G. How does the extracellular matrix direct gene expression? Journal of Theoretical Biology. 1982;99(1):31-68.
19. Murry CE, Keller G. Differentiation of embryonic stem cells to clinically relevant populations: Lessons from embryonic development. Cell. 2008;132(4):661-680.
20. Gurtner GC, Callaghan MJ, Longaker MT. Progress and potential for regenerative medicine. Annual Review of Medicine. 2007;58:299-312.
21. Place ES, Evans ND, Stevens MM. Complexity in biomaterials for tissue engineering. Nature Materials. 2009;8(6):457-470.
22. Khademhosseini A, Langer R. Microengineered hydrogels for tissue engineering. Biomaterials. 2007;28:5087-5092.
23. Langer R, Vacanti JP. Tissue engineering. Science. 1993;260(5110):920-926.
24. Berthiaume F, Maguire TJ, Yarmush ML. Tissue engineering and regenerative medicine: history, progress, and challenges. Annual Review of Chemical and Biomolecular Engineering. 2011;2:403-430.
25. Science and Technology Committee, House of Lords. Regenerative Medicine [Report]. Authority of the House of Lords, London, 2013. Available at: http://www.publications.parliament.uk/pa/Id201314/ldselect/Idsctech/23/23.pdf (Last accessed November 25, 2014)..

26. Daar AS, Greenwood HL. A proposed definition of regenerative medicine. Journal of Tissue Engineering and Regenerative Medicine. 2007;1(3):179-184.
27. Mason C, Dunnill P. A brief definition of regenerative medicine. Regenerative Medicine. 2008;3(1):1-5.
28. Burdick JA, Vunjak-Novakovic G. Engineered Microenvironments for Controlled Stem Cell Differentiation. Tissue Engineering Part A. 2009;15(2):205-219.
29. Martin I, Smith T, Wendt D. Bioreactor-based roadmap for the translation of tissue engineering strategies into clinical products. Trends in Biotechnology. 2009;27(9):495-502.
30. Pellegrini G, Traverso C, Franzi A, Zingirian M, Cancedda R, DeLuca M. Long-term restoration of damaged corneal surfaces with autologous cultivated corneal epithelium. Lancet. 1997;349(9057):990-993.
31. Tsai R, Li L, Chen J. Reconstruction of damaged corneas by transplantation of autologous limbal epithelial cells. New England Journal of Medicine. 2000;343(2):86-93.
32. Macchiarini P, Jungebluth P, Go T, et al. Clinical transplantation of a tissue-engineered airway (vol 372, pg 2023, 2008). Lancet. 2009;373(9662):462-462.
33. Quarto R, Mastrogiacomo M, Cancedda R, et al. Repair of large bone defects with the use of autologous bone marrow stromal cells. New England Journal of Medicine. 2001;344(5):385-386.
34. Atala A, Bauer S, Soker S, Yoo J, Retik A. Tissue-engineered autologous bladders for patients needing cystoplasty. Lancet. 2006;367(9518):1241-1246.
35. Chamuleau R. Artificial liver support in the third millennium. Artificial Cells Blood Substitutes and Immobilization Biotechnology. 2003;31(2):117-126.
36. Griffith L, Naughton G. Tissue engineering - Current challenges and expanding opportunities. Science. 2002;295(5557):1009-1014.
37. Martin I, Wendt D, Heberer M. The role of bioreactors in tissue engineering. Trends in Biotechnology. 2004;22(2):80-86.
38. European Public Assessment Reports, European Medicines Agency. Glybera. London, 2012. Available at: http://tinyurl.com/cse72pf (Last Accessed: November 6, 2015)
39. European Public Assessment Reports, European Medicines Agency. ChondroCelect. London, 2014. Available at: http://tinyurl.com/qfrvayb(Last Accessed: November 6, 2015)
40. George J. Referral criteria for Islet Transplantation. 2012. Available at: www.youngdiabetologists.org.uk/etools/guidelines/islet (Last Accessed: November 6, 2015).
41. Mason C, Dunnill P. Lessons for the nascent regenerative medicine industry from the biotech sector. Regenerative Medicine. 2007;2(5):753-756.
42. Portner R, Nagel-Heyer S, Goepfert C, Adamietz P, Meenen N. Bioreactor design for tissue engineering. Journal of Bioscience and Bioengineering. 2005;100(3):235-245.
43. Naughton GK. From lab bench to market - Critical issues in tissue engineering. Reparative Medicine: Growing Tissues and Organs. 2002;961:372-385.
44. Jaklenec A, Stamp A, Deweerd E, Sherwin A, Langer R. Progress in the Tissue Engineering and Stem Cell Industry "Are we there yet?". Tissue Engineering Part B-Reviews. 2012;18(3):155-166.
45. Lysaght MJ, Jaklenec A, Deweerd E. Great expectations: Private sector activity in tissue engineering, regenerative medicine, and stem cell therapeutics. Tissue Engineering Part A. 2008;14(2):305-315.
46. Marga F, Neagu A, Kosztin I, Forgacs G. Developmental biology and tissue engineering. Birth Defects Research. 2007;81(4):320-328.
47. Johns Hopkins Surgeons Use Woman's Own Tissue to Rebuild Ear Lost to Cancer [press release]. Baltimore, MD, USA, 25 September, 2012 2012.
48. Parson AB. Stem cell biotech: seeking a piece of the action. Cell. 2008;132(4):511-513.
49. Mason C, Manzotti E. Regenerative medicine cell therapies: numbers of units manufactured and patients treated between 1988 and 2010. Regenerative Medicine. 2010;5(3):307-313.
50. Mason C, Dunnill P. The need for a regen industry voice. Regenerative Medicine. 2008;3(5):621-631.
51. Mason C. ISSCR 2009 Industry Panel Session: promoting translation and commercialization. Cell Stem Cell. 2009;5(4):379-384.
52. Martin PA, Coveney C, Kraft A, Brown N, Bath P. Commerical development of stem cell technology: lessons from the past, strategies for the future. Regenerative Medicine. 2006;1(6):801-807.
53. Viswanathan S, Zandstra PW. Towards predictive models of stem cell fate. Cytotechnology. 2003;41(2-3):75-92.
54. Rouwkema J, Gibbs S, Lutolf MP, Martin I, Vunjak-Novakovic G, Malda J. In vitro platforms for tissue engineering: implications for basic research and clinical translation. Journal of Tissue Engineering and Regenerative Medicine. 2011;5(8):E164-E167.

55. Singh H, Hutmacher D. Bioreactor studies and Computational Fluid Dynamics. In: Kasper C, van Griensvan M, Portner R, eds. Bioreactor Systems for Tissue Engineering. Vol 112. Berlin: Springer; 2009:231-249.
56. Wendt D, Jakob M, Martin I. Bioreactor-based engineering of osteochondral grafts: from model systems to tissue manufacturing. Journal of Bioscience and Bioengineering. 2005;100(5):489-494.
57. Weyand B, Israelowitz M, von Schroeder H, Vogt P. Fluid Dynamics in Bioreactor Design: Considerations for the Theoretical and Practical Approach. In: Kasper C, van Griensvan M, Portner R, eds. Bioreactor Systems for Tissue Engineering. Vol 112. Berlin: Springer; 2009:251-268.
58. O'Dea RD, Byrne HM, Waters SL. Continuum modelling of in vitro tissue engineering: a review. In: Geris L, ed. Computational Modeling in Tissue Engineering Vol 10. Berlin Heidelberg: Springer-Verlag; 2013:229-266.
59. Computational Modeling in Tissue Engineering. Vol 10. Berlin Heidelberg: Springer-Verlag; 2013.
60. Fernandes PR. Advances on Modeling in Tissue Engineering. Berlin Heidelberg: Springer Verlag; 2011.
61. Milde F, Bergdorf M, Koumoutsakos P. A hybrid model for three-dimensional simulations of sprouting angiogenesis. Biophysical Journal. 2008;95(7):3146-3160.
62. Ferziger J, Peric M. Computational methods for fluid dynamics. 3, illustrated ed. New York: Springer-Verlag; 2002.
63. Smallwood RH, Holcombe WML, Walker DC. Development and validation of computational models of cellular interaction. Journal of Molecular Histology. 2004;35(7):659-665.
64. Smallwood R, Holcombe M. The Epitheliome Project: Multiscale agent-based modeling of epithelial cells. 2006 3rd IEEE International Symposium on Biomedical Imaging: Macro to Nano, Vols 1-3. 2006:816-819.
65. Meller J. Molecular Dynamics. Encyclopedia of Life Sciences. 2010. DOI: 10.1002/9780470015902.a0003048.pub2
66. Sucosky P, Osorio DF, Brown JB, Neitzel GP. Fluid mechanics of a spinner-flask bioreactor. Biotechnology and Bioengineering. 2004;85(1):34-46.
67. Bilgen B, Sucosky P, Neitzel GP, Barabino GA. Flow characterization of a wavy-walled bioreactor for cartilage tissue engineering. Biotechnology and Bioengineering. 2006;95(6):1009-1022.
68. Nagata S. Mixing - principles and applications. New York: John Wiley and Sons; 1975:124-138.
69. Ye H, Das DB, Triffitt JT, Cui ZF. Modelling nutrient transport in hollow fibre membrane bioreactors for growing three-dimensional bone tissue. Journal of Membrane Science. 2006;272(1-2):169-178.
70. Abdullah NS, Das DB. Modelling nutrient transport in hollow fibremembrane bioreactor for growing bone tissue with consideration of multi-component interactions. Chemical Engineering Science. 2007;62(21):5821-5839.
71. Begley CM, Kleis SJ. The fluid dynamic and shear environment in the NASA/JSC rotating-wall perfused-vessel bioreactor. Biotechnology and Bioengineering. 2000;70(1):32-40.
72. Freed LE, Vunjaknovakovic G. Cultivation of cell-polymer tissue constructs in simulated microgravity. Biotechnology and Bioengineering. 1995;46(4):306-313.
73. Martin Y, Vermette P. Bioreactors for tissue mass culture: Design, characterization, and recent advances. Biomaterials. 2005;26(35):7481-7503.
74. Massey BS, Ward-Smith AJ. Mechanics of fluids. 9th ed. London: Spon; 2012.
75. Vermette P, Martin Y. Bioreactors for tissue mass culture: Design, characterization, and recent advances. Biomaterials. 2005;26(35):7481-7503.
76. Peng CA, Koller MR, Palsson BO. Unilineage model of hematopoiesis predicts self-renewal of stem and progenitor cells based on ex vivo growth data. Biotechnology and Bioengineering. 1996;52(1):24-33.
77. ESI-CFD. CFD-ACE+ User Manual. 2010.
78. Kaviany M. Principles of heat transfer in porous media. 2nd ed. New York: Springer; 1995:15-113.
79. Whitaker S. Flow in porous media I: A theoretical derivation of Darcy's law. Transport in Porous Media. 1986;1(1):3-25.
80. Guo P. Dependency of tortuosity and permeability of porous media on directional distribution of pore voids. Transport in Porous Media. 2012;95(2):285-303.
81. Anderson J. Computational Fluid Dynamics. McGraw-Hill; 1995.
82. Mitchell SA, Vavasis SA. Quality mesh generation in three dimensions. Proceedings of the ACM Computational Geometry Conference. 1992. DOI: 10.1145/142675.142720. Available at: http://www.sandia.gov/~samitch/csstuff/tri/quality-mesh.pdf (Last Accessed: November 3, 2015).
83. Holland EC. Computational Modelling of Transport Phenomena in Cerebral Aneurysms. Oxford: Engineering Science, University of Oxford; 2012.

84. Patankar SV. Numerical heat transfer and fluid flow. Washington ; London: Hemisphere; 1980.
85. Williams KA, Saini S, Wick TM. Computational fluid dynamics modeling of steady-state momentum and mass transport in a bioreactor for cartilage tissue engineering. Biotechnology Progress. 2002;18(5):951-963.
86. Luo L-S, Krafczyk M, Shyy W. Lattice Boltzmann method for computational fluid dynamics. In: Blockley R, Shyy W, eds. Encyclopedia of Aerospace Engineering: John Wiley & Sons, Ltd.; 2010:651-660.
87. Stockman HW. A 3D Lattice Boltzmann code for modeling flow and multi-component dispersion. Albuquerque, NM: Sandia National Laboratories; 1999. Available at: http://citeseerx.ist.psu.edu/viewdoc/summary?doi=10.1.1.30.9347 (Last accessed: November 3, 2015).
88. Porter B, Zauel R, Stockman H, Guldberg R, Fyhrie D. 3-D computational modeling of media flow through scaffolds in a perfusion bioreactor. Journal of Biomechanics. 2005;38(3):543-549.
89. Thürey N, Rüde U, Körner C. Interactive free surface fluids with the lattice boltzman method. University of Erlangen-Nuremberg; 2003.
90. Lappa M. Organic tissues in rotating bioreactors: fluid-mechanical aspects, dynamic growth models, and morphological evolution. Biotechnol Bioeng. 2003;84(5):518-532.
91. Lappa M. A CFD level-set method for soft tissue growth: theory and fundamental equations. Journal of Biomechanics. 2005;38(1):185-190.
92. Sethian JA. Level Set Methods and Fast Marching MethodsEvolving Interfaces in Computational Geometry, Fluid Mechanics, Computer Vision, and Materials Science. 2nd ed: Cambridge University Press; 1999.
93. Osher S, Fedkiw RP. Level set methods: An overview and some recent results. Department of Mathematics, University of California Los Angeles; 2000. Available at: http://physbam.stanford.edu/~fedkiw/papers/cam2000-08.pdf (Last Accessed: November 3, 2015).
94. Obradovic B, Meldon JH, Freed LE, Vunjak-Novakovic G. Glycosaminoglycan deposition in engineered cartilage: Experiments and mathematical model. AIChE Journal. 2000;46(9):1860-1871.
95. Boccaccio A, Ballini A, Pappalettere C, Tullo D, Cantore S, Desiate A. Finite Element Method (FEM), Mechanobiology and Biomimetic Scaffolds in Bone Tissue Engineering. International Journal of Biological Sciences. 2011;7(1):112-132.
96. Kelly DJ, Prendergast PJ. Prediction of the optimal mechanical properties for a scaffold used in osteochondral defect repair. Tissue Engineering. 2006;12(9):2509-2519.
97. Prendergast PJ, Huiskes R, Soballe K. Biophysical stimuli on cells during tissue differentiation at implant interfaces. Journal of Biomechanics. 1997;30(6):539-548.
98. Vaughan BL, Jr., Galie PA, Stegemann JP, Grotberg JB. A Poroelastic Model Describing Nutrient Transport and Cell Stresses Within a Cyclically Strained Collagen Hydrogel. Biophysical Journal. 2013;105(9):2188-2198.
99. Byrne DP, Lacroix D, Planell JA, Kelly DJ, Prendergast PJ. Simulation of tissue differentiation in a scaffold as a function of porosity, Young's modulus and dissolution rate: Application of mechanobiological models in tissue engineering. Biomaterials. 2007;28(36):5544-5554.
100. Milan J-L, Planell JA, Lacroix D. Computational modelling of the mechanical environment of osteogenesis within a polylactic acid-calcium phosphate glass scaffold. Biomaterials. 2009;30(25):4219-4226.
101. Sandino C, Planell JA, Lacroix D. A finite element study of mechanical stimuli in scaffolds for bone tissue engineering. Journal of Biomechanics. 2008;41(5):1005-1014.
102. Fang Z, Starly B, Sun W. Computer-aided characterization for effective mechanical properties of porous tissue scaffolds. Computer-Aided Design. 2005;37(1):65-72.
103. McMahon LA, Reid AJ, Campbell VA, Prendergast PJ. Regulatory effects of mechanical strain on the chondrogenic differentiation of MSCs in a collagen-GAG scaffold: Experimental and computational analysis. Annals of Biomedical Engineering. 2008;36(2):185-194.
104. Detournay E, Cheng AHD. Fundamentals of poroelasticity. In: Fairhurst C, ed. Comprehensive Rock Engineering: Principles, Practice and Projects, Analysis and Design Method, Vol II. Vol 2: Pergamon Press; 1993:113-171.
105. Peng CA, Palsson BO. Cell growth and differentiation on feeder layers is predicted to be influenced by bioreactor geometry. Biotechnology and Bioengineering. 1996;50(5):479-492.
106. Mitchell M. Computation in cellular automata: A selected review. In: Gramss T, Bornholdt S, Gross M, Mitchell M, Pellizzari T, eds. Nonstandard computation. Weinheim: VCH Verlagsgesellschaft; 1998:95-140.

107. Hwang M, Garbey M, Berceli SA, Tran-Son-Tay R. Rule-Based Simulation of Multi-Cellular Biological Systems-A Review of Modeling Techniques. Cellular and Molecular Bioengineering. 2009;2(3):285-294.
108. Coakley S, Smallwood R, Holcombe M. Using X-machines as a formal basis for describing agents in agent-based modelling. Spring Simulation Multiconference 2006; 2006; Huntsville, Alabama, USA. Available at: http://www.flame.ac.uk/pubs/pdf/ADS005_Coakley.pdf (Last Accessed: November 3, 2015).
109. Galvao V, Miranda JGV, Ribeiro-Dos-Santos R. Development of a two-dimensional agent-based model for chronic chagasic cardiomyopathy after stem cell transplantation. Bioinformatics. 2008;24(18):2051-2056.
110. Soares MBP, Lima RS, Rocha LL, et al. Transplanted bone marrow cells repair heart tissue and reduce myocarditis in chronic chagasic mice. American Journal of Pathology. 2004;164(2):441-447.
111. Szabo A, Merks RMH. Cellular potts modeling of tumor growth, tumor invasion, and tumor evolution. Frontiers in oncology. 2013;3:87-87.
112. Voss-Boehme A. Multi-Scale Modeling in Morphogenesis: A Critical Analysis of the Cellular Potts Model. PLoS One. 2012;7(9): e42852.
113. Merks RM, Brodsky SV, Goligorksy MS, Newman SA, Glazier JA. Cell elongation is key to in silico replication of in vitro vasculogenesis and subsequent remodeling. Developmental Biology. 2006;289(1):44-54.
114. Guidolin D, Albertin G, Sorato E, Oselladore B, Mascarin A, Ribatti D. Mathematical Modeling of the Capillary-Like Pattern Generated by Adrenomedullin-Treated Human Vascular Endothelial Cells In Vitro. Developmental Dynamics. 2009;238(8):1951-1963.
115. Chaturvedi R, Huang C, Kazmierczak B, et al. On multiscale approaches to three-dimensional modelling of morphogenesis. Journal of the Royal Society Interface. 2005;2(3):237-253.
116. Zeng W, Thomas GL, Glazier JA. Non-Turing stripes and spots: a novel mechanism for biological cell clustering. Physica A: Statistical Mechanics and Its Applications. 2004;341:482-494.
117. Hirashima T, Iwasa Y, Morishita Y. Dynamic modeling of branching morphogenesis of ureteric bud in early kidney development. Journal of Theoretical Biology. 2009;259(1):58-66.
118. Merks RMH, Perryn ED, Shirinifard A, Glazier JA. Contact-Inhibited Chemotaxis in De Novo and Sprouting Blood-Vessel Growth. PLoS Computational Biology. 2008;4(9):e1004163:.
119. Merks RMH, Glazier JA. A cell-centered approach to developmental biology. Physica A: Statistical Mechanics and Its Applications. 2005;352(1):113-130.
120. Adra S, Coakley S, Kiran M, McMinn P. An Agent-Based software platform for modelling systems biology. 2008:58. Available at: http://tinyurl.com/np93m6y (Last Accessed: November 3, 2015).
121. Jennings NR. On agent-based software engineering. Artificial Intelligence. 2000;117(2):277-296.
122. Wooldridge M. Agent-based software engineering. IEE Proceedings-Software Engineering. 1997;144(1):26-37.
123. Walker DC, Southgate J, Hill G, et al. The epitheliome: agent-based modelling of the social behaviour of cells. Biosystems. 2004;76(1-3):89-100.
124. Walker D, Sun T, Macneil S, Smallwood R. Modeling the effect of exogenous calcium on keratinocyte and HaCat cell proliferation and differentiation using an agent-based computational paradigm. Tissue Engineering. 2006;12(8):2301-2309.
125. Artel A, Mehdizadeh H, Chiu YC, Brey EM, Cinar A. An Agent-Based Model for the Investigation of Neovascularization Within Porous Scaffolds. Tissue Engineering Part A. 2011;17(17-18):2133-2141.
126. Wilensky U. NetLogo 5.1.0 User Manual. NetLogo; 2014: Available at: https://ccl.northwestern.edu/netlogo/docs/NetLogo%20User%20Manual.pdf (Last Accessed: November 3, 2015).
127. Hoehme S, Drasdo D. A cell-based simulation software for multi-cellular systems. Bioinformatics. 2010;26(20):2641-2642.
128. Swat M, Gilberto TL, Julio BM, Shirinifard A, Hmeljak D, Glazier JA. Multi-scale modeling of tissues using CompuCell3D. In: Asthagiri AR, Arkin AP, eds. Computational Methods in Cell Biology. Vol 110: Elsevier; 2012:325-366.
129. Mirams GR, Arthurs CJ, Bernabeu MO, et al. Chaste: An Open Source C plus plus Library for Computational Physiology and Biology. PLoS Computational Biology. 2013;9(3):e1002970.
130. Truskey GA, Yuan F, Katz DF. Transport phenomena in biological systems. Upper Saddle River, N.J.: Pearson/Prentice Hall; 2004.

131. Versteeg HK, Malalasekera W. An introduction to computational fluid dynamics : the finite volume method. 2nd ed. New York: Pearson Education Ltd.; 2007.
132. Yoshino M, Inamuro T. Lattice Boltzmann simulations for flow and heat/mass transfer problems in a three-dimensional porous structure. International Journal for Numerical Methods in FLuids. 2003;43:183-198.
133. Orszag S. Lattice Boltzmann methods for fluid dynamics. 2009. Available at: http://qmcd09.physics.wustl.edu/Presentations/qmcd09Talks/orszag.pdf (Last Accessed: November 3, 2015).
134. Sethian JA, Smereka P. Level set methods for fluid interfaces. Annual Review of Fluid Mechanics. 2003;35:341-372.
135. Folkman J, Moscona A. Role of cell shape in growth control. Nature. 1978;273(5661):345-349.
136. Scadden DT. The stem-cell niche as an entity of action. Nature. 2006;441(7097):1075-1079.
137. Rawles ME. Tissue interactions in scale and feather development as studied in dermal-epidermal recombinations. Journal of Embryology and Experimental Morphology. 1963;11:765-789.
138. Saunders JW, Gasseling MT. The origin of pattern and feather germ tract specificity. Journal of Experimental Zoology. 1957;135(3):503-527.
139. Dhouailly D. Formation of cutaneous appendages in dermo-epidermal recombinations between reptiles, birds and mammals. Wilhelm Roux's Archives of Developmental Biology. 1975;177(4):323-340.
140. Wessells NK. Skin and Its Derivates. Tissue Interactions and Development: W. A. Benjamin Inc.; 1977:55-65.
141. Albrecht DR, Tsang VL, Sah RL, Bhatia SN. Photo- and electropatterning of hydrogel-encapsulated living cell arrays. Lab on a Chip. 2005;5(1):111-118.
142. Anderson DG, Levenberg S, Langer R. Nanoliter-scale synthesis of arrayed biomaterials and application to human embryonic stem cells. Nature Biotechnology. 2004;22(7):863-866.
143. Geckil H, Xu F, Zhang XH, Moon S, Demirci U. Engineering hydrogels as extracellular matrix mimics. Nanomedicine. 2010;5(3):469-484.
144. Graichen R, Xu XQ, Braam SR, et al. Enhanced cardiomyogenesis of human embryonic stem cells by a small molecular inhibitor of p38 MAPK. Differentiation. 2008;76(4):357-370.
145. Nelson CM, Bissell MJ. Of extracellular matrix, scaffolds, and signaling: Tissue architecture regulates development, homeostasis, and cancer. Annual Review of Cell and Developmental Biology. 2006;22:287-309.
146. Roeder I, Lorenz R. Asymmetry of stem cell fate and the potential impact of the niche - Observations, simulations, and interpretations. Stem Cell Reviews. 2006;2(3):171-180.
147. Riggs T, Walts A, Perry N, et al. A comparison of random vs. chemotaxis-driven contacts of T cells with dendritic cells during repertoire scanning. Journal of Theoretical Biology. 2008;250(4):732-751.
148. Casal A, Sumen C, Reddy TE, Alber MS, Lee PP. Agent-based modeling of the context dependency in T cell recognition. Journal of Theoretical Biology. 2005;236(4):376-391.
149. Helbing D. Agent-Based Modeling. In: Helbing D, ed. Social Self-Organization: Springer Berlin Heidelberg; 2012:25-70.
150. Railsback SF, Grimm V. Agent-Based and Individual-Based Modeling. Princeton University Press; 2012.
151. Thorne BC, Bailey AM, Peirce SM. Combining experiments with multi-cell agent-based modeling to study biological tissue patterning. Briefings in Bioinformatics. 2007;8(4):245-257.
152. Calvez B, Hutzler G, Khosla R, Howlett R, Jain L. Parameter space exploration of agent-based models. Knowledge-Based Intelligent Information and Engineering Systems, Pt 4, Proceedings. 2005;3684:633-639.
153. Goldenfeld N, Kadanoff LP. Simple lessons from complexity. Science. 1999;284(5411):87-89.
154. Zahedmanesh H, Lally C. A multiscale mechanobiological modelling framework using agent-based models and finite element analysis: application to vascular tissue engineering. Biomechanics and Modeling in Mechanobiology. 2012;11(3-4):363-377.
155. Hong H, McCullough CM, Stegemann JP. The role of ERK signaling in protein hydrogel remodeling by vascular smooth muscle cells. Biomaterials. 2007;28(26):3824-3833.
156. Tibbitt MW, Anseth KS. Hydrogels as Extracellular Matrix Mimics for 3D Cell Culture. Biotechnology and Bioengineering. 2009;103(4):655-663.
157. Geris L, Sloten JV, Van Oosterwyck H. In silico biology of bone modelling and remodelling: regeneration. Philosophical Transactions of the Royal Society A: Mathematical Physical and Engineering Sciences. 2009;367(1895):2031-2053.

158. Cioffi M, Boschetti F, Raimondi MT, Dubini G. Modeling evaluation of the fluid-dynamic microenvironment in tissue-engineered constructs: A micro-CT based model. Biotechnology and Bioengineering. 2006;93(3):500-510.
159. Maes F, Van Ransbeeck P, Van Oosterwyck H, Verdonck P. Modeling Fluid Flow Through Irregular Scaffolds for Perfusion Bioreactors. Biotechnology and Bioengineering. 2009;103(3):621-630.
160. Bilgen B, Barabino GA. Location of scaffolds in bioreactors modulates the hydrodynamic environment experienced by engineered tissues. Biotechnology and Bioengineering. 2007;98(1):282-294.
161. Consolo F, Caronna M, Montevecchi FM, Flore GB, Redaelli A, Asme. A computational model for the optimization of transport phenomena in a rotating hollow-fiber bioreactor for artificial liver. Proceedings of the ASMA Summer Bioengineering Conference 2008, Pts a and B. 2009:477-478.
162. Cinbiz MN, Tigli RS, Beskardes IG, Gumusderelioglu M, Colak U. Computational fluid dynamics modeling of momentum transport in rotating wall perfused bioreactor for cartilage tissue engineering. Journal of Biotechnology. 2010;150(3):389-395.
163. Song MJ, Dean D, Tate MLK. In Situ Spatiotemporal Mapping of Flow Fields around Seeded Stem Cells at the Subcellular Length Scale. PLoS One. 2010;5(9):e12796.
164. Raimondi MT, Boschetti F, Falcone L, Migliavacca F, Remuzzi A, Dubini G. The effect of media perfusion on three-dimensional cultures of human chondrocytes: Integration of experimental and computational approaches. Biorheology. 2004;41(3-4):401-410.
165. Boschetti F, Raimondi MT, Migliavacca F, Dubini G. Prediction of the micro-fluid dynamic environment imposed to three-dimensional engineered cell systems in bioreactors. Journal of Biomechanics. 2006;39(3):418-425.
166. Yu P, Lee T, Zeng Y, Low HT. A 3D analysis of oxygen transfer in a low-cost micro-bioreactor for animal celll suspension culture. Computer Methods and Programs in Biomedicine. 2007;85(1):59-68.
167. Singh H, Teoh SH, Low HT, Hutmacher DW. Flow modelling within a scaffold under the influence of uni-axial and bi-axial bioreactor rotation. Journal of Biotechnology. 2005;119(2):181-196.
168. Yi-Chin T, Chi Z, Jing Z, et al. A novel 3D mammalian cell perfusion-culture system in microfluidic channels. Lab on a Chip. 2007;7(3):302-309.
169. Pollack SR, Meaney DF, Levine EM, Litt M, Johnston ED. Numerical model and experimental validation of microcarrier motion in a rotating bioreactor. Tissue Engineering. 2000;6(5):519-530.
170. Cui ZF, Xu X, Trainor N, Triffitt JT, Urban JPG, Tirlapur UK. Application of multiple parallel perfused microbioreactors and three-dimensional stem cell culture for toxicity testing. Toxicology in Vitro. 2007;21(7):1318-1324.
171. Smidsrod O, Skjakbraek G. Alginate as immobilization matrix for cells. Trends in Biotechnology. 1990;8(3):71-78.
172. Li CKN. The glucose distribution in 9L rat-brain multicell tumor spheroids and its effect on cell necrosis. Cancer. 1982;50(10):2066-2073.
173. Teixeira JA, Mota M, Venancio A. Model identification and diffusion coefficients determination of glucose and malic acid in calcium alginate membranes. Chemical Engineering Journal and the Biochemical Engineering Journal. 1994;56(1):B9-B14.
174. Melvik JE, Dornish M. Alginate as a carrier for cell immobilisation. Fundamentals of Cell Immobilisation Biotechnology. 2004;8A:33-51.
175. Khalil M, Shariat-Panahi A, Tootle R, et al. Human hepatocyte cell lines proliferating as cohesive spheroid colonies in alginate markedly upregulate both synthetic and detoxificatory liver function. Journal of Hepatology. 2001;34(1):68-77.
176. Gombotz WR, Wee SF. Protein release from alginate matrices. Advanced Drug Delivery Reviews. 1998;31(3):267-285.
177. Goh CH, Heng PWS, Chan LW. Alginates as a useful natural polymer for microencapsulation and therapeutic applications. Carbohydrate Polymers. 2012;88(1):1-12.
178. Pattappa G, Heywood HK, De Bruijn JD, Lee DA. The Metabolism of Human Mesenchymal Stem Cells During Proliferation and Differentiation. Journal of Cellular Physiology. 2011;226(10):2562-2570.
179. Deschepper M, Oudina K, David B, et al. Survival and function of mesenchymal stem cells (MSCs) depend on glucose to overcome exposure to long-term, severe and continuous hypoxia. Journal of Cellular and Molecular Medicine. 2011;15(7):1505-1514.
180. Mehmetoglu U, Ates S, Berber R. Oxygen diffusivity in calcium alginate gel beads containing Gluconobacter suboxydans. Artificial Cells Blood Substitutes and Immobilization Biotechnology. 1996;24(2):91-106.

181. van Doormaal JP, Raithby GD. Enhancements of the simple method for predicting incompressible fluid-flows. Numerical Heat Transfer. 1984;7(2):147-163.
182. Patankar SV, Spalding DB. A calculation procedure for heat, mass and momentum transfer in three-dimensional parabolic flows. International Journal of Heat and Mass Transfer. 1972;15(10):1787-1806.
183. Hutchinson BR, Galpin PF, Raithby GD. Application of additive correction multigrid to the coupled fluid-flow equations. Numerical Heat Transfer. 1988;13(2):133-147.
184. Carrier RL, Rupnick M, Langer R, Schoen FJ, Freed LE, Vunjak-Novakovic G. Perfusion improves tissue architecture of engineered cardiac muscle. Tissue Engineering. 2002;8(2):175-188.
185. Imberti B, Seliktar D, Nerem RM, Remuzzi A. The response of endothelial cells to fluid shear stress using a co-culture model of the arterial wall. Endothelium-New York. 2002;9(1):11-23.
186. Mardikar SH, Niranjan K. Observations on the shear damage to different animal cells in a concentric cylinder viscometer. Biotechnology and Bioengineering. 2000;68(6):697-704.
187. Maul TM, Chew DW, Nieponice A, Vorp DA. Mechanical stimuli differentially control stem cell behavior: morphology, proliferation, and differentiation. Biomechanics and Modeling in Mechanobiology. 2011;10(6):939-953.
188. Yamamoto K, Takahashi T, Asahara T, et al. Proliferation, differentiation, and tube formation by endothelial progenitor cells in response to shear stress. Journal of Applied Physiology. 2003;95(5):2081-2088.
189. Yourek G, McCormick SM, Mao JJ, Reilly GC. Shear stress induces osteogenic differentiation of human mesenchymal stem cells. Regenerative Medicine. 2010;5(5):713-724.
190. Chien S. Mechanotransduction and endothelial cell homeostasis: the wisdom of the cell. American Journal of Physiology-Heart and Circulatory Physiology. 2007;292(3):H1209-H1224.
191. Vunjak-Novakovic G, Meinel L, Altman G, Kaplan D. Bioreactor cultivation of osteochondral grafts. Orthodontics & Craniofacial Research. 2005;8(3):209-218.
192. Kreke MR, Huckle WR, Goldstein AS. Fluid flow stimulates expression of osteopontin and bone sialoprotein by bone marrow stromal cells in a temporally dependent manner. Bone. 2005;36(6):1047-1055.
193. Sikavitsas VI, Bancroft GN, Holtorf HL, Jansen JA, Mikos AG. Mineralized matrix deposition by marrow stromal osteoblasts in 3D perfusion culture increases with increasing fluid shear forces. Proceedings of the National Academy of Sciences of the United States of America. 2003;100(25):14683-14688.
194. Wang YC, Uemura T, Dong R, Kojima H, Tanaka J, Tateishi T. Application of perfusion culture system improves in vitro and in vivo osteogenesis of bone marrow-derived osteoblastic cells in porous ceramic materials. Tissue Engineering. 2003;9(6):1205-1214.
195. Yu XJ, Botchwey EA, Levine EM, Pollack SR, Laurencin CT. Bioreactor-based bone tissue engineering: The influence of dynamic flow on osteoblast phenotypic expression and matrix mineralization. Proceedings of the National Academy of Sciences of the United States of America. 2004;101(31):11203-11208.
196. Ma CYJ, Kumar R, Xu XY, Mantalaris A. A combined fluid dynamics, mass transport and cell growth model for a three-dimensional perfused biorector for tissue engineering of haematopoietic cells. Biochemical Engineering Journal. 2007;35(1):1-11.
197. Garza-Garcia LD, Carrillo-Cocom LM, Araiz-Hernandez D, et al. A biopharmaceutical plant on a chip: continuous micro-devices for the production of monoclonal antibodies. Lab on a Chip. 2013;13(7):1243-1246.
198. Sodian R, Lemke T, Loebe M, et al. New pulsatile bioreactor for fabrication of tissue-engineered patches. Journal of Biomedical Materials Research. 2001;58(4):401-405.
199. Zhao F, Chella R, Ma T. Effects of shear stress on 3-D human mesenchymal stem cell construct development in a perfusion bioreactor system: Experiments and hydrodynamic modeling. Biotechnology and Bioengineering. 2007;96(3):584-595.
200. Unsworth BR, Lelkes PI. Growing tissues in microgravity. Nature Medicine. 1998;4(8):901-907.
201. Dos Santos F, Andrade PZ, Boura JS, Abecasis MM, da Silva CL, Cabral JM. Ex vivo expansion of human mesenchymal stem cells: a more effective cell proliferation kinetics and metabolism under hypoxia. Journal of Cell Physiology. 2010;223(1):27-35.
202. Higuera G, Schop D, Janssen F, van Dijkhuizen-Radersma R, van Boxtel T, van Blitterswijk CA. Quantifying In Vitro Growth and Metabolism Kinetics of Human Mesenchymal Stem Cells Using a Mathematical Model. Tissue Engineering Part A. 2009;15(9):2653-2663.

203. Chen CT, Shih YR, Kuo TK, Lee OK, Wei YH. Coordinated changes of mitochondrial biogenesis and antioxidant enzymes during osteogenic differentiation of human mesenchymal stem cells. Stem Cells. 2008;26(4):960-968.
204. Saki N, Jalalifar MA, Soleimani M, Hajizamani S, Rahim F. Adverse effect of high glucose concentration on stem cell therapy. International Journal of Hematology-Oncology and Stem Cell Research. 2013;7(3):34-40.
205. Robertson RP, Harmon JS. Diabetes, glucose toxicity, and oxidative stress: A case of double jeopardy for the pancreatic islet beta cell. Free Radical Biology and Medicine. 2006;41(2):177-184.
206. Stolzing A, Coleman N, Scutt A. Glucose-induced replicative senescence in mesenchymal stem cells. Rejuvenation Research. 2006;9(1):31-35.
207. Li YM, Schilling T, Benisch P, et al. Effects of high glucose on mesenchymal stem cell proliferation and differentiation. Biochemical and Biophysical Research Communications. 2007;363(1):209-215.
208. Garfinkel A, Tintut Y, Petrasek D, Boström K, Demer LL. Pattern formation by vascular mesenchymal cells. Proceedings of the National Academy of Sciences of the United States of America. 2004;101(25):9247-9250.
209. Checa S, Prendergast PJ. A Mechanobiological Model for Tissue Differentiation that Includes Angiogenesis: A Lattice-Based Modeling Approach. Annals of Biomedical Engineering. 2009;37(1):129-145.
210. Kiskowski MA, Alber MS, Thomas GL, et al. Interplay between activator-inhibitor coupling and cell-matrix adhesion in a cellular automaton model for chondrogenic patterning. Developmental Biology. 2004;271(2):372-387.
211. Glimm T, Headon D, Kiskowski MA. Computational and mathematical models of chondrogenesis in vertebrate limbs. Birth Defects Research Part C-Embryo Today-Reviews. 2012;96(2):176-192.
212. Li X, Upadhyay AK, Bullock AJ, et al. Skin stem cell hypotheses and long term clone survival--explored using agent-based modelling. Scientific Reports. 2013;3:1904.
213. Park YK, Tu TY, Lim SH, Clement IJ, Yang SY, Kamm RD. In Vitro Microvessel Growth and Remodeling within a Three-dimensional Microfluidic Environment. Cell Mol Bioeng. 2014;7(1):15-25.
214. Carrion B, Huang CP, Ghajar CM, et al. Recreating the perivascular niche ex vivo using a microfluidic approach. Biotechnol Bioeng. 2010;107(6):1020-1028.
215. Yeon JH, Ryu HR, Chung M, Hu QP, Jeon NL. In vitro formation and characterization of a perfusable three-dimensional tubular capillary network in microfluidic devices. Lab Chip. 2012;12(16):2815-2822.
216. Chen YC, Lin RZ, Qi H, et al. Functional Human Vascular Network Generated in Photocrosslinkable Gelatin Methacrylate Hydrogels. Adv Funct Mater. 2012;22(10):2027-2039.
217. Amini AR, Laurencin CT, Nukavarapu SP. Bone tissue engineering: recent advances and challenges. Critical Reviews in Biomedical Engineering. 2012;40(5):363-408.
218. O'Keefe RJ, Mao J. Bone Tissue Engineering and Regeneration: From Discovery to the Clinic-An Overview Introduction. Tissue Engineering Part B-Reviews. 2011;17(6):389-392.
219. Atchley WR, Hall BK. A model for development and evolution of complex morphological structures. Biological Reviews of the Cambridge Philosophical Society. 1991;66(2):101-157.
220. Hall BK, Miyake T. All for one and one for all: condensations and the initiation of skeletal development. Bioessays. 2000;22(2):138-147.
221. Jabalee J, Hillier S, Franz-Odendaal TA. An investigation of cellular dynamics during the development of intramembranous bones: the scleral ossicles. Journal of Anatomy. 2013;223(4):311-320.
222. Gilbert S. Developmental Biology. 6 ed. Sunderland, MA: Sinauer Associates Inc.; 2000.
223. Knese KH. Stüzgewebe und Skelettsystem. Handbuch der mikroskopischen Anatomie des Menschen. Berlin: Springer Verlag; 1979:940.
224. Ham AW, Cormack DH. Histophysiology of cartilage, bone, and joints. Philadelphia: Lippincott; 1979.
225. Bloom W, Fawcett DW. A textbook of histology. 10th ed. Philadelphia: Saunders; 1975.
226. Ferretti M, Palumbo C, Contri M, Marotti G. Static and dynamic osteogenesis: Two different types of bone formation. Anatomy and Embryology. 2002;206(1-2):21-29.
227. Romer AS. The vertebrate body. 4th ed. Philadelphia,: Saunders; 1970.
228. Windle WF, Nonidez JF. Textbook of histology. 5th ed. New York: McGraw-Hill; 1976.
229. Palumbo C, Palazzini S, Zaffe D, Marotti G. Osteocyte differentiation in the tibia of newborn rabbit: an ultrastructural study of the formation of cytoplasmic processes. Acta Anatomica. 1990;137(4):350-358.
230. Nefussi JR, Sautier JM, Nicolas V, Forest N. How osteoblasts become osteocytes: a decreasing matrix forming process. Journal de biologie buccale. 1991;19(1):75-82.

231. Grüneberg, H. The pathology of development: A study of inherited skeletal disorders in animals. John Wiley & Sons Inc, New York; 1963.
232. Lian JB, Stein GS. Development of the osteoblast phenotype: molecular mechanisms mediating osteoblast growth and differentiation. The Iowa Orthopaedic journal. 1995;15:118-140.
233. Kaul H, Ventikos Y. Investigating biocomplexity through the agent-based paradigm. Briefings in Bioinformatics. 2015;16(1):137-152.
234. Turing AM. The chemical basis of morphogenesis. Philosophical Transactions of the Royal Society of London Series B-Biological Sciences. 1952;237(641):37-72.
235. Christley S, Zhu XL, Newman SA, Alber MS. Multiscale agent-based simulation for chondrogenic pattern formation in vitro. Cybernetics and Systems. 2007;38(7):707-727.
236. Bailón-Plaza A, van der Meulen MC. A mathematical framework to study the effects of growth factor influences on fracture healing. Journal of Theoretical Biology. 2001;212(2):191-209.
237. Gerhard FA, Webster DJ, van Lenthe GH, Mueller R. In silico biology of bone modelling and remodelling: adaptation. Philosophical Transactions of the Royal Society A: Mathematical Physical and Engineering Sciences. 2009;367(1895):2011-2030.
238. Lacroix D, Prendergast PJ. A mechano-regulation model for tissue differentiation during fracture healing: analysis of gap size and loading. Journal of Biomechanics. 2002;35(9):1163-1171.
239. Bailon-Plaza A, van der Meulen MCH. Beneficial effects of moderate, early loading and adverse effects of delayed or excessive loading on bone healing. Journal of Biomechanics. 2003;36(8):1069-1077.
240. Geris L, Gerisch A, Sloten JV, Weiner R, Van Oosterwyck H. Angiogenesis in bone fracture healing: A bioregulatory model. Journal of Theoretical Biology. 2008;251(1):137-158.
241. Cickovski TM, Huang CB, Chaturvedi R, et al. A framework for three-dimensional simulation of morphogenesis. Ieee-Acm Transactions on Computational Biology and Bioinformatics. 2005;2(4):273-288.
242. Boehm B, Westerberg H, Lesnicar-Pucko G, et al. The Role of Spatially Controlled Cell Proliferation in Limb Bud Morphogenesis. Plos Biology. 2010;8(7):e1000420.
243. Bonabeau E. Agent-based modeling: Methods and techniques for simulating human systems. Proceedings of the National Academy of Sciences of the United States of America. 2002;99:7280-7287.
244. Grimm V, Railsback SF. Agent-Based Models in Ecology: Patterns and Alternative Theories of Adaptive Behaviour. In: Billari FCF, Thomas Prskawetz, Alexia Scheffran, Jürgen, ed. Agent-Based Computational Modelling: Physica-Verlag HD; 2006:139-152.
245. Adra S, Sun T, MacNeil S, Holcombe M, Smallwood R. Development of a Three Dimensional Multiscale Computational Model of the Human Epidermis. PLoS One. 2010;5(1):e8511.
246. Kiran M, Coakley S. Flexible Large-scale Agent-based Modelling Environment User Manual. University of Sheffield. 2010:44. Available at: http://www.flame.ac.uk
247. Stains JP, Civitelli R. Gap junctions in skeletal development and function. Biochimica et Biophysica Acta. 2005;1719(1-2):69-81.
248. Kasperk C, Wergedal J, Strong D, et al. Human bone cell phenotypes differ depending on their skeletal site of origin. Journal of Clinical Endocrinology & Metabolism. 1995;80(8):2511-2517.
249. Beresford JN, Graves SE, Smoothy CA. Formation of mineralized nodules by bone derived cells in vitro: a model of bone formation? American Journal of Medical Genetics. 1993;45(2):163-178.
250. Bhargava U, Barlev M, Bellows CG, Aubin JE. Ultrastructural analysis of bone nodules formed in vitro by isolated fetal rat calvaria cells. Bone. 1988;9(3):155-163.
251. Bellows CG, Aubin JE, Heersche JNM, Antosz ME. Mineralized bone nodules formed in vitro from enzymatically released rat calvaria cell populations. Calcified Tissue International. 1986;38(3):143-154.
252. Bellows CG, Aubin JE, Heersche JNM. Physiological concentrations of glucocorticoids stimulate formation of bone nodules from isolated rat calvaria cells in vitro. Endocrinology. 1987;121(6):1985-1992.
253. Sethe S, Scutt A, Stolzing A. Aging of mesenchymal stem cells. Ageing Research Reviews. 2006;5(1):91-116.
254. Kelley RO, Fallon JF. Identification and distribution of gap junctions in the mesoderm of the developing chick limb bud. Journal of Embryology and Experimental Morphology. 1978;46:99-110.
255. SPSS, USA. The SPSS TwoStep Cluster Component. A scalable component enabling more efficient customer segmentation. White Paper – Technical Report. (2004) Available at: http://www.spss.ch/upload/1122644952_The%20SPSS%20TwoStep%20Cluster%20Component.pdf (Accessed: 15th September 2014).

256. Parfitt AM. Bone-forming cells in clinical conditions. In: Hall BK, ed. Bone. Vol 1: the osteoblast and osteocyte. Boca Raton, FL: Telford Press and CRC Press; 1990:351-429.
257. Ekanayake S, Hall BK. he development of acellularity of the vertebral bone of the Japanese medaka, Oryzias latipes (Teleostei; Cyprinidontidae). Journal of Morphology. 1987;193(3):253-261.
258. Marvaso V, Bernard GW. Initial intramembranous osteogenesis in vitro. American Journal of Anatomy. 1977;149:453-468.
259. Nijweide PJ, Mulder RJP. Identification of osteocytes in osteoblast-like cell cultures using a monoclonal antibody specifically directed against osteocytes.. Histochemistry. 1986;84(4-6):342-347.
260. van der Plas A, Nijweide PJ. Cell-cell interactions in the osteogenic compartment of bone. Bone (New York). 1988;9(2):107-112.
261. Bernard GW, Pease DC. An electron microscopic study of initial intramembranous osteogenesis. American Journal of Anatomy. 1969;125(3):271-290.
262. Platt JR. Strong Inference: Certain systematic methods of scientific thinking may produce much more rapid progress than others. Science. 1964;146(364):347-353.
263. Hall BK, Miyake T. Divide, accumulate, differentiate: Cell condensation in skeletal development revisited. International Journal of Developmental Biology. 1995;39(6):881-893.
264. Bellows CG, Aubin JE. Determination of numbers of osteoprogenitors present in isolated fetal rat calvaria cells in vitro.. Developmental Biology. 1989;133(1):8-13.
265. Ecarotcharrier B, Shepard N, Charette G, Grynpas M, Glorieux FH. Mineralization in osteoblast cultures: a light and electron microscopic study. Bone. 1988;9(3):147-154.
266. Maniatopoulos C, Sodek J, Melcher AH. Bone formation in vitro by stromal cells obtained from bone marrow of young adult rats. Cell and Tissue Research. 1988;254(2):317-330.
267. Nefussi JR, Boylefevre ML, Boulekbache H, Forest N. Mineralization in vitro of matrix formed by osteoblasts isolated by collagenase digestion. Differentiation. 1985;29(2):160-168.
268. Kadow-Romacker A, Hoffmann JE, Duda G, Wildemann B, Schmidmaier G. Effect of Mechanical Stimulation on Osteoblast- and Osteoclast-Like Cells in vitro. Cells Tissues Organs. 2009;190(2):61-68.
269. Adachi T, Sato K, Tomita Y. Directional dependence of osteoblastic calcium response to mechanical stimuli. Biomechanics and Modeling in Mechanobiology. 2003;2(2):73-82.
270. Frenz DA, Jaikaria NS, Newman SA. The mechanism of precartilage mesenchymal condensation: a major role for interaction of the cell surface with the amino-terminal heparin-binding domain of fibronectin. Developmental Biology. 1989;136(1):97-103.
271. Knudson CB, Toole BP. Changes in the pericellular matrix during differentiation of limb bud mesoderm. Developmental Biology. 1985;112(2):308-318.
272. Downie SA, Newman SA. Different roles for fibronectin in the generation of fore and hind limb precartilage condensations. Developmental Biology. 1995;172(2):519-530.
273. Christley S, Alber MS, Newman SA. Patterns of mesenchymal condensation in a multiscale, discrete stochastic model. PLoS Computational Biology. 2007;3(4):e76.
274. Newman SA, Christley S, Glimm T, et al. Multiscale models for vertebrate limb development. Current Topics in Developmental Biology. 2008;81:311-340.
275. Mammoto T, Mammoto A, Torisawa YS, et al. Mechanochemical control of mesenchymal condensation and embryonic tooth organ formation. Developmental Cell. 2011;21(4):758-769.
276. Freshney I, Obradovic B, Grayson W, Cannizzaro C, Vunjak-Novakovic G. Principles of tissue culture and bioreactor design. In: Lanza R, Langer R, Vacanti J, eds. Principles of Tissue Engineering. 3rd ed2007:155–184.
277. Wendt D, Riboldi S, Cioffi M, Martin I. Bioreactors in Tissue Engineering: Scientific Challenges and Clinical Perspectives. In: Kasper C, van Griensven M, Portner R, eds. Bioreactor Systems in Tissue Engineering. Vol 112. Berlin: Springer; 2009:1-27.
278. Chung CA, Yang CW, Chen CW. Analysis of cell growth and diffusion in a scaffold for cartilage tissue engineering. Biotechnology and Bioengineering. 2006;94(6):1138-1146.
279. Langer R, Vacanti JP. Tissue Engineering. Science. 1993;260(5110):920-926.
280. Mertsching H, Hansmann J. Bioreactor Technology in Cardiovascular Tissue Engineering. In: Kasper C, van Griensven M, Portner R, eds. Bioreactor Systems for Tissue Engineering. Vol 112. Berlin: Springer; 2009:29-37.
281. Fuchs JR, Nasseri BA, Vacanti JP. Tissue engineering: A 21st century solution to surgical reconstruction. Annals of Thoracic Surgery. 2001;72(2):577-591.
282. Chung CA, Lin TH, Chen SD, Huang HI. Hybrid cellular automaton modeling of nutrient modulated cell growth in tissue engineering constructs. Journal of Theoretical Biology. 2010;262(2):267-278.

283. Lapin A, Paaschen T, Junghans K, Lubbert A. Bubble column fluid dynamics, flow structures in slender columns with large-diameter ring-spargers. Chemical Engineering Science. 2002;57(8):1419-1424.
284. Lee Y, Kouvroukoglou S, McIntire LV, Zygourakis K. A cellular automaton model for the proliferation of migrating contact-inhibited cells. Biophysical Journal. 1995;69(4):1284-1298.
285. Galbusera F, Cioffi A, Raimondi MT, Pietrabissa R. Computational modeling of combined cell population dynamics and oxygen transport in engineered tissue subject to interstitial perfusion. Computer Methods in Biomechanics and Biomedical Engineering. 2007;10(4):279-287.
286. Galbusera F, Cioffi M, Raimondi MT. An in silico bioreactor for simulating laboratory experiments in tissue engineering. Biomedical Microdevices. 2008;10(4):547-554.
287. Galban CJ, Locke BR. Effects of spatial variation of cells and nutrient and product concentrations coupled with product inhibition on cell growth in a polymer scaffold. Biotechnology and Bioengineering. 1999;64(6):633-643.
288. Lapin A, Muller D, Reuss M. Dynamic behavior of microbial populations in stirred bioreactors simulated with Euler-Lagrange methods: Traveling along the lifelines of single cells. Industrial & Engineering Chemistry Research. 2004;43(16):4647-4656.
289. Lapin A, Schmid J, Reuss M. Modeling the dynamics of E-coli populations in the three-dimensional turbulent field of a stirred-tank bioreactor - A structured-segregated approach. Chemical Engineering Science. 2006;61(14):4783-4797.
290. Lapin A, Klann M, Reuss M. Multi-Scale Spatio-Temporal Modeling: Lifelines of Microorganisms in Bioreactors and Tracking Molecules in Cells. In: Wittmann C, Krull R, eds. Biosystems Engineering Ii: Linking Cellular Networks and Bioprocesses. 2010;121:23-43.
291. Rejniak KA, Anderson ARA. Hybrid models of tumor growth. Wiley Interdisciplinary Reviews-Systems Biology and Medicine. 2011;3(1):115-125.
292. Jiang Y, Pjesivac-Grbovic J, Cantrell C, Freyer JP. A multiscale model for avascular tumor growth. Biophysical Journal. 2005;89(6):3884-3894.
293. Gatenby RA, Smallbone K, Maini PK, et al. Cellular adaptations to hypoxia and acidosis during somatic evolution of breast cancer. British Journal of Cancer. 2007;97(5):646-653.
294. Bailey AM, Thorne BC, Peirce SM. Multi-cell agent-based simulation of the microvasculature to study the dynamics of circulating inflammatory cell trafficking. Annals of Biomedical Engineering. 2007;35(6):916-936.
295. Merks RMH, Brodsky SV, Goligorksy MS, Newman SA, Glazier JA. Cell elongation is key to in silico replication of in vitro vasculogenesis and subsequent remodeling. Developmental Biology. 2006;289(1):44-54.
296. Picioreanu C, van Loosdrecht MCM, Heijnen JJ. A new combined differential-discrete cellular automaton approach for biofilm modeling: Application for growth in gel beads. Biotechnology and Bioengineering. 1998;57(6):718-731.
297. Picioreanu C, Kreft JU, van Loosdrecht MCM. Particle-based multidimensional multispecies Biofilm model. Applied and Environmental Microbiology. 2004;70(5):3024-3040.
298. Alpkvist E, Picioreanu C, van Loosdrecht MCM, Heyden A. Three-dimensional biofilm model with individual cells and continuum EPS matrix. Biotechnology and Bioengineering. 2006;94(5):961-979.
299. Kreft JU, Picioreanu C, Wimpenny JWT, van Loosdrecht MCM. Individual-based modelling of biofilms. Microbiology. 2001;147:2897-2912.
300. Sun T, Adra S, Smallwood R, Holcombe M, MacNeil S. Exploring Hypotheses of the Actions of TGF-beta 1 in Epidermal Wound Healing Using a 3D Computational Multiscale Model of the Human Epidermis. PLoS One. 2009;4(12):e8515.
301. Solovyev A, Mi Q, Tzen Y-T, Brienza D, Vodovotz Y. Hybrid Equation/Agent-Based Model of Ischemia-Induced Hyperemia and Pressure Ulcer Formation Predicts Greater Propensity to Ulcerate in Subjects with Spinal Cord Injury. PLoS Computational Biology. 2013;9(5): e1003070.
302. Drasdo D, Hohme S. A single-cell-based model of tumor growth in vitro: monolayers and spheroids. Physical Biology. 2005;2(3):133-147.
303. Rejniak KA. A single-cell approach in modeling the dynamics of tumor microregions. Mathematical Biosciences and Engineering. 2005;2(3):643-655.
304. Kim Y, Stolarska MA, Othmer HG. A hybrid model for tumor spheroid growth in vitro I: Theoretical development and early results. Mathematical Models & Methods in Applied Sciences. 2007;17(1):1773-1798.

305. Tao S, McMinn P, Coakley S, Holcombe M, Smallwood R, MacNeil S. An integrated systems biology approach to understanding the rules of keratinocyte colony formation. Journal of the Royal Society Interface. 2007;4(17):1077-1092.
306. Liu T, Laurell C, Selivanova G, Lundeberg J, Nilsson P, Wiman KG. Hypoxia induces p53-dependent transactivation and Fas/CD95-dependent apoptosis. Cell Death and Differentiation. 2007;14(3):411-421.
307. Lee Y. Computer-Assisted Analysis of Endothelial Cell Migration and Proliferation. Houston, TX, Rice Univerisity; 1994.
308. Burgess BT, Myles JL, Dickinson RB. Quantitative analysis of adhesion-mediated cell migration in three-dimensional gels of RGD-grafted collagen. Annals of Biomedical Engineering. 2000;28(1):110-118.
309. Weidt C, Niggemann B, Hatzmann W, Zanker KS, Dittmar T. Differential effects of culture conditions on the migration pattern of stromal cell-derived factor-stimulated hematopoietic stem cells. Stem Cells. 2004;22(6):890-896.
310. Muinonen-Martin AJ, Veltman DM, Kalna G, Insall RH. An Improved Chamber for Direct Visualisation of Chemotaxis. PLoS One. 2010;5(12):e15309.
311. Muinonen-Martin A. RE: Insall Chamber - PLoS One. In: Kaul H, ed. Email ed November, 2012.
312. Muinonen-Martin A. RE: Insall Chamber - PLoS One. In: Kaul H, ed. Email ed November, 2012.
313. Selivanova OM, Shiryaev VM, Tiktopulo EI, Potekhin SA, Spirin AS. Compact globular structure of Thermus thermophilus ribosomal protein S1 in solution - Sedimentation and calorimetric study. Journal of Biological Chemistry. 2003;278(38):36311-36314.
314. Muinonen-Martin AJ, Susanto O, Zhang Q, et al. Melanoma Cells Break Down LPA to Establish Local Gradients That Drive Chemotactic Dispersal. PLoS Biology. 2014;12(10):e1001966.
315. Berens P. CircStat: A MATLAB Toolbox for Circular Statistics. Journal of Statistical Software. 2009;31(10):1-21.
316. Kay RR, Langridge P, Traynor D, Hoeller O. Changing directions in the study of chemotaxis. Nature Reviews Molecular Cell Biology. 2008;9(6):455-463.
317. Grayson WL, Bhumiratana S, Cannizzaro C, et al. Effects of Initial Seeding Density and Fluid Perfusion Rate on Formation of Tissue-Engineered Bone. Tissue Engineering Part A. 2008;14(11):1809-1820.
318. Aunins JG, Bader B, Caola A, et al. Fluid mechanics, cell distribution, and environment in CellCube bioreacors. Biotechnology Progress. 2003;19(1):2-8.
319. Klein TJ, Malda J, Sah RL, Hutmacher DW. Tissue Engineering of Articular Cartilage with Biomimetic Zones. Tissue Engineering Part B-Reviews. 2009;15(2):143-157.
320. Schafer M. Finite-Volume Methods. Computational Engineering – Introduction to Numerical Methods. Berlin, Heidelberg: Springer-Verlag; 2006:77-105.
321. Webster R. An algebraic multigrid solver for Navier-Stokes problems. International Journal for Numerical Methods in Fluids. 1994;18(8):761-780.

Appendix

A.1 THE NUMERICAL SCHEME

When working with a cell-centred variable arrangement, the averaged value of any quantity inside a CV is given by its value at the cell centre[83]. **CFD-ACE+** achieves this by employing spatial differencing schemes that interpolate the values of the quantity of interest wherever they are needed; notably on the control volume (inter)faces. The central difference scheme (CDS) is an interpolation scheme offered by **CFD-ACE+** to define the algebraic equations at the cell-centre.

A.1.1 CENTRAL DIFFERENCING SCHEME

The central differencing scheme assumes a linear variation of Φ between two cell centres *P* and *E*, as shown in Figure 2.5, and calculates Φ_S by distance-weighted averaging the values at the cell centres. For the face *e* of the 2D Cartesian grid shown in Figure 3.1, the interpolation is captured mathematically by (A.1).

$$\int_e [\rho U\Phi - \Gamma_\Phi \nabla\Phi].\overrightarrow{n_e} dS = \left(\rho u_1 \Phi - \Gamma \frac{\partial \Phi}{\partial x_1}\right)_e A_e \qquad \text{(A.1)}$$

The conserved quantity at *e* is calculated as follows:

$$\Phi_e = \frac{\Phi_P + \Phi_E}{2} \qquad \text{(A.2)}$$

$$\left(\frac{\partial \Phi}{\partial x_1}\right) = \frac{\Phi_E - \Phi_P}{\delta x_1} \qquad \text{(A.3)}$$

These expressions are then substituted back into the finite-volume expression, and the entire approach is applied to all surfaces of a control volume (in all dimensions). The resulting general expression is as follows:

$$a_P \Phi_P = \sum_{S}^{neighbour\ nodes} a_S \Phi_S + S_P \qquad \text{(A.4)}$$

In (A.4), the coefficients a_P and a_S are related to the summation of terms from equations (A.2) and (A.3) for all faces of CV, and S_P represents the discretised source term. As U and Φ_P are in these coefficients are usually unknown, equations are solved iteratively over the entire mesh.

Central differencing approximations are independent of the direction of the velocity vector. Unphysical oscillations may appear in the numerical solution when using CDS[320] if the mesh is not sufficiently fine. Although CDS can be shown to be second order accurate, if the local strength of normalised convection exceeds the local strength of normalised diffusion (in a Peclet number sense), it may lead to unstable and unbounded solutions.[83] Most iterative methods tend to be unstable when central difference scheme is used to evaluate convection terms, if the grid is not adequately fine. Stability can be achieved by introducing artificial/numerical viscosity or by reducing cell size (i.e. grid refinement).[77] The former is computationally inexpensive but reduces the nominal level of accuracy of the methodology. The latter involves computing on finer grids; it is nevertheless the approach we followed in this study to ensure numerically stable and physically plausible solutions.

A.1.2 TEMPORAL DISCRETISATION

Temporal accuracy is quite essential when simulating problems of transient nature: both flow as well as transport. **CFD-ACE+** allows for the use of both the first-order Euler and the implicit second-order Crank-Nicolson schemes. The transient simulations in this thesis were solved using a variant of the Crank-Nicolson scheme, which enables the user to enter a blending factor (γ). The differencing, in 1D x-direction, is performed as follows:

$$\frac{\Phi_j^{n+1} - \Phi_j^n}{\Delta t} = k\left(\gamma \frac{\Phi_{j+1}^{n+1} - 2\Phi_j^{n+1} + \Phi_{j-1}^{n+1}}{\Delta x^2} + (1-\gamma)\frac{\Phi_{j+1}^{n} - 2\Phi_j^{n} + \Phi_{j-1}^{n}}{\Delta x^2}\right) \quad \text{(A.5)}$$

In (A.5), Δt is the time step, n the current time, and j the current cell in which the computation is being performed for Φ. k represents the diffusion coefficient. The right-hand side of the equation provides both stability (first part) and accuracy (second part). The default blending factor of 0.6 was used for all transient computations in this thesis. The Crank-Nicholson scheme is a time discretisation scheme, which itself is a finite differencing – time, unlike space, is one-dimensional and has no volume. As such, despite the 'finite differencing', the scheme remains applicable for time discretisation in FVM.

A.1.3 PRESSURE CORRECTION

A notable absence in the variables that have been discussed heretofore is that of pressure. Despite the fact that pressure is an important part of the momentum equations, it does not appear in the continuity equation.[77] On the other hand, all velocity components appear in each momentum equation and continuity equation.[131] A method is, therefore, required to ensure that the computed velocity field satisfies the continuity equation. For incompressible flow, where density is constant and hence not linked to pressure, the continuity equation is used to formulate an equation for pressure.[131] This pressure correction equation is solved concurrently with other discretised equations.[83] The resulting pressure correction field is used to update the velocity and pressure field,[131] and ensure that velocity field satisfies continuity at convergence.[83] In **CFD-ACE+**, the inherently iterative *Semi-Implicit for Pressure-Linked Equations Consistent* (SIMPLEC) scheme,[181] an adaptation of the SIMPLE method,[182] is implemented to achieve pressure correction.

The SIMPLEC algorithm starts by guessing a pressure field, p^*. Discretised momentum equations are then solved using p^* yielding velocity component U^*. In (A.6), the u-momentum equation for an arbitrary control volume centred at *e* is given.

$$a_e u_e = \sum a_{nb} u_{nb} + (p_P - p_E) A_e + b_e \tag{A.6}$$

where,

$$a_e = \left(\sum a_{nb} - S_e \Delta V\right)\left(1 + \frac{1}{E}\right) \tag{A.7}$$

In (A.6) and (A.7), *A* represents the area of the face of *P* control volume at *e*, *p* the pressure, *b* the momentum source term, and S_e the coefficient of u_e in the linearised source term. The sub-script *nb* refers to summation taken over all the neighbouring nodes; *P* and *E* to grid points (refer to Figure A.1).

$$a_e u*_e = \sum a_{nb} u*_{nb} + (p*_P - p*_E) A_e + b_e \tag{A.8}$$

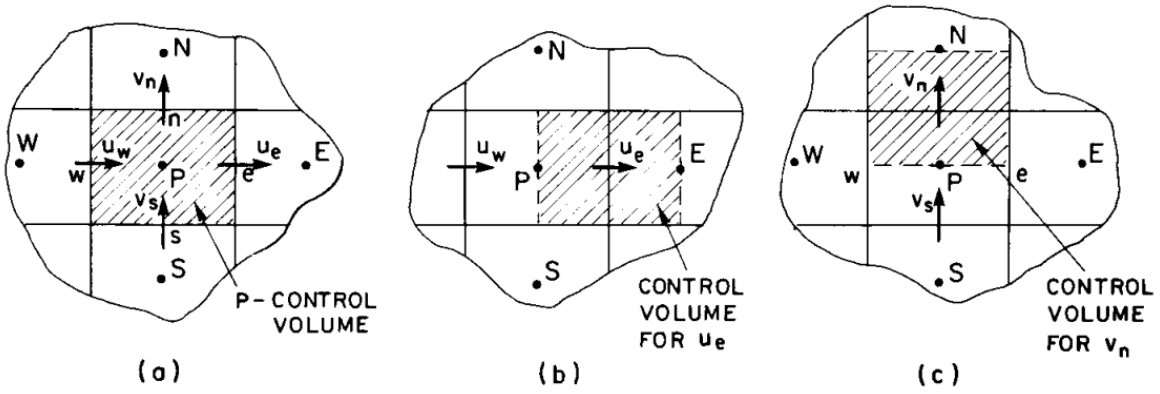

Figure A. 1: Sections of a Cartesian grid showing the placement of control-volume boundaries. Reprinted with kind permission (pending) from Ref. [181] © (1984) Taylor & Francis Online.

Figure A.1 represents this notation system based on grid lines and cell faces. Assuming *p* to be the correct (but generally unknown) pressure, the difference between *p* and p^* results in the correction, p' (refer to A.9).

$$p = p* + p' \tag{A.9}$$

$$u = u* + u' \tag{A.10}$$

u* obtained using (A.8) in general violate continuity and, therefore, require correction, which is based on p' (refer to A.10). Subtracting (A.6) and (A.8) yield the relation between p' and u', shown in (A.11).

$$a_e(u_e - u*_e) = \sum a_{nb}(u_{nb} - u*_{nb}) + [(p_P - p*_P) - (p_E - p*_E)]A_e \tag{A.11}$$

Using (A.10), (A.11) can be written as (A.12).

$$a_e u'_e = \sum a_{nb} u'_{nb} + (p'_P - p'_E)A_e \tag{A.12}$$

Subtracting $\Sigma a_{nb} u'_e$ from both sides of (A.12) yields

$$\left(a_e - \sum a_{nb}\right) u'_e = \sum a_{nb}(u'_{nb} - u'_e) + (p'_P - p'_E)A_e \tag{A.13}$$

This is followed by the main approximation in SIMPLEC, where the first element of the right hand side $[\Sigma a_{nb} (u'_{nb} - u'_e)]$ is neglected. Substituting (A.10) into (A.12) yields

$$u_e = u*_e + (p'_P - p'_E)d_e \tag{A.14}$$

where,

$$d_e = \frac{A_e}{a_e - \sum a_{nb}} \tag{A.15}$$

Once the correct values of pressure and velocity fields are obtained, other discretised transport equations are solved. Figure A.2 depicts the SIMPLEC algorithm that **CFD-ACE+** uses to evaluate pressure and velocity fields.

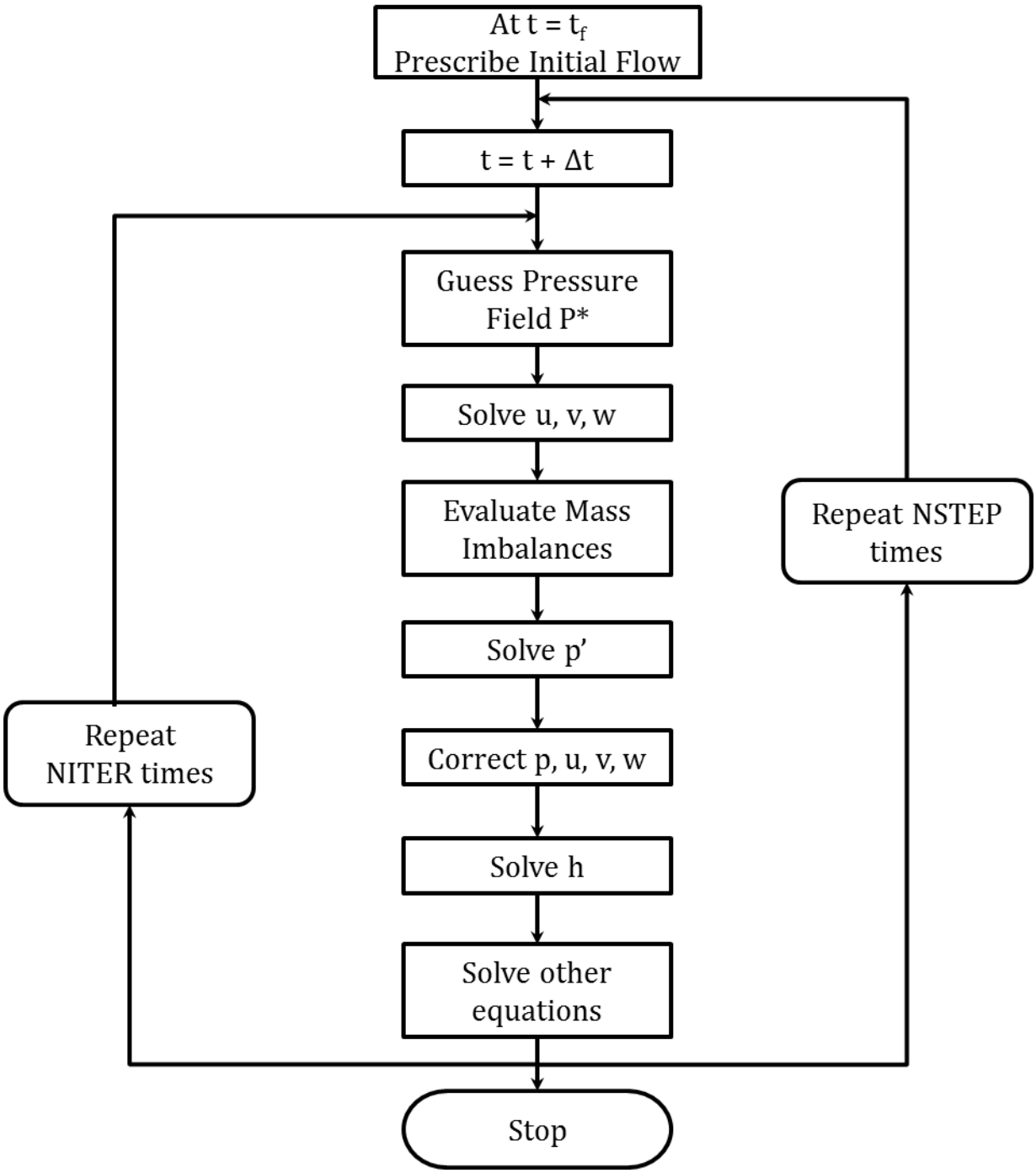

Figure A. 2: The Simplec. The flowchart represents the Simplec algorithm employed to solve for pressure correction[181]. The image was adapted from **CFD-ACE+** User Manual.[77]

A.1.4 ITERATIVE EQUATION SOLVERS – ALGEBRAIC MULTIGRID

After the equation set for a variable has been assembled it can be solved by direct or iterative equation solvers. Iterative equation solvers are preferred as they tend to be economical in terms of memory usage. In **CFD-ACE+**, the *conjugate gradient squared* (CGS) solver and the *algebraic multigrid* (AMG) solver are employed as the iterative equation solvers. The

computational work conducted in this thesis utilised the latter exclusively. The AMG solver uses a hierarchy of grids, from fine to coarse, and back to fine, to solve the resulting set of pseudo-linear equations. After obtaining the residual field on the fine grid, iterations are performed on the coarse grid to obtain corrections (imposing fine-grid residuals as the source term). The AMG solver works by interpolating the corrections to the fine-grid and updating the fine grid solution, and repeating the entire procedure until the residual is reduced to the desired level.[77] This results in reducing error of multiple wavelengths at once, with the significant advantage of faster convergence.[77]

While discussion on the AMG solver is beyond the purview of this thesis, a brief description is provided for the benefit of the reader (details can be found elsewhere[321]). For a generic solution to an equation set, represented below, for the single-variable set **x**, this is achieved by generating a coarse-grid reduced equation set, shown below.

$$Ax = b \tag{A.16}$$

$$A^c x^c = b^c \tag{A.17}$$

$$A^c = KAK^T \tag{A.18}$$

A coarsening operator *K* is applied to obtain A.17. Deriving b^c on the basis of the residual in (A.16), the solution of (A.17) provides a correction xc that can be employed to improve the solution

$$x^{n+1} = x^n + K^T x^c \tag{A.19}$$

where x^n represents the latest iterate and x^{n+1} the next iterate. The procedure is recursively applied to (A.17) and successively coarser grids. Coarsening occurs by seeking nodes with strongest coupling (largest off-diagonals in *A*) and adding their respective equations, thereby, forming a new coarse grid representative of a number of fine grid nodes. AMG requires no

special measures to treat unstructured, non-uniform computational meshes. As long as the boundary conditions are implicitly contained in the equation set, the required information is automatically transferred to the reduced equation sets/coarser grids by the K-operator. As such, the boundary conditions require no special treatment.[321]